

POLISH ACADEMY OF SCIENCES

NALE CZ INSTITUTE OF BIOCYBERNETICS AND BIOMEDICAL ENGINEERING

DOCTORAL THESIS

**Mathematical modeling of the tumor
microenvironment with the aim of
studying its heterogeneity as a driver of
treatment resistance and a potential
therapy target**

Author:
Mgr Julia GRAJEK

Supervisor:
Dr. hab. Jan POLESZCZUK

*A thesis submitted in fulfillment of the requirements
for the degree of Doctor of Philosophy*

in the

Doctoral School of Information and Biomedical Technologies

26.09.2023

Declaration of Authorship

I, Julia Grajek, declare that this thesis titled, “Mathematical modeling of the tumor microenvironment with the aim of studying its heterogeneity as a driver of treatment resistance and a potential therapy target” and the work presented in it are my own. I confirm that:

- This work was done wholly while in candidature for a research degree at the Doctoral School of Information and Biomedical Technologies at the Polish Academy of Sciences.
- Where I have consulted the published work of others, this is always clearly attributed.
- Where I have quoted from the work of others, the source is always given. With the exception of such quotations, this thesis is entirely my own work.
- I have acknowledged all main sources of help.
- Where the thesis is based on work done by myself jointly with others, I have made clear exactly what was done by others and what I have contributed myself.

Signed:

Date:

List of publications

Publications included in the thesis

- [1] **Grajek J**, Kather NL, Poleszczuk J, An in silico model to study the impact of carbonic anhydrase IX expression on tumour growth and anti-PD-1 therapy, *Journal of the Royal Society Interface*; 20(198), 2023, 1742-5662, doi: 10.1098/rsif.2022.0654
- [2] **Grajek J**, Poleszczuk J, Carbonic Anhydrase IX Suppression Shifts Partial Response to Checkpoint Inhibitors into Complete Tumor Eradication: Model-Based Investigation, *International Journal of Molecular Sciences*; 24(12):10068, 2023, doi: 10.3390/ijms241210068
- [3] Schniewind I, Hadiwikarta WW, **Grajek J**, Poleszczuk J et al., Cellular plasticity upon proton irradiation determines tumor cell radiosensitivity, *Cell Reports*; 38(8), 2022, 110422, ISSN 2211-1247, doi: 10.1016/j.celrep.2022.110422

Publication not included in the thesis

- [1] Ghaffari Laleh N, Loeffler CML, **Grajek J**, Staňková K, Pearson AT, et al., Classical mathematical models for prediction of response to chemotherapy and immunotherapy; *PLOS Comput Biol* 2022; 18(2), e1009822. doi: 10.1371/journal.pcbi.1009822

Contents

Declaration of Authorship	iii
List of publications	v
1 Summary	1
1.1 English summary	1
1.1.1 Chapter 1: Introduction	2
1.1.2 Chapter 2: Research Aims and Hypotheses	2
1.1.3 Chapter 3: An in silico model to study the impact of carbonic anhydrase IX expression on tumor growth and anti-PD-1 therapy	2
1.1.4 Chapter 4: Carbonic anhydrase IX suppression shifts partial response to checkpoint inhibitors into complete tumor eradication: model-based investigation	3
1.1.5 Chapter 5: Cellular plasticity upon proton irradiation determines tumor cell radiosensitivity	3
1.1.6 Chapter 6: Discussion	4
1.2 Streszczenie w języku polskim	4
1.2.1 Rozdział 1: Introduction	5
1.2.2 Rozdział 2: Research Aims and Hypotheses	5
1.2.3 Rozdział 3: An in silico model to study the impact of carbonic anhydrase IX expression on tumor growth and anti-PD-1 therapy	6
1.2.4 Rozdział 4: Carbonic anhydrase IX suppression shifts partial response to checkpoint inhibitors into complete tumor eradication: model-based investigation	6
1.2.5 Rozdział 5: Cellular plasticity upon proton irradiation determines tumor cell radiosensitivity	7
1.2.6 Rozdział 6: Discussion	8
2 Introduction	9
2.1 Biological background and significance	9
2.1.1 Immune checkpoint inhibitors	10
Mechanism of action	10
Rationale for further research on ICI resistance	11
State of the art of biomarker research	12
The TME as a biomarker source	13
2.1.2 Radiotherapy	14
Rationale for further research on radioresistance	14
Cancer stem cells as potential resistance drivers	15
Proton beam therapy	16
2.2 <i>In silico</i> modeling in oncology	17
2.2.1 <i>In silico</i> models of immune checkpoint inhibitor therapy	18

2.2.2	<i>In silico</i> models of radiotherapy	21
3	Research Aims and Hypotheses	25
4	An <i>in silico</i> model to study the impact of carbonic anhydrase IX expression on tumor growth and anti-PD-1 therapy	27
4.1	Introduction	27
4.2	Relation of the publication to the research aims of the thesis	27
4.2.1	Build a model of tumor-immune interactions on a single cell level to provide a tool for identifying immunotherapy biomarkers in the TME as well as determining resistance mechanisms that could be promising targets for combination therapy	27
4.2.2	Study the impact of tumoral CAIX expression on the evolution of the TME and ICI effectiveness <i>in silico</i> , and evaluate it as a combination therapy target with ICIs	29
4.3	The publication	30
5	Carbonic anhydrase IX suppression shifts partial response to checkpoint inhibitors into complete tumor eradication: model-based investigation	53
5.1	Introduction	53
5.2	Relation of the publication to the research aims of the thesis	54
5.2.1	Study the impact of tumoral CAIX expression on the evolution of the TME and ICI effectiveness <i>in silico</i> , and evaluate it as a combination therapy target with ICIs	54
5.3	The publication	55
6	Cellular plasticity upon proton irradiation determines tumor cell radiosensitivity	73
6.1	Introduction	73
6.2	Relation of the publication to the research aims of the thesis	74
6.2.1	Model and analyze the influence of cancer cell plasticity on tumor heterogeneity and the effectiveness of X-ray and proton radiotherapy.	74
6.3	The publication	75
7	Discussion	115
7.1	Achievement of research aims	115
7.2	Limitations and future perspectives	117

List of Abbreviations

ABM	agent based model
ALDH	aldehyde dehydrogenase
APC	antigen presenting cell
CA	cellular automaton
CAIX	carbonic anhydrase IX
CC	cancer cell
CSC	cancer stem cell
CTLA-4	cytotoxic T lymphocyte antigen 4
ICI	immune checkpoint inhibitors
irAE	immune-related adverse events
irRC	immune-related response criteria
LQ	linear-quadratic
MHC	major histocompatibility complex
ODE	ordinary differential equation
PBT	proton beam therapy
PD-1	programmed cell death 1
PD-L1	PD-1 ligand 1
RBE	relative biological effectiveness
RECIST	response evaluation criteria in solid tumours
TCR	T-cell receptor
TIL	tumor infiltrating lymphocyte
TMB	tumor mutational burden
TME	tumor microenvironment

Chapter 1

Summary

1.1 English summary

Despite great advances in cancer therapies over the past decades, treatment resistance remains a significant challenge. It can manifest as intrinsic resistance, where patients do not respond to certain therapies at all, or as acquired resistance, which develops over the course of the treatment. Identifying the contributors to this resistance could improve existing therapies, propose promising combination therapy approaches, and possibly even bring about new treatment ideas. Therefore, further investigation of the causes underlying treatment failure is crucial to the improvement of oncology patients' lives.

The tumor microenvironment (TME) harbors some of the putative factors driving treatment resistance. It encompasses the tumor itself and its neighborhood. The TME comprises cancer cells (CC), cancer stem cells (CSC), blood vessels, immune cells, stromal cells, and the extracellular matrix. Importantly, the different parts of the TME are interconnected, creating a complex and heterogeneous network of alleged drug resistance factors, which is not yet fully explored. This offers an exciting opportunity for computational and mathematical modeling, which can capture the intricacies of the TME and aid in identifying or validating resistance drivers and combination therapy targets to improve treatment response rates.

Hence, the aim of this doctoral thesis was to use mathematical and computational modeling to explore the heterogeneity of the tumor microenvironment as a contributor to treatment resistance and source of potential combination therapy targets. In particular, I focused on two parts of the TME: the acidic niche and the stem cell population. First, I investigated tumoral expression of the pH-regulatory enzyme CAIX as a biomarker for immune checkpoint inhibitor therapy (ICI) and a potential combination therapy target. Then, I studied cellular plasticity, i.e. the ability of cancer cells to acquire and lose stemness properties, as a resistance factor for radiotherapy. The results of these investigations have been published in three scientific publications, which form the basis of this thesis. These publications are presented in chapters 3-5 of this thesis, each preceded by a short introduction summarizing the publication, highlighting my contributions, and delineating the relationship between the publications and the research goals and hypotheses stated in this thesis. Additionally, the thesis contains an introduction chapter, which provides some background on the investigated biological problems, reviews relevant literature, and explains the importance of the research topics. This is followed by a chapter consisting of the list of research aims I have set for this thesis and the corresponding research hypotheses. Finally, the thesis concludes with a discussion chapter summarizing the most important results and conclusions, reiterating how the research aims have been achieved, elaborating on the studies' limitations, and pointing to some promising future research perspectives.

1.1.1 Chapter 1: Introduction

This chapter is an introduction to the research topic. It explains the significance of studying drivers of treatment resistance, enumerates known factors of resistance, and proposes the TME as a potential source of treatment resistance factors for immune checkpoint inhibitor therapy (in particular anti-PD-1 and anti-CTLA-4 therapy) and radiotherapy (both conventional photon radiotherapy and proton beam therapy). This chapter consists of two sections. The first gives the necessary biological background: it explains the mechanism of action of the studied treatments, elaborates on the importance of improving their response rates, provides the state of the art in the study of their treatment resistance drivers, and introduces the putative resistance factors that I am investigating in this thesis. The second section gives an outline of mathematical and computational models of radio- and immunotherapy found in the literature, focusing on models that helped clarify causes of treatment resistance.

1.1.2 Chapter 2: Research Aims and Hypotheses

The second chapter enumerates the detailed research aims of this thesis, together with the postulated research hypotheses. The following three chapters are each devoted to one of the publications, which form the basis of the thesis, and their connection with the aforementioned research aims and hypotheses.

1.1.3 Chapter 3: An *in silico* model to study the impact of carbonic anhydrase IX expression on tumor growth and anti-PD-1 therapy

This chapter corresponds to the publication by the same title, of which I am the first and main author and which was published in the *Journal of the Royal Society Interface* in January 2023. Here, I proposed a computational model of the tumor and its microenvironment, in order to investigate the relatively low response rate to immune checkpoint inhibitors and to study CAIX expression as a biomarker and potential combination therapy target for anti-PD-1 therapy. This hybrid model consists of an agent-based part (ABM), which simulates the behavior of cancer and immune cells, and a partial-differential equation model describing substance gradients in the TME. The choice of such a model type was motivated by the fact, that ABMs intrinsically capture heterogeneity and stochasticity of the simulated environment, fitting the aim of the exploration of the heterogeneous TME. Furthermore, they are known to produce emergent phenomena, making them a perfect candidate for identifying potential biomarkers and exploring research hypotheses. The proposed model can serve as a high-throughput tool to identify biomarkers for immunotherapy and explore combination therapy approaches, in line with my first research aim. In my thesis, I used it to qualitatively reproduce findings from *in vivo* experiments on the influence of CAIX on the TME, visualize the impact of CAIX expression on the TME and immune response, and analyze its influence on anti-PD-1 effectiveness in tumors with and without pre-treatment PD-L1 expression. The *in silico* simulations suggest that low PD-L1 expression prior to CAIX inhibition should not disqualify patients from receiving combination therapy with anti-CAIX and anti-PD-1, contributing to the explanation of conflicting findings in studies of PD-L1 as an ICI biomarker and corroborating the use of dynamic PD-L1 expression instead. Furthermore, the findings propose CAIX as a putative ICI biomarker and combination therapy target, in line with my second research aim.

1.1.4 Chapter 4: Carbonic anhydrase IX suppression shifts partial response to checkpoint inhibitors into complete tumor eradication: model-based investigation

In this chapter, I introduce an ordinary differential equation model which I build to supplement the agent-based model presented in the previous chapter. It corresponds to the publication "Carbonic anhydrase IX suppression shifts partial response to checkpoint inhibitors into complete tumor eradication: model-based investigation", of which I am the first and main author and which was published in the *International Journal of Molecular Sciences* in June 2023. This continuous model is informed by the qualitative results obtained from the ABM simulations. However, thanks to its lower complexity this model allowed for calibration with *in vivo* data, quantitative simulations, mathematical analysis, and thus further validation of the previous findings and hypotheses. In this publication, I first studied a simplified yet realistic version of the proposed ordinary differential equation (ODE) model, which allowed for qualitative phase portrait analysis. This analysis, supplemented with numerical simulations, implied that CAIX suppression combined with an abundant immune response (e.g. induced by ICI) could shift the asymptotic behavior of the model from a stable tumor toward tumor eradication, supporting the conclusions derived from the ABM that CAIX suppression improves ICI responses. Motivated by these results obtained from the simplified model, I used the full continuous model to compare various combination therapies: anti-PD-1 and anti-CAIX, anti-CTLA-4 and anti-CAIX, anti-PD-1 and anti-CTLA-4, and finally the triple combination of both ICIs and anti-CAIX. In particular, I simulated transient treatment with various dosages, to reproduce the fact that therapies are not given indefinitely to patients. The *in silico* simulations suggest that monotherapies lead to tumor relapse, even after an initial response, whereas anti-CAIX combined with a sufficient ICI dose leads to a durable and complete response. These results and conclusions additionally contribute to the fulfillment of my second research aim. Furthermore, simulations indicate that anti-CAIX reduces the fraction of cancer stem cells, making it a combination therapy target for treatments that struggle with stem cell removal, such as chemotherapy.

1.1.5 Chapter 5: Cellular plasticity upon proton irradiation determines tumor cell radiosensitivity

The final results chapter was devoted to my contribution to the publication "Cellular plasticity upon proton irradiation determines tumor cell radiosensitivity", which was published in *Cell Reports* in February 2022. This publication was the result of an international collaboration led by dr. Claudia Peitzsch from the National Centre for Tumor Diseases in Dresden, Germany. I am the third author of this publication, however, my contribution constitutes an independent part of the study, i.e. the conceptualization, development and analysis of the ordinary differential equation model of cellular plasticity. The overall aim of this study was to study the impact of the more traditional X-ray and the less conventional proton radiotherapy on tumor heterogeneity, in particular on cancer stem cell (CSC) dynamics. Identification of treatments with superior CSC targeting capabilities is of utmost importance, as CSC removal is believed to be key to long-term tumor control after radiotherapy. The *in vitro* experiments performed by the research group were only able to capture the end effect of each irradiation type on the CSC population. Hence, I saw an opportunity for mathematical modeling, which could dive deeper and help identify the role of

plasticity events in the observed CSC dynamics. Therefore, I built an ordinary differential equation model of CC and CSC and their cellular plasticity. I calibrated the model with *in vitro* data and data found in literature and fitted it to the experimental observations. The model was not only able to represent experimental findings, but also underlined the importance of two types of plasticity events: regular plasticity events where CC acquire stemness, and reverse plasticity events, where CSC lose their stemness. In particular, I showed analytically, that both types of events had to be included in the model to represent a qualitative trend found in the experimental data. Furthermore, data fitting revealed a significantly lower rate of plasticity events after proton than photon irradiation, which could partially explain the higher therapeutic potential of proton therapy. In conclusion, bi-directional cellular plasticity seems to be crucial to explaining the CSC dynamics after irradiation and targeting it could reduce recurrence rates after radiotherapy. My contribution to this publication is in line with my third research aim.

1.1.6 Chapter 6: Discussion

The discussion chapter summarizes the most important conclusions obtained in this thesis while pointing out the limitations of the studies and proposing further research perspectives. In this thesis, I have identified CAIX expression and cancer cell plasticity as putative resistance mechanisms to ICIs and radiotherapy. However, while the mathematical analyses and *in silico* simulations are promising, these findings should be further validated *in vitro* and *in vivo*. During my research, I have also identified interesting avenues for further research, including the interplay between CAIX expression, stroma accumulation and ICI effectiveness, and the impact of ICIs on CSC dynamics. They were out of scope for this thesis, but constitute future perspectives worth further investigation.

In conclusion, this thesis fulfills all three research aims stated in its second chapter, and the obtained results and conclusions support my research hypotheses.

1.2 Streszczenie w języku polskim

Mimo ogromnych postępów w dziedzinie terapii przeciwnowotworowych poczynionych w ciągu ostatnich dziesięcioleci, oporność nowotworu na leczenie pozostaje znaczącym wyzwaniem. Dotyczy to zarówno oporności pierwotnej, polegającej na tym, że pacjenci w ogóle nie reagują na pewne terapie, jak i oporności nabytej, która rozwija się w trakcie leczenia. Zidentyfikowanie przyczyn tej oporności mogłoby pozwolić na poprawienie skuteczności istniejących terapii, zaproponowanie obiecujących terapii łączonych, a być może nawet zasugerowanie nowych opcji terapeutycznych. Dlatego dogłębne zbadanie mechanizmów wpływających na rozwój oporności na leczenie jest kluczowe dla poprawy przeżywalności pacjentów onkologicznych.

Mikrośrodowisko guza (tumor microenvironment, TME) jest potencjalnym źródłem czynników zmniejszających skuteczność leczenia. W skład TME wchodzi nowotworowe komórki macierzyste (cancer stem cells, CSC), zwykle komórki nowotworowe (cancer cells, CC), naczynia krwionośne, komórki układu odpornościowego, podścielisko i macierz pozakomórkowa. Co istotne, różne części TME są ze sobą powiązane, tworząc złożoną i heterogeniczną sieć potencjalnych czynników wpływających na oporność na leczenie, która nie została jeszcze w pełni zbadana.

Modelowanie komputerowe i matematyczne może uchwycić zawiłości TME i pomóc w identyfikacji czynników oporności oraz obiecujących terapii łączonych, poprawiając dzięki temu odpowiedź na leczenie.

Celem niniejszej rozprawy doktorskiej było wykorzystanie modelowania matematycznego i komputerowego do zbadania heterogeniczności mikrośrodowiska guza jako czynnika wpływającego na oporność na leczenie i zaproponowania potencjalnych terapii łączonych. W szczególności skoncentrowałam się na dwóch elementach TME: niskim pH oraz populacji macierzystych komórek nowotworowych. W szczególności zbadalam, czy ekspresja enzymu regulującego pH o nazwie CAIX może służyć jako marker biologiczny dla terapii inhibitorami punktów kontrolnych odporności (immune checkpoint inhibitors, ICI), takich jak anty-PD-1 oraz anty-CTLA-4, i potencjalny cel terapii łączonych. Ponadto badałam wpływ plastyczności komórek, czyli zdolności komórek nowotworowych do zdobywania i tracenia cech komórek macierzystych, na oporność na radioterapię. Wyniki tych badań zostały opublikowane w trzech publikacjach naukowych, które stanowią podstawę tej rozprawy. Publikacje te są przedstawione w rozdziałach 3-5, a każda z nich jest poprzedzona krótkim wprowadzeniem podsumowującym najważniejsze wyniki publikacji, wyszczególniającym mój wkład w artykuł oraz wyjaśniającym związek między publikacjami a celami badawczymi i hipotezami tej rozprawy. Ponadto rozprawa zawiera rozdział wprowadzający, który objaśnia czytelnikowi podstawy badanych problemów biologicznych, przedstawia istotną literaturę i uzasadnia podjęty temat badawczy. Kolejny rozdział zawiera listę celów badawczych, które ustaliłam w tej rozprawie, oraz odpowiadających im hipotez badawczych. Rozprawa kończy się rozdziałem poświęconym dyskusji, w której podsumowuję najważniejsze wyniki i wnioski, wyszczególniam, w jaki sposób cele badawcze zostały osiągnięte, omawiam ograniczenia przeprowadzonych badań oraz przedstawiam pomysły na dalsze badania w tej tematyce.

1.2.1 Rozdział 1: Introduction

Rozdział ten stanowi wprowadzenie do tematu badawczego. Uzasadnia on podjęcie tematyki badania czynników oporności na leczenie, wylicza znane czynniki oporności oraz wprowadza czytelnika w tematykę mikrośrodowiska guza jako źródła potencjalnych mechanizmów oporności na radioterapię i terapię inhibitorami punktu kontrolnego odporności. Rozdział ten składa się z dwóch sekcji. Pierwsza z nich objaśnia tematykę od strony biologicznej: wyjaśnia mechanizm działania badanych terapii, podsumowuje stan wiedzy na temat oporności na te terapie oraz przedstawia przypuszczalne czynniki oporności, które badam w tej rozprawie. Natomiast druga sekcja stanowi krótki przegląd matematycznych i komputerowych modeli radioterapii i immunoterapii znalezionych w literaturze, skupiając się na modelach, które poświęcone były badaniu mechanizmów oporności na te terapie.

1.2.2 Rozdział 2: Research Aims and Hypotheses

Drugi rozdział wylicza szczegółowe cele badawcze rozprawy wraz z postulowanymi hipotezami. Kolejne trzy rozdziały wyjaśniają jak każda z publikacji stanowiących podstawę rozprawy, pomogła w osiągnięciu celów badawczych oraz w potwierdzeniu lub odrzuceniu postawionych hipotez badawczych.

1.2.3 Rozdział 3: An *in silico* model to study the impact of carbonic anhydrase IX expression on tumor growth and anti-PD-1 therapy

Rozdział odpowiada publikacji zatytułowanej "An *in silico* model to study the impact of carbonic anhydrase IX expression on tumor growth and anti-PD-1 therapy", której jestem pierwszym i głównym autorem i która została opublikowana w *Journal of the Royal Society Interface* w styczniu 2023 roku. W publikacji zbudowałam model komputerowy guza i jego mikrośrodowiska w celu wyjaśnienia stosunkowo niskiej odpowiedzi na inhibitory punktów kontrolnych odporności oraz zbadania ekspresji CAIX jako biomarkera i potencjalnego celu terapii łączonej z terapią anti-PD-1. Zaproponowany model hybrydowy składa się z modelu agentowego (agent-based model, ABM), który symuluje zachowanie się komórek nowotworowych i immunologicznych, oraz modelu różniczkowego opisującego gradienty substancji w TME. Wybór tego typu modelu był zmotywowany tym, że modele agentowe są stworzone do modelowania heterogeniczności symulowanego środowiska, co dobrze odpowiada celowi badania zróżnicowanego TME. Ponadto modele agentowe mają zastosowanie w studiowaniu powstawania nowych zachowań w wyniku oddziaływań podsystemów, co czyni je doskonałym kandydatem do identyfikacji potencjalnych biomarkerów. Proponowany model może służyć jako narzędzie do badania biomarkerów immunoterapii i eksploracji terapii łączonych, zgodnie z moim pierwszym celem badawczym. W ramach swojej rozprawy użyłam tego modelu do jakościowej reprodukcji wyników eksperymentów dotyczących wpływu CAIX na TME *in vivo*, wizualizacji wpływu ekspresji CAIX na TME i odpowiedzi immunologiczną oraz analizy jego wpływu na skuteczność terapii anti-PD-1 w odmiennych typach guzów: guzach ze znaczącą ekspresją PD-L1 przed rozpoczęciem leczenia oraz w guzach bez ekspresji PD-L1 przed rozpoczęciem leczenia. Symulacje *in silico* sugerują, że niska ekspresja PD-L1 przed wprowadzeniem leczenia inhibicją CAIX nie powinna dyskwalifikować pacjentów od otrzymywania terapii łączonej anti-CAIX i anti-PD-1, co przyczynia się do wyjaśnienia sprzecznych wyników badań nad PD-L1 jako biomarkerem ICI i uzasadnia dalszą pracę nad mierzaniem dynamicznej ekspresji PD-L1 w celu przewidywania odpowiedzi na leczenie anti-PD-1, zamiast statycznej ekspresji. Ponadto wyniki sugerują, że ekspresja CAIX jest obiecującym kandydatem na biomarker dla ICI, uzasadniając dalsze badania terapii łączonej anti-PD-1 i anti-CAIX, zgodnie z moim drugim celem badawczym.

1.2.4 Rozdział 4: Carbonic anhydrase IX suppression shifts partial response to checkpoint inhibitors into complete tumor eradication: model-based investigation

W rozdziale czwartym przedstawiam model różniczkowy, który zbudowałam w celu uzupełnienia modelu agentowego przedstawionego w poprzednim rozdziale. Został on opisany w publikacji "Carbonic anhydrase IX suppression shifts partial response to checkpoint inhibitors into complete tumor eradication: model-based investigation", której jestem pierwszym i głównym autorem i która została opublikowana w czerwcu 2023 roku. Założenia modelu oparte są na wynikach jakościowych uzyskanych z symulacji ABM. Jednak niższa złożoność tego modelu pozwoliła na jego kalibrację przy użyciu danych *in vivo*, symulacje ilościowe, analizę matematyczną i tym samym dalszą walidację wcześniejszych wyników i hipotez. Analizy i symulacje numeryczne sugerują, że inhibicja CAIX w połączeniu z dostatecznie silną odpowiedzią immunologiczną (na przykład wywołaną przez ICI) może zmienić asymptotyczne zachowanie modelu i zmienić stabilną chorobę na eliminację guza,

co potwierdza wnioski wyciągnięte z ABM, że inhibicja CAIX poprawia odpowiedź na ICI w guzach z ekspresją CAIX. Następnie, za pomocą modelu różniczkowanego porównałam różne rodzaje terapii łączonych: przeciwciała anti-PD-1 z anti-CAIX, przeciwciała przeciwko CTLA-4 z anti-CAIX, anti-PD-1 z anti-CTLA-4, a wreszcie potrójna kombinacja obu ICI z anti-CAIX. W szczególności symulowałam różne dawki i długości leczenia, aby odtworzyć fakt, że terapie nie są stosowane u pacjentów bez końca. Symulacje *in silico* sugerują, że monoterapie prowadzą do nawrotu guza, nawet po początkowej odpowiedzi na leczenie, podczas gdy inhibicja CAIX w połączeniu z wystarczającą dawką ICI prowadzi do trwałej i całkowitej odpowiedzi. Te wyniki i wnioski dodatkowo przyczyniają się do realizacji mojego drugiego celu badawczego. Ponadto symulacje wskazują, że inhibicja CAIX redukuje udział komórek macierzystych w guzie, co mogłoby wspomóc terapie mające trudności z usuwaniem komórek macierzystych, takie jak chemioterapia.

1.2.5 Rozdział 5: Cellular plasticity upon proton irradiation determines tumor cell radiosensitivity

Ostatni rozdział z wynikami poświęcony był mojemu wkładowi w publikację "Cellular plasticity upon proton irradiation determines tumor cell radiosensitivity", która została opublikowana w *Cell Reports* w lutym 2022 roku. Publikacja była wynikiem międzynarodowej współpracy pod kierownictwem dr. Claudii Peitzsch z National Centre for Tumor Diseases w Dreźnie. W tym badaniu porównaliśmy wpływ tradycyjnej radioterapii fotonowej z mniej konwencjonalną radioterapią protonową na heterogeniczność guza, w szczególności na dynamikę komórek macierzystych nowotworu (CSC). Usunięcie CSC uważane jest za kluczowe dla długotrwałej kontroli nowotworu po radioterapii, dlatego istotne jest ustalenie, który rodzaj promieniowania skuteczniej usuwa CSC. Eksperymenty *in vitro* przeprowadzone przez grupę badawczą były w stanie uchwycić jedynie efekt końcowy każdego rodzaju napromieniania na populację CSC. Zauważyłam w tym dobrą okazję dla zastosowania modelowania matematycznego, które mogłoby pomóc zidentyfikować rolę plastyczności komórkowej w obserwowanej dynamice CSC. Dlatego zbudowałam model równań różniczkowych zwyczajnych przedstawiający populację CC i CSC. Skalibrowałam model danymi *in vitro* oraz danymi znalezionymi w literaturze, dopasowując go do obserwacji eksperymentalnych. Model dobrze odwzorował wyniki eksperymentalne, a także podkreślił znaczenie dwóch rodzajów plastyczności: zwykłej plastyczności, polegającej na zdobywaniu komórki cech komórek macierzystych przez CC, oraz odwrotnej plastyczności, polegającej na utracie właściwości macierzystych przez CSC. W szczególności jakościowa analiza modelu wykazała, że oba rodzaje plastyczności musiały zostać ujęte w modelu, aby odzwierciedlić jakościowy trend w danych eksperymentalnych. Ponadto, dopasowanie modelu do danych ujawniło, że radioterapia z wykorzystaniem protonów istotnie rzadziej indukuje plastyczność niż promieniowanie fotonowe, co częściowo może wyjaśniać wyższy potencjał terapeutyczny terapii protonowej. Podsumowując, dwukierunkowa plastyczność komórek jest kluczowa do wyjaśnienia dynamiki CSC po napromienianiu i jej głębsze zbadanie mogłoby zmniejszyć częstotliwość nawrotów po radioterapii. Mój wkład w tę publikację wpisuje się w ramy mojego trzeciego celu badawczego.

1.2.6 Rozdział 6: Discussion

Rozdział podsumowuje najważniejsze wnioski uzyskane w rozprawie, jednocześnie zwracając uwagę na ograniczenia przeprowadzonych badań i perspektywy dalszych badań. W rozprawie zidentyfikowałem ekspresję CAIX i plastyczność komórkową jako przypuszczalne mechanizmy oporności na ICI i radioterapię. Jednak, mimo że analizy matematyczne i symulacje *in silico* są obiecujące, uzyskane wyniki powinny być poddane dalszej weryfikacji *in vitro* i *in vivo*. Podczas moich badań zidentyfikowałem także interesujące ścieżki dalszych badań, w tym ciekawy wpływ leczenia ICI na dynamikę CSC oraz złożone interakcje między ekspresją CAIX, wzrostem podścieliska nowotworu, a skutecznością ICI. Nie wchodzi one w zakres rozprawy, ale stanowią obiecującą tematykę dalszych badań.

Podsumowując, ta rozprawa spełnia wszystkie trzy cele badawcze określone w jej drugim rozdziale, a uzyskane wyniki i wnioski wspierają moje hipotezy badawcze.

Chapter 2

Introduction

2.1 Biological background and significance

Even today, cancer remains a serious public health concern that decreases life expectancy and quality of life. Based on the GLOBOCAN estimates of cancer incidence and mortality created by the International Agency for Research on Cancer, there were about 19 million new cancer cases and almost 10 million cancer deaths in 2020 globally [1], [2]. Importantly, according to World Health Organization's pre-pandemic data from 2019, cancer is one of the leading causes of premature death (i.e. death occurring between the ages of 30-70 years) in 127 countries and ranks as the most common cause in 57 countries [3]. Moreover, this number is believed to rise in the future. Despite tremendous progress in cancer treatment in recent years, several open challenges persist.

One of these challenges is the full understanding of treatment failure. Unfortunately, some tumors do not respond to certain therapies at all. Additionally, even initially favorable responses may ultimately result in treatment failure. This resistance that develops during treatment is known as acquired resistance, while the inability to elicit any response in treatment-naive tumors is called intrinsic resistance [4]. A deeper understanding of the factors contributing to these phenomena is critical to improving response rates and prolonging the overall survival of cancer patients.

Many promoters of drug resistance are already known. They include genetic factors, for example, genetic mutations of the cancer cells that bypass the drug's mechanism, as well as epigenetic factors, such as DNA methylation [5]. Furthermore, certain membrane transporter proteins reduce drug accumulation in the tumor cell by extruding the drug molecules [4]. Emergent evidence designates intratumoral heterogeneity and microenvironmental factors as promising yet underexplored contributors [4], [6]. The tumor microenvironment (TME) generally comprises tumor cells, various immune cells, stroma, blood vessels, secreted substances, and the extracellular matrix [7]. These components interact with and influence each other, thereby creating an interlaced network that may have either a pro- or antitumorogenic effect. For example, oxygen gradients in the TME determine which tumor cells are hypoxic, thereby significantly affecting their properties and susceptibility to treatment [8]. On the other hand, the induced tumoral heterogeneity then contributes to a heterogeneous nutrient distribution. For instance, hypoxia rewires the metabolism of tumor cells, affecting the metabolic byproducts secreted into the TME [9]. Overall, the TME is believed to harbor many promising resistance factors and treatment targets yet to be elucidated. The main aim of this thesis was to explore the heterogeneous tumor microenvironment via mathematical modeling as a contributor to treatment resistance and evaluate whether its components may serve as potential treatment targets.

2.1.1 Immune checkpoint inhibitors

Mechanism of action

A classic example of treatment resistance can be seen in immunotherapy, in particular, immune checkpoint inhibitor (ICI) therapy. Immunotherapy harnesses the immune system to eliminate cancer cells. It is based on the observation that immune cells can recognize tumor cells and limit their accumulation, which is termed immunoediting [10]. Tumors generally go through three phases of this immunoediting process [11]. At the beginning of tumor initiation, there is the elimination phase, where immune cells identify and remove potentially malignant cells. Then, during the equilibrium phase, immune cells control tumor growth. Finally, some tumors reach the evasion phase, in which tumor cells escape the immune system and the tumor grows and metastasizes. Numerous mechanisms contribute to this final immune evasion, including the expression of immune checkpoints on cancer cells [10].

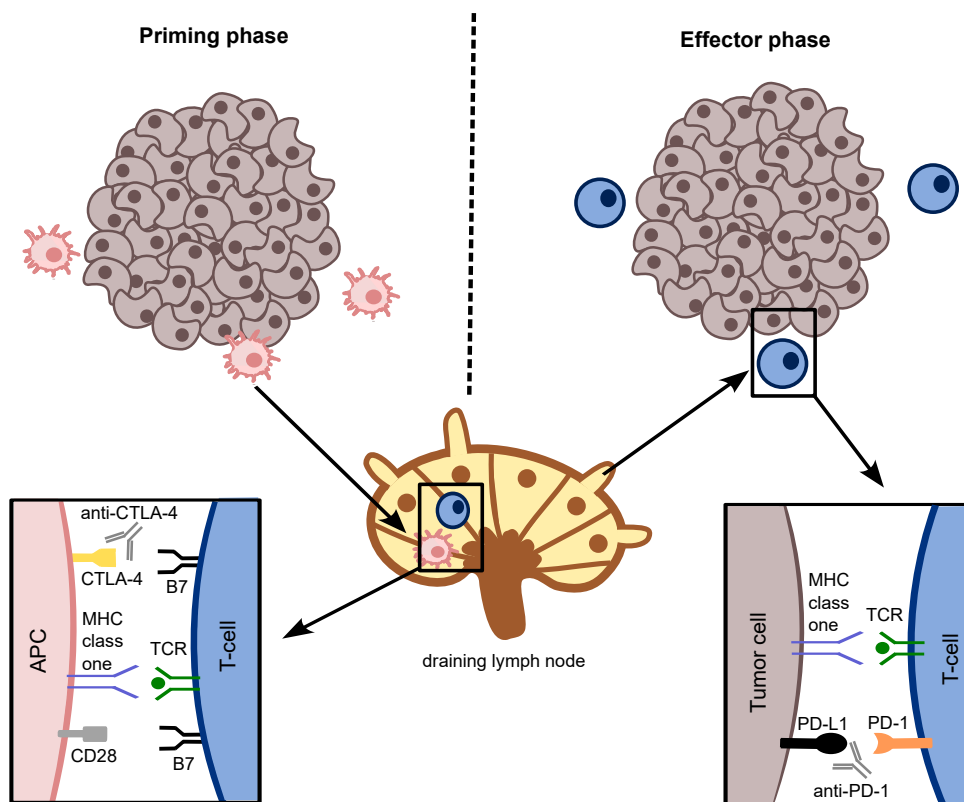


FIGURE 2.1: Diagram showing the basic mechanisms of anti-CTLA-4 and anti-PD-1 therapy. In the lymph nodes, antigen-presenting cells present tumor antigens to T cells resulting in T cell activation, a process which can be attenuated by CTLA-4 upregulation. Activated T-cells travel to the tumor site and launch an attack, which might be suppressed via the binding of PD-1 with PD-L1.

Immune checkpoints are intrinsic regulatory pathways that are hardwired into the immune response and are thus essential to central and peripheral tolerance [12]. Their inhibitors work by disrupting these pathways and reinvigorating immune responses. This mechanism is presented in figure 2.1 and shortly described in this paragraph. Antigen-presenting cells (APCs) transport tumor antigens from the tumor site to the lymph nodes, where they present them to T cells via the major histocompatibility complex (MHC). Once this antigen is recognized by the T-cell receptor

(TCR), T cell activation is initiated and the T cell upregulates cytotoxic T lymphocyte antigen 4 (CTLA-4) expression in response [13]. For full T-cell activation, costimulation by the binding of the CD28 molecule and its ligand B is needed. However, CTLA-4 competes with CD28 for B7 ligands, attenuating T cell activation [14]. Hence, CTLA-4 is mainly responsible for the regulation of T-cell activation in the priming phase. The immune cells that do get activated migrate to the tumor site to eliminate cancer cells. In the TME, another regulatory mechanism is present. Activated T cells (and to a lesser degree other immune cells) express the programmed cell death 1 receptor (PD-1), whose ligand PD-1 ligand 1 (PD-L1) is canonically found on APCs and cancer cells [15]. Upon binding, inhibitory signals are sent out and suppress T cell activation, proliferation, and cytotoxic activity [14]. This induced inability to attack tumor cells is sometimes called T-cell exhaustion, and it supports immune evasion by cancer cells [15], [16]. Therefore, the PD-1–PD-L1 pathway regulates immune response mainly during the effector phase. Interestingly, while some cancer cells express PD-L1 constitutively, others do it as a defense mechanism in response to IFN- γ that is produced by active T cells, so its expression may be dynamic and heterogeneous [17].

Since the immune checkpoints CTLA-4, PD-1, and PD-L1 inhibit immune response and thus reinforce tumor growth, targeting them should help control tumor progression. Certain drugs called immune checkpoint inhibitors (also called anti-PD-1, anti-PD-L1, and anti-CTLA-4 depending on their target) have been developed based on this premise. These inhibitors are antibodies that bind to their given target like PD-1 and CTLA-4, preventing their binding with their canonical ligands and thus their inhibitory mechanism. For a more detailed explanation of the mechanisms of ICIs see [18].

Rationale for further research on ICI resistance

Over the last decade, ICIs have become a pillar of cancer therapy and are recommended for an ever-growing number of malignancies. In clinical practice, the most used ICIs are monoclonal antibodies targeting PD-1 and PD-L1. These inhibitors are also commonly used in combination with other ICIs, such as those targeting CTLA-4 [19]. In 2022, the combination of a PD-1 inhibitor and a new antibody targeting the lymphocyte activation gene 3 (LAG-3) has been FDA-approved [20], becoming the first ICI targeting receptors other than those mentioned above. However, in my thesis, I will focus on two of the ICIs established in clinical practice, i.e., anti-PD-1 alone and in combination with anti-CTLA-4.

CTLA-4 blocking antibodies were the first ICI to be FDA-approved in 2011 for the treatment of metastatic melanoma, irrevocably changing the treatment of advanced malignancies. Its clinical effectiveness was proven in a three-arm randomized phase iii trial [21]. The trial compared patients treated with the CTLA-4 inhibitor ipilimumab with patients receiving the peptide vaccine gp100 and patients treated with a combination of both drugs. The median overall survival was 10 months, 10.1 months, and 6.4 months in the combination therapy group, ipilimumab alone group, and gp100 group, respectively, making it the first treatment to successfully prolong the survival of metastatic melanoma patients in a randomized trial.

Nowadays, anti-PD-1 is preferred, as it tends to have a superior therapeutic effect to anti-CTLA-4 while being better tolerated by the patients [18]. Nevertheless, all ICIs come with caveats. First and foremost, they have a relatively low response rate. It is to be noted that defining a beneficial response to ICIs is difficult due to a phenomenon called pseudo-progression [22]. During pseudo-progression, the tumor

seems initially resistant to treatment. That is, at first, growth is observed which is later followed by a decrease in tumor burden. Usually, response to cancer treatment is evaluated by RECIST criteria, which are based on measuring lesion diameters using imaging techniques such as CT scans. In this system, progressive disease denotes an increase of 20% in the sum of the longest diameters of the lesion compared with the smallest value recorded and absolute growth of at least 5 mm [23]. Some patients with pseudo-progression meet these guidelines for disease progression, even though they ultimately experience durable responses. Therefore, other response criteria for immunotherapy were created, such as immune-related response criteria (irRC) and irRECIST [24]. Response rates may thus have different meanings in distinct trials. However, regardless of the methodology, response to ICIs is for most tumors observed in less than half of the patients [14], [25]. Moreover, immune-related adverse events (irAE) are often associated with this therapy, impairing the nervous system, gastrointestinal system, and skin. Ipilimumab, a CTLA-4 inhibitor, causes irAEs in 70 – 88% of patients, including severe events in 10 – 27% of patients [26]. Similarly, pembrolizumab, a PD-1 antibody, leads to grade III/IV events in 10 – 13.3% of patients [12]. Although combination therapy with anti-PD-1 and anti-CTLA4 increases response rates (to ca. 57.6% in advanced melanoma, ca. 23% in non-small cell lung cancer), it has also a significantly higher incidence of severe irAE at ca. 55.5% [12], while still lacking in response rate. Improving response rates to ICIs could tremendously improve the lives of cancer patients. Moreover, the identification of putative non-responders could help avoid unnecessary toxicity. Therefore, there is a dire need for the identification of resistance mechanisms as well as predictive biomarkers for ICI therapy.

State of the art of biomarker research

Various factors have been and are being investigated as potential biomarkers. For a comprehensive review see [27]. Here, I will summarize the limitations of the two factors, which are nowadays used in clinical practice.

The most thoroughly investigated biomarker for anti-PD-1 therapy is the expression of its ligand PD-L1 on cancer cells which can be assayed by immunohistochemistry assays. However, it remains an imperfect marker, as demonstrated by the fact, that some studies have observed a correlation between PD-L1 expression and ICI effectiveness, while others have not [28]. Additionally, some PD-L1 negative patients respond to anti-PD-1. Several explanations for this discordance have been proposed. First, independent studies use different assays and PD-L1 cut-off values [27]. Secondly, PD-L1 expression is heterogeneous in time and space, as mentioned before, so insufficient sampling may skew the results. Finally, other resistance mechanisms might hinder PD-L1-positive patients from deriving clinical benefits.

The second most popular biomarker is tumor mutational burden (TMB), which quantifies the density of nonsynonymous mutations in the tumor genome. The rationale for using it as an ICI biomarker is that mutations generate immunogenic neo-antigens and thus stimulate immune response. However, TMB is still a controversial marker. Some studies and meta-analyses seemingly confirm its association with ICI effectiveness in a subset of cancers [29], [30], while others find only weak or even a lack of correlation [31]. Even studies supporting TMB as a biomarker, report some tumor types as significant outliers [30]. Again, these discrepancies may be partially explained by the lack of standardized TMB quantification methods and thresholds, implying a need for standardization and further validation. On the other

hand, other factors might confound the association between TMB and ICI effectiveness. For example, McGrail et al. observed that TMB-high tumors in which TMB did not correlate with a high T cell infiltration, did not have better response rates to ICI than TMB-low tumors [32]. They speculated that the immune infiltrate is responsible for the predictive power in the TMB-high cohorts.

To summarize, although some biomarkers are used in clinical practice, and even more are under investigation, they require further validation. Furthermore, they probably cannot discriminate fully between responders and non-responders. Due to the complexity of tumor-immune interactions and the heterogeneity of the TME, finding a single effective biomarker might be impossible [27]. Hence, predictive models taking into account multiple factors should be developed. This poses opportunities for computational modeling which allows us to quickly and inexpensively identify new promising biomarkers and resistance mechanisms, as well as integrate them into one model that can be used in research and clinical practice.

The TME as a biomarker source

In my research, I have focused on investigating the heterogeneous TME as a source of resistance mechanisms to ICIs. In particular, I focused on the acidic niche, which is usually a part of the microenvironment of solid tumors (see figure 2.2). This is partially due to the Pasteur effect, i.e. the reliance of cells on anaerobic glycolysis in the absence of oxygen. Tumors are usually poorly perfused by vasculature, leading to hypoxic (oxygen-deprived) areas within the tumor, further away from the blood vessels. This hypoxic environment induces cells to rely on anaerobic glycolysis, a metabolic pathway that produces protons and lactate, acidifying the neighborhood. Moreover, cancer cells tend to have an aberrant metabolism and often revert to glycolysis even in the presence of oxygen - a phenomenon that is termed the Warburg effect [33]. Finally, many cancer cells express enzymes from the family of carbonic anhydrases, which aid in regulating their internal pH. Of particular interest is the protein carbonic anhydrase IX (CAIX), as it is overexpressed in many cancers and promotes tumor growth [34]. It catalyzes the reversible hydration of CO_2 , thereby acidifying the extracellular space while regulating intracellular pH. Therefore, it not only contributes to the development of the acidic niche but also protects the cancer cell from the detrimental effects of low pH, such as anergy and death [35]. On the other hand, immune cells do not have such protective measures. Hence, the acidic TME suppresses immune cells, in particular subduing the cytotoxicity of tumor-infiltrating lymphocytes (TILs) [36] and making CAIX inhibition a promising synergist of immunotherapy. Chafe et al. showed in a pre-clinical study that suppressing CAIX with the inhibitor SLC-0111 improves the effectiveness of combination therapy with anti-PD-1 and anti-CTLA-4 in mouse models [37]. However, mouse models rarely translate to human studies [38]. Computational and mathematical models, especially when calibrated with clinical data, provide a stepping stone between murine experiments and human trials. This led me to investigate CAIX as a biomarker for ICI therapy *in silico*, which I have done in [39], [40].

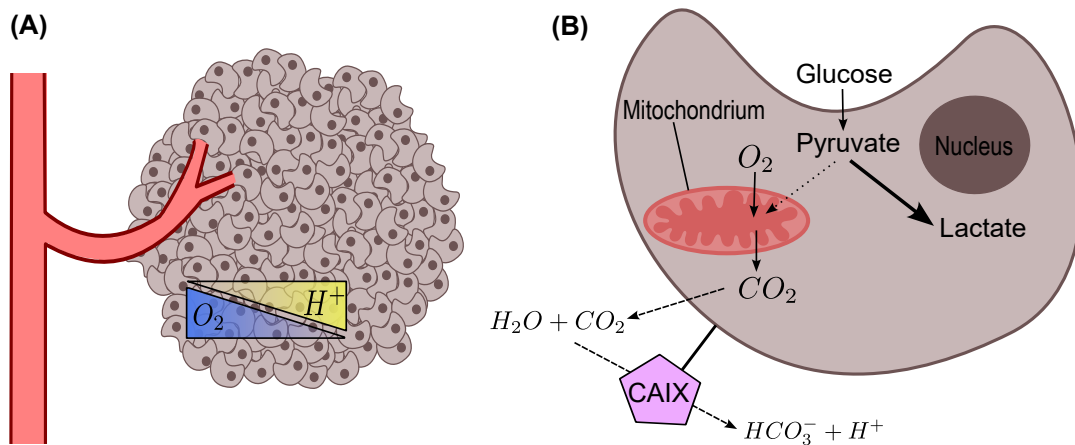


FIGURE 2.2: Diagram showing the main causes of TME acidification. **(A)** Large distance from blood vessels turns tumor cells hypoxic. Due to the Pasteur effect, these cells revert to anaerobic glycolysis and produce lactate, acidifying the TME. **(B)** Due to the Warburg effect, cancer cells prefer glycolysis (bold arrow) to oxidative phosphorylation (dotted arrow) even in the presence of oxygen, leading to lactate accumulation. Moreover, CAIX catalyzes the hydration of CO_2 , enhancing proton production and thus acidifying the extracellular space.

2.1.2 Radiotherapy

Rationale for further research on radioresistance

Radiotherapy (RT) is one of the main treatments for solid tumors, with the majority of patients receiving it as a first-line treatment, in an adjuvant setting, or as palliative care [41], [42]. Localized radiation - usually consisting of X-rays or γ -rays delivered via photons, although proton beam therapy (PBT) is also gaining traction - impairs cancer cells either by directly damaging their DNA or by generating reactive oxygen species that induce cancer cell injury via oxidative stress [43]. If the damage cannot be repaired, this results in cell cycle arrest. However, certain tumors seem to be resistant to irradiation.

Many approaches to enhance radiosensitivity have been proposed, including inhibition of intracellular antioxidants to increase cell death via oxidative stress. Other approaches targeted the radioresistance-inducing TME and aimed at combatting tumor hypoxia or modulating the cancer-associated fibroblast-mediated remodeling of the TME. Combination of radiotherapy with immunotherapy to increase antitumor immunity locally as well as strengthen the abscopal effect was also considered [44], [45]. Despite this constantly deepening understanding of radioresistance, testing of new treatment protocols, and technological advancements, radioresistance in cancer remains a problem, especially since not all pre-clinical findings translate into clinical practice [46], [47].

Additionally, even seemingly responding patients experience tumor recurrence after radiotherapy, which is one of the main challenges in radiation oncology. In head and neck cancer, 10 – 25% of irradiated tumors metastasize after treatment, resulting in a median overall survival of 3-4 months after the metastasis diagnosis [48]. One study on radiotherapy after breast-conserving surgery observed a 7.3% rate of locoregional recurrence within 5.1 years, which climbed to 19.5% for patients younger than 40 years old [49]. Another study observed regional recurrence in 90% of cervical cancer patients undergoing definitive radiotherapy [50]. In early-stage

non-small-cell lung cancer, recurrence was diagnosed in 18% of patients [51]. Concluding, for various malignancies, there is significant room for improvement when it comes to relapse rates after radiotherapy. Identifying the causes of radioresistance and recurrence post-radiotherapy could lead to the development of superior treatment strategies and increase the overall survival of patients.

Cancer stem cells as potential resistance drivers

In recent years, researchers have focused on a specific subset of cancer cells known as cancer stem cells (CSCs) due to their potential role in tumor growth and recurrence. According to the CSC hypothesis, these self-renewing cells with differentiation potential may be the driving force behind tumor development and resistance to treatment [52], see figure 2.3(A). They are generally believed to be radioresistant for most tumor types [52], although some studies report contradicting findings [53]. This might be partly explained by the differences in behavior between CSCs in distinct cancer types [54]. Additionally, the difficulty in correct CSC identification might be confounding study results. Although several surface markers of CSCs have been identified, such as ALDH, CD44, CXCR4, and CD133, they distinguish between CC and CSC only in some tumor types [54]–[56]. Nonetheless, several mechanisms of CSC radioresistance have been uncovered, supporting the hypothesis that the removal of CSC is crucial for a durable response to therapy. These mechanisms include the activation of various pro-survival signaling pathways, e.g. Wnt/ β -catenin, Notch, Hedgehog, TGF- β , and the PI3K, AKT/mTOR pathway [57]. Furthermore, various CSC populations seem to have superior DNA repair capacities and enhanced protection from oxidative stress, diminishing radiation-induced death [58]. Finally, pre-clinical studies suggest that the number of tumorigenic cells determines radiosensitivity, and CSCs have an enhanced ability to initiate tumors [59]. In conclusion, CSC removal is believed to be the key to complete and durable tumor eradication.

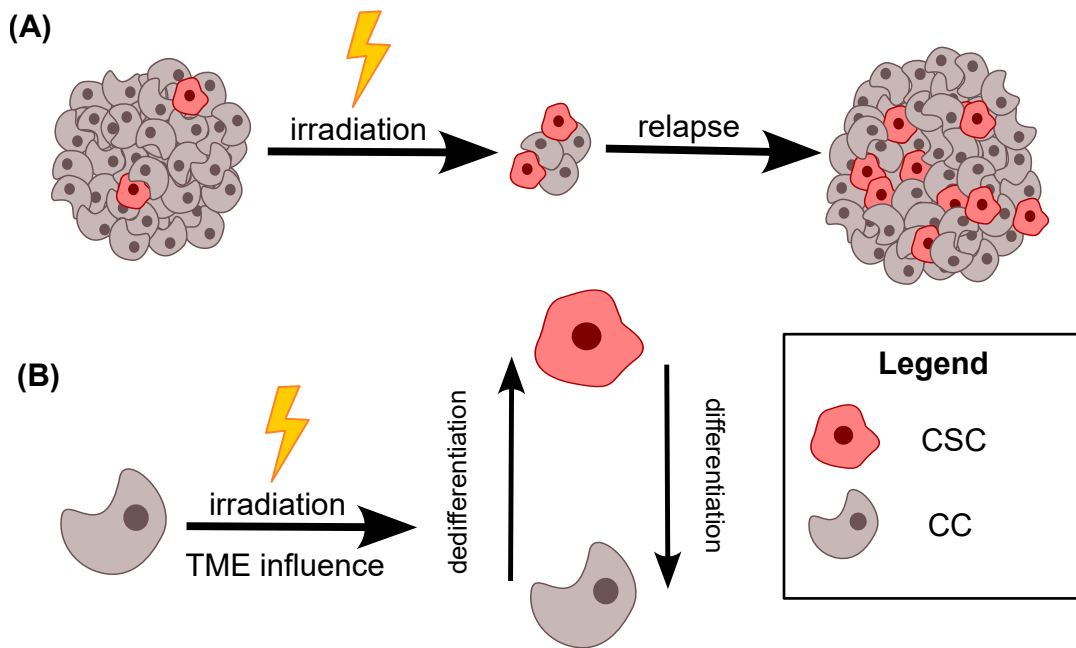


FIGURE 2.3: Interplay between irradiation and CSC. **(A)** CSC are more radioresistant and have an enhanced ability to initiate tumors, hence, they survive treatment and repopulate the tumor. **(B)** Environmental and therapeutic factors trigger cellular plasticity.

Apart from their high tumorigenic potential and intrinsic drug resistance, cancer cells seem to display bi-directional plasticity, where they can lose or acquire a stem phenotype [60], [61], as illustrated in figure 2.3(B). This allows them to adapt to their ever-changing environment and contributes to spatial and temporal tumor heterogeneity [60], [62]. The TME heavily contributes to this cancer cell plasticity. For example, signaling factors secreted by stromal cells or immune cells fuel phenotypic plasticity [63]. Moreover, hostile environments such as hypoxic or acidic niches may trigger the transition from CC to CSC [62], [63]. Another factor contributing to cancer cell plasticity is therapeutic pressure, including radiotherapy. Partially, this is due to the upregulation of certain transcription factors following irradiation, but also to the effect of radiotherapy on the TME, i.e. the induction of a pro-inflammatory TME and increased secretion of signaling factors by the stromal and immune cells [61]. Therefore, radiotherapy itself contributes to the emergence of a treatment-refractory population in the tumor. A deeper understanding of the interactions between radiotherapy, TME heterogeneity, and CSC plasticity could therefore improve radioresponse rates and minimize the risk of cancer regrowth after irradiation.

Proton beam therapy

Proton radiotherapy has the benefit of superior dose distribution to photon radiotherapy, with a distinctly pronounced dose deposition peak (called the Bragg peak) at a penetration depth that is largely dependent on the initial energy of the protons [64]. Hence, the bulk of the radiation dose can be placed inside the tumor, thus achieving maximal tumor eradication, and sparing healthy tissue. Additionally, by superimposing several proton fields, the radiation dose can be precisely calibrated to the given tumor and minimize damage to the peripheral tissue. Therefore, PBT is nowadays most commonly used to treat tumors close to vital organs [65]. However, in other cases, it is unclear whether this enhanced dose distribution justifies the higher cost and the limited availability of PBT facilities, especially, since there is

no consensus about whether proton therapy offers a significant clinical benefit over photon therapy [65]. The biological effect of PBT is usually quantified as the relative biological effectiveness (RBE), which is the ratio of photon radiation to the proton dose required to elicit the same biological effect. Although the RBE of proton therapy is generally assumed to be equal to 1.1 [66], the mechanisms underlying this enhanced biological effect as well as its real extent are not yet determined.

Some pre-clinical studies indicate that proton beam therapy has superior CSC-targeting capacity than photon radiotherapy for various cell lines [67], [68]. Interestingly, photon radiation has been shown to upregulate CSC markers *in vitro* [69]. In [56], we set out to investigate the impact of proton therapy on several different cell lines and determine whether the putative-enhanced CSC removal might be due to radiation-induced cellular plasticity. In particular, we compared the impact of photon and proton irradiation on the dynamics of CSCs to see, if proton radiation also enriches for CSCs and whether the mechanisms governing this enrichment are the same for both therapies. My mathematical model allowed me to investigate the dynamic cellular plasticity, i.e. the ability of cancer cells to acquire or lose stemness properties over time, which is difficult to observe *in vitro*. The ultimate goal of the study was to determine whether PBT and its impact on tumor heterogeneity might reduce radioresistance.

2.2 *In silico* modeling in oncology

In silico models are increasingly used in cancer research [70]. This term usually refers to mathematical or computational models, which allow for simulations, e.g. of biological experiments, and thus complement *in vitro* and *in vivo* experiments. Importantly, *in silico* experiments do not raise any ethical concerns, as opposed to their *in vivo* counterparts. Thereby, they help to adhere to the three principles of animal research, postulated by William Russel and Rex Burch in the 1950s and dubbed the 3Rs: Replacement, Reduction, and Refinement [71]. These principles suggest that animal models should be replaced with more humane methods whenever possible, the number of animals participating should be reduced to the absolute minimum, and the experiment design should be refined to reduce harm to the animals. Nowadays, they are broadly accepted by the scientific community and even mandated by the European Parliament's and Council's Directive 0220/06/63/EU [72]. Computational models offer a replacement for animal studies, as postulated by the first principle. Furthermore, *in silico* experiments are not constrained by the remaining two principles, allowing for the testing of scenarios that would be unfeasible in real life either due to ethical concerns, financial burden, time constraints, or simply the complexity of the scenario, which is harder to control in living organisms or to recreate *in vitro*. In particular, *in silico* experiments may supplement the planning of experiments by testing out various experimental protocols and identifying those which are the most likely to be informative and should be validated *in vivo*.

Moreover, it should be noted that findings from animal experiments are not always confirmed by studies in humans, implying that animal models are not ideal representatives of the human body [38]. Mathematical and computational models, especially when calibrated with clinical, experimental, and pre-clinical data, may help translate animal studies to humans. For example, mice models are believed to successfully illustrate specific processes of cancer development [38], that may be then combined in an *in silico* model to better represent the complex disease in a human setting.

Furthermore, *in silico* experiments are relatively easy to reproduce, especially when the model and its implementation are shared. This is especially important in cancer research, where an analysis found that only about 10% of landmark studies were reproducible [73]. In the case of *in vivo* or *in vitro* studies, it can be quite challenging to determine, whether this difficulty in reproducing the findings results from insufficient information on the experiment design, natural variability, lack of expertise of the reproducing team, or whether the original results were wrong, whereas mathematical analyses and computational simulations can generally be thoroughly reviewed.

Finally, mathematical and computational models can be used to make sense of already available data. Such models can incorporate variables that were not originally observed and help determine, whether they could be responsible for the observed results.

In conclusion, *in silico* experiments have their place in cancer research. They can be used to generate and initially test hypotheses, interpret experimental results, predict long-term outcomes that were not measured in original experiments, and help design future *in vitro* and *in vivo* experiments and trials. However, we must be aware of their limitations and be informed about the advantages and disadvantages of different types of models. More complex models might be more accurate and convincing for biologists and medical professionals. On the other hand, they are usually analytically intractable, allowing only for simulations. Moreover, increased complexity induces more time-consuming and computationally expensive simulations. Finally, such models also require more data for calibration and validation and have increased intrinsic uncertainty. Simpler models, on the other hand, might be more useful in clinical practice as they can be easily calibrated, validated, and analyzed and their computation is quicker. Yet, oversimplification might ignore important features and lead to wrong conclusions. All in all, no model will ever perfectly replicate reality, but it can provide important insights and advance cancer research, a sentiment beautifully phrased by the statistician George Box in the aphorism "All models are wrong, but some are useful" [74].

2.2.1 *In silico* models of immune checkpoint inhibitor therapy

The mechanisms of immune checkpoint inhibitors are highly complex, providing an abundance of modeling opportunities. In this subsection, I will provide a short overview of mathematical and computational models that have been used to investigate the interplay between tumors and the immune system, immune checkpoint inhibitor therapy biomarkers, and combination therapies.

Mathematical modeling of tumor-immune interactions has a long history, starting with non-spatial ordinary differential equation models. One of the most basic ways to model the interactions between a tumor and the immune system is to take a classic one-equation tumor growth model (exponential growth, logistic growth, Gompertz model, Bertalanffy model) and add a second equation describing the behavior of effector cells, i.e. immune cells with the ability to kill cancer cells [75]. The two equations usually follow a predator-prey model, in which effector cells are the predators killing their prey: the cancer cells [75]. The probably most well-known predator-prey-type tumor model was proposed by Kuznetsov in 1994, which - while staying fairly simple and being mathematically tractable - simulates interesting cell behaviors, such as oscillatory dynamics, tumor dormancy and a phenomenon termed "sneaking through" [76]. "Sneaking through" refers to the observation that in certain cases a smaller amount of inoculated cells may lead to

tumor progression in animal models, while a medium amount results in tumor rejection, and is explained by the fact that the small initial tumor is not immunogenic enough to mount an efficient immune response [76]. However, this model consists only of two variables and ignores numerous factors impacting tumor-immune interactions, so it is too simplistic for certain research questions. Therefore, depending on the research question, one or more components might be added to the model, including variables describing other immune cells, cytokines, normal tissue, or other parts of the TME. For an overview of simple extensions of the above-mentioned two-equation model, see [77]. Here, I will focus on more modern models used to investigate immune checkpoint inhibitors or combination therapies.

First, let us look at continuous models, which are used when the bulk behavior of cells is of interest, e.g. when predicting treatment outcomes or testing treatment protocols. They describe the bulk of the tumor or its subsets (such as CC and CSC) by differential equations, including the above-mentioned ordinary differential equations, delayed differential equations that consider time delays, and partial differential equations that capture spatial tumor growth. For example, in [78], Butner et al. proposed a mechanistic model of tumor growth throughout immunotherapy, that accurately replicated the ultimate tumor burden in clinical trials. Two of the model's parameters - the growth rate at first re-staging and a parameter quantifying the collective immune response strength - were identified as potential predictive biomarkers of immunotherapy. Partial differential equation models capturing the spatial distribution of cells have also been proposed, e.g. to investigate the synergy between ICIs and a dendritic cell vaccine at various dosages [79]. The spatial aspect of the model captured the uneven infiltration of T cells whose density increased toward the tumor rim. Multicompartmental models have also contributed to the study of immunotherapy. For example, in [80] the authors considered a three-compartment ODE model of the spleen, blood, and tumor, and they used this model to simulate various treatment protocols with anti-PD-L1 in randomly generated tumors. Another compartmental model representing a generic virtual patient that included pharmacokinetics was proposed in [81]. The model was calibrated with clinical data and proven to reproduce several types of clinically observed responses to immunotherapy. Finally, the model was used to make predictions about combination therapies, for which human clinical data was not available, and reported increased efficiency of administering anti-PD-1 before CTLA-4 than vice-versa.

On the other end of the spectrum, there are discrete models, such as agent-based models (ABMs) or cellular automata (CAs), which are commonly used when the tumor heterogeneity or TME must be captured (see figure 2.4 for an example). They simulate each cell individually, accounting for its interaction with other cells and the environment. Sometimes, they are coupled with continuous models to connect the cellular scale represented by the discrete model with the tumor/organ scale, e.g. by modeling cancer cells discretely and substances in the TME continuously. For example, Gong et al. proposed a multiscale agent-based model of tumor-immune interactions for spatial simulations of tumor growth in response to anti-PD-1 and anti-PD-L1 [82]. The model was calibrated with values from literature, without representing a specific tumor type. By varying parameters quantifying tumor mutational burden and antigen strength, they simulated tumors with histological patterns that resembled patients' biopsies, showing, that these genetic mutations might be drivers of heterogeneous tumor architectures. Finally, they used their model to

semi-quantitatively assess PD-L1 expression in the outer rim of a tumor as a potential biomarker for anti-PD-L1 therapy. In [83] Kather et al. build an ABM of colorectal cancer that included tumor, immune, and stromal cells and investigated the impact of stroma on immune response and ICI effectiveness. The simulations allowed them to conclude that stroma can be both pro- and antitumorigenic, depending on the immune infiltrate, making it an attractive ICI combination target. Later, the research group used an extended three-dimensional version of their model to compare combination immunotherapy approaches in colorectal cancer [84]. They concluded that distinct tumor phenotypes - in terms of adjuvanticity and antigenicity - might require different combinatorial strategies.

In conclusion, mathematical and computational models have offered valuable insights into the mechanisms of ICI resistance and potential combination therapies. In [39] and [40] I contributed to these efforts by investigating anti-CAIX therapy alone and in combination with ICIs *in silico*. First, I built a discrete, holistic model of the TME which allowed for the qualitative replication of experimental findings and the evaluation of CAIX expression alone and in combination with tumor PD-L1 expression as a biomarker for ICI therapy and combination therapy with anti-CAIX. Then, in [40], I used the insights from the discrete model to build an ODE model that was able to quantitatively replicate experimentally observed tumor volume dynamics, observe variables that had not been measured experimentally, such as the CSC fraction, and investigate the synergy of the combination of anti-CAIX, anti-PD-1, and anti-CTLA-4.

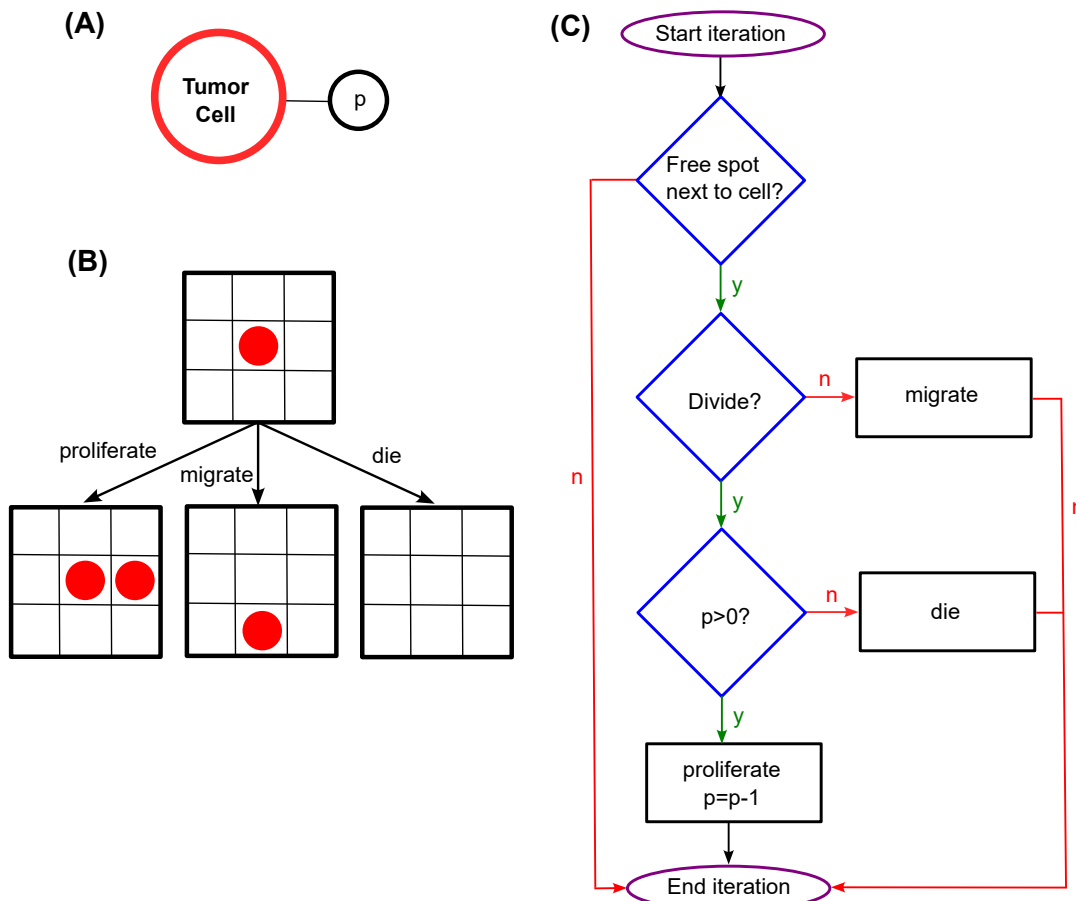


FIGURE 2.4: A simple lattice-based agent-based model. **(A)** The model has one type of agent: a cancer cell with the attribute p , denoting proliferation capacity. **(B)** The agent (denoted by a red dot) lives on a lattice, occupying one spot. Its neighborhood can be defined in various ways. In this example, we have drawn its Moore neighborhood, comprised of the occupied cell and the eight surrounding cells. The agent can perform three actions: proliferate, migrate, and die. For proliferation and migration, an empty space in the neighborhood is necessary. **(C)** A diagram showing the rules governing the agent's behavior. Black rectangles denote decision-making rules and blue ellipses the resulting actions. In each iteration, each agent's behavior follows the presented rules.

2.2.2 *In silico* models of radiotherapy

In radiotherapy, mathematical modeling has most commonly been used to predict treatment outcomes and determine promising treatment schedules, but also to improve our understanding of its biological effect. This subsection will be a short review of mathematical and computational models that have been used to study the impact of radiotherapy on radioresistance and stem cell dynamics and vice versa. For a more in-depth review of mathematical models of cellular plasticity see [85].

First, it should be noted that mathematical modeling has aided our understanding of radiotherapy for decades. Most prominently, the linear quadratic (LQ) model describing the probability of cell survival as a function of radiation dose is widely adopted in oncology and used to compare different treatment protocols, optimize treatment schedules, or adjust irradiation protocols after missed doses [86]. This popularity is probably partially due to its simplicity and its extensive validation [86]. However, it is a great simplification of the effects of irradiation and may not be

applicable in all cases. For example, if a very heterogeneous cell population in terms of cell cycle phases were to be modeled, each subpopulation's survival might correspond to a differently parametrized LQ model, and fitting an LQ model to the entire population might not be informative [87]. Similarly, when considering *in vivo* models, the TME might influence a cell population's sensitivity to radiation and therefore its survival probability. Hypoxic cancer cells tend to be more radio-resistant and hence, modeling a population of hypoxic and non-hypoxic cells with an LQ model could confound the relationship with oxygen distribution [87].

The above-mentioned limitations can be overcome using multi-compartment LQ models. In [88], Yu et al. coupled a differential equation model of CSCs and CCs exposed to fractionated radiation treatment with LQ models of cell survival to determine the radiosensitivity parameters. They compared a single-compartment LQ model yielding the same radiobiological parameters to both cancer cell phenotypes with a dual-compartment model differentiating between CSC and CC. Their dual-compartment model offered a superior method for the estimation of radiobiology parameters in the case of fractionated radiotherapy, while preserving the assumptions of the conventional single-compartment LQ model. Simulations using the ODE model with the parameters obtained from the dual compartment LQ model indicated that hypofractionation might help overcome radioresistance for some tumors, which was in line with clinical observations but could not be shown using the conventional LQ model. Moreover, their simulations offered a possible explanation for the ineffectiveness of radiotherapy in glioblastoma multiforme, which was in contrast with radiosensitivity status *in vitro*. They hypothesized that this was due to the very high radioresistance of their CSC population that survived the treatment and led to fast tumor regrowth. Later, the research group used with double-compartment LQ model coupled with a new ODE model of solid tumor growth to optimize treatment schedules for glioblastoma multiforme radiotherapy [89]. In this new model, they considered the induction of a stem cell phenotype after irradiation. Their proposed super hyper-fractionated approach resulted in significant recurrence delay in comparison to conventional approaches. This dual-compartment LQ was also used to determine the radiosensitivity of four breast cancer cell lines, with the conclusion that CSC in breast cancer is more radioresistant [90]. The authors also fitted the model to clinical data and determined that both the single and dual-compartment models fit the data well for large radiation doses and yielded similar radiobiological parameters. However, due to lacking clinical data, the fitted parameters were calculated with large uncertainties. These uncertainties were even larger for small doses, and the two models no longer resulted in similar parameters.

In [91], the necessity of eradicating the CSC population to achieve tumor control was explored using a stochastic model of the stem, progenitor, and mature cells. Their model considered unidirectional plasticity of CSC, that is stem cells could turn into progenitor cells, but not the other way around. The authors considered CD133 as a biomarker for CSC and compared the probability of eradicating the theoretical CSC population with the probability of eradicating the CD133+ population, which would be measurable for experimental data, concluding, that CD133+ cells are a reliable, even if not perfect, representation of CSCs. In [92], Forouzannia et al. build on this idea of calculating the tumor control probability with respect to CSC only, by incorporating reverse plasticity events as well, i.e. non-stem cells acquiring stemness. Then, they compared different radiotherapy schedules for tumors with and without plasticity, concluding, that plasticity does indeed impede radiotherapy. Leder et al. also developed a model incorporating bidirectional plasticity and used it to identify promising radiotherapy schedules for glioblastoma mouse models [93]. Here,

stemness acquisition was radiation-induced only. Interestingly, the optimal schedule led to CSC enrichment in the tumor, indicating, that the relationship between CSC and tumor progression is more complex than previously believed. Later, they used the model to predict clinical outcomes of the previously developed schedule and translate it from mice to humans and inform a small-cohort Phase 1 clinical trial [94].

Discrete models have also contributed to our understanding of the impact of cellular plasticity on radioresistance. In [95], Poleszczuk et al. built an agent-based model of tumor growth and studied among others radiotherapy outcomes on tumors with different plasticity probabilities, showing that plasticity-free tumors respond best to radiotherapy. However, while low- or plasticity-free tumors grew after treatment, high-plasticity tumors were generally eradicated after treatment, probably due to CSC exhaustion due to the frequent plasticity events.

In [56], I have proposed a differential model of CC and CSC dynamics after irradiation and radiation-induced bi-directional plasticity. I have calibrated it with *in vitro* data to replicate CSC dynamics after X-ray and proton radiotherapy in various cell lines and investigated the differences between these two types of radiation. My aim was to analyze the impact of both irradiation types on cellular plasticity and evaluate their CSC targeting potential.

Chapter 3

Research Aims and Hypotheses

The main aim of this thesis is to use mathematical and computational modeling to explore the tumor microenvironment and its heterogeneity as a contributor to treatment resistance and evaluate whether its components may serve as potential targets for combination therapy. More specifically, I have set the following detailed research aims:

1. Build a model of tumor-immune interactions on a single cell level to provide a tool for identifying immunotherapy biomarkers in the TME as well as determining resistance mechanisms that could be promising targets for combination therapy.
2. In particular, study the impact of tumoral CAIX expression on the evolution of the TME and ICI effectiveness *in silico*, and evaluate it as a combination therapy target with ICIs.
3. Model and analyze the influence of cancer cell plasticity on tumor heterogeneity and the effectiveness of X-ray and proton radiotherapy.

Achieving these aims will support the following four hypotheses:

1. By incorporating tumor-immune interactions and their interdependence with the TME in a computational model, we can identify resistance mechanisms and promising biomarkers for ICI therapy.
2. Tumoral CAIX expression induces an immunosuppressive TME, thereby impairing ICI effectiveness and serving as a confounder for immune-related predictive ICI biomarkers such as PD-L1 expression.
3. For CAIX expressing tumors, combining transient ICI therapy with CAIX suppression can improve the treatment outcome.
4. Mathematical modeling can help explain the differences between proton and X-ray radiotherapy that are not immediately visible in experimental data.

Work on these research aims has led to the publication of three journal articles, which are the basis for this thesis. The following three chapters correspond to one publication each and explain how the given publication is connected with the research aims and how the obtained results and conclusions support the above-enumerated research hypotheses. Additionally, my contributions to each publication are stated in the introduction of each chapter.

Chapter 4

An *in silico* model to study the impact of carbonic anhydrase IX expression on tumor growth and anti-PD-1 therapy

4.1 Introduction

In [39], I tackled the challenge of overcoming the relatively low response to immune checkpoint inhibitors. More precisely, I proposed a hybrid computational model of the tumor and its microenvironment and used it to investigate the expression of the enzyme CAIX as a predictive biomarker for anti-PD-1 therapy and a combination therapy target. Using numerical simulations, I studied the influence of CAIX expression and suppression on the temporal and spatial development of the TME and immunotherapy effectiveness. The model is based on a previously developed and validated hybrid model [83], [84], that I have significantly extended to capture TME features and treatment options that were crucial to my research aims and hypotheses, as described in section 4.2 of this thesis. Additionally, I performed all of the numerical simulations presented in the publication and analyzed the results. My supervisor prof. Jan Poleszczuk's main role in this publication was supervision and guidance throughout the conceptualization of the project. Our co-author prof. Jakob Nikolas Kather proposed and performed the survival analysis on TCGA data as described in section 3.5 and part of section 2.3 of the publication. I was the main investigator of this study, wrote the original draft of the paper, and it corresponds to my first research aim to build a model of the tumor and its microenvironment, and partially contributes to my second research aim, i.e. the study of the impact of CAIX expression on immunotherapy, which was elaborated on in [40].

4.2 Relation of the publication to the research aims of the thesis

4.2.1 Build a model of tumor-immune interactions on a single cell level to provide a tool for identifying immunotherapy biomarkers in the TME as well as determining resistance mechanisms that could be promising targets for combination therapy

The model proposed in this publication is a hybrid model consisting of two parts: an agent-based model describing the behavior of tumor cells and T cells and a partial differential equation model of the substances that are present in the TME. The cells

consume or produce the described substances (oxygen, glucose, protons) influencing the nutrient and pH distribution profile in the TME. On the other hand, the actions of the cells depend on nutrient availability and the acidity of the TME. Hence, both parts of the model influence each other, as is the case in the human body. Besides these substances, which are simulated using reaction-diffusion equations, the model also considers other environmental factors such as fibrotic stroma and IFN- γ , which is produced by active T-cells and induces PD-L1 expression.

As stated in the research aim, immune and cancer cells are simulated on a single-cell level as agents which move on a lattice. The reasons for choosing an agent-based model as the basis of this hybrid model were three-fold. First, ABMs are an obvious candidate for capturing a system's heterogeneity. They do not model the bulk of cells like differential equations do. Instead, each cell is modeled as an autonomous agent, equipped with its features, properties, and history [96]. Its location in the heterogeneous environment directly impacts the agent's behavior and properties and vice versa. By design, ABMs also allow for the incorporation of stochasticity in a way that induces a heterogeneous population or environment, instead of including it as a noise term. Secondly, ABMs capture emergent phenomena, which are not easily deduced by looking at the system's assumption alone, as they depend on the agents' interactions with each other and their environment in a complex way [96], [97]. By only determining a set of rules to which our autonomous agents adhere, which might be based on observations of single-cell behavior *in vitro* or our hypotheses, we can simulate the evolution of the entire system made up of various agents and their environment, making it a perfect model for identifying and studying biomarker candidates. Finally, ABMs can be built modularly, facilitating the expansion or modification of such a model to incorporate or remove biomarker or combination therapy candidates [96].

The heterogeneity of the TME is incorporated in the model by considering acidic and hypoxic niches, various types of cancer cells (e.g. stem and non-stem, highly and barely antigenic, with or without CAIX- or PD-L1 expression), a varied immune infiltrate in terms of T-cell anergy, as well as the ABM-intrinsic spatial heterogeneity. Most of these properties are not set in stone and may change over time due to the influence of microenvironmental factors, cell interactions, or randomness, allowing for the study of dynamic biomarkers and emergent resistance mechanisms.

As mentioned before, the model is an extension of an agent-based model developed mainly by my supervisor and presented in [83], [84]. However, I have significantly modified and expanded the model to adapt it to my research problem. Most importantly, I have added a model of tumor cell metabolism, included the distribution of glucose, protons, and IFN- γ in the TME as well as their effect on the agents, included dynamic CAIX and PD-L1 expression on cancer cells, removed macrophages, and changed the implementation of lymphocytes to better represent infiltration of most solid tumors. Moreover, I have added a pharmacokinetics model of anti-PD-1 and anti-CAIX treatment. The exact modifications together with their justifications are presented in the materials and methods section of the paper, subsections 2.1 and 2.2.

To my knowledge, this is the first ABM combining tumor-immune interactions and a model of the acidosis-inducing tumor metabolism, allowing for the simulation of the combination of immunotherapy with acidosis-targeting treatments. In this research, I focused on the enzyme CAIX an immunotherapy desensitizer, however, the model considers many other factors of the TME which could drive immunotherapy resistance, such as e.g. tumoral antigenicity, hypoxia, fibrotic stroma accumulation, or the fraction and distribution of cancer stem cells. Moreover, the model is built

modularly and may be easily extended to incorporate other factors that might be decreasing sensitivity to immunotherapy. The proposed model offers a tool to investigate these factors as drivers of resistance or putative biomarkers for ICI therapy either alone or in combination to create a promising biomarker panel and identify novel combination therapy approaches. Its implementation in C++ and Matlab is publicly available at <https://github.com/JuliaGrajek/acidicTumorABM3D>.

4.2.2 Study the impact of tumoral CAIX expression on the evolution of the TME and ICI effectiveness *in silico*, and evaluate it as a combination therapy target with ICIs

Having established and implemented the model, I applied it to study the influence of tumoral CAIX expression on the TME and immunotherapy effectiveness. This investigation was motivated by the first two hypotheses of this thesis. First, I wanted to demonstrate how our model can aid in identifying resistance mechanisms and biomarkers. Secondly, I sought to support my hypothesis that tumoral CAIX expression induces an immunosuppressive TME, impairing immune checkpoint inhibitor effectiveness and potentially serving as a confounder for certain immune-related ICI biomarkers.

First, I investigated the impact of CAIX expression on the TME. I simulated $n = 20$ CAIX expressing and $n = 20$ CAIX knockout tumors (CAIX KO) for 40 days (see sections 3.1 and 3.2 of [39]). The model confirmed *in-vitro* observations that CAIX expression significantly and persistently decreases mean extracellular pH turning the TME acidic. Moreover, our simulated CAIX-expressing tumors had a higher tumor burden, which was in line with experimental findings postulating that CAIX expression in melanoma is associated with increased grade. Unlike the pre-clinical experiments, *in silico* simulations allowed us to investigate the drastically altered tumor composition of CAIX-expressing tumors, with an increased tumor cell fraction and low stroma accumulation (see Figure 2 of [39]). Interestingly this lack of stroma accumulation concealed the increased tumor burden in the volume measurements. Finally and most importantly, these changes in the TME seemed to impact the immune cell infiltrate. CAIX-expressing tumors were characterized by reduced T cell infiltration and a lack of exhausted T cells, supporting the hypothesis that CAIX diminishes T cell activity. Conversely, there was a subset of quiescent cells, i.e. cells that are repressed by acidity and unable to attack, again, supporting the notion of an immunosuppressive TME. A final clue supporting the immunosuppressive effect of CAIX was the decreased PD-L1 expression in CAIX-positive tumors, which implied diminished T-cell-induced PD-L1 expression.

Apart from studying the impact of CAIX expression on the evolution of the TME, my objective was to investigate its influence on immune checkpoint inhibitor effectiveness and its potential as a combination therapy target (section 3.3 of the publication). In the discussed publication, I focused on anti-PD-1 therapy. Figure 4 in [39] shows the efficacy of anti-PD-1 therapy in four heterogeneous tumor groups: tumors with and without CAIX expression that either express PD-L1 constitutively or not. Three doses of anti-PD-1 were compared. The simulations suggest that immune checkpoint blockade is much more effective in CAIX KO tumors than CAIX-expressing tumors, while pre-treatment PD-L1 expression appears to have no impact on the long-term outcome. This lends support to my hypothesis that CAIX impairs ICI effectiveness independently of pre-treatment PD-L1 expression. Furthermore, CAIX expression might actually be masking a potentially PD-L1-positive tumor, that could benefit from anti-PD-1 therapy, by preventing immune-induced

PD-L1 expression. Critically, this suggests that low PD-L1 expression prior to CAIX inhibition should not disqualify patients from receiving combination therapy with anti-CAIX and anti-PD-1. Moreover, my results indicate that measuring the dynamic PD-L1 expression during treatment might increase its accuracy as a biomarker, especially in CAIX-positive tumors.

Backed by the above summarized *in silico* findings, I propose tumoral CAIX expression as a biomarker for ICI therapy and a driver of treatment resistance, as well as a potential combination therapy target, in line with my second research aim and hypothesis. In accordance with my first research aim and hypothesis, my model deepened the understanding of acidosis of the TME as a resistance mechanism of immunotherapy and suggested CAIX inhibition as a combination therapy target to overcome this resistance. While my results corroborate the potential of CAIX as a biomarker and therapeutic target, they should be further validated *in vitro* and *in vivo*. Moreover, like all models, our model has certain limitations, as presented in the discussion of this publication. Some of these limitations could be overcome by supplementing these results with observations from other modeling approaches. In particular, in [40] I proposed a continuous model, that could contribute to my research aims in a way, that the hybrid model was not designed to. This publication is presented in the following chapter.

4.3 The publication

INTERFACE

royalsocietypublishing.org/journal/rsif

Research



Cite this article: Grajek J, Kather JN, Poleszczuk J. 2023 An *in silico* model to study the impact of carbonic anhydrase IX expression on tumour growth and anti-PD-1 therapy. *J. R. Soc. Interface* **20**: 20220654. <https://doi.org/10.1098/rsif.2022.0654>

Received: 5 September 2022

Accepted: 4 January 2023

Subject Category:

Life Sciences–Mathematics interface

Subject Areas:

computational biology, biomedical engineering, biomathematics

Keywords:

carbonic anhydrase IX, immune checkpoint inhibitors, agent-based model, computational model, immunotherapy

Author for correspondence:

Julia Grajek

e-mail: jgrajek@ibib.waw.pl

Electronic supplementary material is available online at <https://doi.org/10.6084/m9.figshare.c.6384994>.

THE ROYAL SOCIETY
PUBLISHING

An *in silico* model to study the impact of carbonic anhydrase IX expression on tumour growth and anti-PD-1 therapy

Julia Grajek¹, Jakob Nikolas Kather² and Jan Poleszczuk¹

¹Nalecz Institute of Biocybernetics and Biomedical Engineering, Polish Academy of Sciences, Warsaw 02-109, Poland

²Else Kroener Fresenius Center for Digital Health, Technical University Dresden, Dresden 01309, Germany

JG, 0000-0003-4449-9846

Immune checkpoint inhibitors (ICIs) are revolutionary cancer treatments. However, the mechanisms behind their effectiveness are not yet fully understood. Here, we aimed to investigate the role of the pH-regulatory enzyme carbonic anhydrase IX (CAIX) in ICI success. Consequently, we developed an *in silico* model of the tumour microenvironment. The hybrid model consists of an agent-based model of tumour-immune cell interactions, coupled with a set of diffusion-reaction equations describing substances in the environment. It is calibrated with data from the literature, enabling the study of its qualitative behaviour. In our model, CAIX-expressing tumours acidified their neighbourhood, thereby reducing immune infiltration by 90% ($p < 0.001$) and resulting in a 25% increase in tumour burden ($p < 0.001$). Moreover, suppression of CAIX improved the response to anti-PD-1 (23% tumour reduction in CAIX knockouts and 6% in CAIX-expressing tumours, $p < 0.001$), independently of initial PD-L1 expression. Our simulations suggest that patients with CAIX-expressing tumours could respond favourably to combining ICIs with CAIX suppression, even in the absence of pre-treatment PD-L1 expression. Furthermore, when calibrated with tumour-type-specific data, our model could serve as a high-throughput tool for testing the effectiveness of such a combinatorial approach.

1. Introduction

Immune checkpoint inhibitors (ICIs), such as anti-PD-1 and anti-CTLA-4, reinvigorate the immune response and thereby deter immune evasion by tumours. They have revolutionized the treatment of various malignancies, particularly metastatic melanoma [1,2]. Nowadays, ICIs are a cornerstone of the treatment of malignancies of almost any organ system, including cancer of the lungs, breast, skin, gastrointestinal and genitourinary tract. However, while some patients exhibit durable benefits, the majority do not respond to the treatment [3–6]. Moreover, ICI therapy is associated with a high incidence of immune-related adverse effects (irAEs) with some of the PD-1 inhibitors causing irAEs in ca 70% of patients and severe irAEs in 10–13% of patients [7,8]. Therefore, it is critical to understand what separates responders from non-responders. Furthermore, there is an acute need for the development of combination therapies that target factors driving resistance to ICI.

Over the past 10 years, considerable effort has been put into the search for ICI biomarkers. The most extensively investigated factor is the expression of the PD-1 ligand PD-L1 on tumour cells [9]. However, this does not discriminate fully between responders and non-responders. For example, some PD-L1-negative patients respond to anti-PD-1 therapy, presumably due to measurement errors such as assay limitations or insufficient sampling that does not capture the heterogeneous and dynamic expression [10]. Furthermore, other patients respond

despite the lack of PD-L1 on tumour cells, since it is PD-L1-expressing immune cells that block the immune response [10]. On the other hand, not all PD-L1-positive patients benefit from the therapy because of other inhibitory pathways subduing the immune response [10]. A comprehensive review of the investigated biomarkers with their limitations has been prepared by Havel *et al.* [11]. Ultimately, there is no definite predictive marker yet. It is believed that finding a single biomarker might be impossible as numerous factors influence the success of immunotherapy. This poses an opportunity for computational modelling, which enables us to quickly and inexpensively build a predictive model that incorporates various elements contributing to ICI effectiveness.

The effect of the immune system on tumour growth has been modelled in various ways, including differential equations [12,13], agent-based or hybrid models [14] and evolutionary game theory models [15], offering new insights into the intricate tumour-immune system interactions. A deeper understanding of the role of immune cells in tumour development has paved the way for the modelling of immunotherapies such as ICI. Gong *et al.* [16] developed an agent-based model (ABM) simulating the effects of pre-treatment PD-L1 expression and tumour neoantigen profile on anti-PD-1 therapy. Lai *et al.* [17] built and analysed a continuous model of anti-PD-1 coupled with anti-TNF- α therapy. Byun *et al.* [18] used a compartmental model to study the synergistic combination of anti-PD-1 and radiotherapy. However, the intricacies of the influence of the tumour microenvironment (TME) on the success of ICI therapy are still underexplored [19,20].

Here, we have developed a hybrid model, which combines an ABM of tumour-immune system interactions with a partial-differential equation model describing the substances present in the TME. While there are models of tumour metabolism and the resulting acidic niche in the TME [21–24] and models of tumour-immune interactions [25,26], to our knowledge, this is the first computational model which takes into account both of these factors. Therefore, it allows us to study combination therapies that target immune response and the immuno-suppressive TME.

In particular, we focus on the combination of PD-1 and carbonic anhydrase IX (CAIX) inhibitors, such as SLC-0111, which has been deemed safe in a Phase 1 clinical trial [27]. CAIX is an enzyme present on the surface of cancer cells, which acidifies the microenvironment by catalysing the hydration of CO₂. The extracellular acidification contributes to immune escape as low pH subdues T-cell cytotoxicity [28], while CAIX expression protects the cancer cells from the effects of acidosis by regulating their intracellular pH [29,30]. It is thus not surprising that CAIX expression has recently piqued the interest of researchers investigating ICIs. A preclinical study has shown CAIX inhibition in combination with ICI to be a promising treatment in mouse tumour models of melanoma and breast cancer [31]. However, treatments tested in mouse models rarely translate to actual patients [32]. We believe that *in silico* models, especially when calibrated with clinical data, may bridge the gap between *in vivo* experiments and clinical practice.

In the present study, we have used our model to study the role of CAIX expression in ICI therapy success. We simulated the influence of CAIX on tumour growth, immune response and the TME and evaluated the effectiveness of combining PD-1 and CAIX inhibitors. Thanks to its bottom-up approach,

our ABM allows us to simulate emergent behaviour, such as ICI effectiveness, based on simple assumptions about the interactions between cells and their environment [33], making it a well-suited model for biomarker investigation. Due to its dynamical nature and three-dimensionality, the model provides insights into the composition of the simulated TME, as well as the dynamic evolution of markers such as PD-L1 expression. Furthermore, our model is built in a modular fashion, hence it can be easily extended to incorporate other components contributing to ICI effectiveness.

2. Materials and methods

2.1. Model assumptions and implementation

We have built a three-dimensional computational framework based on a previously developed well-characterized ABM [25,26]. It is a hybrid model, composed of an on-grid agent-based part responsible for the modelling of tumour-immune interactions and a partial-differential equation model describing the substances present in the TME. The previous model simulated tumour growth in the presence of immune cells, fibrotic stroma accumulation and necrosis induction due to the lack of oxygen. The influence of the TME on immune cells was considered via an umbrella variable termed adjuvanticity. To adapt this model to our research problem, we expanded the notion of the TME by incorporating tumour cell metabolism, which is responsible for an acidic and nutrient-depleted TME, which impairs the immune response. We assume that tumour cells consume oxygen and glucose available in their neighbourhood and in turn produce ATP and protons via aerobic and anaerobic respiration. Nutrient scarcity may lead to the death or impairment of tumour and immune cells. In particular, if the amount of ATP produced by a certain tumour cell is too small, the cell becomes necrotic. On the other hand, the accumulation of protons may turn both cell types quiescent, i.e. suppress their proliferation, or induce cell death. A more detailed explanation of how tumour metabolism and the influence of substances present in the TME on the agents are modelled is given in the electronic supplementary material.

Furthermore, to focus on targeted therapies, we included CAIX and PD-L1 expression on tumour cells in our model. We assume that each new tumour cell may express CAIX with a fixed probability $CAIX_{freq}$. CAIX acidifies the TME and increases the tumour cell's resistance to low pH, as described in the electronic supplementary material. On the other hand, PD-L1 expression is dependent on T-cell activity [34,35]. Attacking T cells produce IFN- γ in their vicinity, and, once the IFN- γ concentration surpasses a certain threshold, cancer cells in the neighbourhood start expressing PD-L1. When lymphocytes try to attack cancer cells with PD-L1 expression, the attack fails, and they become exhausted, i.e. they irreversibly lose their ability to attack.

The previous model contained two types of immune cells, T cells and macrophages. Since the current model had already been heavily extended by modelling the TME in more detail, thereby increasing computation costs, we simplified the immune response to cut down on computation time, memory requirements and the number of parameters. As T cells were more fundamental to the mechanisms we wanted to model, and their infiltration was supported by the experimental data we tried to recreate, we removed macrophages from the model. Similarly, we assumed that stroma was fully permeable to both lymphocytes and tumour cells, as we were not focusing on stroma-targeting therapies.

Finally, the previous model represented colorectal cancer, which usually consists of densely packed cells. Due to this property, it was assumed that immune cells could not occupy the

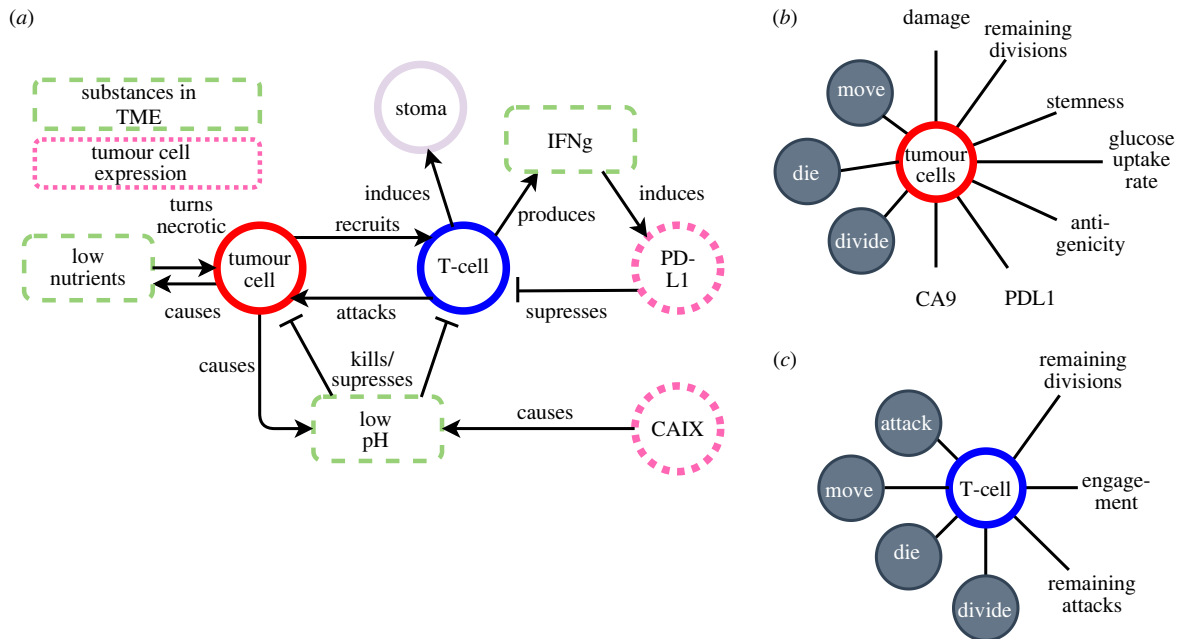


Figure 1. Short overview of the ABM. (a) Diagram of the interactions between the agents and the environment. (b) Actions (dark grey) and properties (white) of tumour cells. (c) Actions (dark grey) and properties (white) of T cells.

same grid cell as tumour cells. However, we performed our simulations without focusing on a specific tumour type, so we removed this simplification. We set the grid size equal to the average tumour cell diameter and thus assumed that only one tumour cell can occupy one grid cell. This applied to both active tumour cells and necrotic cells. Lymphocytes, however, are much smaller than tumour cells; hence we allowed them to occupy the same grid cell without limits. Moreover, since T cells can usually slip in between tumour cells to infiltrate tumours, we assumed that they can also occupy the same grid cell as tumour cells.

In short, we have an on-grid ABM that considers two types of agents: tumour cells and lymphocytes. Their actions are stochastic but depend on the environment (in particular, on other agents in their neighbourhood and the substance gradient in their grid cell (figure 1a)). Moreover, agents have certain properties such as stemness or proliferation capacity, which influence their actions and thereby take into account the history of the given agent (figure 1b,c). Simplified diagrams explaining the rules that govern their behaviour in each iteration are presented in electronic supplementary material, figure S1.

The main simulation engine is implemented in the C++ programming language. The simulations have been run and visualized using Matlab 2020Rb. All source codes are freely available at <https://github.com/JuliaGrajek/acidicTumorABM3D>.

2.2. Treatment optimization in heterogeneous tumours

For the comparison of ICI efficacy in heterogeneous tumour groups, we simulated anti-PD-1 treatment at three dose levels: $d = 33\%$, 66% , 100% of the maximal dose. For this experiment, we assumed that anti-PD-1 decreases the probability of T-cell suppression by PD-L1, denoted $PDL1SuppProb$, by 25%, 50% and 75%, respectively, for the entire duration of the simulation.

To test several treatment schedules, we then introduced simple pharmacokinetics in the model. We assume that the serum concentrations of anti-PD-1 and CAIX inhibitors decay exponentially with rate constant $k = \ln(2)/t_{1/2}$, where $t_{1/2}$ is the serum elimination half-life specific for the drug. Additionally,

CAIX inhibitors are administered orally, their concentration at the administration site again decreases monoexponentially, and it is fully absorbed into the bloodstream. The absorption rate constant can be calculated by knowing the time of maximal drug concentration in the body t_{max} in the following way: maximal drug concentration occurs when the absorption rate equals the elimination rate, i.e. $k_a(X_a)_{t_{max}} = k(X)_{t_{max}}$, where X_a denotes the drug concentration at the site of administration and X the drug serum concentration. From this, we get $t_{max} = \ln(k_a/k)/(k_a - k)$ and can determine the value of k_a . By contrast, anti-PD-1 is administered intravenously and is absorbed immediately. We assume that drug concentration linearly corresponds to the drug effect, i.e. $PDL1SuppProb = 1 - 0.75 \times X_{antiPD1}$, where $X_{antiPD1}$ is the anti-PD-1 concentration in serum. The coefficient 0.75 was chosen to correspond to the maximal dose tested in the prior experiment. Similarly, CAIX inhibitors suppress CAIX expression on cancer cells, i.e. they increase the probability that a cancer cell stops expressing CAIX in the given iteration, which we denote $CAIXSup = X_{antiCAIX}$.

2.3. Statistical analysis and visualization

Pairwise comparisons between CAIX knockout and CAIX tumours were carried out on the results of the simulations without treatment. Statistical significance was analysed using the two-sided Wilcoxon rank-sum test implemented in Matlab (Mathworks Inc. Matlab 2020Rb) in the *ranksum* function. Visualization of the obtained data was performed using Python's *matplotlib* library.

Comparisons between multiple groups (treatment efficacy) were analysed using the Kruskal–Wallis test with Dunn *post hoc* analysis. Bonferroni correction was applied. Results were plotted using Python's *seaborn* library.

Survival analysis was performed in The Cancer Genome Atlas (TCGA) database using the Kaplan–Meier Plotter developed by Lanczyk *et al.* and presented in [36]. Significance was measured with the log-rank test. The cut-off value distinguishing high and low CAIX expression was determined for each tumour type by computing all possible cut-off values between the upper and

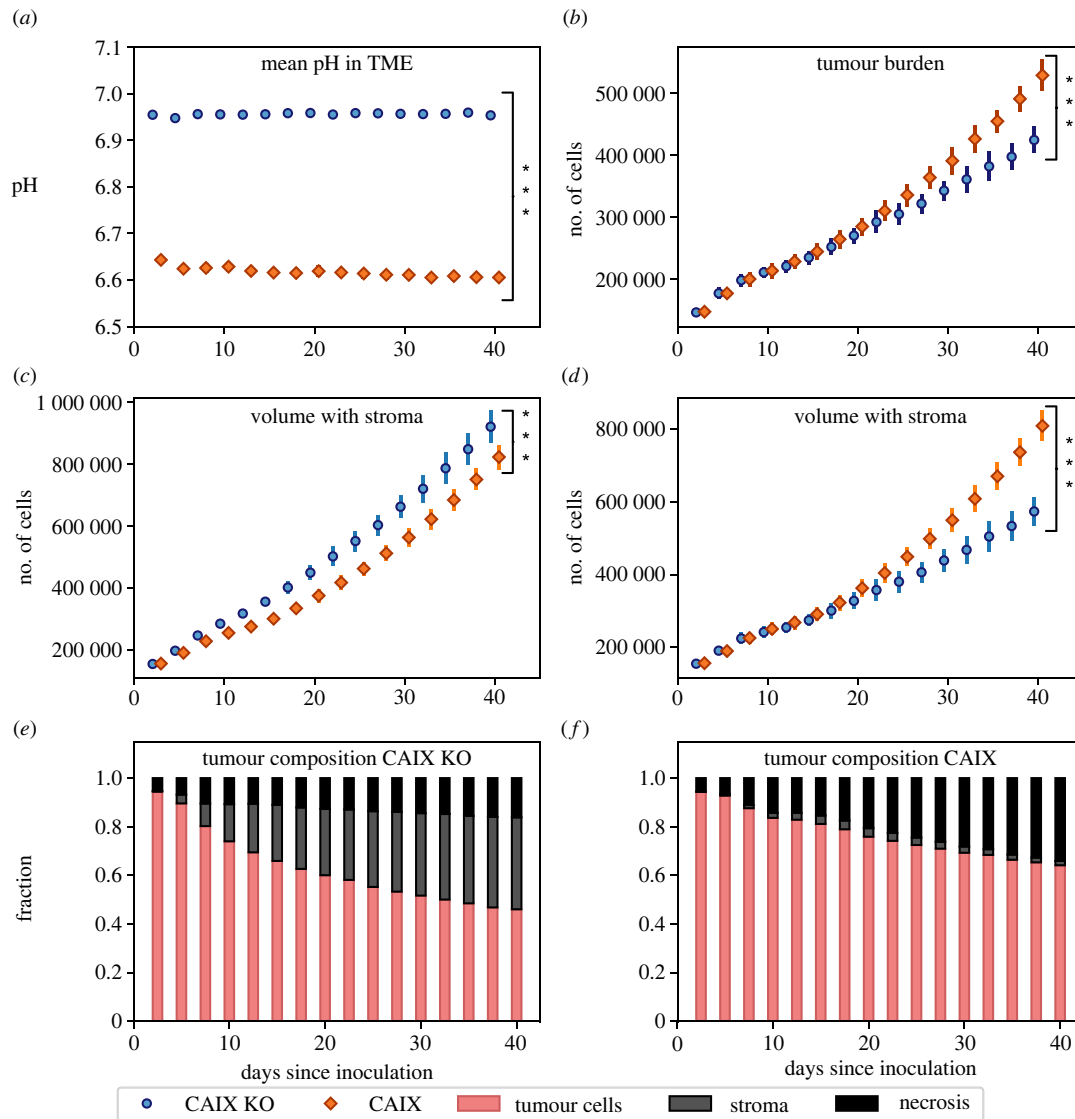


Figure 2. Influence of CAIX expression on the tumour and the TME. The mean results of 20 simulations are plotted. Error bars indicate s.d. (a) For each independent simulation mean pH over the entire domain is measured. (b) Tumour burden is here defined as the number of tumour cells in the domain. (c,d) Volume denotes the number of tumour cells and necrotic cells, either including stromal cells or not. (e,f) Tumour composition is shown as the fraction of cell types that make up the tumour. Lymphocytes are much smaller than tumour cells, hence they are omitted.

lower quartile and choosing the best performing one, i.e. the most significant one in terms of the log-rank test. To account for this multiple hypothesis testing, we also report the false discovery rate. The follow-up threshold was set to 60 months.

3. Results

3.1. Carbonic anhydrase IX induces acidification of the tumour microenvironment and supports tumour growth

To validate that the model is biologically plausible, we independently simulated $n = 20$ CAIX knockout tumours (CAIX KO) and $n = 20$ CAIX-expressing tumours (CAIX). Simulations started from a spheroid with a radius of 30 tumour cells. Starting with a spheroid as opposed to a single tumour cell allowed us to drastically cut simulation time. At the same time, the

initialized tumours were still too small to cause significant nutrient shortage that would induce a less homogeneous tumour spheroid, e.g. having a significant necrotic core. The nutrient gradients were always calculated as a steady state solution, hence, this initialization did not have an impact on the TME. As this was simply due to an efficiency issue, the publicly available codes allow to start the simulation from a single tumour cell as well. A randomly sampled fraction of CAIX^{freq} tumour cells expressed CAIX at the beginning of the simulation in CAIX tumours, while CAIX expression was non-existent in CAIX KO tumours. We recorded tumour behaviour and changes in TME for 40 days, taking measurements every 2.5 days.

Our model showed that CAIX expression significantly and durably decreased mean extracellular pH (from 7 to *ca* 6.6; $p < 0.001$) (figure 2a). This decrease in pH seemed favourable to tumour growth, as our simulated CAIX tumours were considerably bigger in terms of the number of tumour cells

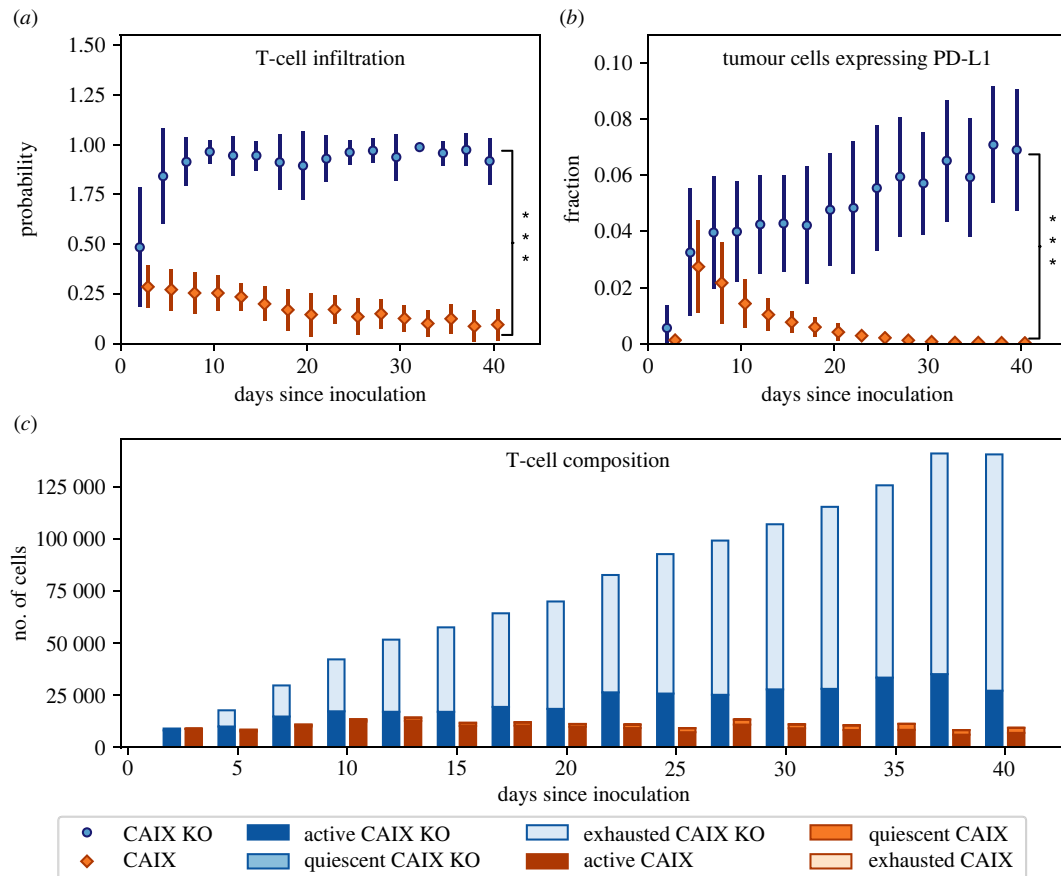


Figure 3. Influence of CAIX on the immune response. The mean results of 20 simulations are plotted. Error bars indicate s.d. (a) T-cell infiltration is measured as the probability of finding a T cell with a distance smaller or equal to two grid cells to a tumour cell. (b) Fraction of tumour cells with PD-L1 expression. (c) Types of T cells in the TME: exhausted cells have either used up their killing capacity or been suppressed by PD-L1 and cannot ever recover their cytotoxicity. Quiescent cells are reversibly suppressed by low pH.

(figure 2b). More specifically, CAIX tumours consisted on average of *ca* 25% more tumour cells than CAIX KO tumours ($p < 0.001$).

Since tumours consist of more than just cancer cells, we also analysed tumour volume, defined as the number of tumour cells, necrotic cells and stromal cells. We decided to omit lymphocytes as their diameters are much smaller than those of tumour cells and the grid cells of our domain, and hence we may assume that they can slip in between other cells and do not contribute to the tumour volume. Contrary to the tumour cell burden, we observed that CAIX KO tumours had a larger volume than CAIX tumours ($p < 0.001$) (figure 2c). This could be explained by the salient change in tumour composition (figure 2e). CAIX tumours consisted mainly of tumour cells (more than 60% of tumour composition), whereas CAIX KO tumours had a considerable fibrotic stroma fraction. Removing stroma from our calculations induced a dramatic difference in tumour volume between CAIX and CAIX KO tumours, in favour of the CAIX tumours (figure 2d, $p < 0.001$).

3.2. Carbonic anhydrase IX expression impairs immune response and PD-L1 expression

The abundant accumulation of stroma (figure 3c) implied a superior immune response in CAIX KO tumours, which

could explain the hampered tumour growth. To quantify T-cell infiltration in our simulations, we calculated the probability of finding a T cell in the vicinity of a tumour cell, i.e. the fraction of tumour cells that have a T cell present within the distance of two grid cells. We found that tumours lacking CAIX expression have significantly increased T-cell infiltration (92% versus 10%, $p < 0.001$, figure 3a). Moreover, we observed higher PD-L1 expression in CAIX KO (figure 3b), which supports the notion of an enhanced immune response, since PD-L1 is induced by T-cell activity.

Furthermore, our computational model allowed us to look deeper and analyse the composition of the infiltrating T-cell population (figure 3c). In CAIX KO tumours, we observed more active T cells. However, there was also a dramatic increase in exhausted T cells, indicating that immune cells launch more attacks in CAIX KO tumours. On the other hand, in CAIX tumours, we found a fraction of quiescent T cells, which are cells suppressed by low pH that are thus unable to attack.

3.3. Testing treatment efficacy in heterogeneous tumour types

Having established that CAIX expression is beneficial to tumour growth, we wanted to test whether CAIX inhibition can improve anti-PD-1 treatment effectiveness. In addition,

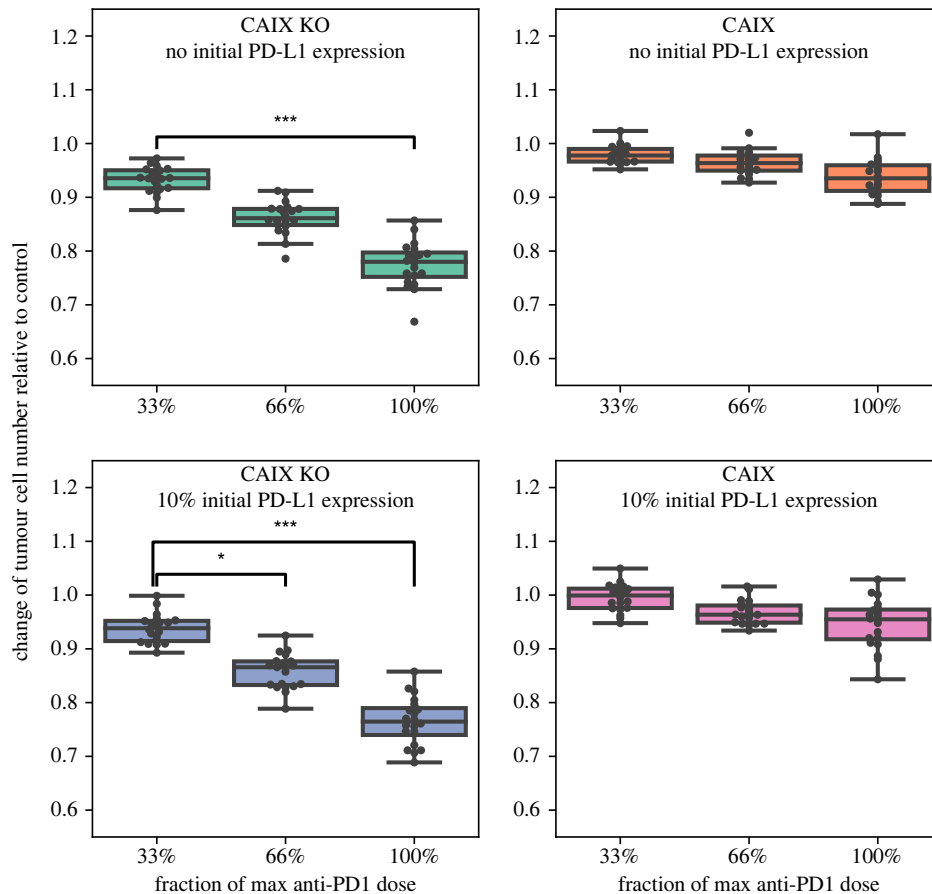


Figure 4. Efficacy of anti-PD1 treatment in four heterogeneous tumour groups at three dose levels (33%, 66% and 100% of maximum dose). Per dose and tumour group, 20 tumours were simulated and compared with the control group that did not receive anti-PD-1. Black circles indicate individual repeats. Immune checkpoint blockade was significantly more effective in CAIX KO than CAIX tumours ($p < 0.001$ for medium and high drug dose, $p = 0.03$ for low dose for tumours without initial PD-L1 expression; Bonferroni correction was applied). There was no significant difference between tumours without PD-L1 expression at treatment begin and tumours with 10% PD-L1 expression at beginning of treatment. Significance between doses within the same tumour group is marked on the plots with their given p -value.

we decided to investigate the significance of PD-L1 expression at beginning of treatment on therapy success. Therefore, we simulated ICI treatment for three different doses in four distinct tumour groups: CAIX KO without initial PD-L1 expression, CAIX KO with initial PD-L1 expression, CAIX-expressing tumours without initial PD-L1 expression and CAIX-expressing tumours with initial PD-L1 expression. Again, tumours were grown from a sphere with a radius of 30 tumour cells. We conducted 80 simulations per tumour group (20 independent repeats per tested anti-PD-1 dose and 20 control tumours that did not receive anti-PD1 treatment) and measured the change in tumour cell number in the treatment group relative to the appropriate control group. Treatment was administered on day 0 and response was assessed on day 40.

ICI therapy was significantly more effective in the CAIX KO groups than in the CAIX groups (figure 4). In the groups without initial PD-L1 expression, we observed on average 22% tumour reduction for CAIX KO versus 6% tumour reduction for CAIX for the highest studied anti-PD-1 dose, 14% for CAIX KO versus 4% for CAIX for the medium dose (66% of maximum dose) and 7% for CAIX KO versus 2% for CAIX for the lowest dose (33% of maximum dose). All of these differences were significant with $p < 0.05$ (Kruskal-Wallis test and *post hoc* Dunn analysis with Bonferroni

correction, see electronic supplementary material, figure S2). On the contrary, initial PD-L1 expression was not required for long-term efficacy, and we did not observe any statistically significant difference in the median treatment effectiveness between the PD-L1-expressing tumours and their PD-L1 non-expressing counterparts. The only factor in which these groups differed was the effectiveness of the lowest anti-PD-1 dose, which was significantly better in the CAIX KO no PD-L1 group than the CAIX no PD-L1 ($p = 0.03$), while there was no difference between the CAIX KO PD-L1 and CAIX PD-L1 groups. Concerning dose escalation, in CAIX KO tumours, the highest dose was significantly more effective than the lowest dose ($p < 0.001$). In the CAIX KO group without initial PD-L1 expression, there was no difference between the low and medium dose, unlike in the group with initial PD-L1 expression, where we observed a slight difference ($p = 0.047$).

Exemplary tumours treated with the maximal anti-PD-1 dose for each studied tumour type are shown in figure 5. We can see that all tumours have a necrotic core. CAIX KO tumours are fully infiltrated by T cells and filled with fibrotic stroma. It is clear that CAIX tumours have lower T-cell infiltration and that the present lymphocytes tend to stay outside of the tumour, where the pH is higher. In short, the immune response is not only greater in CAIX KO tumours, but the immune cells are also better distributed.

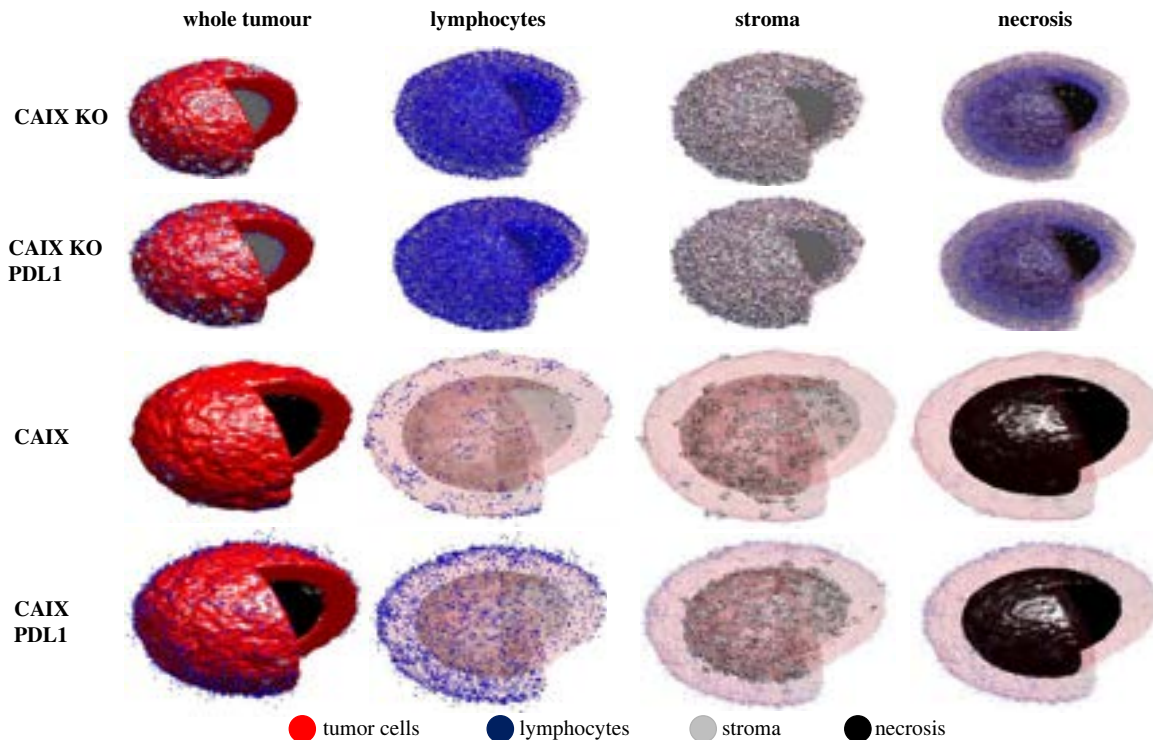


Figure 5. Examples of tumours treated with the maximal anti-PD1 dose 40 days after treatment start. The first column shows the entire tumour, while the other columns focus on a certain cell type and the remaining cells are plotted with increased transparency.

3.4. Simulation of combination therapy schedules

The results discussed in the previous section urged us to study combination therapy between CAIX inhibition and anti-PD1 treatment more in depth and perform a preliminary study of possible therapy schedules. Considering that CAIX KO tumours had superior immune infiltration and response to anti-PD-1, we hypothesized that administering CAIX inhibitors prior to anti-PD-1 might increase the effectiveness of combination therapy compared with simultaneous administration. The reasoning for this hypothesis was that CAIX inhibition would induce a hotter TME, thus increasing immunotherapy effectiveness. To test this hypothesis, we simulated seven treatment schedules in 20 independent *in silico* tumours. We started each simulation from a spherical tumour with a radius of 30 tumour cells and let it grow for 5 days. Daily anti-CAIX administration (in line with the protocol in [27]) started on day 5.5. As shown in figure 6a, T-cell infiltration reached its peak on day 8.5. Hence, we tested treatment schedules during which anti-PD-1 was injected once on days 5.5 to 8.5. Anti-PD-1 is administered at two- to four-week intervals, so we decided to look at the change in tumour burden within two weeks after the anti-PD-1 treatment start. We did not observe any significant difference between the treatment schedules (figure 6b).

3.5. Carbonic anhydrase IX is a prognostic biomarker in certain tumour types

To initially test our hypothesis that CAIX benefits tumour progression in clinical data, we performed a survival analysis for 21 tumour types divided into high and low CAIX-expressing cohorts (overall $n = 7489$). We observed decreased overall

survival, determined by the HR and the p -value of the log-rank test, in the CAIX-expressing cohort for 10 tumour types, and a reversed relationship in two tumour types (see electronic supplementary material, table S2). However, out of these 12 tumour-type-specific analyses, only two had a low FDR (liver hepatocellular carcinoma: HR 2.4, $p < 0.001$, FDR = 1% and lung adenocarcinoma: HR 1.72, $p < 0.001$, FDR = 10%). In both cases, high CAIX expression was associated with poor prognosis.

4. Discussion

Driven by the clinical need for increasing the effectiveness of ICI therapy, we have developed a computational model of tumour-immune interactions. Using this model, we studied the influence of CAIX expression on tumour development and ICI success. To our knowledge, this is the first ABM that incorporates tumour metabolism and the resulting acidosis, as well as immune cells, and allows thus for the modelling of combination therapies that target both immune checkpoints and the immuno-suppressive low pH. Our *in silico* simulations produced a TME with pH values that are in line with the literature, where the pH of the TME is reported to fall within 5.7–7 [37] and most commonly oscillates around 6.5–6.8 [28]. Moreover, we showed that CAIX expression significantly impairs immune response and is therefore beneficial to tumour growth. Furthermore, CAIX-expressing tumours did not respond to ICIs, as opposed to CAIX KO tumours. This indicates that CAIX expression might be one of the factors driving resistance to ICI treatment. Our results provide a basis for further research into CAIX as a biomarker for ICI therapy and as a target for combination therapy. Importantly,

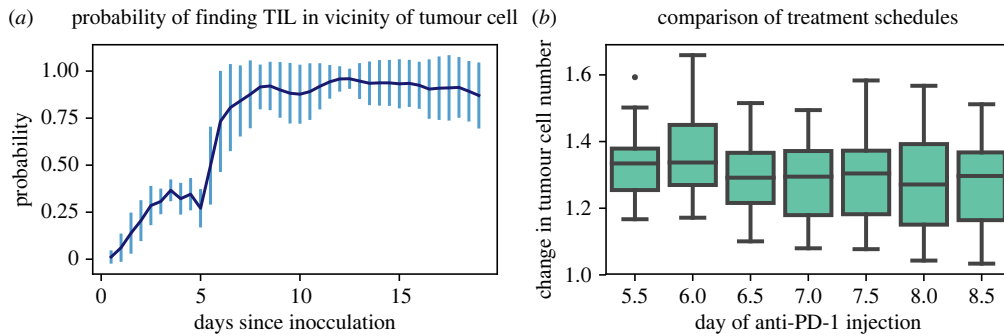


Figure 6. Initial analysis of combination therapy schedules. The CAIX inhibitor SLC-0111 is being administered on day 5.5. (a) T-cell infiltration into the tumour after pH normalization. The line plot represents averages of 20 simulations, the error bars represent s.d. (b) Change in tumour cell number within two weeks after anti-PD-1 administration. We observe no statistically significant difference between the treatment schedules. TIL: tumour-infiltrating lymphocyte.

our model may be used as a high-throughput tool for testing combination therapy protocols, when calibrated with tumour-specific data.

According to our simulations, CAIX-expressing tumours are 25% larger than CAIX KO tumours in terms of tumour cell number. This implies that CAIX-expressing tumours might be more aggressive, which corroborates experimental findings in [31], where Chafe *et al.* identified CAIX as a biomarker for worse overall survival in melanoma, which was associated with increased grade and risk of metastasis. Similarly, we also observed an association between high CAIX expression and poor prognosis in liver hepatocellular carcinoma and lung adenocarcinoma. It must be noted that we have only performed a preliminary survival analysis, which did not take into account other variables which might influence ICI effectiveness. Further multivariate analysis should be performed to rule out any confounding variables. Moreover, we observed that the decreased tumour burden of CAIX KO tumours might not be observed by volume measurements alone, as the tumour composition changes significantly when suppressing CAIX. In particular, CAIX KO tumours seem to have a high stroma fraction, which might mask the decrease in the number of tumour cells.

In our simulations, we also observed that CAIX expression dramatically decreases T-cell infiltration and suppresses their effector function. As T-cell quiescence is reversible [4], inhibiting CAIX might reinvigorate immune response by increasing T-cell infiltration and cytotoxicity. Taken together with the observation that CAIX expression inhibits PD-L1 expression on tumour cells, this supports our hypothesis that combination therapy with anti-CAIX might improve ICI efficacy. Considering that our model assumed that PD-L1 is induced by lymphocyte activity, this was also another indicator of improved immune response in CAIX KO tumours.

The enhanced immune response in CAIX KO tumours led to abundant stroma accumulation in our *in silico* experiments. Studying the effects of stroma on treatment success was out of the scope of this study, but remains an interesting question for further research that focuses on cancer types that are linked to chronic-inflammation-induced fibrosis. In [25], Kather *et al.* postulated that fibrosis might have both pro-tumorigenic and tumour-suppressive properties, depending on the immune cell infiltration. Hence, research considering combination approaches consisting of immunotherapy and treatments targeting stroma and CAIX expression seems promising.

Finally, our simulations of anti-PD1 therapy in CAIX-expressing and CAIX KO tumours suggest that CAIX is a potential biomarker for ICIs and combination therapy might be more effective for patients with CAIX-expressing tumours than monotherapies. On the other hand, PD-L1 expression at beginning of treatment was not crucial for ICI therapy effectiveness. This might be explained by the fact that PD-L1 expression is dynamic, which is a limitation of this biomarker that has been raised before, see [10]. In particular, we believe PD-L1 expression in the pre-treatment TME to be a misleading biomarker for combination therapy with anti-CAIX, as CAIX expression induces a T-cell-depleted TME. Inhibiting CAIX may then reinvigorate immune response and therefore up-regulate PD-L1 expression. Hence, PD-L1 negative patients should not be excluded from the treatment based on this marker alone.

Our simulations did not find a significant difference between treatment protocols that assume simultaneous administration of anti-PD1 and anti-CAIX versus protocols with a time delay. However, our model's smallest discrete time step is equal to 12 h. Therefore, it cannot be assumed that simultaneous administration of both drugs is the best treatment strategy, based on our results alone. For future investigations, the model could be recalibrated to allow for smaller time steps and more precise modelling of treatment response. Yet, this would significantly increase the already quite time-consuming computation time. Hence, we believe that a continuous model would be more suitable to optimize the exact treatment protocol. Such a simpler and computationally cheaper model would also allow for the simulation of longer treatment and various treatment cycles that could actually eradicate the tumour instead of slowing down its growth. Moreover, it could be interesting to evaluate more complex pharmacodynamics models which represent the treatment effect more accurately.

It should be noted that in our simulations treatment was administered while the tumour consisted of less than 200 000 cells. This obviously does not reflect clinical reality, where such a small tumour would probably not be detected and treated. Since the behaviour of the agents depends only on the TME and the interactions between the single agents, as opposed to the absolute number of modelled cells, we believe that our simulations reflect realistic qualitative results despite the smaller scale. If our model were to be used for quantitative analysis, larger tumours should be simulated. To avoid drastically increasing computation costs, the model could be

modified. One idea would be to forgo the three-dimensional structure and perform two-dimensional simulations, which would of course be a simplification, but would allow to model larger tumours without increasing the number of modelled agents. Another very interesting approach would be to recalibrate the model in such a way that each grid cell would represent a packet of homogeneous cancer cells, as proposed in [38].

Our study's limitation is that our model is currently only calibrated with data from the literature. We aimed at elucidating the general impact of CAIX expression on tumour growth and immune response, and therefore decided on performing qualitative simulations. An obvious future step would be the thorough calibration and validation of the model with tumour-type-specific data to conduct quantitative analyses. Moreover, as with all computational models, our framework is a simplification of reality. For example, our model assumes that CAIX expression is random, although CAIX is a known hypoxia-related biomarker [39]. This simplification allowed us to decrease model complexity without significantly impacting qualitative model results. However, if somebody were interested in studying the spatial distribution of CAIX, our model could be extended by incorporating this mechanism. Furthermore, our model is ignorant of other pH regulatory pathways, such as other carbonic anhydrases, anion exchangers and monocarboxylate transporters [40]. While it has been shown that inhibiting CAIX alone increases extracellular pH and decreases tumour growth, some studies report that CAIX suppression may result in CAXII upregulation, and suppressing both enzymes simultaneously results in superior tumour eradication [41,42]. Hence, it could be interesting to

incorporate more pH regulatory mechanisms into our model to study their interplay and impact on treatment effectiveness. Finally, our model neglects other factors driving resistance to ICIs, such as the presence of immune-suppressive cells in the TME, like regulatory T cells, pro-tumour macrophages or myeloid-derived suppressor cells. Nevertheless, we were able to capture emergent behaviour which agrees with studies performed on mice, while giving us deeper insight into the underlying mechanisms, providing a bridge between animal and human models. Thanks to its modular fashion, it can be easily extended to test other hypotheses or treatment strategies to quickly and inexpensively determine which are worth further investigation.

Data accessibility. Survival analysis was performed on the $n=7489$ samples available for pan-cancer mRNA analysis in the Kaplan–Meier Plotter database [36]. The data are publicly available at TCGA (<https://portal.gdc.cancer.gov/>). Source codes for the ABM are freely available at <https://github.com/JuliaGrajek/acidicTumorABM3D>.

The data are provided in the electronic supplementary material [43].

Authors' contributions. J.G.: conceptualization, formal analysis, methodology, software, visualization and writing—original draft; J.N.K.: formal analysis, methodology and writing—review and editing; J.P.: conceptualization, methodology, software, supervision and writing—review and editing.

All authors gave final approval for publication and agreed to be held accountable for the work performed therein.

Conflict of interest declaration. The authors declare no potential conflicts of interest.

Funding. Project is supported by ESE, POWR.03.02.00-00-I028/17-00.

References

- Hodi FS *et al.* 2010 Improved survival with ipilimumab in patients with metastatic melanoma. *New Engl. J. Med.* **363**, 711–723. (doi:10.1056/NEJMoa1003466)
- Eggermont AMM *et al.* 2018 Adjuvant pembrolizumab versus placebo in resected stage III melanoma. *New Engl. J. Med.* **378**, 1789–1801. (doi:10.1056/NEJMoa1802357)
- Topalian SL *et al.* 2012 Safety, activity, and immune correlates of anti-PD-1 antibody in cancer. *New Engl. J. Med.* **366**, 2443–2454. (doi:10.1056/NEJMoa1200690)
- Sun L *et al.* 2020 Clinical efficacy and safety of anti-PD-1/PD-L1 inhibitors for the treatment of advanced or metastatic cancer: a systematic review and meta-analysis. *Sci. Rep.* **10**, 1–13. (doi:10.1038/s41598-019-56847-4)
- Johnson DB, Peng C, Sosman JA. 2015 Nivolumab in melanoma: latest evidence and clinical potential. *Ther. Adv. Med. Oncol.* **7**, 97. (doi:10.1177/1758834014567469)
- Carlino MS, Larkin J, Long GV. 2021 Immune checkpoint inhibitors in melanoma. *Lancet* **398**, 1002–1014. (doi:10.1016/S0140-6736(21)01206-X)
- Almutairi AR, McBride A, Slack M, Erstad BL, Abraham I. 2020 Potential immune-related adverse events associated with monotherapy and combination therapy of ipilimumab, nivolumab, and pembrolizumab for advanced melanoma: a systematic review and meta-analysis. *Front. Oncol.* **10**, 91. (doi:10.3389/fonc.2020.00091)
- Rausch MP, Hastings KT. 2017 Immune checkpoint inhibitors in the treatment of melanoma: from basic science to clinical application. In *Cutaneous melanoma: etiology and therapy*, pp. 121–142. Brisbane, Australia: Codon Publications.
- Doroshov DB *et al.* 2021 PD-L1 as a biomarker of response to immune-checkpoint inhibitors. *Nat. Rev. Clin. Oncol.* **18**, 345–362. (doi:10.1038/s41571-021-00473-5)
- Cottrell TR, Taube JM. 2018 PD-L1 and emerging biomarkers in PD-1/PD-L1 blockade therapy. *Cancer J.* **24**, 41. (doi:10.1097/PP0.0000000000000301)
- Havel JJ, Chowell D, Chan TA. 2019 The evolving landscape of biomarkers for checkpoint inhibitor immunotherapy. *Nat. Rev. Cancer.* **19**, 133–150. (doi:10.1038/s41568-019-0116-x)
- Mahlbacher GE, Reihmer KC, Frieboes HB. 2019 Mathematical modeling of tumor-immune cell interactions. *J. Theor. Biol.* **469**, 47. (doi:10.1016/j.jtbi.2019.03.002)
- Laleh NG *et al.* 2022 Classical mathematical models for prediction of response to chemotherapy and immunotherapy. *PLoS Comput. Biol.* **18**, e1009822. (doi:10.1371/journal.pcbi.1009822)
- Norton KA, Gong C, Jamalain S, Popel AS. 2019 Multiscale agent-based and hybrid modeling of the tumor immune microenvironment. *Processes* **7**, 37. (doi:10.3390/pr7010037)
- Tavakoli F, Sartakhti JS, Manshaei MH, Basanta D. 2020 Cancer immunoeediting: a game theoretical approach. *In Silico Biol.* **14**, 1. (doi:10.3233/ISB-200475)
- Gong C, Milberg O, Wang B, Vicini P, Narwal R, Roskos L, Popel AS. 2017 A computational multiscale agent-based model for simulating spatio-temporal tumour immune response to PD1 and PDL1 inhibition. *J. R. Soc. Interface* **14**, 20170320. (doi:10.1098/rsif.2017.0320)
- Lai X, Hao W, Friedman A. 2020 TNF- α inhibitor reduces drug-resistance to anti-PD-1: a mathematical model. *PLoS ONE* **15**, e0231499. (doi:10.1371/journal.pone.0231499)
- Byun JH, Yoon IS, Jeong YD, Kim S, Jung IH. 2020 A tumor-immune interaction model for synergistic combinations of anti PD-L1 and ionizing irradiation treatment. *Pharmaceutics* **12**, 830. (doi:10.3390/pharmaceutics12090830)
- Damgaci S, Enriquez-Navas PM, Pilon-Thomas S, Guvenis A, Gillies RJ, Ibrahim-Hashim A. 2020

- Immunotherapy on acid: opportunities and challenges. *Eur. J. Clin. Nutr.* **74**, 3–6. (doi:10.1038/s41430-020-0683-7)
20. Jin MZ, Jin WL. 2020 The updated landscape of tumor microenvironment and drug repurposing. *Signal Transduct. Targeted Therap.* **5**, 1–16. (doi:10.1038/s41392-019-0089-y)
 21. Gerlee P, Anderson ARA. 2008 A hybrid cellular automaton model of clonal evolution in cancer: the emergence of the glycolytic phenotype. *J. Theor. Biol.* **250**, 705–722. (doi:10.1016/j.jtbi.2007.10.038)
 22. Smallbone K, Gatenby RA, Gillies RJ, Maini PK, Gavaghan DJ. 2007 Metabolic changes during carcinogenesis: potential impact on invasiveness. *J. Theor. Biol.* **244**, 703–713. (doi:10.1016/j.jtbi.2006.09.010)
 23. Patel AA, Gawlinski ET, Lemieux SK, Gatenby RA. 2001 A cellular automaton model of early tumor growth and invasion: the effects of native tissue vascularity and increased anaerobic tumor metabolism. *J. Theor. Biol.* **213**, 315–331. (doi:10.1006/jtbi.2001.2385)
 24. Robertson-Tessi M, Gillies RJ, Gatenby RA, Anderson ARA. 2015 Impact of metabolic heterogeneity on tumor growth, invasion, and treatment outcomes. *Cancer Res.* **75**, 1567–1579. (doi:10.1158/0008-5472.CAN-14-1428)
 25. Kather JN *et al.* 2017 *In silico* modeling of immunotherapy and stroma-targeting therapies in human colorectal cancer. *Cancer Res.* **77**, 6442–6452. (doi:10.1158/0008-5472.CAN-17-2006)
 26. Kather JN *et al.* 2018 High-throughput screening of combinatorial immunotherapies with patient-specific *in silico* models of metastatic colorectal cancer. *Cancer Res.* **78**, 5155–5163. (doi:10.1158/0008-5472.CAN-18-1126)
 27. McDonald PC *et al.* 2020 A phase 1 study of SLC-0111, a novel inhibitor of carbonic anhydrase IX, in patients with advanced solid tumors. *Am. J. Clin. Oncol.* **43**, 484–490. (doi:10.1097/COC.0000000000000691)
 28. Erra Diaz F, Dantas E, Geffner J. 2018 Unravelling the interplay between extracellular acidosis and immune cells. *Mediators Inflamm.* **2018**, 1–11. (doi:10.1155/2018/1218297)
 29. Lee SH, McIntyre D, Honess D, Hulikova A, Pacheco-Torres J, Cerdán S, Swietach P, Harris AL, Griffiths JR. 2018 Carbonic anhydrase IX is a pH-stat that sets an acidic tumour extracellular pH *in vivo*. *Br. J. Cancer* **119**, 622–630. (doi:10.1038/s41416-018-0216-5)
 30. Swietach P, Patiar S, Supuran CT, Harris AL, Vaughan-Jones RD. 2009 The role of carbonic anhydrase 9 in regulating extracellular and intracellular pH in three-dimensional tumor cell growths. *J. Biol. Chem.* **284**, 20 299–20 310. (doi:10.1074/jbc.M109.006478)
 31. Chafe SC *et al.* 2019 Targeting hypoxia-induced carbonic anhydrase IX enhances immune-checkpoint blockade locally and systemically. *Cancer Immunol. Res.* **7**, 1064–1078. (doi:10.1158/2326-6066.CIR-18-0657)
 32. Mak IWY, Evaniew N, Ghert M. 2014 Lost in translation: animal models and clinical trials in cancer treatment. *Am. J. Transl. Res.* **6**, 114.
 33. Metzcar J, Wang Y, Heiland R, Macklin P. 2019 A review of cell-based computational modeling in cancer biology. *JCO Clin. Cancer Inform.* **3**, 1–13. (doi:10.1200/CCI.18.00069)
 34. Kaunitz GJ *et al.* 2017 Melanoma subtypes demonstrate distinct PD-L1 expression profiles. *Lab. Invest.* **97**, 1063–1071. (doi:10.1038/labinvest.2017.64)
 35. Chen S, Crabill GA, Pritchard TS, McMiller TL, Wei P, Pardoll DM, Pan F, Topalian SL. 2019 Mechanisms regulating PD-L1 expression on tumor and immune cells. *J. Immunother. Cancer* **7**, 305. (doi:10.1186/s40425-019-0770-2)
 36. Lániczky A, Gyórfi B. 2021 Web-based survival analysis tool tailored for medical research (KMplot): development and implementation. *J. Med. Internet Res.* **23**, e27633. (doi:10.2196/27633)
 37. Feng L, Dong Z, Tao D, Zhang Y, Liu Z. 2018 The acidic tumor microenvironment: a target for smart cancer nano-theranostics. *Natl. Sci. Res.* **5**, 269–286. (doi:10.1093/nsr/nwx062)
 38. Piotrowska MJ, Angus SD. 2009 A quantitative cellular automaton model of *in vitro* multicellular spheroid tumour growth. *J. Theor. Biol.* **258**, 165–178. (doi:10.1016/j.jtbi.2009.02.008)
 39. Huizing FJ, Hoeben BAW, Franssen GM, Boerman OC, Heskamp S, Bussink J. 2019 Quantitative imaging of the hypoxia-related marker CAIX in head and neck squamous cell carcinoma xenograft models. *Mol. Pharm.* **16**, 701–708. (doi:10.1021/acs.molpharmaceut.8b00950)
 40. Neri D, Supuran CT. 2011 Interfering with pH regulation in tumours as a therapeutic strategy. *Nat. Rev. Drug Discovery* **10**, 767–777. (doi:10.1038/nrd3554)
 41. Chiche J, Ilc K, Laferrière J, Trottier E, Dayan F, Mazure NM, Brahimi-Horn MC, Pouyssegur J. 2009 Hypoxia-inducible carbonic anhydrase IX and XII promote tumor cell growth by counteracting acidosis through the regulation of the intracellular pH. *Cancer Res.* **69**, 358–368. (doi:10.1158/0008-5472.CAN-08-2470)
 42. Teixeira SA *et al.* 2021 The carbonic anhydrase inhibitor E7070 sensitizes glioblastoma cells to radio- and chemotherapy and reduces tumor growth. *Mol. Neurobiol.* **58**, 4520–4534. (doi:10.1007/s12035-021-02437-3)
 43. Grajek J, Kather JN, Poleszczuk J. 2023 An *in silico* model to study the impact of carbonic anhydrase IX expression on tumor growth and anti-PD-1 therapy. Figshare. (doi:10.6084/m9.figshare.c.6384994)

Supplementary methods accompanying the paper “An in silico model to study the impact of Carbonic Anhydrase IX expression on tumor growth and anti-PD-1 therapy” by Julia Grajek, Jakob Nikolas Kather, Jan Poleszczuk, Journal of the Royal Society Interface

Supplementary methods

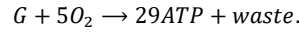
Modeling of substances present in the TME and tumor metabolism

To properly model TME acidification we have to consider oxygen, glucose, and proton concentrations. These spatiotemporal substance concentrations are described by the following set of reaction-diffusion equations:

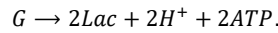
$$\begin{aligned}\frac{\delta O}{\delta t} &= D_O \Delta O - a_O O \mathbb{1}_{TC}, \\ \frac{\delta G}{\delta t} &= D_G \Delta G - a_G G \mathbb{1}_{TC}, \\ \frac{\delta H}{\delta t} &= D_H \Delta H + b_H \mathbb{1}_{TC},\end{aligned}$$

where O , G , and H denote oxygen, glucose, and protons, respectively. The substances S diffuse with rate D_S and are consumed by tumor cells with rate $a_S S$ or produced with rate b_S . The reactions only occur in grid cells in which tumor cells are present, as denoted by the indicator function $\mathbb{1}_{TC}$. We assume Dirichlet boundary conditions, i.e., $S = S_{phys}$ on the boundary, where S_{phys} is the physiological concentration of the given substance. Since diffusion occurs at a much faster timescale than the time step of our discrete simulations ($t = 12h$), we can solve these equations in their steady-state using the finite difference method.

Tumor cells may produce energy using two metabolic pathways: aerobic respiration and anaerobic respiration. The process of aerobic respiration can be described by the simplified reaction:



The exact amount of ATP produced may differ for different cell types but is reported to generally be around 30 (1). We have chosen 29, in line with the model proposed by Tessi et al. (2). Anaerobic respiration, on the other hand, is described by the reaction:



We assume that all uptaken oxygen goes to aerobic respiration, i.e. five oxygen molecules bind with one glucose molecule to produce 29 ATP molecules. The glucose surplus, that is not used for aerobic respiration, i.e. $\max(0, f_G - \frac{f_O}{5})$, goes to anaerobic respiration, producing 2 ATP molecules per glucose molecule. Combining the two reactions, we obtain an equation for ATP production by a single tumor cell:

$$ATP = 29 \min(f_G, \frac{f_O}{5}) + 2 \max(0, f_G - \frac{f_O}{5}),$$

where f_S denotes the uptake of substance S by the tumor cell, $f_S = u_S S$. It is worth noting that cancer cells revert to anaerobic glycolysis in two scenarios: in the absence of oxygen (Pasteur effect) and the presence of oxygen (Warburg effect) (3). We model the Pasteur effect by increasing the glucose uptake rate in case of hypoxia. The Warburg effect is included in the respective uptake rates.

Apart from the protons produced from aerobic respiration, CAIX expression also contributes to TME acidification. We consider the following equation describing proton production by a single tumor cell:

$$b_H = b \left(\frac{2 \max(0, f_G - \frac{f_G}{5})}{\text{aerobic respiration}} + c \right),$$

where c is the number of protons produced due to CAIX expression and b denotes the proton buffering coefficient.

The assumptions about the effect of the substance concentrations on the agents are as follows:

- In the case of lack of nutrients, i.e. if $ATP < ATP_{\text{thresh}}$, the tumor cell becomes necrotic (4).
- If $O < hyp_{\text{Thresh}}$, the given grid cell becomes hypoxic. Hypoxia increases the apoptosis rate of lymphocytes (5) and the glucose uptake rate of tumor cells (Pasteur effect).
- If $G < gluc_{\text{Thresh}}$, lymphocytes cannot migrate or attack (6).
- If $H > TUp_{\text{protThreshQuiescence}}$ tumor cells become quiescent; i.e., they don't proliferate. Moreover, they may become necrotic with probability

$$\frac{H - TUp_{\text{protThreshQuiescence}}}{TUp_{\text{protThresh}} - TUp_{\text{protThreshQuiescence}}},$$

where $TUp_{\text{protThresh}}$ denotes the proton concentration at which tumor cells die with probability 1 (7). This value is higher for tumor cells that express CAIX (8–10).

- If $H > Im_{\text{protThreshQuiescence}}$ lymphocytes become quiescent; i.e., they cannot proliferate or attack. Similar to tumor cells, quiescent lymphocytes may die with a probability dependent on the proton concentration (11–13).

All of these effects are reversible except those resulting in cell death. The values of the threshold parameters are given in Supplementary Table 1.

Param.	Description	Default	Source
seedUnderneath	if fibrosis can be seeded below the cell	False	Assumption
dx	Grid cell width in cm	14.9*1e-4	(14)
TUp _{prol}	probability of tumor cell proliferation	0.5055	(14)
TUp _{mig}	probability of tumor cell migration	0.35	(14)
TUp _{death}	probability of tumor cell death	0.1216	(14)
TUp _{max}	max. proliferation capacity	10	(14)
TU _{danti}	antigenicity strength of mutating tumor cell	0.1	(14)
TU _{damageThresh}	T cell inflicted damage threshold for tumor cell	2	(14)
TUp _s	Tumor stem cell probability of symmetric division	0.42	(14)
TU _{pmut}	mutation probability (increases antigenicity)	0.4	Assumption
IM _{kmax}	killing capacity of lymphocytes	10	Assumption
IM _{pmax}	proliferation capacity of lymphocytes	10	(14)
IM _{pmig}	probability of lymphocyte migration	0.3	Assumption

IMrwalk	random influence on lymphocyte movement	0.5	(14)
IMspeed	Lymphocyte migration speed relative to tumor cells	97	(14)
IMpprol	Lymphocyte proliferation probability	4.623e-04	(14)
IMpdeath	Lymphocyte death probability	1.517e-04	(14)
IMhypoDeath	Scaling factor for lymphocyte death probability in hypoxic areas	1.2	(5)
engagementDuration	how many intermed. steps is a killing cell engaged? default 48 (=6 hrs)	48	(14)
AntiThresh	antigenicity threshold for lymphocyte activation	0.3	(14)
IMinfluxProb	probability of lymphocyte influx per round	0.33	(14)
IMinfluxRate	Scaling factor for number of inflowing lymphocytes	1	(14)
<i>IMrateDynamic</i>	Linear scaling factor for number of inflowing lymphocytes per round, will be multiplied with tumor cell number	0.04	Assumption
IMIFNg	Production rate of IFNgamma by lymphocytes [pg/(cells*h)]	1.02*1e-4	(15)
IFNgDecay	Rate of IFNgamma decay [1/h]	0.1	(15)
IFNgRange	Range of the effect of the IFNgamma produced by a lymphocyte	2	Arbitrary
IFNgThresh	Threshold of IFNgamma concentration above which PD-L1 gets induced on tumor cells [pg]	1e-4	Assumption, chosen so that the fraction of PD-L1 expressing tumor cells corresponds to plausible values, as given in (16)
DCchemo	diffusion/consumption in the stationary diffusion-consumption equation for the chemotaxis map	100	(14)
SCchemo	secretion in the stationary diffusion-secretion equation for the chemotaxis map	1	
<i>physiologicalOxygen</i>	Oxygen concentration in blood [mM]	0.056	(2)
oxygenDiffusion	Oxygen diffusion coefficient [cm ² /s]	2.5*1e-5	(14)
oxygenPointConsumption	Oxygen consumed by tumor cell [cm ² *O ₂ /(cell*s)]	3.8*1e-13	(14)
carryingCapacity	Carrying capacity given in [Cells]	2.1*10 ¹¹ /2	(17)
DCnecro	Oxygen diffusion coefficient after normalization (division by (3dx) ² is due to the fact that we solve the diffusion-reaction equations on a sparser grid in which each grid cell is equal to 9 grid cells of the ABM)	31.4	oxygenDiffusion/oxygenPointConsumption/carryingCapacity/(3* dx) ²
TCnecro	total consumption by a single tumor cell (because of normalization D/c)	1	Arbitrary
hypThresh	Oxygen threshold below which we assume hypoxia [mM]	0.056/12	(17)
ATPThresh	ATP threshold below which the tumor cell might die [mM]	0.05* (physiologicalOxygen)*	Assumption, similar/proportional to oxygen*

		oxygenPointConsumption*29/5)	the oxygen threshold in (14,18)
physiologicalGlucose	Glucose concentration in blood [mM]	5	(2)
glucoseDiffusion	Glucose diffusion coefficient [cm ² /s]	2.6*1e-6	(19)
glucosePointConsumption	Glucose consumed by tumor cell [cm ² G/(cell*s)]	1.2*1e-10	In physiological conditions ca. 70% of uptaken glucose is used for anaerobic glycolysis (20), so this value is calculated based on the knowledge of the oxygen uptake rate
DCglucose	Glucose diffusion coefficient after normalization	436.8	glucoseDiffusion/glucosePointConsumption/carryingCapacity/(3*dx) ²
TCglucose	total glucose consumption by a single tumor cell (because of normalization D/c)	1	Arbitrary
glucThresh	Threshold of glucose consumption below which lymphocytes' effector functions and motility are impaired [mM]	0.5	(6)
GlycTumRate	Factor by which glucose consumption is scaled in case of hypoxia	9/7	(20)
protonDiffusion	Proton diffusion coefficient [cm ² /s]	1.08*1e-5	(2)
physiologicalProton	Proton concentration in blood [mM]	3.98*1e-5	(2)
pHbuffer	Buffering coefficient for proton secretion	5*1e-5	Assumption
DCproton	Proton diffusion coefficient after normalization	0.0012	protonDiffusion/protonPointSecretion/carryingCapacity/(3*dx) ²
SCproton	Proton secretion in the stationary diffusion-secretion equation (because of normalization D/s)	1	Arbitrary
TUprotThresh	Proton threshold above which tumor cells die with probability 1 [mM]	1e-3	(21)
TUARprotThresh	Proton threshold above which CA9 expressing tumor cells die with probability 1 [mM]	1.5*1e-3	Assumption, higher than TUprotThresh
TUprotThreshQuiescence	Proton threshold above which tumor cells become quiescent [mM]	3.98*1e-4	(21)
IMprotThresh	Proton threshold above which lymphocytes die with probability 1 [mM]	3.98*1e-4	Assumption, higher than IMprotThreshQuiescence
IMprotThreshQuiescence	Proton threshold above which lymphocytes become quiescent [mM]	2*1e-4	(11)
smoothRadius	Smoothing radius for desmoplastic stroma seeds	3	(14)
probSeedFibr	probability of fibrosis seeding	0.06	(14)
fibrFrac	Size of the fibrotic seed	0.3	Arbitrary
stromaPerm	0 = stroma not permeable, 1 = fully permeable, default very small	1	Assumption

maxCells	Maximum allowed size of tumor	Inf	Assumption
requireAlive	require tumor to be alive for N iterations, prevents spontaneous tumor death	150	(14)
maxAntigenicity	Tumor cell maximum antigenicity	1	Arbitrary
PDL1SuppProb	Probability of T cell suppression when attacking a PD-L1 expressing cell	1	Assumption, gets reduced by anti-PD1
PDL1freq	Probability of PD-L1 expression by tumor cell at simulation begin	0 or 0.1	Assumption, falls into the range of PD-L1 expression in melanoma (16)
CA9freq	Probability of CA9 expression on tumor cell	0.3	(22)
CA9protons	Protons produced due to CA9 on a single tumor cell in one iteration	2.1*1e-9	Assumption, set so that the obtained pH values are physiologically plausible
keSLC0111	Rate of elimination of the CAIX inhibitor SLC-0111	$\log(2)/(11.1/12)$	(23)
kaSL0111	Rate of absorption into the serum of the CAIX inhibitor SLC-0111	0.93*12	(23)
keantiPD1	Rate of elimination of the PD-1 inhibitor pembrolizumab	$\log(2)/(26*2)$	(24)

Suppl. Table 1: Details on parameters for our 3D agent-based model, default values and references.

One model iteration corresponds to 12 hours and all parameters are scaled accordingly (Please note, that all diffusion-reaction equations are solved in their steady-state, thus, units do not matter as long as they are the same for the diffusion and the reaction coefficient). Arbitrary parameters can have any value as they linearly scale other parameters or by definition have no influence on the model outcome. Still, they are included for better clarity. Parameters labeled “Assumption” were arbitrarily fixed at a biologically plausible value. Parameters listed in cursive were present in the model presented in (14), but their values have been changed. Parameters listed in bold have been added to the model.

References for the Supplementary Methods

1. Rich PR. The molecular machinery of Keilin's respiratory chain. *Biochemical Society Transactions*. 2003;31(6):1095–105.
2. Robertson-Tessi M, Gillies RJ, Gatenby RA, Anderson ARA. Impact of Metabolic Heterogeneity on Tumor Growth, Invasion, and Treatment Outcomes. *Cancer Research* [Internet]. 2015 Apr 15 [cited 2022 Feb 14];75(8):1567–79. Available from: <https://cancerres.aacrjournals.org/content/75/8/1567>
3. Devic S. Warburg Effect - a Consequence or the Cause of Carcinogenesis? *J Cancer* [Internet]. 2016 [cited 2022 Apr 29];7(7):817. Available from: </pmc/articles/PMC4860798/>
4. Zong WX, Thompson CB. Necrotic death as a cell fate. *Genes & Development* [Internet]. 2006 Jan 1 [cited 2022 Feb 15];20(1):1–15. Available from: <http://genesdev.cshlp.org/content/20/1/1.full>
5. Sun J, Zhang Y, Yang M, Zhang Y, Xie Q, Li Z, et al. Hypoxia induces T-cell apoptosis by inhibiting chemokine C receptor 7 expression: the role of adenosine receptor A2. *Cellular & Molecular*

- Immunology 2010 7:1 [Internet]. 2009 Dec 23 [cited 2021 Nov 4];7(1):77–82. Available from: <https://www.nature.com/articles/cmi2009105>
6. Jacobs SR, Herman CE, MacIver NJ, Wofford JA, Wieman HL, Hammen JJ, et al. Glucose Uptake Is Limiting in T Cell Activation and Requires CD28-Mediated Akt-Dependent and Independent Pathways. *The Journal of Immunology* [Internet]. 2008 Apr 1 [cited 2022 Feb 15];180(7):4476–86. Available from: <https://www.jimmunol.org/content/180/7/4476>
 7. Casciari JJ, Sotirchos S v., Sutherland RM. Variations in tumor cell growth rates and metabolism with oxygen concentration, glucose concentration, and extracellular pH. *Journal of Cellular Physiology* [Internet]. 1992 May 1 [cited 2022 Feb 15];151(2):386–94. Available from: <https://onlinelibrary.wiley.com/doi/full/10.1002/jcp.1041510220>
 8. Swietach P, Patiar S, Supuran CT, Harris AL, Vaughan-Jones RD. The role of carbonic anhydrase 9 in regulating extracellular and intracellular pH in three-dimensional tumor cell growths. *Journal of Biological Chemistry* [Internet]. 2009 Jul 24 [cited 2022 Feb 2];284(30):20299–310. Available from: <http://www.jbc.org/article/S0021925817493136/fulltext>
 9. Lee SH, McIntyre D, Honess D, Hulikova A, Pacheco-Torres J, Cerdán S, et al. Carbonic anhydrase IX is a pH-stat that sets an acidic tumour extracellular pH in vivo. *British Journal of Cancer* 2018 119:5 [Internet]. 2018 Sep 12 [cited 2022 Feb 2];119(5):622–30. Available from: <https://www.nature.com/articles/s41416-018-0216-5>
 10. S P, RJ G. The role of carbonic anhydrase IX in cancer development: links to hypoxia, acidosis, and beyond. *Cancer Metastasis Rev* [Internet]. 2019 Jun 15 [cited 2021 Sep 7];38(1–2):65–77. Available from: <https://pubmed.ncbi.nlm.nih.gov/31076951/>
 11. Calcinotto A, Filipazzi P, Grioni M, Iero M, de Milito A, Ricupito A, et al. Modulation of microenvironment acidity reverses anergy in human and murine tumor-infiltrating T lymphocytes. *Cancer Research* [Internet]. 2012 Jun 1 [cited 2021 May 28];72(11):2746–56. Available from: <http://cancerres.aacrjournals.org/>
 12. Jin MZ, Jin WL. The updated landscape of tumor microenvironment and drug repurposing [Internet]. Vol. 5, *Signal Transduction and Targeted Therapy*. Springer Nature; 2020 [cited 2020 Sep 29]. p. 1–16. Available from: <https://doi.org/10.1038/s41392-020-00280-x>
 13. Zhang YX, Zhao YY, Shen J, Sun X, Liu Y, Liu H, et al. Nanoenabled Modulation of Acidic Tumor Microenvironment Reverses Anergy of Infiltrating T Cells and Potentiates Anti-PD-1 Therapy. *Nano Letters* [Internet]. 2019 May 8 [cited 2021 May 19];19(5):2774–83. Available from: <https://pubs.acs.org/doi/abs/10.1021/acs.nanolett.8b04296>

14. Kather JN, Charoentong P, Suarez-Carmona M, Herpel E, Klupp F, Ulrich A, et al. High-throughput screening of combinatorial immunotherapies with patient-specific in silico models of metastatic colorectal cancer. *Cancer Research* [Internet]. 2018 Sep 1 [cited 2021 Apr 21];78(17):5155–63. Available from: <http://cancerres.aacrjournals.org/>
15. Banerjee S, Khajanchi S, Chaudhuri S. A Mathematical Model to Elucidate Brain Tumor Abrogation by Immunotherapy with T11 Target Structure. *PLOS ONE* [Internet]. 2015 May 8 [cited 2021 Oct 13];10(5):e0123611. Available from: <https://journals.plos.org/plosone/article?id=10.1371/journal.pone.0123611>
16. Sunshine JC, Nguyen PL, Kaunitz GJ, Cottrell TR, Berry S, Esandrio J, et al. PD-L1 Expression in Melanoma: A Quantitative Immunohistochemical Antibody Comparison. *Clinical Cancer Research* [Internet]. 2017 Aug 15 [cited 2021 Oct 13];23(16):4938–44. Available from: <https://clincancerres.aacrjournals.org/content/23/16/4938>
17. Powathil G, Kohandel M, Milosevic M, Sivaloganathan S. Modeling the Spatial Distribution of Chronic Tumor Hypoxia: Implications for Experimental and Clinical Studies. *Computational and Mathematical Methods in Medicine* [Internet]. 2012 [cited 2022 Mar 4];2012:11. Available from: </pmc/articles/PMC3287099/>
18. Anderson ARA. A hybrid mathematical model of solid tumour invasion: the importance of cell adhesion. *Mathematical Medicine and Biology: A Journal of the IMA* [Internet]. 2005 Jun 1 [cited 2022 Mar 4];22(2):163–86. Available from: <https://academic.oup.com/imammb/article/22/2/163/770979>
19. Bashkatov AN, Genina EA, Sinichkin YP, Kochubey VI, Lakodina NA, Tuchin V v. Glucose and Mannitol Diffusion in Human Dura Mater. *Biophysical Journal* [Internet]. 2003 [cited 2022 Mar 3];85(5):3310. Available from: </pmc/articles/PMC1303608/>
20. Ratnikov BI, Scott DA, Osterman AL, Smith JW, Ronai ZA. Metabolic rewiring in melanoma. *Oncogene* 2017 36:2 [Internet]. 2016 Jun 6 [cited 2021 Sep 21];36(2):147–57. Available from: <https://www.nature.com/articles/onc2016198>
21. Patel AA, Gawlinski ET, Lemieux SK, Gatenby RA. A cellular automaton model of early tumor growth and invasion: The effects of native tissue vascularity and increased anaerobic tumor metabolism. *Journal of Theoretical Biology*. 2001 Dec 7;213(3):315–31.
22. Chafe SC, McDonald PC, Saberi S, Nemirovsky O, Venkateswaran G, Burugu S, et al. Targeting Hypoxia-Induced Carbonic Anhydrase IX Enhances Immune-Checkpoint Blockade Locally and Systemically. *Cancer Immunology Research* [Internet]. 2019 Jul 1 [cited 2022 Feb 2];7(7):1064–78. Available from: <https://cancerimmunolres.aacrjournals.org/content/7/7/1064>

23. McDonald PC, Chia S, Bedard PL, Chu Q, Lyle M, Tang L, et al. A Phase 1 Study of SLC-0111, a Novel Inhibitor of Carbonic Anhydrase IX, in Patients with Advanced Solid Tumors. *American Journal of Clinical Oncology: Cancer Clinical Trials* [Internet]. 2020 Jul 1 [cited 2022 Feb 17];43(7):484–90. Available from: https://journals.lww.com/amjclinicaloncology/Fulltext/2020/07000/A_Phase_1_Study_of_SLC_0111,_a_Novel_Inhibitor_of.5.aspx
24. Dang TO, Ogunniyi A, Barbee MS, Drilon A. Pembrolizumab for the treatment of PD-L1 positive advanced or metastatic non-small cell lung cancer. *Expert Rev Anticancer Ther* [Internet]. 2016 Jan 2 [cited 2022 Mar 7];16(1):13. Available from: [/pmc/articles/PMC4993158/](https://pubmed.ncbi.nlm.nih.gov/26411111/)

Supplementary table accompanying the paper "An in silico model to study the impact of Carbonic Anhydrase IX expression on tumor growth and anti-PD-1 therapy" by Julia Grajek, Jakob Nikolas Kather, Jan Poleszczuk, *Journal of the Royal Society Interface*

Cancer	Number at risk at day 0 (CAIX high)	Number at risk at day 0 (CAIX low)	HR	p	FDR	3 year OS (high)	3 year OS (low)	5 year OS (high)	5 year OS (low)
Bladder Carcinoma	147	257	0.73	0.064	100%	0.6	0.45	0.58	0.4
Breast Cancer	727	362	1.99	0.004**	>50%	0.9	0.95	0.8	0.9
Cervical squamous cell carcinoma	164	140	1.88	0.017*	>50%	0.7	0.8	0.6	0.78
Esophageal Adenocarcinoma	60	20	1.92	0.12	100%	0.38	0.63	0.18	0.57
Esophageal Squamous Cell Carcinoma	26	55	0.42	0.11	100%	0.85	0.38	0.42	0.18
Head-neck squamous cell carcinoma	210	289	1.26	0.11	100%	0.58	0.6	0.5	0.57
Kidney renal clear cell carcinoma	399	131	0.61	0.044*	>50%	0.8	0.72	0.76	0.58
Kidney renal papillary cell carcinoma	85	202	2.3	0.009**	>50%	0.82	0.92	0.62	0.83
Liver hepatocellular carcinoma	194	176	2.4	2.9e-6***	1%	0.57	0.8	0.4	0.61
Lung Adenocarcinoma	255	249	1.72	5e-4***	10%	0.58	0.72	0.48	0.5
Lung squamous cell carcinoma	169	326	0.86	0.36	100%	0.62	0.6	0.58	0.56
Ovarian Cancer	95	278	0.65	0.01*	>50%	0.77	0.61	0.42	0.39
Pancreatic ductal adenocarcinoma	75	102	1.76	0.007**	50%	0.3	0.5	0.19	0.41
Pheochromocytoma and Paraganglioma	45	133	11.8	0.005**	50%	0.86	1	0.86	1
Rectum adenocarcinoma	60	105	0.46	0.11	100%	0.84	0.81	0.63	0.43

Sarcoma	69	109	1.86	0.005**	50%	0.57	0.73	0.42	0.6
Stomach adenocarcinoma	110	261	0.71	0.08	100%	0.57	0.5	0.57	0.4
Testicular Germ Cell Tumor	101	33	0	0.003**	20%	1	0.9	1	0.9
Thymoma	31	87	3.05	0.16	100%	0.88	0.96	0.88	0.96
Thyroid Carcinoma	137	365	3.22	0.02*	>50%	0.97	1	0.9	0.98
Uterine corpus endometrial carcinoma	172	370	1.49	0.075	100%	0.78	0.84	0.77	0.81

Suppl. Table 2: Results of the survival analysis in two cohorts: high CAIX expression vs low CAIX expression. FDR denotes the false discovery rate resulting from the determination of the best possible cut-off value. P denotes the p-value of the Cox-Mantel (log-rank) test.

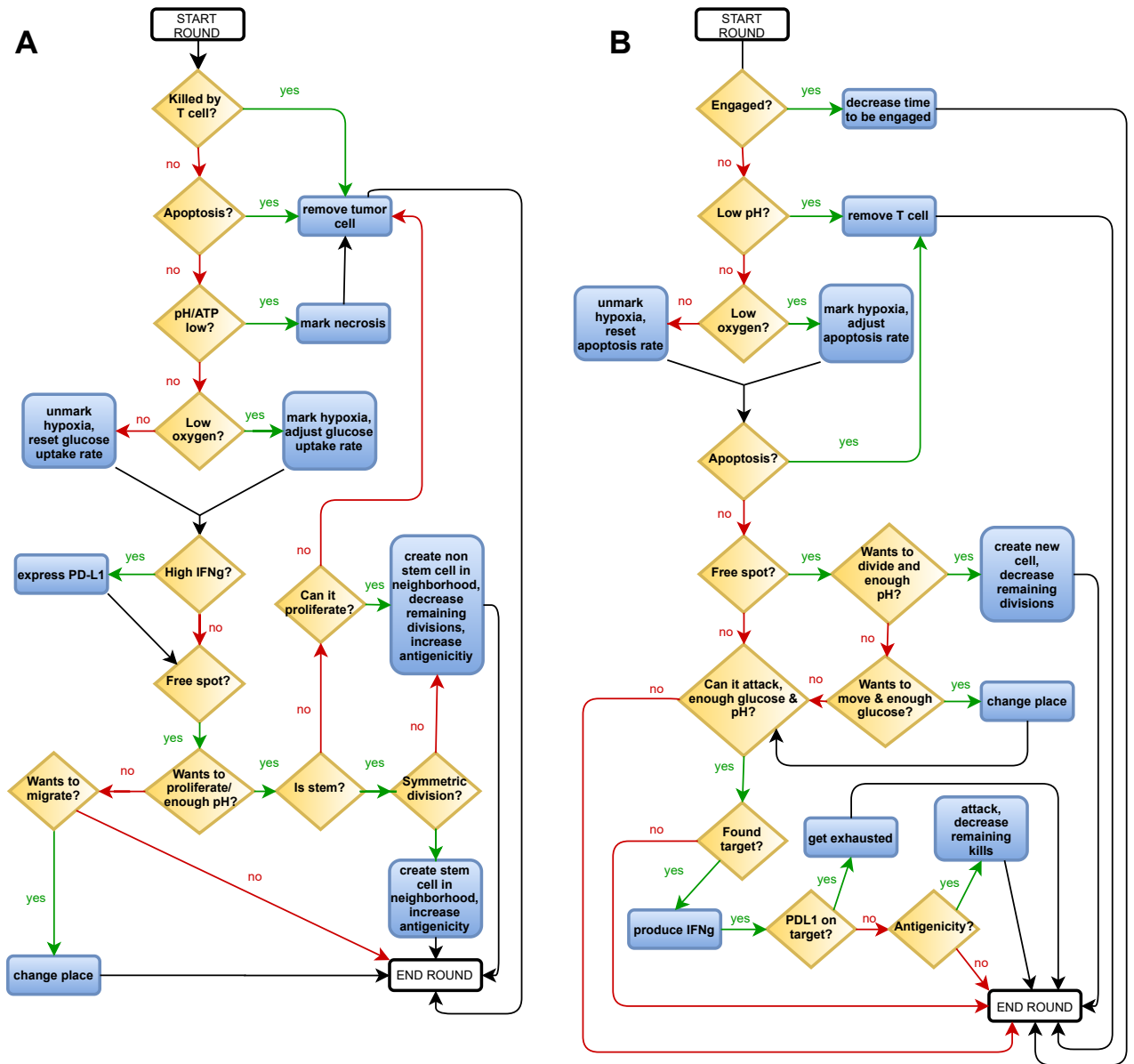


FIGURE 4.1: Supplementary Figure S1 from An in silico model to study the impact of carbonic anhydrase IX expression on tumour growth and anti-PD-1 therapy. Simplified diagrams showing the rules of the ABM that govern the actions of tumor cells (A), and lymphocytes (B).

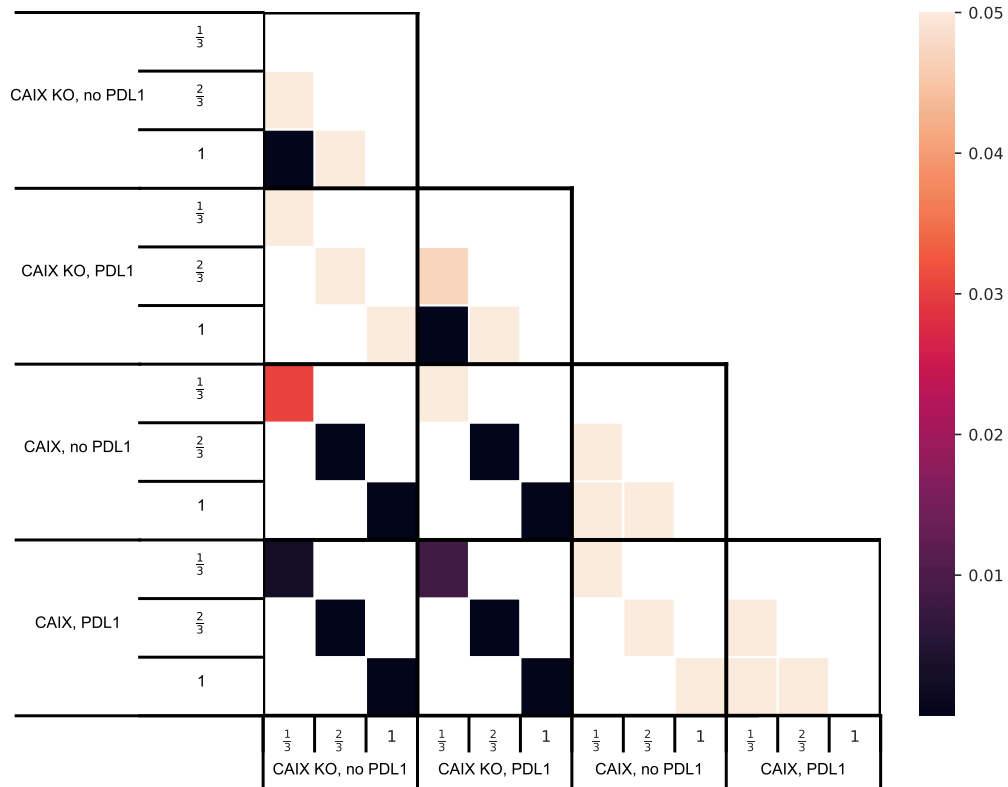


FIGURE 4.2: **Supplementary Figure S2 from An *in silico* model to study the impact of carbonic anhydrase IX expression on tumour growth and anti-PD-1 therapy.** Heatmap showing the p-values of the post-hoc pairwise comparison using Dunn test with Bonferroni correction. We compared the treatment response to different doses within tumor groups as well as the response to the same dose between groups, yielding 30 pairwise comparisons. White squares represent comparisons that weren't performed, light beige squares represent insignificant differences.

Chapter 5

Carbonic anhydrase IX suppression shifts partial response to checkpoint inhibitors into complete tumor eradication: model-based investigation

5.1 Introduction

The research presented in [40] was motivated by my second research aim, especially the study of combination therapies, as explained in section 5.2.1 of this thesis. It is thus an extension of work presented in [39], informed by the previously obtained results. While the model presented in the preceding chapter was developed with the objective of exploring new hypotheses and identifying biomarkers or resistance mechanisms, here I propose a model designed for further validation of the results and conclusions derived from the previous modeling approach. Having qualitatively confirmed my hypothesis that CAIX-induced acidosis might be a vital resistance mechanism of immunotherapy, and thus, targeting CAIX might reinvigorate immune response and increase anti-PD-1 therapy effectiveness, I proposed a continuous model aimed at quantitative validation. The continuous model is a simplification of the hybrid model, offering fewer opportunities for exploration. However, it better fits the purpose of quantitative validation, as it has fewer parameters and is less computationally expensive, facilitating its calibration with the *in vivo* data presented in [37]. Moreover, unlike the hybrid model, the new one is mathematically tractable, allowing for its mathematical analysis and more generalizable conclusions than the previous numerical simulations.

I was the main investigator in this study, responsible for conceptualization, model building, mathematical analysis of the model, the performance of numerical simulations, and the interpretation of the results, with guidance from my supervisor. In addition to elaborating on my second research aim, this publication supports my second and especially third hypothesis, i.e. the positive effect of combining even just transient treatment with ICI therapy and CAIX inhibition.

5.2 Relation of the publication to the research aims of the thesis

5.2.1 Study the impact of tumoral CAIX expression on the evolution of the TME and ICI effectiveness *in silico*, and evaluate it as a combination therapy target with ICIs

The previous model had quite extensively illustrated the impact of CAIX expression on the TME. With the new model, on the other hand, I set out to focus on its influence on ICI effectiveness and potential for a combination therapy target. As an extension of my previous work, here I investigated its combination with not only anti-PD-1 but also anti-CTLA-4 therapy. As mentioned in the introduction, combining anti-PD-1 with anti-CTLA-4 increases response rates compared to monotherapies, but it was not clear, whether adding CAIX inhibition could further increase treatment efficacy.

First, I was interested in the mathematical analysis of the proposed model, to assess its asymptotic behavior (see section 2.1 of [40]). The originally proposed model consisted of five non-linear ordinary differential equations (see equations (14)-(15) in [40]). To allow for its phase plane analysis, I decided to simplify the model to the form presented in equation (16) of [40], which I will refer to as the simplified model from here on. Here, we assume that all substances are in their steady state. This approximation is motivated by the fact, that the modeled substances (protons, IGN- γ) are produced and decay at a much faster rate than cellular actions such as proliferation occur. Secondly, we ignore the distinction between CC and CSC and model only cancer stem cells. While this is a substantial modification of the model, I believe that the conclusions resulting from the analysis of the simplified model are still of interest, since CSC are the main driver between cancer progression and recurrence, and their dynamics critically impact treatment outcomes. However, it should be noted that the results from the phase plane analysis of the simplified model do not translate one-to-one to the original model, and only serve as an initial exploration of the model. I proved analytically that this simplified model could have one or two equilibria, dependent on the parameters. Furthermore, numerical simulations indicated, that CAIX inhibition could vitally change the asymptotic behavior of the model and have the solutions tend to the tumor-free steady state, whereas solutions starting from the same initial conditions but with high CAIX expression stabilized at the steady state corresponding to stable disease. Importantly, this shift in asymptotic behavior required an abundant immune response. Such a strong immune response can be achieved using ICIs, supporting the notion of combining these two treatments, in line with my research hypothesis.

These initial results motivated me to study the effect of combination therapy in the original model. In particular, I wanted to test my third research hypothesis, postulating the positive effect of transiently combining anti-CAIX and ICIs. The previous simulations had assumed that treatment consistently impacted the model's parameters as if it were applied continuously, which is not the case in clinical practice. Hence, I performed numerical simulations with finite duration treatments followed by a long observation period of the tumor volume (see section 2.2. of [40]). I performed the simulations for various treatment dosages and durations with the conclusion that CAIX-expressing tumors seem to require a combination of anti-CAIX and a high enough dose of ICI for a complete and durable response. For monotherapies, we observed disease recurrence, even after pseudo-elimination during the treatment window.

Finally, the model was fitted to pre-clinical data presented in [37] (see section 2.23 of [40]). While the obtained fit seemed good, it should be noted, that this model fitting is preliminary. Due to the limited data, it was impossible to validate the model fitting on an independent data set, as I have elaborated in the discussion section of the paper. Nevertheless, this initial model calibration shows that our model might be used to reproduce experimental findings and provides some initial parameter guesses for the numerical simulations performed in this study.

Another interesting, although preliminary observation resulting from the model simulations was the depletion of CSC in the tumor after CAIX inhibition. This observation is derived from the model calibration with a small dataset, so it requires further validation. However, it supports certain experimental observations, as enumerated in the discussion section of the publication, and thus constitutes a promising perspective for further research.

In summary, the publication [40] was motivated by my second research aim and contributed to answering the second and third research hypotheses of this thesis. The conclusions derived from the analysis of the presented model require further validation with a bigger data set, but they support the notion of investigating combinations of CAIX inhibition and ICIs in CAIX-expressing tumors as a way of increasing ICI effectiveness.

5.3 The publication



Article

Carbonic Anhydrase IX Suppression Shifts Partial Response to Checkpoint Inhibitors into Complete Tumor Eradication: Model-Based Investigation

Julia Grajek and Jan Poleszczuk *

Nalecz Institute of Biocybernetics and Biomedical Engineering Polish Academy of Sciences,
02-109 Warsaw, Poland; jgrajek@ibib.waw.pl

* Correspondence: jpoleszczuk@ibib.waw.pl

Abstract: Immune checkpoint inhibitors (ICIs) have revolutionized the treatment of solid malignancies, including non-small-cell lung cancer. However, immunotherapy resistance constitutes a significant challenge. To investigate carbonic anhydrase IX (CAIX) as a driver of resistance, we built a differential equation model of tumor-immune interactions. The model considers treatment with the small molecule CAIX inhibitor SLC-0111 in combination with ICIs. Numerical simulations showed that, given an efficient immune response, CAIX KO tumors tended toward tumor elimination in contrast to their CAIX-expressing counterparts, which stabilized close to the positive equilibrium. Importantly, we demonstrated that short-term combination therapy with a CAIX inhibitor and immunotherapy could shift the asymptotic behavior of the original model from stable disease to tumor eradication. Finally, we calibrated the model with data from murine experiments on CAIX suppression and combination therapy with anti-PD-1 and anti-CTLA-4. Concluding, we have developed a model that reproduces experimental findings and enables the investigation of combination therapies. Our model suggests that transient CAIX inhibition may induce tumor regression, given a sufficient immune infiltrate in the tumor, which can be boosted with ICIs.

Keywords: CAIX; immunotherapy; immune checkpoint inhibitors; mathematical model; combination therapy; acidosis; resistance



Citation: Grajek, J.; Poleszczuk, J. Carbonic Anhydrase IX Suppression Shifts Partial Response to Checkpoint Inhibitors into Complete Tumor Eradication: Model-Based Investigation. *Int. J. Mol. Sci.* **2023**, *24*, 10068. <https://doi.org/10.3390/ijms241210068>

Academic Editors: Andrzej Swierniak and Marek Kimmel

Received: 2 May 2023

Revised: 4 June 2023

Accepted: 8 June 2023

Published: 13 June 2023



Copyright: © 2023 by the authors. Licensee MDPI, Basel, Switzerland. This article is an open access article distributed under the terms and conditions of the Creative Commons Attribution (CC BY) license (<https://creativecommons.org/licenses/by/4.0/>).

1. Introduction

The advent of immune checkpoint inhibitors (ICIs) was a pivotal turning point in the history of cancer treatment. Unprecedentedly, monoclonal antibodies blocking the immune checkpoints PD-1 and CTLA-4 even prolong the survival of patients with advanced, metastatic malignancies [1,2]. Nevertheless, intrinsic or acquired resistance to these drugs prevents some patients from benefiting from this therapy [3,4]. Identifying the drivers of this resistance and potential combination therapy targets would allow us to fully harness the power of ICI treatment by turning non-responders into responders.

In [3,5], the predictive biomarkers of ICI therapy have been comprehensively reviewed, including PD-L1 expression on cancer cells and other cells in the tumor microenvironment (TME), tumor mutational burden and other genetic and epigenetic factors, microbiome composition, IFN- γ signatures, and the composition and distribution of tumor-infiltrating lymphocytes. Ultimately, the authors concluded that no definite marker distinguishing responders from non-responders has been identified yet. Furthermore, it is believed that only a panel of markers would have sufficient predictive power, and the search for potential drivers of resistance is still ongoing.

In non-small-cell lung cancer, CTLA-4- and PD-1-blocking antibodies have shown promising anti-tumoral activity, either alone or in combination with chemotherapy [1,6]. Importantly, ICIs induced significant and durable responses in a subset of patients with chemotherapy-refractory disease [6]. Unfortunately, the response rate across all trials

was relatively low at around 20% [7]. Among PD-L1+ patients or patients treated with a combination therapy of anti-PD-1 and anti-CTLA-4, the response rate was higher, but still more than half of the patients were resistant to the therapy [7], indicating a need for further investigation of resistance mechanisms.

An emerging factor impacting treatment resistance is TME acidosis, which suppresses the immune response and selects for more aggressive, treatment-resistant cancer cells, thereby helping cancer escape immune surveillance [8]. Tumors generally have an acidic extracellular space, with pH values in the TME amounting to around 6.5–7 [8], partially due to tumor hypoxia and the cancer cells' aberrant metabolism. Additionally, cancer cells express several molecules, such as carbonic anhydrase IX (CAIX), which assist in the acidification of the TME [9]. These enzymes catalyze the reversible hydration of CO_2 , leading to an accumulation of protons [10]. Importantly, they are an attractive treatment target since they are overexpressed in many cancers, e.g., they are highly expressed in more than one-third of non-small-cell lung cancers (NSCLCs) [11]. Meanwhile, they are rare in healthy tissue [12]. Hence, inhibiting them might reinvigorate the immune response in the TME without causing unwanted side effects in the rest of the body. Currently, a small-molecule inhibitor of CAIX called SLC-0111 is undergoing clinical trials [13]. Studies investigating the combination of ICIs and CAIX inhibition, however, are still pre-clinical. In [14,15], the effectiveness of anti-CAIX CAR T-cells secreting anti-PD-L1 was shown to decrease tumor size in mice models and prevent metastasis in clear-cell renal cell carcinoma. In [16], Chafe et al. showed decreased tumor growth in mouse tumor models when combining it with anti-PD-1 and anti-CTLA-4, unlike anti-CAIX monotherapy or ICI therapy alone. In [17], we used a computational model to investigate the impact of CAIX expression on the TME and the effectiveness of anti-PD-1 with anti-CAIX. Our model simulations suggested that patients with CAIX-expressing tumors would benefit from dual inhibition with anti-PD-1 and anti-CAIX, regardless of pre-treatment PD-L1 expression, making it an independent marker.

In this study, we set out to expand on our previous work. Here, we have developed a differential equation model informed by pre-clinical data. Our main goal was to not only analyze the effectiveness of combination therapy with anti-CAIX, anti-PD-1, and anti-CTLA-4, as in the previously mentioned studies, but also the durability of the response after stopping the treatment. Furthermore, given a few realistic assumptions, we were able to analyze the model's asymptotic behavior mathematically, which was impossible for the complex hybrid model presented in our previous study [17]. Finally, we wanted to show that our model could quantitatively reproduce experimental findings. Thanks to its computational efficiency and interpretable parameters, the proposed model can be easily calibrated to represent different solid tumor types and analyze ICI and anti-CAIX effectiveness.

2. Results

2.1. Phase Portrait Analysis Reveals Two Possible Steady States

In order to gain a deeper understanding of the qualitative behavior of our model, we analytically analyzed the number of steady states of the simplified model (16) and deduced the following proposition:

Proposition 1. *The point (0,0) is a steady state of the system (16). Depending on parameter values, the system might also have a positive steady state (S^* , ES^*).*

Proof of Proposition 1. First, let us assume that $S > 0$, because otherwise, system (16) is trivial. Then, let us denote ES by x . From the third equation of system (16), we have

$$I = \frac{rx}{\omega S}. \quad (1)$$

Substituting this into the second Equation (15), we obtain

$$L = \alpha + \beta \left(\frac{\frac{rx}{\omega S}}{\zeta + \frac{rx}{\omega S}} \right). \quad (2)$$

Now, let us solve the steady-state equation for the second Equation (16). Please note that the equation for the steady-state solution for protons implies

$$H = \frac{\delta + q + vH_0}{v}, \quad (3)$$

hence, H is independent of our variables. Therefore, the last component of the second equation of system (16) is equal to $-constx$, where $const$ is a non-negative constant. Hence, we can omit this part in our calculations by incorporating it in the parameter d . Then, we have

$$\begin{aligned} 0 &= \frac{dx}{dt} \\ \Leftrightarrow 0 &= b\mu S - dx - am\mu px \left(\alpha + \beta \left(\frac{\frac{rx}{\omega S}}{\zeta + \frac{rx}{\omega S}} \right) \right) \\ \Leftrightarrow 0 &= b\mu S \left(\zeta + \frac{rx}{\omega S} \right) - dx \left(\zeta + \frac{rx}{\omega S} \right) - am\mu px \left(\alpha \left(\zeta + \frac{rx}{\omega S} \right) + \beta \frac{rx}{\omega S} \right) \\ \Leftrightarrow 0 &= b\mu S \left(\zeta S + \frac{rx}{\omega} \right) - dx \left(\zeta S + \frac{rx}{\omega} \right) - am\mu px \left(\alpha \left(\zeta S + \frac{rx}{\omega} \right) + \beta \frac{rx}{\omega} \right) \\ \Leftrightarrow 0 &= -x^2 \frac{r}{\omega} (d + am\mu p(\alpha + \beta)) + xS \left(b\mu \frac{r}{\omega} - d\zeta - am\mu p\alpha\zeta \right) + b\mu\zeta S^2 \end{aligned} \quad (4)$$

By treating the last Equation (4) as a quadratic function of x , we can determine the number of candidates for the steady states. In fact, we know that we have two roots, since

$$\Delta = S^2 \left(b\mu \frac{r}{\omega} - d\zeta - am\mu p\alpha\zeta \right)^2 + 4b\mu\zeta S^2 \frac{r}{\omega} (d + am\mu p(\alpha + \beta)) > 0. \quad (5)$$

From Vieta's formula, the roots have opposite signs:

$$x_1 x_2 = -\frac{b\mu\zeta S^2}{\frac{r}{\omega} (d + am\mu p(\alpha + \beta))} < 0. \quad (6)$$

Finally, the equations for the roots are

$$\begin{aligned} x_{1,2} &= \frac{-S \left(b\mu \frac{r}{\omega} - d\zeta - am\mu p\alpha\zeta \right) \pm S \sqrt{\left(b\mu \frac{r}{\omega} - d\zeta - am\mu p\alpha\zeta \right)^2 + 4b\mu\zeta \frac{r}{\omega} (d + am\mu p(\alpha + \beta))}}{-2 \frac{r}{\omega} (d + am\mu p(\alpha + \beta))} \\ &= c_1 S, \end{aligned} \quad (7)$$

where $c_1 > 0$ for the positive root, since we assumed $S > 0$.

Now, let us look at the first equation of system (16). For simplicity purposes, let us transform the third equation of system (16) into

$$I = \frac{rE}{\omega}. \quad (8)$$

Hence, we have

$$L = \alpha + \beta \left(\frac{rE}{\zeta\omega + rE} \right) \quad (9)$$

and we can calculate the second nullcline:

$$\begin{aligned} 0 &= \frac{dS}{dt} \\ \Leftrightarrow 0 &= \phi S \left(1 - \frac{S}{K}\right) - av_c m \mu (1 - pL)x \\ \Leftrightarrow x &= \frac{\phi S \left(1 - \frac{S}{K}\right)}{av_c m \mu \left(1 - p \left(\alpha + \beta \frac{rE}{\zeta\omega + rE}\right)\right)} \end{aligned} \quad (10)$$

Since we are looking for steady states, we can assume that $E \equiv \text{const}$, i.e., Equation (10) is equivalent to

$$x = c_2 S \left(1 - \frac{S}{K}\right), \quad (11)$$

where c_2 is a positive constant. From (7) and (11), we deduce that there are two possible phase portraits, which are dependent on the values of c_1 and c_2 . In particular, the S-coordinates of the steady states are the solutions of the equation

$$c_1 S = c_2 S \left(1 - \frac{S}{K}\right). \quad (12)$$

From Equations (12) and (7), $(0, 0)$ is one of the steady states. The other one is positive if and only if

$$\begin{aligned} S &= \left(1 - \frac{c_1}{c_2}\right) K > 0 \\ \Leftrightarrow c_1 &< c_2. \end{aligned} \quad (13)$$

Concluding, our system (16) can have either one or two non-negative steady states. The steady state at the origin always exists. The existence of the positive steady state (S^*, ES^*) depends on the model's parameter values in a complex way. \square

Having inferred the possible existence of two qualitatively different phase portraits, we wanted to investigate whether they were attainable for plausible biological parameters. For illustration purposes, we set the free parameters to the values obtained from the data fitting procedure (see Table 1), with the exception of the parameters b and η . The first reason for modifying these parameters is that complete tumor eradication, i.e., one of the phase portrait types, was not observed in the data that we used for model calibration. Hence, to obtain this phase portrait, we increased the T-cell infiltration to $b = 3 \times 10^4$. Please note that this may correspond either to a more immunogenic tumor than the one investigated in the in vivo experiments, or an immune response that had been boosted by immunotherapy. Furthermore, we increased the impact of TME acidification on the T-cell population to $\eta = 10^6$ to widen the distance between the steady states and make the figure more legible. However, the phase portraits were qualitatively the same for smaller values of the parameter η , as shown in Figure 1c. The zero and the positive equilibrium exist for all simulated values of parameter η . With decreasing η , the S-coordinate of the steady state decreases toward zero. Due to the large ranges on the phase portrait axes, we opted for a large η -value for the exemplary phase portrait to ensure that the steady states were easily distinguishable on the plot.

We were able to obtain both types of phase portraits by only manipulating the parameter denoting CAIX expression on cancer cells. As shown in Figure 1, we can obtain two non-negative steady states for the parameter value $q = 7.6258 \times 10^{-13}$, corresponding to the acidification of the TME to ca. 6.6, which falls within the boundary values reported in the literature [18]. The solutions tend to the positive equilibrium. On the other hand, when simulating a CAIX KO tumor, i.e., setting $CAIX = 0$, we obtain one asymptotically stable steady state at the origin, indicating the elimination of the CAIX KO tumor.

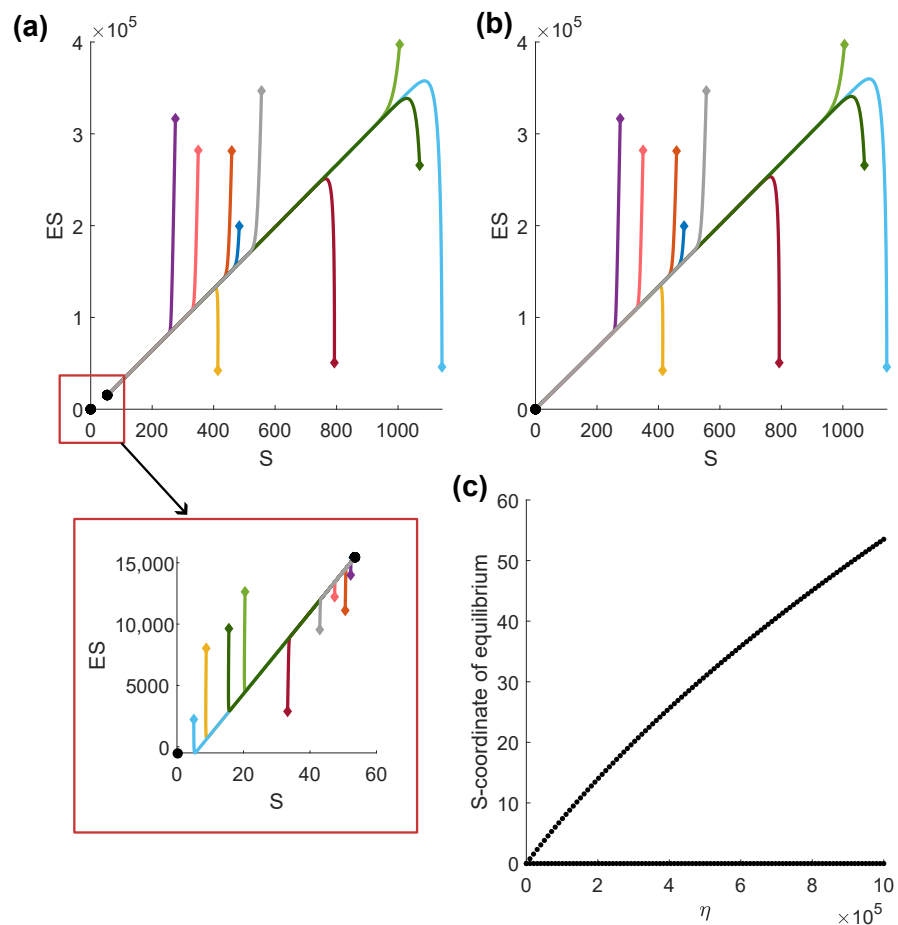


Figure 1. Phase portraits of the simplified model (16). Black dots denote the steady states. The colored lines represent distinct solutions starting from the initial conditions, which are marked with diamond shapes. (a) Phase portrait of the CAIX-expressing tumor, including an inset, which shows the behavior of the solutions starting close to the steady states. (b) Phase portrait of the CAIX-expressing tumor. (c) Influence of parameter η on the S-coordinate of the steady state.

2.2. Synergistic Combination Therapy with Anti-CAIX and Immune Checkpoint Inhibitors

In the previous section, we showed an example of how CAIX KO tumors might have a drastically different outcome than CAIX-expressing tumors, especially in the presence of a strong immune response. However, in clinical practice, therapy is usually not given indefinitely. Motivated by the promising initial results obtained for the simplified model, we investigated transient combination therapy with anti-CAIX and immune checkpoint inhibitors using the full model (14). We calibrated the model with the parameters resulting from the data-fitting procedure (see Table 1) and standardized the initial conditions by setting $inocCells = 0.1$ to facilitate therapy comparison. Then, we simulated different treatments on this exemplary tumor. First, we let the tumors grow for twenty days prior to initiating any treatment. Then, the treatment with parameters $d_3 = 1$, $d_1 = 0.4$, and $d_2 = 4$ was simulated for a finite duration. Finally, we observed tumor growth until day 200 after inoculation. The control tumor (treatment-free) grew until reaching a maximum volume of 1179 mm³ on day 40.

Figure 2a shows the effects of 2-week treatment simulations. Monotherapy with anti-CAIX, combination therapy with two immune checkpoint inhibitors (anti-PD-1 and anti-CTLA-4), as well as combination therapy with anti-CAIX and anti-PD-1 resulted in a short decrease in tumor volume, followed by renewed growth. The tumor growth accelerated upon stopping treatment, and the tumor eventually reached the same size as the control tumor. Combining anti-CAIX and anti-CTLA-4 resulted in tumor recurrence about 2 weeks after treatment suspension, even after seemingly eradicating the tumor during the therapy window. On the other hand, combining anti-CAIX with both immune checkpoint inhibitors decreased tumor size substantially during the treatment time window, and this decrease in size continued after therapy ended, resulting in complete tumor elimination.

To ensure that the scenario presented above was not just a result of short treatment duration, we simulated the same treatments for a longer time period. In Figure 2b, we can see the effect of the same treatments given for 90 days. Here, we can infer that a lack of complete and durable response for treatments that did not combine both anti-CAIX and ICI was not due to the short treatment window. The increased treatment duration induced tumor volume stabilization during treatment. However, tumor growth immediately resumed after stopping the treatment, reaching the size of the control tumor. Hence, prolonging the treatment did not impact the long-term outcome. Conversely, longer treatment with a combination of anti-CAIX and anti-CTLA-4 led to a response that continued after stopping treatment, as opposed to the two-week treatment.

These observations motivated us to hypothesize that in the presence of sufficient CAIX expression that leads to a significant acidification of the TME, combining anti-CAIX with a high enough dose of ICI is necessary for a complete and durable response, regardless of ICI type. To initially test this hypothesis, we analyzed the long-term outcomes of combination therapy with varying doses of anti-PD-1 and anti-CTLA-4 in CAIX-expressing and CAIX KO tumors. Treatment was again given for three months (90 days) and tumor volume was measured on day 200 after inoculation, i.e., another 90 days after the end of therapy. In Figure 2c, we can see that, in fact, no dose of ICI elicited durable response in the CAIX-expressing tumors. All therapy regimens resulted in tumor growth to virtually the same size. On the other hand, as shown in Figure 2d, monotherapy with either ICI or combination therapy with both ICIs resulted in a lack of tumor regrowth after treatment end in CAIX KO tumors, provided that the ICI dose was sufficiently high.

2.3. Model Fitting

Finally, we wanted to investigate whether our model could correctly replicate experimental findings. We were able to obtain a good fit for the *in vivo* data, as shown in Figure 3a,b. The final values of the free parameters are shown in Table 1. The loss function was 1.32. Figure 3a confirms the conclusions in [16] that knocking out CAIX expression significantly decreases tumor growth. However, the *in vivo* experiments showed only the beginning of the tumor growth and did not show any sign of stabilization of the tumor volume. To gain a deeper understanding of the system's behavior, we performed simulations with the calibrated model for longer time spans. Figure 4c shows that our model confirmed that CAIX acidifies the TME, lowering the pH steady state from approximately 7 to 6.6. Furthermore, Figure 4a,b indicate that the tumor volume and the number of infiltrating T-cells stabilized after around 60 days at ca. 759 mm^3 for the CAIX KO tumor and 1179 mm^3 for the CAIX-expressing tumor. Strikingly, there was a significant difference in the ratio of CSC to CC between both simulations, with the CAIX KO tumor having a decreased CSC fraction.

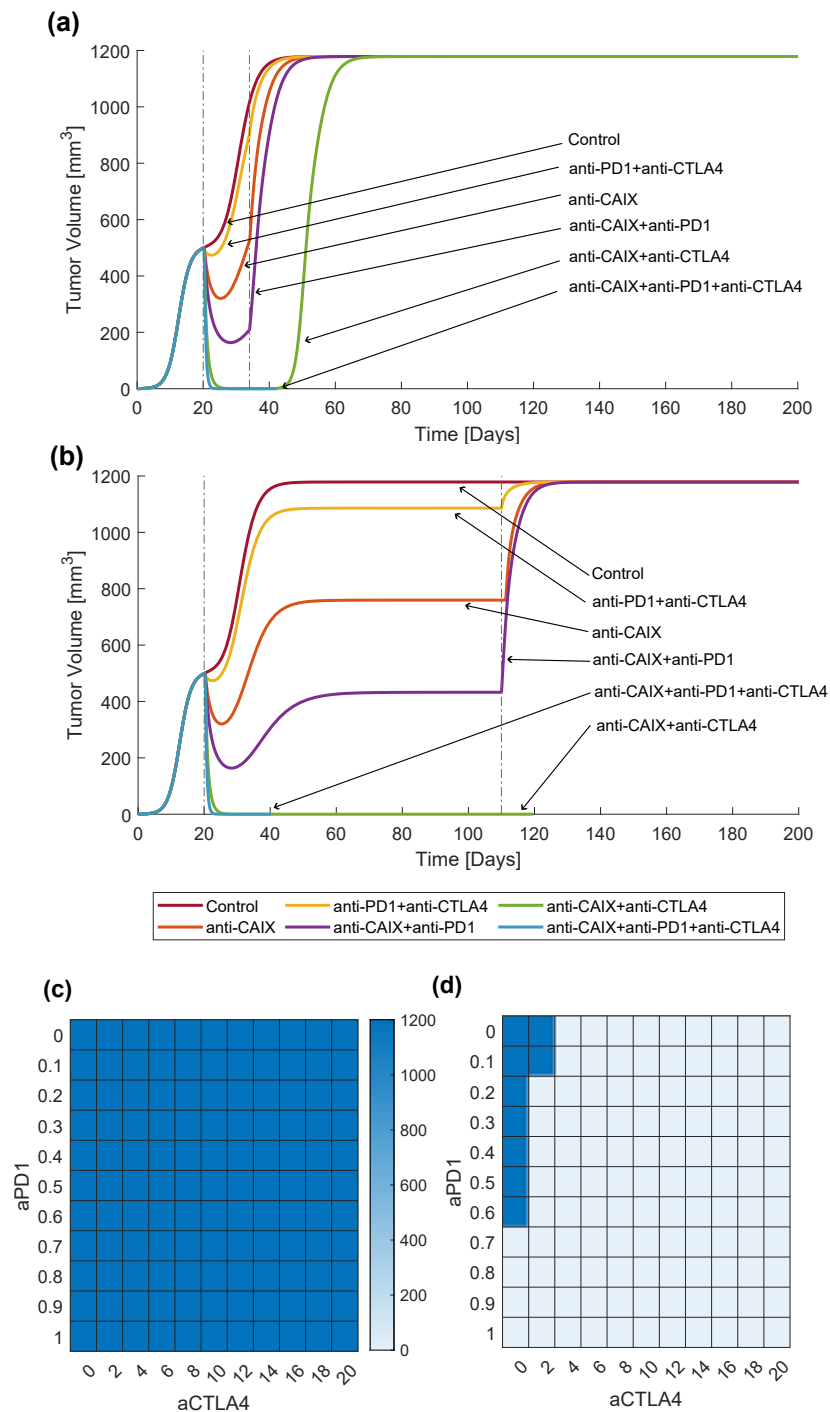


Figure 2. Comparison of the effectiveness of treatment combinations for shorter and longer durations. The lineplots correspond to treatment with the parameters $d_3 = 1$, $d_1 = 0.4$, and $d_2 = 4$. Vertical lines mark treatment start and end. The heatmaps show the tumor volume at day 200 for increasing doses of the combination treatment with anti-PD-1 and anti-CTLA-4. (a) Long-term outcome of two weeks of therapy. (b) Long-term outcome of 3 months of therapy. (c) Volumes of CAIX-expressing tumors for various anti-PD-1 and anti-CTLA-4 doses on day 200 after inoculation. (d) Volumes of CAIX KO tumors for various anti-PD-1 and anti-CTLA-4 doses on day 200 after inoculation.

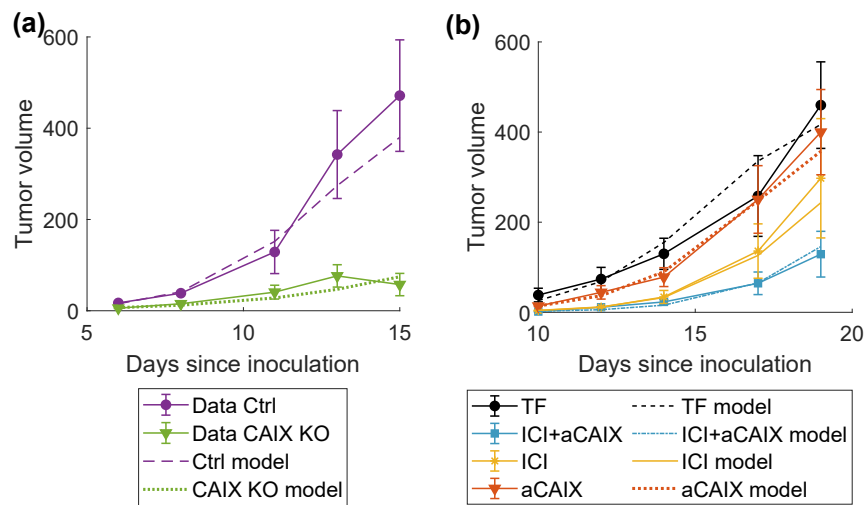


Figure 3. Results of the data-fitting procedure. Markers denote the mean of the experimental data. Error bars represent standard error of the mean. (a) Fit of the model to the data on tumor growth for CAIX-expressing (Ctrl) and CAIX KO cells. (b) Fit of the model to the data on the comparison of treatment combinations. TF: treatment free; ICI: anti-PD-1+anti-CTLA-4; aCAIX: anti-CAIX.

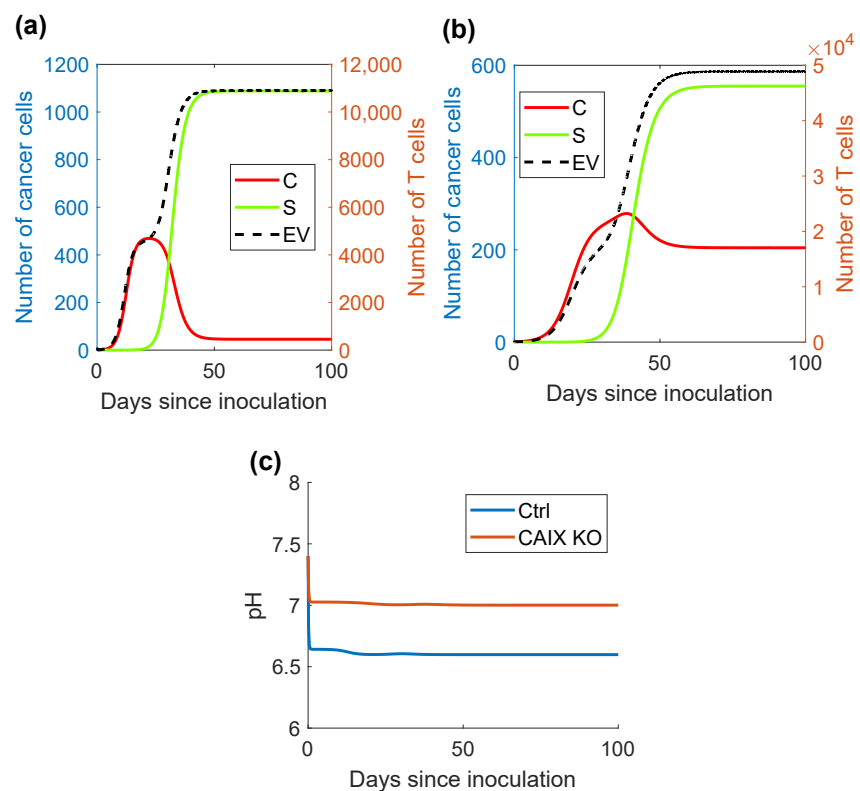


Figure 4. Comparison of a CAIX-expressing and a CAIX KO tumor: (a) Number of cells in the model with CAIX expression. (b) Number of cells in the CAIX KO model. (c) Comparison of the pH level between the CAIX-expressing (Ctrl) and the CAIX KO models.

Table 1. Model parameter values resulting from the data-fitting procedure. Asterisks denote substituted variables.

Parameter Name	Value	Lower Bound	Upper Bound
$a^* = am\mu$	834.16	0	10^3
$b^* = b\mu$	5.821×10^3	0	6×10^3
eta	2.485×10^3	0	10^6
n	0.799	0	10
q	7.6258×10^{-13}	5×10^{-13}	3×10^{-12}
d_1	0.028	0	1
d_2	0.011	0	20
d_3	0.066	0	1
initCSCrat	3.083×10^{-5}	0	1
i_{ctrl}	0.210	0	1
i_{caixko}	0.336	0	1
i_{c_v}	0.044	0	1
i_{c_s}	0.027	0	1
i_{pc}	0.007	0	1
i_{pcs}	0.004	0	1

3. Discussion

Herein, we have introduced a new mathematical model of tumor-immune interactions and applied it to investigate the effectiveness of immunotherapy and CAIX inhibition. Our model suggests a synergistic combination of anti-CAIX with immune checkpoint inhibitors. Importantly, we have shown that immunotherapy alone or anti-CAIX monotherapy might lead to tumor recurrence after treatment interruption. On the other hand, combining immune checkpoint inhibitors with anti-CAIX might change the TME in favor of the immune cells and elicit a complete and durable response. However, this required a sufficiently boosted immune response. Combining low doses of immunotherapy with CAIX suppression resulted in tumor regrowth after stopping the therapy. Interestingly, for low ICI doses combined with CAIX inhibition, we observed non-obvious simulation results, such as pseudo-elimination, followed by disease recurrence long after ending treatment.

Our main finding was that adding short-term CAIX inhibition can turn partial and temporary responses to immune checkpoint inhibitors into a response that continues after treatment until tumor eradication. This is a significant observation since immune checkpoint inhibitors have relatively low response rates, and improving them would fundamentally change the outlook for countless cancer patients. Importantly, we observed this synergistic combination only for tumors with efficient immune responses. Hence, choosing the optimal ICI dosage remains vitally important. A limitation worth noting is that our model is not defined in the absence of a tumor. Due to numerical precision, some of our simulations in Figure 2 reached a tumor volume of zero, forcing a premature end of the simulation to avoid division by zero. Therefore, we cannot predict what happens afterward, so we cannot state for sure how durable the response would be. Regardless, we can see that in some cases of combination treatment with anti-CAIX and a high enough dose of ICIs, the treatment response continues after treatment, as opposed to monotherapies, showing a synergistic instead of just an additive effect. These initial simulations imply that a combination of ICIs and anti-CAIX might lead to a more durable response in CAIX-expressing patients and allow for a more relaxed treatment schedule.

Moreover, we have proven analytically that a simplified yet realistic model version may have either one or two steady states, depending on the parameters. One of the equilibria denotes tumor eradication, while the other corresponds to stable disease. Numerically, we have shown that CAIX expression has a pivotal impact on the stability of the tumor-free equilibrium. Provided an abundant immune response, which might be achieved via immunotherapy, CAIX KO tumors tend to the zero equilibrium, whereas their CAIX-expressing counterparts stabilize at the positive steady state. Importantly, the

simplified version of the model overcomes the problem of instability close to zero values of tumor volume.

Another interesting observation was that the data-fitting procedure revealed a lower CSC fraction in the CAIX KO tumor. This was probably due to the subdued immune response in the acidic TME, which diminished T-cell-mediated cancer cell killing. Therefore, the apoptotic death of CCs had a graver impact on the number of CCs in the acidic tumor than T-cell-mediated killing. This observation was based on calibrating the model via a small data set, so we cannot draw any definite conclusions. Nevertheless, it shines a light on an interesting research topic. CSCs are believed to be the main drivers of tumor progression and treatment recurrence, and yet they seem to be resistant to most conventional treatments. In lung cancer, for example, chemotherapy failure is commonly believed to be due to CSC resistance [19]. Interestingly, some pre-clinical studies show that CAIX inhibition sensitizes previously resistant tumor cells to chemotherapy. In [20], Lock et al. observed reduced lung cancer growth and metastasis, when combining paclitaxel with anti-CAIX. If the effectiveness of CAIX inhibition on CSC elimination were confirmed, it would be a promising combination therapy target with chemotherapy. Lock et al. have reported CSC depletion due to CAIX inhibition in orthotopic breast tumor models, but also a lack of CSC expansion in vitro when coupled with CAIX inhibition, indicating that immune-unrelated mechanisms are at play as well [20]. However, the impact of the different mechanisms of CSC depletion via CAIX is not yet fully elucidated. For future research, our model could be expanded to allow for further investigation of the intricate relationships between CSCs and CAIX.

Finally, our model can reproduce experimental in vivo data with and without treatment. It should be noted that our model is now only calibrated with a small data set, produced by taking the average results instead of the individual repeats from the in vivo experiments. This was sufficient for our exploratory analysis that aimed at establishing hypotheses concerning the combination of CAIX inhibition and ICI therapy and initially validating the model. More data concerning tumor growth in CAIX expressing and CAIX KO tumors are needed to further validate the model. In particular, currently we do not know whether our model generalizes well to unseen data. If more data were available, we could test the prediction capabilities of the model and refine it, e.g., by using regularization techniques to minimize the danger of overfitting (see, for example, ref. [21] for an overview of techniques that can be used to select the most vital parameters for the data-fitting procedure). We see two possibilities for testing the model's prediction capabilities. For example, longer data sets could be used to calibrate the model on initial time points and then test its prediction accuracy on unseen data points. Alternatively, if data from the individual repeats were available, it would be possible to calibrate the model using a subset of the data sets, and then validate it using the remaining ones. Due to this lack of data, we have opted to model the treatments by assuming a constant inhibition effect for the entire treatment duration. In reality, drugs are removed from the body and their effect tapers off over time. If our model were to be used to compare different treatment schedules and identify optimal treatment protocols, the pharmacokinetics of the drugs should be included in the equations. However, this would increase the number of model parameters and thus require more data for calibration.

4. Materials and Methods

4.1. Differential Equation Model Formulation

Our model's domain is the tumor itself. Therefore, the variables describing cancer cells denote volumes, whereas other variables describe the density or concentration of the described cell type or substance in the tumor. Let C and S denote the volume of cancer cells and cancer stem cells (mm^3), respectively. Let E denote the density of active T-cells in the tumor ($\frac{\text{cells}}{\text{mm}^3}$). Let I and H denote the $IFN\gamma$ and proton concentrations in the tumor

$(\frac{Pg}{mm^3}, \frac{mol}{mm^3})$, respectively. Let the fraction of PD-L1-expressing cancer cells be denoted by L . Finally, assuming that T-cells do not significantly contribute to the tumor volume, let

$$V(t) = C(t) + S(t)$$

be the tumor volume. This assumption is a certain simplification based on the fact that the diameter of T-cells is much smaller than that of cancer cells, and that cancer cells outnumber lymphocytes in the tumor. Then, instead of modeling the temporal changes in the densities E , I , and H , we can model the temporal changes in the number of cells and molecules by multiplying the densities by the tumor volume, obtaining equations with respect to the products $E \cdot V$, $I \cdot V$, and $H \cdot V$. Hence, we consider the following system of differential equations:

$$\left\{ \begin{array}{l} \frac{dC}{dt} = f(C) + \sigma f(S) - av_c m \mu (1 - p(1 - d_1)L)C \cdot E - nC \\ \frac{dS}{dt} = (1 - \sigma)f(S) - av_c m \mu (1 - p(1 - d_1)L)S \cdot E \\ \frac{dE \cdot V}{dt} = b\mu(1 + d_2)V - dE \cdot V - am\mu p(1 - d_1)LV \cdot E \\ \quad - \eta E \cdot V \max\left(1 - \frac{H_{thresh}}{H}, 0\right) \\ \frac{dI \cdot V}{dt} = rE \cdot V - wI \cdot V \\ \frac{dH \cdot V}{dt} = \delta(C + S) + q(1 - d_3)(C + S) - v(H - H_0) \cdot V, \end{array} \right. \quad (14)$$

where

$$f(X) = \phi X \cdot \left(1 - \frac{V}{K}\right), \quad (15)$$

and $L = \alpha + \beta \frac{I}{\zeta + I}, \beta \leq 1 - \alpha$

for $X = C$ or $X = S$. The parameters pertaining to treatment effectiveness (d_i for $i = 1, 2, 3$) or CAIX expression (q) are assumed to be non-negative. All other parameters are positive. Moreover, we assert $V > 0$, because the system assumes tumor existence.

The model is based on the following assumptions:

1. *Tumor growth* Tumor growth is logistic with the carrying capacity K . The model differentiates between cancer non-stem cells (denoted in the manuscript as CCs) and cancer stem cells (denoted as CSCs). CSCs can only be killed by immune cells, whereas CCs experience apoptosis with the rate n [22]. CSCs divide asymmetrically with rate σ and symmetrically otherwise.
2. *Tumor-immune interactions* T-cells' infiltration is proportional to the tumor volume, and their number EV decreases exponentially due to cell death. They attack and kill cancer cells at a rate proportional to their density in the tumor, as proposed in [23]. Notably, this is a spin on the classical Kuznetsov-type interactions as presented in [24], where tumor cell killing is proportional to the product of the number of tumor cells and T-cells. We believe that our modification suits our needs better than the original interaction term. In particular, let us consider the scenario in which we compare two tumors consisting of the same number of CCs and T-cells. Let us assume further that one of the tumors also has a large population of CSCs, while the second has none. If we used the original Kuznetsov-type term, the CC decay due to interactions with T-cells would be the same in both tumors. On the other hand, in our model, the decay of CCs is smaller in the tumor with CSCs, since the T-cell density is smaller in this tumor. This seems more plausible, as the lymphocytes are then more likely to attack CSCs instead of just CCs. However, our model tacitly assumes that the tumor

infiltration by lymphocytes is not over-saturated, i.e., the interactions between T-cells and cancer cells are not limited by a lack of cancer cells. In particular, T-cell decay due to interactions with cancer cells depends only on the number of T-cells. Finally, only cancer cells expressing MHC class I on their surface are recognized and attacked by T-cells. Moreover, the immune response is higher for tumors with a higher tumor mutational burden. Therefore, the rate of tumor cell killing is equal to $am\mu$, where a indicates the interaction rate between tumor and immune cells, m the fraction of cancer cells expressing MHC class I, and μ quantifies TMB, as proposed in [25].

3. *PD-1-PD-L1 pathway* Tumor cell killing by immune cells is inhibited via the binding of PD-1 and PD-L1, which induces T-cell anergy. We assume that the fraction of PD-1-expressing cells is constant and equal to p . The expression of PD-L1, however, can be either constitutive or adaptive, i.e., induced by $IFN\gamma$ as a way of escaping the immune response [26]. We assume that the fraction of cancer cells with constitutive PD-L1 expression is constant and equal to α . Adaptive PD-L1 expression is dynamic and bounded from above by the parameter β .
4. *Substances in the TME* $IFN-\gamma$ is produced by active lymphocytes with rate r and decays naturally with rate ω . Protons are produced due to cancer cell metabolism with rate δ and due to CAIX expression with rate q . Outside of the tumor, we assume a physiological pH. The flux of protons into and out of the TME is proportional to the difference between the pH in the TME and the physiological pH. Immune cells that are exposed to acidosis die. The lower the pH, the greater the induced death rate.

Additionally, the model considers treatment with three inhibitors: anti-CAIX, anti-PD-1, and anti-CTLA-4. The treatment is modeled with the following assumptions:

1. Anti-CAIX suppresses CAIX expression by the fraction d_3 .
2. Anti-PD-1 suppresses PD-1 expression by the fraction d_1 .
3. Anti-CTLA-4 is mainly responsible for reinvigorating early T-cell activation in the lymph nodes, which we include in our model by increasing lymphocyte influx by the rate d_2 .

For qualitative analysis, we consider a simplified version of the model, which is two-dimensional and allows for a phase portrait analysis. Here, we assume that all cancer cells are stem cells. The reason for choosing CSCs instead of CCs is that those are the cells that are crucial to treatment success or failure. Moreover, since the production and decay of protons and $IFN-\gamma$ are much faster than cell actions, we may assume that protons and $IFN-\gamma$ are in their steady states. For simplicity purposes, we will analyze the treatment-free version of the model, but please note that the phase portrait analysis also works for the model that includes treatment. In this case, the effect of treatment can be included in the parameters b , p , and δ . The treatment-free simplified version of the model looks as follows:

$$\begin{cases} \frac{dS}{dt} = f(S) - av_c m \mu (1 - pL) S \cdot E, \\ \frac{dE \cdot S}{dt} = b \mu S - dE \cdot S - am \mu p L E \cdot S - \eta E \cdot S \max\left(1 - \frac{H_{thresh}}{H}, 0\right) \\ 0 = rE \cdot S - wI \cdot S \\ 0 = \delta S + qS - v(H - H_0) \cdot S. \end{cases} \quad (16)$$

4.2. Model Calibration

Most of the model's parameters were calibrated with values found in the literature, see Table 2. However, a few parameters could not be determined from the literature and were denoted as free parameters. To estimate their value, we fitted our model to experimental data presented in [16]. In particular, we took average data representing the growth of B16F10 cell lines with and without CAIX expression, as well as the growth of four treatment cohorts: cells treated with the CAIX inhibitor SLC-0111 (aCAIX), anti-PD-1 and anti-CTLA-4 (ICI), combination therapy of anti-CAIX, anti-PD-1, and anti-CTLA-4

(aCAIX+ICI) and a treatment-free control group (TF). Tumor volume was measured on days 6, 8, 11, 13, and 15 when comparing CAIX-expressing and CAIX KO cell lines, and on days 10, 12, 14, 17, and 19 for the comparison of different treatments. This yielded six data sets of five data points each. In the in vivo experiments, 5×10^5 tumor cells in 100 μ L PBS were inoculated subcutaneously onto the back of female C57Bl/6J mice. In our in silico simulations, we assume that only the fraction *inocCells* of these 5×10^5 tumor cells initiates the tumor and that a fraction *CSCrat* of these initiating tumor cells are CSCs. Model calibration was performed based on all data sets simultaneously. All parameters except *inocCells* were asserted to be the same for each data set. We allowed the fraction *inocCells* to be different for each data cohort to account for the variability of inoculation effectiveness and initial conditions in distinct experiments. In our model, CAIX suppression was modeled by setting the parameter *CAIX* to zero. Similarly, lack of treatment was modeled by setting the appropriate treatment parameter to zero (*d*₁, *d*₂, *d*₃). Fitting our model to data was performed using the MATLAB function *lsqnonlin*, i.e., using the least squares method. This function performs simultaneous fitting of all parameters using a subspace trust region method. As the loss function, we took the sum of squares of the residuals, scaled by the data values, i.e., $loss = \sum_{i=1}^n \left(\frac{y_i - \hat{y}_i}{y_i} \right)^2$, where *y*_{*i*} denotes the actual data value, \hat{y}_i denotes the volume calculated from the model, and *n* = 30 is the number of data points. Data fitting was performed 1000 times by sampling the initial values of the parameters from a multivariate uniform distribution bounded by the upper and lower bounds of the parameter space. The fit with the lowest loss function was selected.

Table 2. Model parameters. An empty value column denotes free parameters.

Par	Interpretation	Value	Unit	Source
ϕ	maximal rate of tumor cell growth	$\frac{24}{172}$	day ⁻¹	[27]
K	carrying capacity for tumor cells	1200	mm ³	permitted tumor volume limit [16]
σ	probability of asymmetric division	0.42	-	[17]
a	interaction rate between tumor cells and TILs	-	day ⁻¹	free parameter
<i>v</i> _c	volume of one tumor cell	6.2×10^{-6}	$\frac{\text{mm}^3}{\text{cell}}$	[25]
m	mean MHC class I expression	2.3%	-	[25]
μ	antigenicity strength (single nucleotide variations)	908	-	[25]
p	mean PD-1 expression by TILs	54%	-	[25]
n	tumor cell apoptosis rate	-	day ⁻¹	free parameter
b	infiltration rate of T-cells into TME	-	$\frac{\text{cells}}{\text{mm}^3 \cdot \text{day}}$	free parameter
d	apoptosis rate of T-cells	0.406	day ⁻¹	[25]
η	rate of T-cell death due to acidosis	-	day ⁻¹	free parameter
r	rate of <i>IFN</i> γ production	24.48×10^{-4}	$\frac{\text{pg}}{\text{cell} \cdot \text{day}}$	[17]

Table 2. Cont.

Par	Interpretation	Value	Unit	Source
ω	rate of $IFN\gamma$ decay	2.4	day^{-1}	[17]
δ	rate of proton production due to tumor cell metabolism	3×10^{-13}	$\frac{\text{mol}}{\text{mm}^3 \cdot \text{day}}$	assumption to yield realistic pH values
q	rate of proton production due to CAIX expression	-	$\frac{\text{mol}}{\text{mm}^3 \cdot \text{day}}$	free parameter
v	rate of proton flux into and out of the TME	5	day^{-1}	assumption to yield realistic pH values
H_0	proton concentration at physiological pH	$3.98 \times 1 \times 10^{-14}$	$\frac{\text{mol}}{\text{mm}^3}$	
H_{thresh}	proton concentration equivalent to pH = 6.7	$2 \times 1 \times 10^{-13}$	$\frac{\text{mol}}{\text{mm}^3}$	[17]
α	constitutive PD-L1 expression	0.1	-	[17]
β	rate of adaptive PD-L1 expression	0.1	-	assumption, $< 1 - \alpha$
ζ	saturation constant	0.01×10^{-3}	$\frac{\text{pg}}{\text{mm}^3}$	assumption
d_1	effect of anti-PD-1	-	-	free parameter
d_2	effect of anti-CTLA-4	-	-	free parameter
d_3	effect of anti-CAIX	-	-	free parameter
CSCrat	ratio of CSC at inoculation	-	-	free parameter
inocCells	ratio of inoculated cells that initiates the tumor	-	-	free parameter

5. Conclusions

Here, we have presented a new differential equation model of the impact of acidity and CAIX expression on tumor–immune interactions. Initial calibration with pre-clinical data showed that the model can accurately replicate experimental findings. Analytical and numerical analysis implicates that a combination of CAIX suppression with boosted immune response, e.g., via immune checkpoint inhibitors, is synergistic. Importantly, it can turn a partial response to monotherapies that leads to immediate recurrence after treatment end into a complete response that continues after treatment. In the future, our model could be calibrated with more data to further validate it, investigate the impact of CAIX expression on cancer stem cell dynamics, and compare treatment protocols. In particular, as of now, the model has only been calibrated with murine data, which does not always translate to human studies, so further investigation of these findings is needed.

Author Contributions: Conceptualization, J.G. and J.P.; methodology, J.G. and J.P.; software, J.G.; formal analysis, J.G.; writing—original draft preparation, J.G.; writing—review and editing, J.P.; visualization, J.G.; supervision, J.P.; All authors have read and agreed to the published version of the manuscript.

Funding: Project is supported by ESF, POWR.03.02.00-00-I028/17-00.

Institutional Review Board Statement: Not applicable.

Informed Consent Statement: Not applicable.

Data Availability Statement: Data sharing not applicable.

Conflicts of Interest: The authors declare no conflict of interest.

Abbreviations

The following abbreviations are used in this manuscript:

CAIX	carbonic anhydrase IX
PD-1	programmed cell death protein 1
CTLA-4	cytotoxic T-lymphocyte-associated protein 4
CC	cancer cells
CSC	cancer stem cells
TME	tumor microenvironment
KO	knock-out
NSCLC	non-small-cell lung cancer

References

- Topalian, S.L.; Hodi, F.S.; Brahmer, J.R.; Gettinger, S.N.; Smith, D.C.; McDermott, D.F.; Powderly, J.D.; Carvajal, R.D.; Sosman, J.A.; Atkins, M.B.; et al. Safety, Activity, and Immune Correlates of Anti-PD-1 Antibody in Cancer. *N. Engl. J. Med.* **2012**, *366*, 2443–2454. [CrossRef]
- Seidel, J.A.; Otsuka, A.; Kabashima, K. Anti-PD-1 and Anti-CTLA-4 Therapies in Cancer: Mechanisms of Action, Efficacy, and Limitations. *Front. Oncol.* **2018**, *8*, 86. [CrossRef]
- Bagchi, S.; Yuan, R.; Engleman, E.G. Immune Checkpoint Inhibitors for the Treatment of Cancer: Clinical Impact and Mechanisms of Response and Resistance. *Annu. Rev. Pathol. Mech. Dis.* **2021**, *16*, 223–249. [CrossRef]
- Ciccolini, J.; Benzekry, S.; Barlesi, F. Deciphering the response and resistance to immune-checkpoint inhibitors in lung cancer with artificial intelligence-based analysis: When PIONeeR meets QUANTIC. *Br. J. Cancer* **2020**, *123*, 337–338. [CrossRef] [PubMed]
- Havel, J.J.; Chowell, D.; Chan, T.A. The evolving landscape of biomarkers for checkpoint inhibitor immunotherapy. *Nat. Rev. Cancer* **2019**, *19*, 133–150. [CrossRef] [PubMed]
- Brahmer, J.R. Harnessing the immune system for the treatment of non-small-cell lung cancer. *J. Clin. Oncol.* **2013**, *31*, 1021–1028. [CrossRef] [PubMed]
- Herzberg, B.; Campo, M.J.; Gainor, J.F. Immune Checkpoint Inhibitors in Non-Small Cell Lung Cancer. *Oncologist* **2017**, *22*, 81–88. [CrossRef] [PubMed]
- Corbet, C.; Feron, O. Tumour acidosis: From the passenger to the driver's seat. *Nat. Rev. Cancer* **2017**, *17*, 577–593. [CrossRef] [PubMed]
- Lee, S.H.; McIntyre, D.; Honess, D.; Hulikova, A.; Pacheco-Torres, J.; Cerdán, S.; Swietach, P.; Harris, A.L.; Griffiths, J.R. Carbonic anhydrase IX is a pH-stat that sets an acidic tumour extracellular pH in vivo. *Br. J. Cancer* **2018**, *119*, 622–630. [CrossRef]
- Chiche, J.; Ilc, K.; Laferrière, J.; Trottier, E.; Dayan, F.; Mazure, N.M.; Brahimi-Horn, M.C.; Pouyssegur, J. Hypoxia-Inducible Carbonic Anhydrase IX and XII Promote Tumor Cell Growth by Counteracting Acidosis through the Regulation of the Intracellular pH. *Cancer Res.* **2009**, *69*, 358–368. [CrossRef]
- Giatromanolaki, A.; Koukourakis, M.I.; Sivridis, E.; Pastorek, J.; Wykoff, C.C.; Gatter, K.C.; Harris, A.L. Expression of Hypoxia-inducible Carbonic Anhydrase-9 Relates to Angiogenic Pathways and Independently to Poor Outcome in Non-Small Cell Lung Cancer. *Cancer Res.* **2001**, *61*, 7992–7998. Available online: <http://xxx.lanl.gov/abs/https://aacrjournals.org/cancerres/article-pdf/61/21/7992/2489028/ch2101007992.pdf> (accessed on 22 April 2023).
- Neri, D.; Supuran, C.T. Interfering with pH regulation in tumours as a therapeutic strategy. *Nat. Rev. Drug Discov.* **2011**, *10*, 767–777. [CrossRef] [PubMed]
- McDonald, P.C.; Chia, S.; Bedard, P.L.; Chu, Q.; Lyle, M.; Tang, L.; Singh, M.; Zhang, Z.; Supuran, C.T.; Renouf, D.J.; et al. A Phase 1 Study of SLC-0111, a Novel Inhibitor of Carbonic Anhydrase IX, in Patients with Advanced Solid Tumors. *Am. J. Clin. Oncol. Cancer Clin. Trials* **2020**, *43*, 484–490. [CrossRef] [PubMed]
- De Campos, N.S.P.; de Oliveira Beserra, A.; Pereira, P.H.B.; Chaves, A.S.; Fonseca, F.L.A.; da Silva Medina, T.; dos Santos, T.G.; Wang, Y.; Marasco, W.A.; Suarez, E.R. Immune Checkpoint Blockade via PD-L1 Potentiates More CD28-Based than 4-1BB-Based Anti-Carbonic Anhydrase IX Chimeric Antigen Receptor T Cells. *Int. J. Mol. Sci.* **2022**, *23*, 5448. [CrossRef]
- Suarez, E.R.; Chang, D.K.; Sun, J.; Sui, J.; Freeman, G.J.; Signoretti, S.; Zhu, Q.; Marasco, W.A.; Suarez, E.R.; Chang, D.K.; et al. Chimeric antigen receptor T cells secreting anti-PD-L1 antibodies more effectively regress renal cell carcinoma in a humanized mouse model. *Oncotarget* **2016**, *7*, 34341–34355. [CrossRef] [PubMed]
- Chafe, S.C.; McDonald, P.C.; Saberi, S.; Nemirovsky, O.; Venkateswaran, G.; Burugu, S.; Gao, D.; Delaidelli, A.; Kyle, A.H.; Baker, J.H.; et al. Targeting Hypoxia-Induced Carbonic Anhydrase IX Enhances Immune-Checkpoint Blockade Locally and Systemically. *Cancer Immunol. Res.* **2019**, *7*, 1064–1078. [CrossRef] [PubMed]
- Grajek, J.; Kather, J.N.; Poleszczuk, J. An in silico model to study the impact of carbonic anhydrase IX expression on tumour growth and anti-PD-1 therapy. *J. R. Soc. Interface* **2023**, *20*, 20220654. [CrossRef] [PubMed]
- Feng, L.; Dong, Z.; Tao, D.; Zhang, Y.; Liu, Z. The acidic tumor microenvironment: A target for smart cancer nano-theranostics. *Natl. Sci. Rev.* **2018**, *5*, 269–286. [CrossRef]

19. Cortes-Dericks, L.; Galetta, D. Impact of Cancer Stem Cells and Cancer Stem Cell-Driven Drug Resiliency in Lung Tumor: Options in Sight. *Cancers* **2022**, *14*, 267. [[CrossRef](#)]
20. Lock, F.E.; McDonald, P.C.; Lou, Y.; Serrano, I.; Chafe, S.C.; Ostlund, C.; Aparicio, S.; Winum, J.Y.; Supuran, C.T.; Dedhar, S. Targeting carbonic anhydrase IX depletes breast cancer stem cells within the hypoxic niche. *Oncogene* **2012**, *32*, 5210–5219. [[CrossRef](#)]
21. Kravaris, C.; Hahn, J.; Chu, Y. Advances and selected recent developments in state and parameter estimation. *Comput. Chem. Eng.* **2013**, *51*, 111–123. [[CrossRef](#)]
22. Poleszczuk, J.; Macklin, P.; Enderling, H. Agent-Based Modeling of Cancer Stem Cell Driven Solid Tumor Growth. *Methods Mol. Biol.* **2016**, *1516*, 335. [[CrossRef](#)] [[PubMed](#)]
23. Poleszczuk, J.; Enderling, H. The Optimal Radiation Dose to Induce Robust Systemic Anti-Tumor Immunity. *Int. J. Mol. Sci.* **2018**, *19*, 3377. [[CrossRef](#)] [[PubMed](#)]
24. Kuznetsov, V.A.; Makalkin, I.A.; Taylor, M.A.; Perelson, A.S. Nonlinear dynamics of immunogenic tumors: parameter estimation and global bifurcation analysis. *Bull. Math. Biol.* **1994**, *56*, 295–321. [[CrossRef](#)] [[PubMed](#)]
25. Valentinuzzi, D.; Simončič, U.; Uršič, K.; Vrankar, M.; Turk, M.; Jeraj, R. Predicting tumour response to anti-PD-1 immunotherapy with computational modelling. *Phys. Med. Biol.* **2019**, *64*, 025017. [[CrossRef](#)]
26. Cottrell, T.R.; Taube, J.M. PD-L1 and Emerging Biomarkers in PD-1/PD-L1 Blockade Therapy. *Cancer J.* **2018**, *24*, 41. [[CrossRef](#)]
27. Danciu, C.; Falamas, A.; Dehelean, C.; Soica, C.; Radeke, H.; Barbu-Tudoran, L.; Bojin, F.; Pinzaru, S.C.; Munteanu, M.F. A characterization of four B16 murine melanoma cell sublines molecular fingerprint and proliferation behavior. *Cancer Cell Int.* **2013**, *13*, 75. [[CrossRef](#)]

Disclaimer/Publisher's Note: The statements, opinions and data contained in all publications are solely those of the individual author(s) and contributor(s) and not of MDPI and/or the editor(s). MDPI and/or the editor(s) disclaim responsibility for any injury to people or property resulting from any ideas, methods, instructions or products referred to in the content.

Chapter 6

Cellular plasticity upon proton irradiation determines tumor cell radiosensitivity

6.1 Introduction

This part of my thesis deals with the challenge of understanding the role of the heterogeneous TME in radioresistance, corresponding to my third research aim and fourth research hypothesis. In particular, in [56], we investigated the impact of X-ray and proton irradiation on tumor heterogeneity and cancer stem cell dynamics in the tumor. As mentioned in the introduction, CSC are part of the TME, contributing to its heterogeneity due to their nonhomogeneous distribution in space and their plasticity, i.e., the ability to dynamically acquire and lose their stemness. This plasticity can be, among others, induced by irradiation and thus constitutes a potential radioresistance driver. Therefore, understanding this cellular plasticity and eliminating CSC in the tumor is of utmost importance for a durable and complete response. My role in [56] was to investigate the differences in cellular plasticity between the two irradiation types and their CSC-removing potential using mathematical modeling.

Hence, I proposed a differential equation model of cancer cell plasticity, as presented in the methods subsection titled "Mathematical modeling of cancer cell plasticity upon irradiation". Moreover, I calibrated the model (see supplementary table S1), fitted it to *in vitro* data which was obtained by my co-workers (Figure 2B in [56]), and was responsible for the interpretation of the model simulation's results. I have also qualitatively analyzed the model to show the importance of including reverse plasticity events in the modeling framework. Furthermore, I have written the first draft of the parts of the manuscript that deal with the differential equation model, including the methods subsection "Mathematical modeling of cancer cell plasticity upon irradiation", the results subsection "Mathematical modeling distinguishes proton from photon irradiation through plasticity events", and parts of the discussion. Finally, I am also the author of figure 2, showing a diagram representation of the mathematical model, as well as the data fitting results, and supplementary figure S2, which additionally explains the mathematical framework used in this study.

6.2 Relation of the publication to the research aims of the thesis

6.2.1 Model and analyze the influence of cancer cell plasticity on tumor heterogeneity and the effectiveness of X-ray and proton radiotherapy.

My co-workers analyzed the dynamics of putative stem cell markers such as ALDH after irradiation using flow cytometry analysis, observing heterogeneous dynamics but finding no significant differences between photon and proton irradiation (Fig. 1A) in [56]. Moreover, they analyzed the effects of proton irradiation on putative stem populations and identified ALDH+ and ALDH- cells' survival fraction and RBE of proton radiotherapy (fig. 1D and 1E in [56]). However, the performed experiments were only able to capture the final effect of both irradiation types on the putative CSC population identified via CSC markers such as ALDH1, without illustrating the influence on plasticity events. I wanted to dive deeper and analyze whether the radiation types differed in their impact on either plasticity event type, while not having a statistically significant final effect on the ALDH+ population, as shown in figure S1A in [56]. Hence, I proposed a model that aimed to elucidate differences between both irradiation types that could not be derived immediately from the experimental data, in line with my fourth research hypothesis.

The proposed differential equation model considers CC and CSC and their plasticity. The model is illustrated by figures 2A and S2 in [56] and formally described in the methods subsection "Mathematical modeling of cancer cell plasticity upon irradiation". I have derived the model from previously proposed and validated agent-based models of cellular plasticity [98], [99]. These computational models were not suitable for my research aim due to the lack of sufficient data to calibrate an agent-based approach. The available data was in time series format (see Fig.1A in [56]), which can be approximated using ODE models. Furthermore, my research aim of comparing plasticity was not inherently spatial or exploratory, justifying the use of an agent-based model, so I decided to derive a differential equation model for this task, that had fewer parameters to calibrate, lower computational complexity, and was mathematically tractable. In accordance with the previously introduced models, we consider symmetric self-renewal and asymmetric CSC division that contribute to tumor heterogeneity regardless of plasticity. Likewise, we assume that CC can only divide a finite amount of times due to replication-dependent telomere shortening [100], whereas CSC proliferation capacity is unlimited [101]. Additionally, CC may undergo apoptosis, whereas CSC do not [102]. Similarly, we assume that CSC are protected from irradiation-induced damage, to simulate their enhanced radioresistance. In contrast to the previously proposed models, we only consider irradiation-induced plasticity, so only damaged cells undergo plasticity events. Therefore, our model has distinct variables for irradiated and non-irradiated cells. Additionally, to consider the finite proliferation capacity within the setting of an ODE model, we have to distinguish CC by their remaining division attempts. Hence, our final model has $2(p_{cap} + 1)$ variables, where p_{cap} denotes the default proliferation capacity of a cancer cell that has not divided yet. Finally, our model considers mutations of CC that repair irradiation-induced DNA damage and can turn damaged CC into undamaged CC over time [103].

After partially calibrating the model with *in vitro* data presented in [56] and data from the literature (see supplementary table S1 in [56]), I fitted the model to the flow cytometry analysis of ALDH activity data, as presented in fig. 1A in [56]. Details

of the data fitting procedure can be found in the methods section of [56]. Then, I compared the obtained parameters for each treatment and analyzed the differences in parameter values. As the residuals were not normally or even symmetrically distributed, the assumptions of the paired t-test or the Wilcoxon signed-rank test were not met, so I used the sign test. This analysis revealed a lower rate of plasticity events after proton irradiation than after photon irradiation (p-value=0.03, see supplementary table S1). That is, the model simulations indicate that CC acquire stemness less frequently after proton irradiation than after photon irradiation, which could partially explain the enhanced therapeutic potential of proton over photon irradiation, which is reflected in the RBE of 1.1. for proton therapy [66]. Furthermore, we observed that we could not fit our model to the *in vitro* data when ignoring reverse plasticity events (i.e. setting the parameter v to zero). In fact, as demonstrated in the methods section, we were able to analytically prove that the model had to include reverse plasticity events to reproduce a non-monotonic trend commonly seen in the data: an at-first decreasing ALDH+ ratio that later increases. This suggests that reverse plasticity events were crucial to our modeling and play a vital role in CSC dynamics after irradiation.

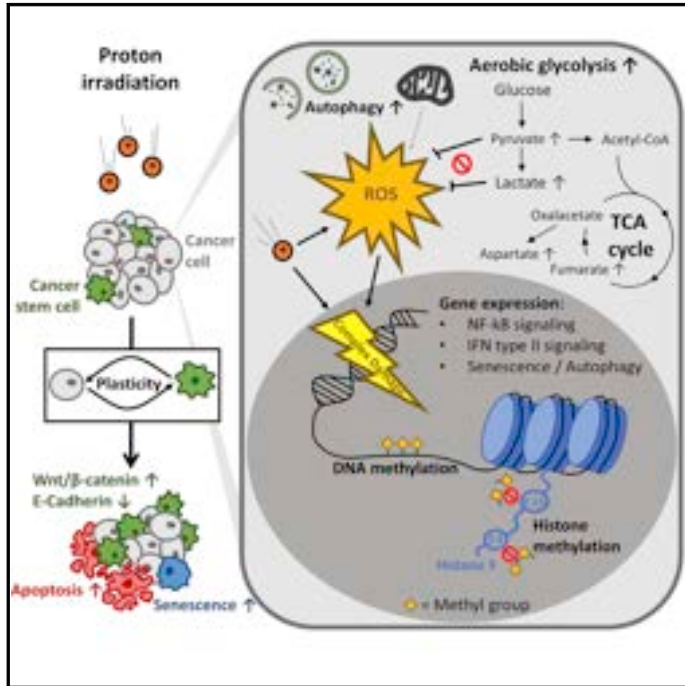
In conclusion, in [56] I proposed a mathematical model of radiation-induced cancer cell plasticity and analyzed its impact on the CSC fraction in the tumor, in line with my third research aim. My model shed some light on the differences between the impact of two types of irradiation on cellular plasticity, which could not be inferred immediately from the experimental data. Hence, this supports my fourth research hypothesis, that mathematical modeling can complement biological experiments and elucidate the differences between proton and photon irradiation. The conclusions derived from the modeling are significant, as they underline the importance of the impact of bi-directional plasticity events on CSC dynamics and aid in explaining the putative higher therapeutic potential of proton radiotherapy. Furthermore, model simulations indicate that cellular plasticity is an interesting treatment target, and reducing the occurrence rate of plasticity events could increase radioreponse rates.

6.3 The publication

Cell Reports

Cellular plasticity upon proton irradiation determines tumor cell radiosensitivity

Graphical abstract



Authors

Iñaki Schniewind,
Wahyu Wijaya Hadiwikarta,
Julia Grajek, ..., Cläre von Neubeck,
Ina Kurth, Claudia Peitzsch

Correspondence

claudia.peitzsch@uniklinikum-dresden.de

In brief

Schniewind et al. explore the therapeutic potential of proton irradiation to eliminate cancer stem-like cells. The authors find profound differences in histone methylation pattern, DNA damage complexity, cellular plasticity rates, and senescence between proton and photon irradiation.

Highlights

- Proton and photon irradiation induce dynamic changes in cancer stem cell markers
- Proton irradiation targets cancer stem-like cells with high efficacy
- Differential histone methylation and cellular plasticity rates are caused by protons
- Proton irradiation induces complex DNA damages and less senescence than photons



Schniewind et al., 2022, Cell Reports 38, 110422
February 22, 2022 © 2022 The Author(s).
<https://doi.org/10.1016/j.celrep.2022.110422>

Article

Cellular plasticity upon proton irradiation determines tumor cell radiosensitivity

İñaki Schniewind,^{2,15} Wahyu Wijaya Hadiwikarta,⁸ Julia Grajek,¹⁰ Jan Poleszczuk,¹⁰ Susan Richter,⁹ Mirko Peitzsch,⁹ Johannes Müller,⁴ Daria Klusa,^{1,2,3} Elke Beyreuther,^{2,4,13} Steffen Löck,^{2,3,5} Armin Lühr,¹¹ Susanne Frosch,⁵ Christer Groeben,⁶ Ulrich Sommer,⁷ Mechthild Krause,^{1,2,3,4,5,8} Anna Dubrovka,^{1,2,3,4,8} Cläre von Neubeck,¹² Ina Kurth,^{8,14} and Claudia Peitzsch^{1,2,3,16,17,*}

¹National Center for Tumor Diseases (NCT), Faculty of Medicine and University Hospital Carl Gustav Carus, Technical University Dresden, 01307 Dresden, Germany

²OncoRay - National Center for Radiation Research in Oncology, Faculty of Medicine and University, Hospital Carl Gustav Carus, Technische Universität Dresden and Helmholtz-Zentrum Dresden-Rossendorf, 01307 Dresden, Germany

³German Cancer Consortium (DKTK), Partner Site Dresden, 01307 Dresden, Germany

⁴Institute of Radiooncology–OncoRay, Helmholtz-Zentrum Dresden-Rossendorf (HZDR), 01307 Dresden, Germany

⁵Department of Radiation Oncology, University Hospital Carl Gustav Carus, 01307 Dresden, Germany

⁶Department of Urology, University Hospital Carl Gustav Carus, 01307 Dresden, Germany

⁷Institute of Pathology, University Hospital Carl Gustav Carus, 01307 Dresden, Germany

⁸German Cancer Research Center (DKFZ), 69120 Heidelberg, Germany

⁹Institute of Clinical Chemistry and Laboratory Medicine, University Hospital Carl Gustav Carus at the Technische Universität Dresden, 01307 Dresden, Germany

¹⁰Nalecz Institute of Biocybernetics and Biomedical Engineering, Polish Academy of Sciences, 02-109 Warsaw, Poland

¹¹Medizinphysik und Strahlentherapie, Technische Universität Dortmund, 44227 Dortmund, Germany

¹²Department for Particle Therapy, University Hospital Essen, University of Duisburg-Essen, 45147 Essen, Germany

¹³Institute of Radiation Physics, Helmholtz-Zentrum Dresden-Rossendorf, 01328 Dresden, Germany

¹⁴Heidelberg Institute of Radiation Oncology (HIRO), National Center for Radiation Oncology (NCRO), Heidelberg University, 69120 Heidelberg, Germany

¹⁵Present address: Department of Neurology, Carl Gustav Carus University Hospital, Technische Universität Dresden, 01307 Dresden, Germany

¹⁶Present address: Center for Regenerative Therapies Dresden (CRTD), Technische Universität Dresden, 01307 Dresden, Germany

¹⁷Lead contact

*Correspondence: claudia.peitzsch@uniklinikum-dresden.de

<https://doi.org/10.1016/j.celrep.2022.110422>

SUMMARY

Proton radiotherapy has been implemented into the standard-of-care for cancer patients within recent years. However, experimental studies investigating cellular and molecular mechanisms are lacking, and prognostic biomarkers are needed. Cancer stem cell (CSC)-related biomarkers, such as aldehyde dehydrogenase (ALDH), are known to influence cellular radiosensitivity through inactivation of reactive oxygen species, DNA damage repair, and cell death. In a previous study, we found that ionizing radiation itself enriches for ALDH-positive CSCs. In this study, we analyze CSC marker dynamics in prostate cancer, head and neck cancer, and glioblastoma cells upon proton beam irradiation. We find that proton irradiation has a higher potential to target CSCs through induction of complex DNA damages, lower rates of cellular senescence, and minor alteration in histone methylation pattern compared with conventional photon irradiation. Mathematical modeling indicates differences in plasticity rates among ALDH-positive CSCs and ALDH-negative cancer cells between the two irradiation types.

INTRODUCTION

The rationale for the use of protons in radiotherapy is based on their distinct physical characteristics, allowing a more precise dose deposition and thus a better therapeutic ratio in comparison with conventional photons (Tanner et al., 1967; Wilson, 1946). In this context, proton beam therapy is predominantly used for tumors near organs at risk and in pediatric patients (Tseng et al., 2017; Weber et al., 2018). However, knowledge regarding the biological effects of proton therapy is still limited and controversial.

Of particular importance for treatment success is an effective targeting of cancer stem cells (CSCs), as they possess unlimited self-renewal capacity and differentiation potential (Peitzsch et al., 2019; Reya et al., 2001). Markers associated with a higher likelihood to identify cells with stemness characteristics include transmembrane glycoproteins CD133 and CD44, chemokine C-X-C motif receptor 4 (CXCR4), and the aldehyde dehydrogenase (ALDH) family and have been described as putative CSC markers for different tumor entities, such as prostate cancer (PCa) (Collins et al., 2005; Dubrovka et al., 2012; Li et al.,





2010; Patrawala et al., 2006), head and neck squamous cell carcinoma (HNSCC) (Clay et al., 2010; Prince et al., 2007; Zhang et al., 2010), and brain tumors, such as glioblastoma multiforme (GBM) (Flahaut et al., 2016; Pietras et al., 2014; Singh et al., 2004). While CSCs effectively evade photon irradiation-induced death, e.g., through more effective DNA repair, enhanced scavenging of reactive oxygen species (ROS), and overly activated pro-survival pathways (Bao et al., 2006; Schulz et al., 2019; Tsao et al., 2019), preclinical studies suggest that protons have a higher CSC-targeting efficacy (Alan Mitteer et al., 2015; Fu et al., 2012; Narang et al., 2015; Zhang et al., 2013). The CSC subpopulation is not static within tumors but rather characterized by dynamic features and heterogeneous cellular phenotypes. Tumor cells can transition between states of stemness and differentiation through plastic events regulated by various factors, such as the tumor microenvironment and metabolic changes, as well as therapeutic stimuli, such as ionizing radiation or chemotherapy (Bao et al., 2006; Dirkse et al., 2019; Ghisolfi et al., 2012; Kreso and Dick, 2014; Peitzsch et al., 2016).

In previous work, our group observed an upregulation of putative CSC markers in PCa and HNSCC cell lines after single-dose photon irradiation (Cojoc et al., 2015; Kurth et al., 2015). This phenotypic switch was accompanied by active histone H3 methylation within the promoter region of the *ALDH1A1* gene in PCa cell lines (Peitzsch et al., 2016). Furthermore, higher ALDH activity was linked to a more radioresistant (RR) progenitor phenotype with improved DNA repair capabilities, activated epithelial-mesenchymal transition (EMT), and increased cell migration. Interestingly, pharmacological inhibition of histone methyltransferase enhancer of zeste 2 polycomb repressive complex 2 subunit (EZH2) using 3-deazaneplanocin A (DZNep) led to a sensitization of RR PCa cells and impaired tumorigenicity. In this study, we characterized the biological effects of proton irradiation in PCa, HNSCC, and GBM cells with a focus on the CSC subpopulation. Besides standard radiobiological and cell biological methods to investigate radiosensitivity and stemness, we applied comparative transcriptome, DNA methylome, and Krebs cycle metabolome analysis to assess putative resistance mechanisms to proton irradiation that may serve as putative therapeutic targets in the future.

RESULTS

Proton irradiation induces changes in putative CSC markers

Alterations in putative CSC marker expression upon photon irradiation have been described for various tumor entities (Cojoc et al., 2015; Kurth et al., 2015; Lagadec et al., 2012; Peitzsch et al., 2016; Phillips et al., 2006). Conversely, knowledge concerning a possible CSC dynamic after proton irradiation is scarce and inconsistent. Therefore, we analyzed effects of single physical dose of 4 Gy protons versus photons on putative CSC populations in six tumor cell lines originating from PCa, HNSCC, and GBM. CD44, CD133, and CXCR4 expression as well as ALDH activity were measured by flow cytometry at different time points over 14 days. While we saw a heterogeneous response comparing the different markers, the dynamics of the individual markers were similar in all investigated entities (Figures 1A and

S1A). All tested cell lines demonstrated a dynamic response with an increased ALDH activity and CD44 expression in the first week after irradiation before dropping below baseline level. In comparison, CXCR4 expression showed an inverse dynamic and CD133 expression declined steadily. To further assess the functional properties of CSCs, we determined the self-renewal capacity by sphere-formation assay. Sphere-forming potential was significantly reduced after proton irradiation in PCa and HNSCC cells compared with photons (Figure 1B). We were able to validate these findings in primary prostate cultures originating from matched benign and cancer biopsies despite heterogeneous response rates between different patient samples (Figure 1C).

To further characterize proton-specific effects on a defined CSC population, ALDH⁺ and ALDH⁻ populations were purified by fluorescence-activated cell sorting and plated for 3D colony-formation assay. We found ALDH⁺ cells to be less sensitive to both irradiation types compared with the ALDH⁻ population, particularly in PCa and HNSCC cells (Figure 1D). This resulted in a significantly lower relative biological effectiveness (RBE) of protons in ALDH⁺ compared with ALDH⁻ cells (Figure 1E). Although the ALDH⁺ population is enriched for cells with an enhanced sphere-forming capacity (Figure S1B), spherogenicity seems to be mediated by only a subset of ALDH isoforms and is additionally determined by EMT, altered cholesterol homeostasis, TNF- α /NF- κ B signaling, and estrogen response (Figures S1C, S1D, and S1E). Taken together, our data demonstrate that proton irradiation leads to dynamic changes in the expression of putative CSC markers and has a higher efficiency to reduce the sphere-forming capacity of cancer cells in comparison with photons.

Mathematical modeling distinguishes proton from photon irradiation through plasticity events

The biological and experimental data allow only a snap-shot view into the dynamic processes within the cancer cultures after irradiation. Therefore, we used a mathematical model of tumor cell growth that considers cellular plasticity and dynamics (Figures 2A, S2A, and S2B). After calibrating the model to fit the experimental data, it was capable of correctly reflecting the dynamics of ALDH activity after irradiation with protons and photons (Figure 2B). Importantly, we were able to show rigorously that the model had to include reverse plasticity events, when CSCs lose their stem-like features, to replicate the qualitative behavior observed in 28 of the 48 experimental repeats, namely a decrease in the ALDH⁺ population followed by an increase. Moreover, the model calibration yielded a significantly lower rate of plasticity events, when cancer cells acquire a stem-like phenotype, denoted by parameter c , after proton than after photon irradiation ($p = 0.03$, Table S1). In summary, the developed model suggests that both types of plasticity events are crucial for explaining ALDH dynamics after irradiation. Interestingly, proton irradiation seems to induce less plasticity events compared with photons.

Proton irradiation induces long-lasting DNA damages

Proton irradiation led to a significant reduction of clonogenic survival in GBM and PCa cell lines in comparison with photons while no difference was seen in HNSCC lines (Figure 3A). In

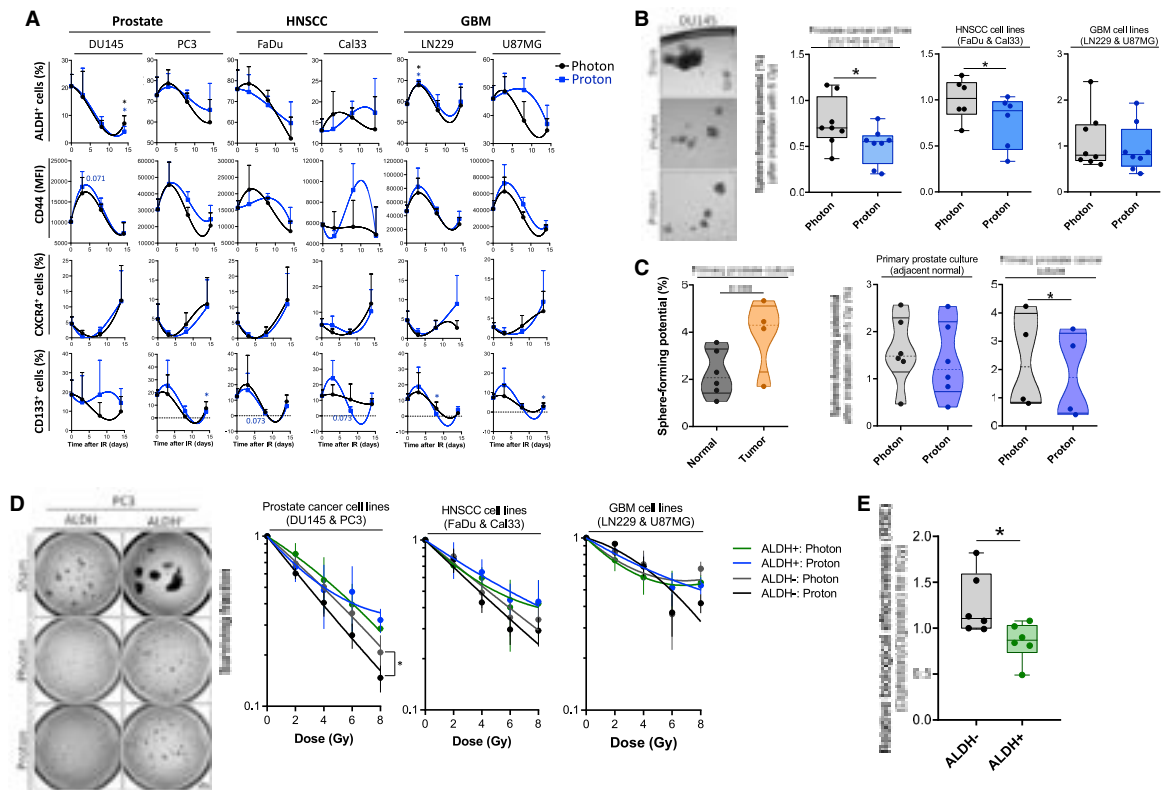


Figure 1. Regulation and targeting of putative cancer stem cells (CSCs) by proton irradiation

(A) Flow cytometry analysis of ALDH activity as well as CD44, CD133, and CXCR4 surface expression measured at days 0, 3, 7, and 14 after 4 Gy photon versus proton irradiation in DU145, PC3, FaDu, Cal33, LN229, and U87MG ($n = 4$, mean \pm SEM, $^*p < 0.05$, paired t test, comparison of day 14 with baseline). (B) Sphere-formation assay after 6 Gy photon versus proton irradiation ($n = 3-4$, median \pm min-max, $^*p < 0.05$). (C) Sphere-forming potential of primary normal prostate and cancer cultures after 6 Gy photon versus proton irradiation ($n = 4-6$, $^*p < 0.05$). (D) 3D colony-formation assay of ALDH⁺ and ALDH⁻ populations after 0, 2, 4, 6, and 8 Gy photon versus proton irradiation. The dose-response curve is illustrated as geometric mean of two cell lines per tumor entity ($n = 6$, mean \pm SEM, $^*p < 0.05$). (E) The relative biological effectiveness (RBE) in ALDH⁺ and ALDH⁻ cells was calculated as ratio between proton and photon doses resulting in a biological isoeffect that was defined as the survival fraction at 6 Gy with photons. The calculations are based on the α and β values determined with the linear-quadratic model ($n = 6$, median \pm min-max, $^*p < 0.05$) (see also Figure S1 and Table S2).

previous studies, our group showed that repeated photon irradiation of PCa and HNSCC cell lines selected sublines with a decreased radiosensitivity that exhibited a higher DNA damage repair capacity, an increased expression of putative CSC markers, and an enhanced tumorigenicity in mice (Cojoc et al., 2015; Kurth et al., 2015). We hypothesized that these pre-irradiated and RR sublines may be more susceptible to proton irradiation. Indeed, proton irradiation showed a higher efficiency than photons in reducing the clonogenic survival in both tumor entities (Figure 3D), while causing no increased toxicity in normal prostate cell line RWPE-1 (Figure 3B). These findings could be validated in four primary PCa and matched benign cultures (Figure 3C). As in the parental cell lines (Figure 1B), the sphere-forming capability was significantly reduced for the RR-sublines after proton irradiation in comparison with photons (Figure 3E).

To further investigate the molecular basis of the increased biological effect of protons as well as putative proton-specific resistance mechanisms, we analyzed the number of DNA double-strand breaks (DSBs) after irradiation indicated by phosphorylation of histone H2AX on serine 139 (γ H2AX). Unrepaired, residual foci 24 h after proton treatment were significantly increased in HNSCC cells in comparison with photons, while only a trend was seen in PCa ($p = 0.175$) and no differences in GBM cells (Figure 3F). We saw a similar trend in a primary prostate biopsy 24 h after *ex vivo* proton irradiation, while γ H2AX levels were markedly lower in adjacent normal tissue compared with photons (Figure S5A). On the other hand, we saw no significant differences in p53-binding protein 1 (53BP1) foci number between both irradiation types (Figure S3A).

We further analyzed oxidative stress with chloromethyl-2',7'-dichlorodihydrofluorescein-diacetate (CM-H2DCFDA) staining as

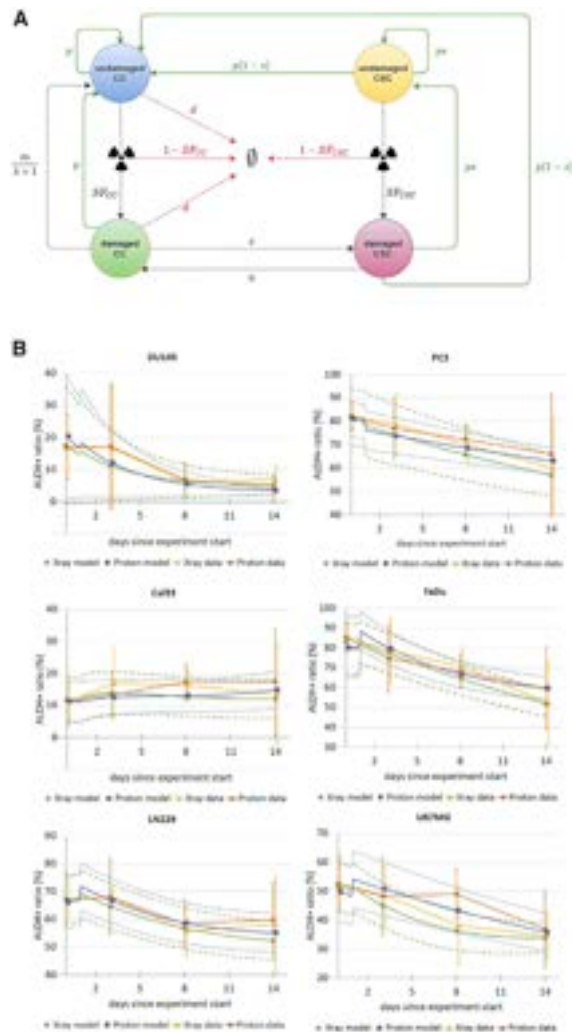


Figure 2. Mathematical model to predict tumor cell growth and dynamics within the ALDH⁺ population upon irradiation

(A) Diagram illustrating the relationships between the four main compartments: irradiated non-stem cancer cells (damaged CC, y), non-irradiated non-stem cancer cells (undamaged CC, x), irradiated cancer stem cells (damaged CSC, w), and non-irradiated cancer stem cells (undamaged CSC, z). This diagram does not distinguish between the cells with distinct remaining numbers of divisions. Green solid arrows indicate events during which new cells appear (proliferation) and red dashed arrows indicate events during which cells disappear (apoptosis or irradiation-induced cell death). Black dotted arrows indicate that a cell changes its compartment, that is the total number of cells stays constant. Each arrow is annotated with the rate at which the given event occurs. The empty set symbol denotes cells that are removed from the system. (B) The plots show the comparison between the ALDH⁺ ratio obtained from flow cytometry analyses and the ratio predicted by the model. The error bars indicate the standard deviation in the data, the dashed lines indicate the standard deviation in the model predictions for photons and the dotted lines indicate the standard deviation in the model predictions for proton treatment. In this experiment the cell cultures were irradiated at day 1 and the ALDH⁺ ratio was observed until day 14 (see also [Figure S2](#) and [Table S1](#)).

well as intracellular glutathione levels indicated by monochlorobimane using flow cytometry 24 h after irradiation and found a heterogeneous response between the investigated cell lines and entities. Exclusively the GBM cell lines showed significantly decreased ROS levels after proton in comparison with photon irradiation ([Figure 3G](#)). However, PCa cells showed no significant differences in ROS levels between the two irradiation types, but significantly lower glutathione (GSH) levels after protons ([Figure 3H](#)). To summarize, proton irradiation significantly reduces the clonogenic survival of PCa and GBM but not HNSCC cell lines in comparison with photons. Our results support the body of literature indicating the induction of more complex DNA damages and delayed repair as one of the underlying mechanisms ([Carter et al., 2018](#); [Cuaron et al., 2016](#); [Fu et al., 2012](#); [Hojo et al., 2017](#); [Oeck et al., 2018](#); [Sertorio et al., 2020](#); [Vitti and Parsons, 2019](#)). However, we found no increase in oxidative stress following proton irradiation in comparison with photons.

Induction of cell death pathways after proton irradiation

We found the clonogenic potential of the cancer cell lines significantly affected by proton irradiation ([Figure 3A](#)). However, no differences were seen for cell growth after proton and photon irradiation in comparison with sham control ([Figure 4A](#)). Tumor cells may bypass programmed cell death despite unrepaired DNA damage and escape proton-specific killing as we have seen for the ALDH⁺ population ([Figure 1A](#)). Apoptosis induction measured by Annexin V staining as well as caspase-3/7 activity and autophagy determined by autophagosome formation did not differ between the irradiation types 48 h after treatment ([Figures 4B, 4C and S4A](#)). However, we found significantly reduced senescence indicated by β -galactosidase activity in PCa and GBM cells after proton in comparison with photon irradiation ([Figure 4D](#)). Transcriptome analysis of DU145 and PC3 cells identified 46 genes significantly upregulated 12 h after 4 Gy proton irradiation that regulate NF- κ B, IL-17, TNF, and apoptosis signaling while no alteration was found for photons at that time point ([Figures 4E, S4B, and S4C](#)). In particular, *NFKBIA*, *BIRC3* and *ATF3* are known to be upregulated upon stress and inflammation and may be involved in proton-specific early response. However, some cancer cells may bypass cell death induction.

Cellular plasticity and epigenetic changes upon proton irradiation

Cellular plasticity is a major resistance factor in heterogeneous tumors and is driven by the CSC population. Previously, our group showed that the upregulation of putative CSC markers after photon irradiation coincided with modifications in histone methylation, whose inhibition led to radiosensitization of PCa cells ([Peitzsch et al., 2016](#)). Within this study we found a comparable CSC marker dynamic after proton irradiation ([Figure 1A](#)). We also examined histone methylation marks and CSC markers after single-dose irradiation with 4 Gy by western blot analysis at different time points over 21 days ([Figure 5A](#)). Both irradiation types led to a dynamic increase of β -catenin protein expression, a central regulator of the canonical Wnt signaling pathway that coordinates cell-cell adhesion and induces stem cell regulators. Interestingly, E-cadherin expression, as well as trimethylation at lysine 4 (H3K4me3) and lysine 36 (H3K36me3) of histone 3, was

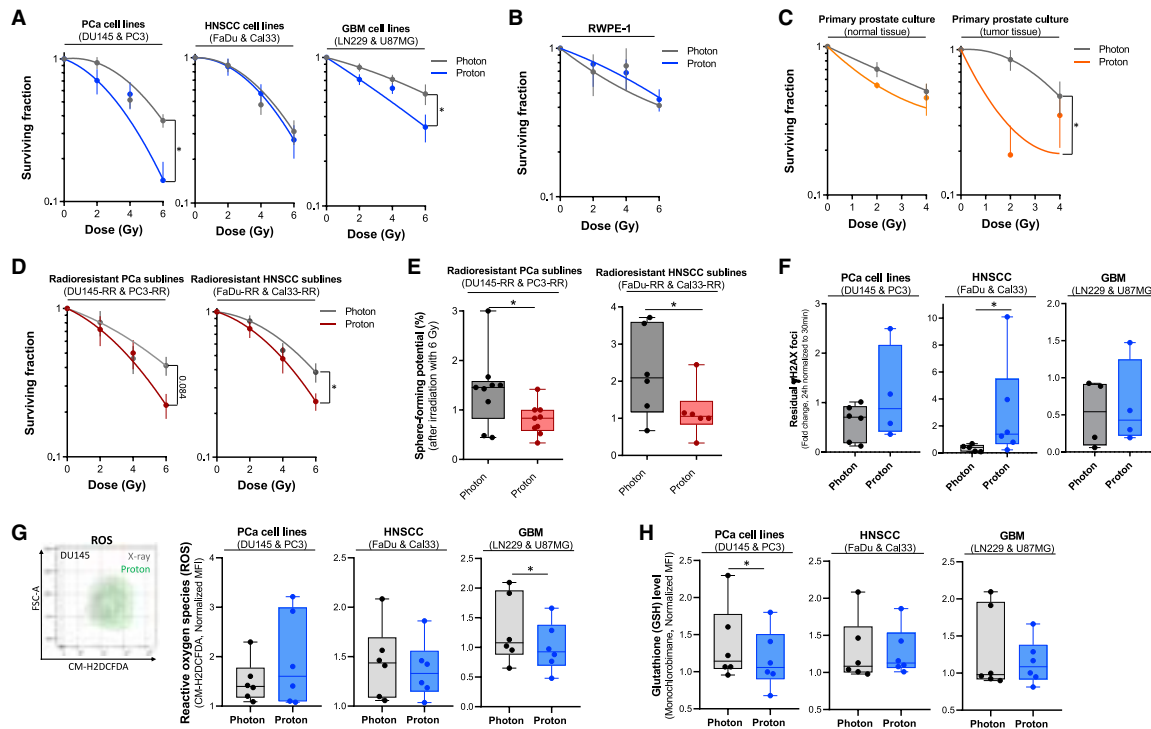


Figure 3. Radiobiological determination of cellular sensitivity to proton irradiation

(A) 3D colony-formation assay of the PCa cell lines DU145 and PC3, the HNSCC cell lines FaDu and Cal33, and the GBM cell lines LN229 and U87MG after increasing doses of photons and protons ($n = 6$, mean \pm SEM, $^*p < 0.05$).
 (B) Clonogenic survival illustrates the cellular response of the immortalized normal prostate cell line RWPE-1 after treatment with 0, 2, 4, and 6 Gy photon versus proton irradiation ($n = 3$, mean \pm SEM).
 (C) 3D colony-formation assay of primary prostate cultures originating from tumor and adjacent normal tissue after photon versus proton irradiation with 0, 2, and 4 Gy ($n = 4-6$, mean \pm SEM, $^*p < 0.05$).
 (D) 3D clonogenic survival assay of previously selected radioresistant (RR) PCa and HNSCC sublines after multiple fractions with 4 Gy ($n = 6$, mean \pm SEM, $^*p < 0.05$).
 (E) Sphere-formation assay of RR PCa and HNSCC sublines after irradiation with 6 Gy photon versus proton ($n = 6$, median \pm min-max, $^*p < 0.05$).
 (F) Normalized residual γ H2AX foci 24 h after 4 Gy photon versus proton irradiation in PCa, HNSCC, and GBM cell lines ($n = 6$, median \pm min-max, $^*p < 0.05$).
 (G) Flow cytometry analysis of CM-H2DCFDA and (H) monochlorobimane as markers for oxidative stress and glutathione consumption 24 h after irradiation with 4 Gy photons in comparison with protons. Depicted are normalized mean fluorescence intensity values combining the two cell lines used per entity, e.g., prostate cancer (DU145, PC3) and glioblastoma (LN229 and U87MG) ($n = 6$, median \pm min-max, $^*p < 0.05$) (see also Figure S3 and Table S2).

significantly lower after proton versus photon irradiation (Figure 5A). While photons led to an induction of these activating histone marks, consequently facilitating gene expression as well as access of DNA damage repair machinery, no changes were observed upon proton irradiation (Figure 5A). Differing epigenetic modifications between the two irradiation types were also found in HNSCC xenograft tumors generated from SAS and UT-SSC-14 cells, with a significantly reduced trimethylation of histone 3 at lysine 27 (H3K27me3) and higher ALDH1A1 expression 24 h after local tumor irradiation with protons then with photons (Figure 5B). Conversely, an *ex vivo* irradiated primary prostate biopsy showed a trend toward downregulation of CXCR4, ALDH1A1, and H3K36me3 24 h after both irradiation types in comparison with sham (Figure S5A). To further characterize adaptive effects accompanying the observed ALDH and CD44 expression dy-

namics (Figure 1A), we conducted comparative gene expression analysis 5 days after 4 Gy single-dose irradiation. In all six cancer cell lines, we found a higher percentage of up- than downregulated genes following both irradiation types in comparison with sham control (Figure 5C). Despite commonly regulated genes between the different cell lines being sparse, we identified growth differentiation factor 15 (*GDF15*), baculoviral IAP repeat containing 3 (*BIRC3*), and activating transcription factor 3 (*ATF3*), known regulators of apoptosis, metabolism, immunity, and oncogenesis, to be induced in at least two entities after proton irradiation in comparison with sham control (Figures 5D and S5C). Ingenuity pathway analysis of all significantly regulated genes revealed alterations in NF- κ B signaling-mediated cell survival, immune regulation, and cell death pathways. Particularly senescence and autophagy upon proton irradiation are validating the functional data in

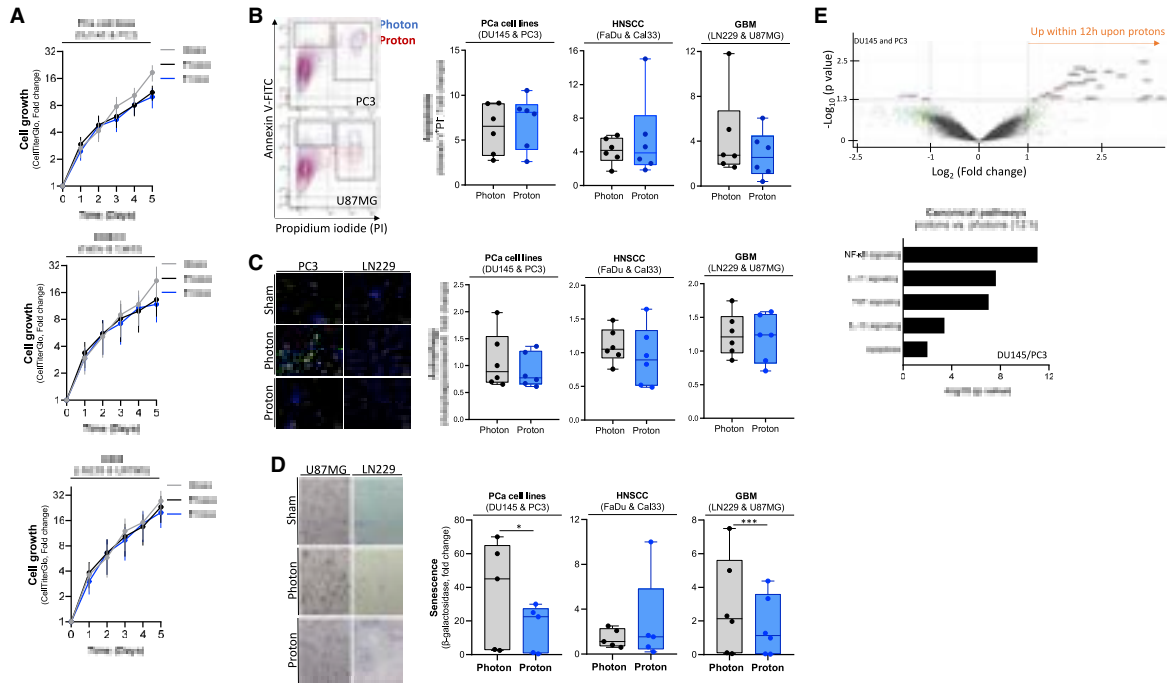


Figure 4. Different cell death modes induced by proton versus photon irradiation

(A) Cell proliferation determined daily over a course of 5 days after irradiation using CellTiterGlo assay ($n = 3$, mean \pm SEM). (B) Flow cytometry-based analysis of Annexin V-FITC and propidium iodide (PI) in PCa (DU145, PC3), HNSCC (FaDu, Cal33), and GBM cell lines (LN229 and U87MG) 48 h after irradiation with 4 Gy photons versus protons. Apoptotic cells were defined as Annexin V-positive and PI-negative ($n = 6$, median \pm min-max). (C) Representative immunofluorescence staining of autophagosomes (green) and the calculation of autophagosome formation per cell 24 h after irradiation ($n = 6$, median \pm min-max, scale bars = 50 μ m). (D) β -Galactosidase activity to analyze senescence 5 days after irradiation. Depicted are values normalized to sham control ($n = 6$, median \pm min-max, ratio paired t test, * $p < 0.05$, *** $p < 0.001$). (E) Volcano blots illustrating comparative transcriptome analysis in PCa cell lines DU145 and PC3 12 h after single-dose irradiation with 4 Gy of protons in comparison with photons ($n = 4$, two each). Highlighted genes are differentially regulated with a fold change >2 or <-2 and $p < 0.05$. Ingenuity pathway analysis combining all significantly differentially regulated genes identified an upregulated NF- κ B pathway, and IL-17 and TNF signaling, within 12 h after proton irradiation (see also Figure S4).

Figures 4C and 4D (Figures 5D and 5B). Surprisingly, we found no mentionable differences in gene expression patterns comparing proton with photon irradiation, which suggests comparable adaptive intracellular processes (Figure 5C). Besides histone modifications, we analyzed changes in DNA methylation patterns 5 days after irradiation. Differential methylation levels indicated by beta values showed only minor alterations comparing proton irradiation and sham control (Figure 5E).

Besides epigenetic mechanisms, metabolic adaptations and the interplay of both are major determinants of cellular plasticity and radioresistance (Martínez-Reyes and Chandel, 2020; Wong et al., 2017). Therefore, we investigated the static concentrations of tricarboxylic acid cycle (TCA) metabolites in whole-cell lysates 5 days after irradiation (Figure 5F). We found elevated levels of most TCA metabolites in PCa and HNSCC cells, while the GBM cell lines exhibited significantly lower amounts of TCA metabolites following proton irradiation compared with sham control. However, these findings may be influenced by media composition as

glutamine and other amino acids replenish the TCA cycle and potentially obscure changes. In particular, we found significantly higher pyruvate and succinate concentrations in HNSCC cells after proton irradiation in comparison with sham control, which may be indicative of an induction of aerobic glycolysis in response to irradiation-induced stress. In addition, proton irradiation induced a trend toward increased concentrations of aspartate ($p = 0.096$) and the onco-metabolite fumarate ($p = 0.093$), which has been described to inhibit prolyl hydroxylase activity and stabilize hypoxia-inducible factor-1 α , thus inducing pseudohypoxia. In summary, proton irradiation evokes differing histone modifications in comparison with photons concomitant with metabolic adaptations that constitute putative therapeutic targets.

Chemical library screen to identify proton-specific radiosensitizers

Epigenetic and metabolic changes of cancer cells in response to external stimuli, such as therapeutic pressure, are key regulators

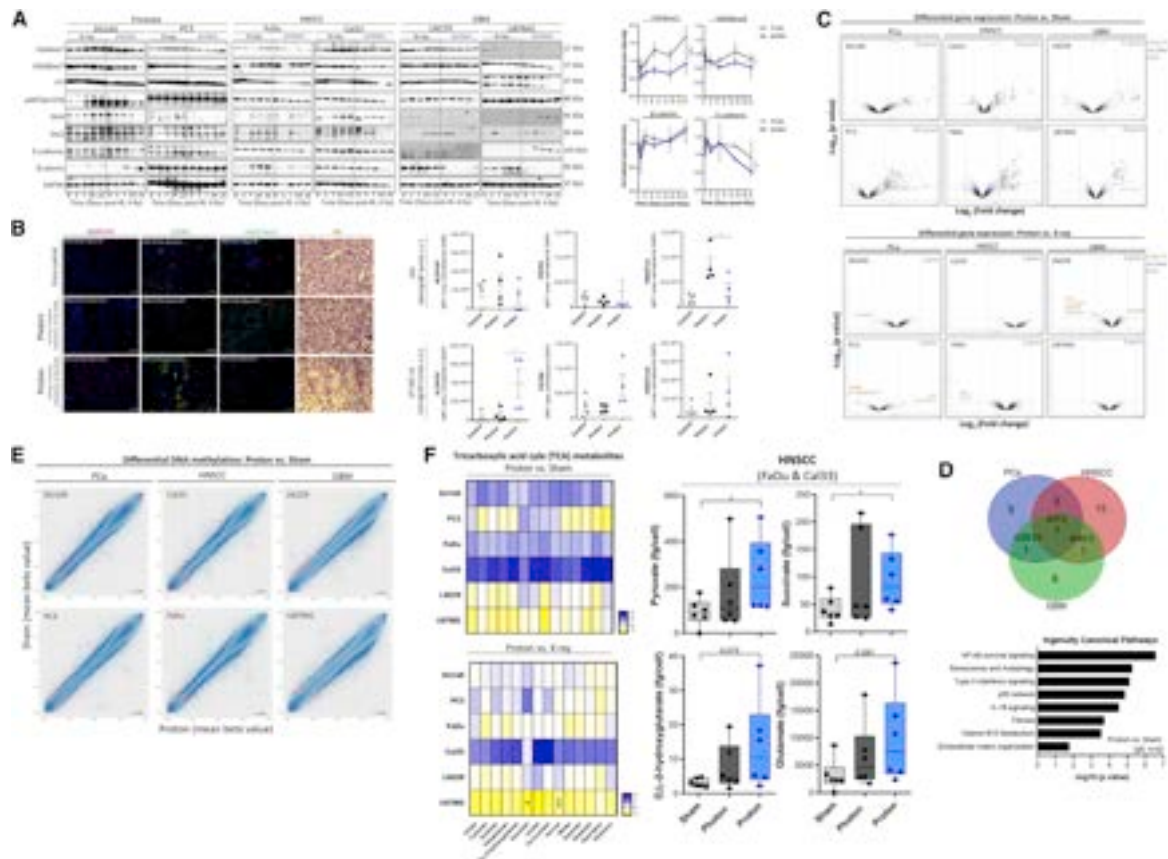


Figure 5. Characterization of molecular mechanisms driving proton irradiation-induced cellular plasticity and epigenetic modulation

(A) Western blot analysis of cell lysates from DU145, PC3, FaDu, Cal33, LN229, and U87MG cells prepared 0, 3, 7, 14, and 21 days after single-dose irradiation with 4 Gy of photons versus protons ($n = 2$). Signal intensities from western blot bands of H3K4me3, H3K36me3, β -catenin, and E-cadherin determined by ImageJ analysis combined for all cell lines and normalized to loading control illustrates dynamic changes ($n = 6$, mean \pm SEM, * $p < 0.05$, *** $p < 0.001$).

(B) Exemplary images of immunohistochemical staining for ALDH1A1, CXCR4, H3K27me3, and hematoxylin-eosin in tissue sections of subcutaneous xenograft tumors derived from HNSCC cell lines SAS and UT-SSC-14. Local fractionated irradiation was performed after tumor formation and randomization. The cohort treated with photons received a total dose of 26 Gy in 5 fractions of 5.2 Gy. Proton dose calculation included normalization to 1.1 RBE and was performed with a total dose of 24 Gy in 5 fractions of 4.8 Gy. Tumors were harvested 24 h after last fraction, fixed, and cryopreserved. Automated imaging and calculation of mean pixel intensity per area normalized to DAPI signal was performed for all markers for four tumors including two different locations ($n = 4$, * $p < 0.05$). Scale bars, 50 μ m.

(C) Volcano blots illustrating comparative transcriptome analysis 5 days after single-dose proton irradiation with 4 Gy in comparison with sham and photons ($n = 3$). Highlighted genes are differentially regulated with a fold change >2 or <-2 and $p < 0.05$.

(D) Venn diagram to illustrate overlap of differentially regulated genes within the three tumor entities revealing *ATF3*, *GDF15*, and *BIRC3* as key regulators for proton-specific response. Ingenuity pathway analysis combining all significantly differential regulated genes from all tested cell lines identified altered NF- κ B pathway, senescence, and autophagy, as well as type II interferon signaling.

(E) Differential DNA methylation analysis using Illumina EPIC Human Methylation array 5 days after irradiation illustrates only minor changes in DNA methylation levels throughout different sites shown as mean β value correlation between sham control and proton irradiation ($n = 3$, *cmp1*, *rc1*).

(F) Tricarboxylic acid cycle (TCA) metabolites were analyzed by ultra-high-performance liquid chromatography with tandem mass spectrometry in total cell extracts of DU145, PC3, FaDu, Cal33, LN229, and U87MG cells 5 days after irradiation either with photons or protons in comparison with sham control. Comparative changes in metabolite concentration per cell is illustrated as a heatmap that depicts normalized mean fold changes. Significant alterations were found in GBM and HNSCC cells ($n = 6$, median \pm min-max, * $p < 0.05$) (see also Figure S5).

for cellular plasticity, preventing therapy-induced cell death and reducing treatment success. Within a previously published study, we showed the radiosensitizing potential of the histone methyltransferase inhibitor 3-deazaneplanocin A (DZNeP) in

experimental PCa models (Gorodetska et al., 2019; Peitzsch et al., 2016). To test the potential of epigenetic targeting agents in the two GBM cell lines LN229 and U87MG, we performed a 96-well-based chemical library screening with 146 compounds in

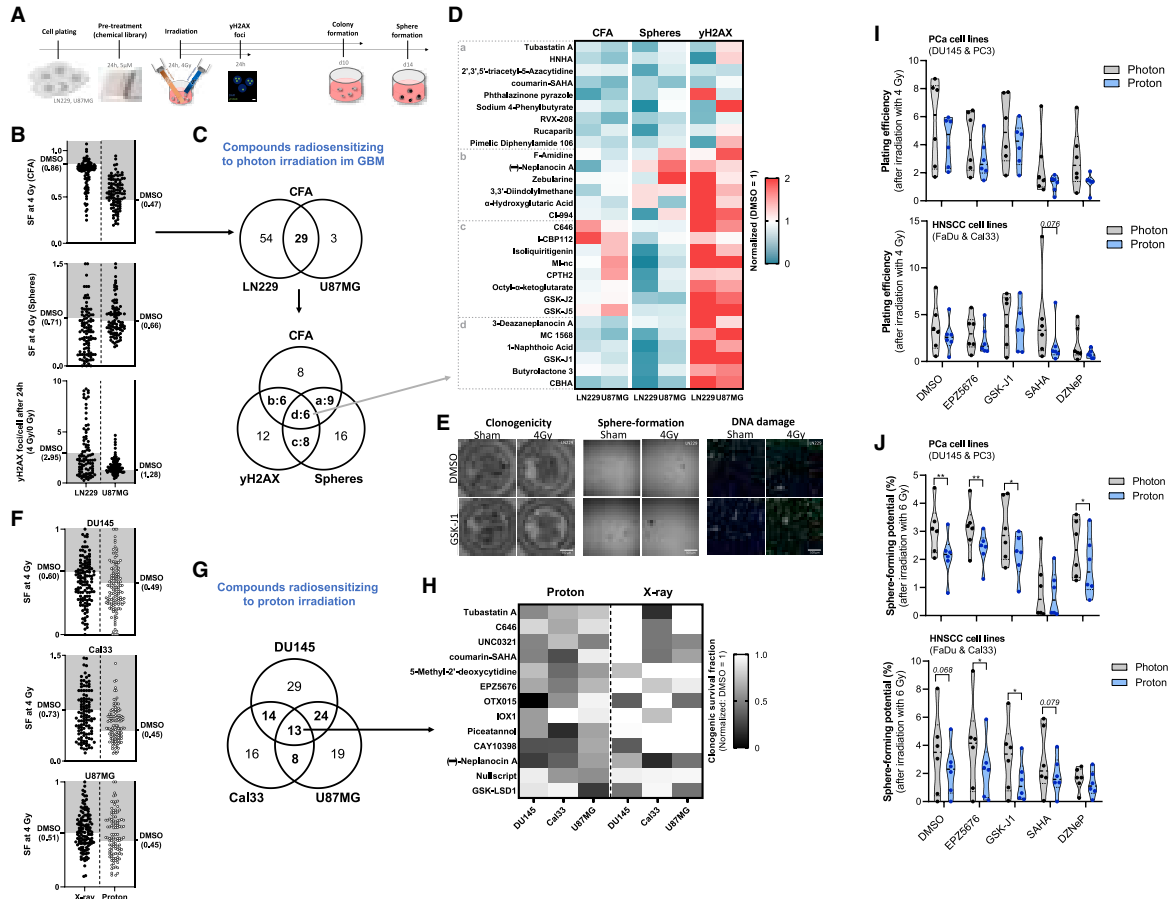


Figure 6. Chemical library screen with epigenetic targeting agents for proton-specific radiosensitization of cancer cells

(A) Schematic illustration of experimental setup including cell plating, treatment, and readout of clonogenicity, DNA repair capacity, and self-renewal potential. Cells were seeded in 96-well plates followed by 24 h of pre-treatment with 5 μ M of the Epigenetics Screening Library (Cayman Chemical, cat. no. 11076) consisting of 146 therapeutically relevant compounds and irradiated afterward either with 4 Gy photons or protons including sham control.

(B) The setup was established and tested with photon irradiation in GBM cell lines LN229 and U87MG ($n = 2$). Toxic compounds with a plating efficiency (PE) < 0.05 in the sham control of the colony-formation assay were dismissed. Each data point in the scatterplot represents one individual compound. Compounds resulting in a clonogenic/spherogenic surviving fraction or yH2AX foci count $<$ DMSO control value or $>$ DMSO control value, respectively, were regarded as radiosensitizing.

(C) Venn diagram illustrating the overlap of radiosensitizing compounds between LN229 and U87MG as well as the three different readouts.

(D) Heatmap including compounds with a radiosensitizing effect to photon irradiation in LN229 and U87MG in ≥ 2 readouts. Values are normalized to the DMSO control.

(E) Representative images showing the effect of GSK-J1 on LN229 cells in the respective readouts.

(F) The established experimental setup and calculation were applied together with 4 Gy proton versus photon irradiation in DU145, Cal33, and U87MG cells with 3D colony formation as readout ($n = 1$).

(G) Venn diagram illustrating the overlap of compounds radiosensitizing to proton irradiation between the three cell lines.

(H) Heatmap including compounds with a radiosensitizing effect to proton irradiation in all three cell lines. Values are normalized to the DMSO control.

(I) 3D colony formation assay after 24 h pre-treatment with EPZ5676 (DOT1L inhibitor), GSK-J1 (JMJD3/UTX inhibitor), SAHA (HDAC inhibitor), and DZNeP (EZH2 inhibitor) (5 μ M) before irradiation with photons or protons in PCA and HNSCC cells ($n = 6$).

(J) Sphere-forming assay after treatment with EPZ5676, GSK-J1, SAHA, and DZNeP in combination with either photons or protons. DMSO was used as solvent control ($n = 6$, * $p < 0.05$, ** $p < 0.01$) (see also Figure S6).

combination with 4 Gy single-dose photon irradiation, assessing clonogenic and spherogenic survival, as well as DNA repair (Figures 6A and 6B). In total, six compounds showed a radiosensitizing

potential in all three readouts (Figures 6C and 6D). Interestingly, we were able to validate the therapeutic potential for DZNeP for GBM cells. Other promising candidates include

Cell Reports

Article



GSK-J1, an inhibitor of the H3K27 demethylase JMJD3 (Figure 6E), and MC1568, a selective inhibitor of class IIa histone deacetylase (HDAC). To further test whether epigenetic targeting confers therapeutic benefit in combination with proton irradiation, we repeated the screening in DU145, Cal33, and U87MG cells using photon and proton irradiation, this time evaluating the clonogenic survival under 3D conditions (Figure 6F). In total, 13 compounds exhibited a radiosensitizing potential in combination with proton irradiation in all three cell lines, e.g., HDAC inhibitor Tubastatin A, histone acetyltransferase inhibitor C646, and histone methyltransferase G9a inhibitor UNC0321 (Figures 6G, 6H, S6A and S6B). Of note, we only found a minor overlap between the 2D and 3D colony-formation assay readout for U87MG cells indicating the importance to implement different biological readouts within chemical screens to identify compounds that may be clinically relevant in the future (Figure S6C). Therefore, we performed validation experiments for three identified compounds (EPZ5676, SAHA, and GSK-J1) in two PCa (DU145 and PC3) and two HNSCC cell lines (FaDu, Cal33). The cells were pre-treated for 24 h with 5 μ M inhibitor before irradiation and plated for 3D clonogenic survival and sphere formation. The EZH2 inhibitor DZNeP, which was previously found to be a radiosensitizing agent, was added as control. While we could not confirm the proton-specific radiosensitizing effect in 3D clonogenic survival (Figure 6I), all compounds reduced the sphere-forming potential significantly in combination with proton irradiation in comparison with photons (Figure 6J). These results validated the high therapeutic potential of epigenetic targeting agents for radiotherapy. However, preclinical validation *in vivo* is necessary to evaluate the clinical potential.

DISCUSSION

Tumor heterogeneity is a major driver for tumor progression, therapy relapse, and metastatic spread, and is underlined by dynamic cellular adaptations upon microenvironmental changes, therapeutic pressure, or immune cell attack (Easwaran et al., 2014; Meacham and Morrison, 2013). Increased CSC marker expression and cellular plasticity after irradiation have been described by us and others for a variety of tumor entities (Bao et al., 2006; Ghisolfi et al., 2012; Lagadec et al., 2012; Peitzsch et al., 2016). Moreover, various groups have shown that proton irradiation elicits enhanced cytotoxic effects on CSCs in comparison with conventional photons (Alan Mitteer et al., 2015; Fu et al., 2012; Narang et al., 2015; Zhang et al., 2013). In this study, we confirmed an enhanced targeting of stem-like cells with sphere-forming capacity in PCa and HNSCC cell lines, as well as in primary PCa cultures. Interestingly, we found comparable dynamics of different CSC marker, such as ALDH, CD44, CD133, and CXCR4, after proton and photon irradiation. This indicates irradiation-induced cellular plasticity as putative escape and resistance mechanisms and cannot explain the higher therapeutic efficacy of protons over photons. By contrast, Zhang et al. reported a significant decline of β -catenin expression and side population 96 h after 4 Gy proton irradiation in comparison with photons in the chemo-resistant and stem-like subpopulation of non-small cell lung cancer (NSCLC) cell line H460 (Zhang et al., 2013). Narang et al. described a lower ALDH activity and CD44 expression in NSCLC cell line A549 48 h after

2 Gy proton compared with photon irradiation (Narang et al., 2015). However, these reports did not investigate dynamic changes of CSCs over time and differed in the analyzed tumor entity. The intensive time-course analysis within our experimental dataset allowed mathematical modeling that indicates a reduced rate of plasticity events after proton irradiation compared with photons as a putative factor influencing cellular radiosensitivity. This mechanism might even have the potential to explain radioresponse rates within complex tumors and, at least partially, the enhanced therapeutic potential of proton over photon irradiation, which is reflected in the use of an RBE value of 1.1 in the clinical setup.

Surprisingly, the purified ALDH⁺ population did not show higher responsiveness to proton irradiation. The identification of putative resistance mechanisms was realized by comparative gene expression analysis in spheres and monolayer cultures, which revealed differently expressed ALDH isoforms as well as an activation of motility and ECM interaction in the ALDH⁺ population while sphere cultures were characterized by altered cholesterol homeostasis and TNF/NF- κ B signaling, which may explain the observed differences. The observed CSC marker dynamics were concomitant with an upregulation of Wnt signaling protein β -catenin. Interestingly, this was accompanied by significantly lower expression levels of epithelial marker E-cadherin as well as reduced methylation of the activating histone mark H3K4 and H3K36 after proton irradiation in comparison with photons. On the contrary, other groups found lower levels of EMT markers, vimentin and fibronectin, as well as a reduced migration and invasiveness after proton irradiation compared with photons (Narang et al., 2015; Ogata et al., 2005; Zhang et al., 2013). Data concerning epigenetic regulation following proton irradiation are scarce. We found one study reporting a non-significant trend toward decreased H3K14 acetylation and increased H3K9, H3K36, and H3K79 trimethylation 4 h after irradiation with high linear energy transfer (LET) protons (Carter et al., 2018). Together, these findings point toward epigenetic differences in the otherwise similar regulation of putative CSC and epithelial markers between both irradiation types. In addition, Carter et al. (2018) investigated post-translational histone modifications and involvement of histone H2B ubiquitylated on lysine 120 in complex DNA damage upon protons. The obtained results indicated that, besides stemness, the repair of proton-induced complex DNA DSBs is a key determinant of intracellular sensitivity. We also observed a higher amount of residual γ H2AX foci indicative of unrepaired DNA DSBs after proton irradiation in comparison with photons, which supports the notion that proton irradiation results in more complex DNA damages, especially at regions with a higher LET (Carter et al., 2018; Cuaron et al., 2016; Fu et al., 2012; Hojo et al., 2017; Oeck et al., 2018; Sertorio et al., 2020; Vitti and Parsons, 2019). Besides direct DNA damages, high intracellular ROS levels contribute to indirect DNA damages and other cytotoxic effects. ROS levels have been described to be higher after proton than photon irradiation in lymphoma cell lines (Sertorio et al., 2020) as well as in stem-like populations of GBM and NSCLC (Alan Mitteer et al., 2015; Zhang et al., 2013). On the contrary, we found reduced ROS production in GBM cells and decreased GSH levels in PCa cells after proton irradiation in comparison with photons. In addition, no



differences in proliferation, apoptosis, and autophagy rates were seen, but with a rather reduced senescence induction after proton versus photon irradiation. As senescence and autophagy represent putative escape mechanisms from irradiation-induced cell death, these findings provide a possible explanation for the lower number of plasticity events following proton irradiation.

As cellular plasticity is a major factor influencing escape from proton-induced cell death and is epigenetically regulated, we performed transcriptome, DNA methylome, and TCA metabolome analysis 5 days after proton irradiation. We found alterations in NF- κ B signaling, senescence, and autophagy as well as interferon response determined by the key regulatory genes *ATF3*, *GDF15*, and *BIRC3*. Other groups reported an altered gene expression 4 to 12 h after proton irradiation with upregulated DNA repair, unfolded protein response and cell-cycle arrest (Ha et al., 2015; Narang et al., 2015; Sertorio et al., 2020). Similar findings were reported on the phospho-proteome level in 3D pancreatic tumoroid cultures, which displayed alterations in core components of the DNA repair system, such as ataxia telangiectasia mutated and checkpoint kinase 1/2 (Chk1/2) after proton irradiation (Görte et al., 2020). Efficient DNA repair, as well as cellular plasticity, is regulated on the level of epigenetic remodelers that influence chromatin packaging. Therefore, we hypothesized that epigenetic targeting in combination with proton irradiation may prevent DNA repair as well as cellular plasticity and may effectively sensitize cancer cells, in particular resistant CSCs. An epigenetic targeting screen identified several compounds with a radiosensitizing effect in all tested cell lines. These data demonstrate a high therapeutic potential of epigenetic targeting agents in combination with proton irradiation *in vitro*. However, further studies are needed to determine timing and dosing schedules and confirm a putative clinical potential *in vivo*. All in all, the discovered proton-specific mechanisms, such as increased complex DNA damages, lower cellular plasticity rates, and reduced senescence may represent putative prognostic and therapeutic targets for proton radiotherapy of cancer patients in the future. However, radiobiological data for fractionated proton irradiation are urgently needed before clinical translation.

Limitations of the study

A limitation of our study is a high data variability due to a limited availability of the proton beam facility for radiobiological experiments leading to time intervals of 3–4 months between biological repeats. The data interpretation was additionally complicated by the experimental setup consisting of six cancer cell lines belonging to three different tumor entities with distinct biological features, genetic background, and cellular response to ionizing radiation. Future studies are needed to validate our radiobiological findings within clinical datasets. Currently, there are no publicly available datasets reporting comparative gene expression data for cancer patients treated with proton radiotherapy.

STAR★METHODS

Detailed methods are provided in the online version of this paper and include the following:

- KEY RESOURCES TABLE

- RESOURCE AVAILABILITY
 - Lead contact
 - Material availability
 - Data and code availability
- EXPERIMENTAL MODEL AND SUBJECT DETAILS
 - Cell lines and culture conditions
 - Subcutaneous xenograft tumor model and tumor irradiation
 - Primary prostate cultures
- METHOD DETAILS
 - Cell irradiation
 - Colony formation assay
 - Treatment with epigenetic compounds and CSC-targeting agents
 - Sphere formation assay
 - Flow cytometry analysis and fluorescence-activated cell sorting (FACS)
 - Mass spectrometry-based analysis of Krebs cycle metabolites
 - Differential gene expression analysis
 - Genome-wide DNA methylation analysis
 - Western blot analysis
 - Determination of glutathione, reactive oxygen species, and mitochondrial membrane potential
 - Cell proliferation
 - Immunofluorescence staining
 - Cell death analysis
 - Mathematical modeling of cancer cell plasticity upon irradiation
- QUANTIFICATION AND STATISTICAL ANALYSIS

SUPPLEMENTAL INFORMATION

Supplemental information can be found online at <https://doi.org/10.1016/j.celrep.2022.110422>.

ACKNOWLEDGMENTS

The authors thank Dorothee Pfitzmann, Andrea Petzold, Liane Stolz-Kieslich, Daniela Pollack, and Vasyli Lukiyanichuk for their technical support. In particular, we would like to thank members of the H⁺-team: Antje Dietrich, Theresa Suckert, and Elisabeth Bodenstern for their tremendous help to perform the cell irradiation within the experimental room of UPTD; Rebecca Bütof for providing xenograft tumor material and student supervision (J.M.); Michael Baumann and Daniel Smith for critical discussion and proofreading of the manuscript. The staff of the Flow Cytometry Core Facility (Katja Bernhard and Anne Gompf) at the Center for Regenerative Therapies (CRTD), TU Dresden (Germany) performed the cell sorting. The staff of the Genomics and Proteomics Core Facility (GPCF) at the German Cancer Research Center (DKFZ) in Heidelberg (Germany) who performed the global gene expression and DNA methylation analysis. The authors received following academic funding to perform this study: the MeDDrive Grant of the Medical Faculty Carl Gustav Carus, DresdenTechnischen Universität Dresden in 2018 (C.P.), the DTK Dresden internal funding in 2019 (C.P. and M.K.), the Gesellschaft von Freunden und Förderern e.V. der Technische Universität Dresden, 2019 (I.S.) and the ESF (PWR.03.03.00-00-1028/17-00) (J.G.). The University Proton Therapy Dresden (UPTD) is part of a project that has received funding from the European Union's Horizon 2020 Research and Innovation Programme (grant agreement no: 730983) (INSPIRE).

AUTHOR CONTRIBUTIONS

Conceptualization, C.P.; methodology, I.S., S.R., J.M., J.G., W.W.H., M.P., E.B., A.L., and C.P.; validation and formal analysis, I.S., W.W.H., S.R., M.P., J.G., J.P., D.K., S.L., C.G., U.S., S.F., and C.P.; investigation, I.S., D.K., J.G., and C.P.; writing – original draft preparation, I.S. and C.P.; writing – review & editing, I.S., M.K., C.v.N., I.K., J.P., A.L., and A.D.; supervision, C.P., A.D., and C.v.N.; project administration, C.P.; funding acquisition, C.P. All authors have read and agreed to the published version of the manuscript.

DECLARATION OF INTERESTS

In the past 5 years, M.K. received funding for her research projects by IBA (2016), Merck KGaA (2014–2018 for preclinical study; 2018–2020 for clinical study), and Medipan GmbH (2014–2018). M.K. is involved in an ongoing publicly funded (German Federal Ministry of Education and Research) project with the companies Medipan, Attomol GmbH, GA Generic Assays GmbH, Gesellschaft für medizinische und wissenschaftliche genetische Analysen, Lipotype GmbH, and PolyAn GmbH (2019–2021). For this study, M.K. confirms that none of the above-mentioned funding sources were involved. The other authors declare no competing interests.

Received: June 23, 2021

Revised: November 24, 2021

Accepted: February 1, 2022

Published: February 22, 2022

SUPPORTING CITATIONS

The following references appear in the supplemental information: Abbaspour et al., 2017; Cowley et al., 2014; Hu et al., 2017; Jiang et al., 2018; Kim et al., 2008; Liu et al., 2018; Lubanska et al., 2014; Portz et al., 2012; Shao et al., 2019; Stone et al., 1978; Wang et al., 2015; Yen et al., 2016.

REFERENCES

- Abbaspour, B.M., Zaman, H.H., Kamalidehghan, B., Yeap, S.K., and Ahmadi-pour, F. (2017). Apoptotic induction and inhibition of NF- κ B signaling pathway in human prostatic cancer PC3 cells by natural compound 2,2'-oxybis (4-allyl-1-methoxybenzene), biseugenol B, from *Litsea costalis*: an in vitro study. *Oncotargets Ther.* *10*, 277–294.
- Alan Mitteer, R., Wang, Y., Shah, J., Gordon, S., Fager, M., Butter, P.-P., Jun Kim, H., Guardiola-Salmeron, C., Carabe-Fernandez, A., and Fan, Y. (2015). Proton beam radiation induces DNA damage and cell apoptosis in glioma stem cells through reactive oxygen species. *Scientific Rep.* *5*, 13961.
- Allen, M., Bjerke, M., Edlund, H., Nelander, S., and Westermark, B. (2016). Origin of the U87MG glioma cell line: good news and bad news. *Sci. Transl. Med.* *8*, 354re3.
- Bao, S., Wu, Q., McLendon, R.E., Hao, Y., Shi, Q., Hjelmeland, A.B., Dewhirst, M.W., Bigner, D.D., and Rich, J.N. (2006). Glioma stem cells promote radioresistance by preferential activation of the DNA damage response. *Nature* *444*, 756–760.
- Beyreuther, E., Baumann, M., Enghardt, W., Helmbrecht, S., Karsch, L., Krause, M., Pawelke, J., Schreiner, L., Schürer, M., von Neubeck, C., et al. (2018). Research facility for radiobiological studies at the university proton therapy dresden. *Int. J. Part Ther.* *5*, 172–182.
- Carter, R.J., Nickson, C.M., Thompson, J.M., Kacperek, A., Hill, M.A., and Parsons, J.L. (2018). Complex DNA damage induced by high linear energy transfer alpha-particles and protons triggers a specific cellular DNA damage response. *Int. J. Radiat. Oncol. Biol. Phys.* *100*, 776–784.
- Clay, M.R., Tabor, M., Owen, J.H., Carey, T.E., Bradford, C.R., Wolf, G.T., Wicha, M.S., and Prince, M.E. (2010). Single-marker identification of head and neck squamous cell carcinoma cancer stem cells with aldehyde dehydrogenase. *Head Neck* *32*, 1195–1201.
- Cojoc, M., Peitzsch, C., Kurth, I., Trautmann, F., Kunz-Schughart, L.A., Telegueev, G.D., Stakhovsky, E.A., Walker, J.R., Simin, K., Lyle, S., et al. (2015). Aldehyde dehydrogenase is regulated by β -catenin/TCF and promotes radioresistance in prostate cancer progenitor cells. *Cancer Res.* *75*, 1482–1494.
- Collins, A.T., Berry, P.A., Hyde, C., Stower, M.J., and Maitland, N.J. (2005). Prospective identification of tumorigenic prostate cancer stem cells. *Cancer Res.* *65*, 10946–10951.
- Cowley, G., Weir, B., Vazquez, F., et al. (2014). Parallel genome-scale loss of function screens in 216 cancer cell lines for the identification of context-specific genetic dependencies. *Sci. Data* *1*, 140035.
- Cuaron, J.J., Chang, C., Lovelock, M., Higginson, D.S., Mah, D., Cahlon, O., and Powell, S. (2016). Exponential increase in relative biological effectiveness along distal edge of a proton Bragg peak as measured by deoxyribonucleic acid double-strand breaks. *Int. J. Radiat. Oncol. Biol. Phys.* *95*, 62–69.
- Dirkse, A., Golebiewska, A., Buder, T., Nazarov, P.V., Muller, A., Poovathingal, S., Brons, N.H.C., Leite, S., Sauvageot, N., Sarkisjan, D., et al. (2019). Stem cell-associated heterogeneity in Glioblastoma results from intrinsic tumor plasticity shaped by the microenvironment. *Nat. Commun.* *10*, 1787.
- Drost, J., Karthaus, W.R., Gao, D., Driehuis, E., Sawyers, C.L., Chen, Y., and Clevers, H. (2016). Organoid culture systems for prostate epithelial and cancer tissue. *Nat. Protoc.* *11*, 347–358.
- Dubrovskaya, A., Elliott, J., Salamone, R.J., Telegueev, G.D., Stakhovsky, A.E., Schepotin, I.B., Yan, F., Wang, Y., Bouchez, L.C., Kularatne, S.A., et al. (2012). CXCR4 expression in prostate cancer progenitor cells. *PLoS one* *7*, e31226.
- Easwaran, H., Tsai, H.-C., and Baylin, S.B. (2014). Cancer epigenetics: tumor heterogeneity, plasticity of stem-like states, and drug resistance. *Mol. Cell* *54*, 716–727.
- Flahaut, M., Jauquier, N., Chevalier, N., Nardou, K., Balmes Bourlout, K., Joseph, J.-M., Barras, D., Widmann, C., Gross, N., Renella, R., et al. (2016). Aldehyde dehydrogenase activity plays a key role in the aggressive phenotype of neuroblastoma. *BMC Cancer* *16*, 781.
- Frame, F.M., Pellacani, D., Collins, A.T., and Maitland, N.J. (2016). Harvesting human prostate tissue material and culturing primary prostate epithelial cells. *Methods Mol. Biol.* *1443*, 181–201.
- Fu, Q., Quan, Y., Wang, W., Mei, T., Wu, J., Li, J., Yang, G., Ren, X., Xue, J., and Wang, Y. (2012). Response of cancer stem-like cells and non-stem cancer cells to proton and γ -ray irradiation. *Nucl. Instr. Methods Phys. Res. Section B: Beam Interactions Mater. Atoms* *286*, 346–350.
- Ghisolfi, L., Keates, A.C., Hu, X., Lee, D., and Li, C.J. (2012). Ionizing radiation induces stemness in cancer cells. *PLoS One* *7*, e43628.
- Gorodetska, I., Lukiyanchuk, V., Peitzsch, C., Kozaretska, I., and Dubrovskaya, A. (2019). BRCA1 and EZH2 cooperate in regulation of prostate cancer stem cell phenotype. *Int. J. Cancer* *145*, 2974–2985.
- Görte, J., Beyreuther, E., Danen, E.H.J., and Cordes, N. (2020). Comparative proton and photon irradiation combined with pharmacological inhibitors in 3D pancreatic cancer cultures. *Cancers* *12*, 3216.
- Ha, B.G., Park, J.-E., Cho, H.-J., Lim, Y.-B., and Shon, Y.H. (2015). Inhibitory effects of proton beam irradiation on integrin expression and signaling pathway in human colon carcinoma HT29 cells. *Int. J. Oncol.* *46*, 2621–2628.
- Helmbrecht, S., Baumann, M., Enghardt, W., Fiedler, F., Krause, M., and Lühr, A. (2016). Design and implementation of a robust and cost-effective double-scattering system at a horizontal proton beamline. *J. Inst.* *11*, T11001.
- Hojo, H., Dohmae, T., Hotta, K., Kohno, R., Motegi, A., Yagishita, A., Maki-noshima, H., Tsuchihara, K., and Akimoto, T. (2017). Difference in the relative biological effectiveness and DNA damage repair processes in response to proton beam therapy according to the positions of the spread out Bragg peak. *Radiat. Oncol.* *12*, 111.
- Hu, W.Y., Hu, D.P., Xie, L., Li, Y., Majumdar, S., Nonn, L., Hu, H., Shioda, T., and Prins, G.S. (2017). Isolation and functional interrogation of adult human prostate epithelial stem cells at single cell resolution. *Stem Cell Res.* *23*, 1–12.
- Jiang, Y., Miao, J., Wang, D., Zhou, J., Liu, B., Jiao, F., Liang, J., Wang, Y., Fan, C., and Zhang, Q. (2018). MAP30 promotes apoptosis of U251 and U87 cells



- by sup-pressing the LGR5 and Wnt/ β -catenin signaling pathway, and enhancing Smac expression. *Oncol. Lett.* **15**, 5833–5840.
- Kim, M., Wu, X., Song, I., Fu, M., Chang, S.H., Lisanti, M.P., and Pestell, R. (2008). Selective cytotoxicity of synthesized procyanidin 3-O-galloylprocatechin-4b, 8-3-O-galloylprocatechin to human cancer cells. *Cell Cycle* **7**, 1648–1657.
- Kreso, A., and Dick, J.E. (2014). Evolution of the cancer stem cell model. *Cell Stem Cell* **14**, 275–291.
- Kurth, I., Hein, L., Mäbert, K., Peitzsch, C., Koi, L., Cojoc, M., Kunz-Schughart, L., Baumann, M., and Dubrovskaya, A. (2015). Cancer stem cell related markers of radioresistance in head and neck squamous cell carcinoma. *Oncotarget* **6**, 34494–34509.
- Lagadec, C., Vlashi, E., Donna, L.D., Dekmezian, C., and Pajonk, F. (2012). Radiation-induced reprogramming of breast cancer cells. *Stem Cells* **30**, 833–844.
- Li, T., Su, Y., Mei, Y., Leng, Q., Leng, B., Liu, Z., Stass, S.A., and Jiang, F. (2010). ALDH1A1 is a marker for malignant prostate stem cells and predictor of prostate cancer patients' outcome. *Lab Invest.* **90**, 234–244.
- Liu, C.C., Lin, W.W., Wu, C.C., Hsu, S.L., Wang, C.Y., Chung, J.G., and Chiang, C.S. (2018). Lauryl gallate induces apoptotic cell death through caspase-dependent pathway in U87 human glioblastoma cells in vitro. *In Vivo* **32**, 1119–1127.
- Lubanska, D., Market-Velker, B.A., deCarvalho, A.C., Mikkelsen, T., Fidalgo da, S.E., and Porter, L.A. (2014). The cyclin-like protein Spy1 regulates growth and division characteristics of the CD133+ population in human glioma. *Cancer Cell* **13**, 64–76.
- Martínez-Reyes, I., and Chandel, N.S. (2020). Mitochondrial TCA cycle metabolites control physiology and disease. *Nat. Commun.* **11**, 102.
- Meacham, C.E., and Morrison, S.J. (2013). Tumor heterogeneity and cancer cell plasticity. *Nature* **501**, 328–337.
- Mukha, A., Kahya, U., Linge, A., Chen, O., Löck, S., Lukiyanchuk, V., Richter, S., Alves, T.C., Peitzsch, M., Telychko, V., et al. (2021). GLS-driven glutamine catabolism contributes to prostate cancer radiosensitivity by regulating the redox state, stemness and ATG5-mediated autophagy. *BioRxiv*. <https://doi.org/10.7150/thno.58655>.
- Müller, F., Scherer, M., Assenov, Y., Lutsik, P., Walter, J., Lengauer, T., and Bock, C. (2019). RnBeads 2.0: comprehensive analysis of DNA methylation data. *Genome Biol.* **20**, 55.
- Narang, H., Kumar, A., Bhat, N., Pandey, B.N., and Ghosh, A. (2015). Effect of proton and gamma irradiation on human lung carcinoma cells: gene expression, cell cycle, cell death, epithelial-mesenchymal transition and cancer-stem cell trait as biological end points. *Mutat. Res.* **780**, 35–46.
- Oeck, S., Szymonowicz, K., Wiel, G., Krysztofiak, A., Lambert, J., Koska, B., Iliakis, G., Timmermann, B., and Jendrossek, V. (2018). Relating linear energy transfer to the formation and resolution of DNA repair foci after irradiation with equal doses of X-ray photons, plateau, or bragg-peak protons. *Int. J. Mol. Sci.* **19**, 3779.
- Ogata, T., Teshima, T., Kagawa, K., Hishikawa, Y., Takahashi, Y., Kawaguchi, A., Suzumoto, Y., Nojima, K., Furusawa, Y., and Matsuura, N. (2005). Particle irradiation suppresses metastatic potential of cancer cells. *Cancer Res.* **65**, 113–120.
- Oshlack, A., Emslie, D., Corcoran, L.M., and Smyth, G.K. (2007). Normalization of boutique two-color microarrays with a high proportion of differentially expressed probes. *Genome Biol.* **8**, R2.
- Patrawala, L., Calhoun, T., Schneider-Broussard, R., Li, H., Bhatia, B., Tang, S., Reilly, J.G., Chandra, D., Zhou, J., Claypool, K., et al. (2006). Highly purified CD44+ prostate cancer cells from xenograft human tumors are enriched in tumorigenic and metastatic progenitor cells. *Oncogene* **25**, 1696–1708.
- Peitzsch, C., Cojoc, M., Hein, L., Kurth, I., Mäbert, K., Trautmann, F., Klink, B., Schröck, E., Wirth, M.P., Krause, M., et al. (2016). An epigenetic reprogramming strategy to resensitize radioresistant prostate cancer cells. *Cancer Res.* **76**, 2637–2651.
- Peitzsch, C., Kurth, I., Ebert, N., Dubrovskaya, A., and Baumann, M. (2019). Cancer stem cells in radiation response: current views and future perspectives in radiation oncology. *Int. J. Radiat. Biol.* **95**, 900–911.
- Phillips, T.M., McBride, W.H., and Pajonk, F. (2006). The response of CD24-/low/CD44+ breast cancer-initiating cells to radiation. *J. Natl. Cancer Inst.* **98**, 1777–1785.
- Pidsley, R., Wong, C.C., Volta, M., Lunnon, K., Mill, J., and Schalkwyk, L.C. (2013). A data-driven approach to preprocessing Illumina 450K methylation array data. *BMC Genomics* **14**, 293.
- Pietras, A., Katz, A.M., Ekström, E.J., Wee, B., Halliday, J.J., Pitter, K.L., Werbeck, J.L., Amankulor, N.M., Huse, J.T., and Holland, E.C. (2014). Osteopontin-CD44 signaling in the glioma perivascular niche enhances cancer stem cell phenotypes and promotes aggressive tumor growth. *Cell Stem Cell* **14**, 357–369.
- Poleszczuk, J., and Enderling, H. (2016). Cancer stem cell plasticity as tumor growth promoter and catalyst of population collapse. *Stem Cells Int.* **2016**, 3923527.
- Poleszczuk, J., Hahnfeldt, P., and Enderling, H. (2015). Evolution and phenotypic selection of cancer stem cells. *PLoS Comput. Biol.* **11**, e1004025.
- Poleszczuk, J., Walker, R., Moros, E., Latifi, K., Caudell, J., and Enderling, H. (2018). Predicting patient-specific radiotherapy protocols based on mathematical model choice for proliferation saturation index. *Bull. Math. Biol.* **80**, 1195–1206.
- Portz, T., Kuang, Y., and Nagy, J.D. (2012). A clinical data validated mathematical model of prostate cancer growth under intermittent androgen suppression therapy. *AIP Adv.* **2**, 011002.
- Prince, M.E., Sivanandan, R., Kaczorowski, A., Wolf, G.T., Kaplan, M.J., Dalerba, P., Weissman, I.L., Clarke, M.F., and Ailles, L.E. (2007). Identification of a subpopulation of cells with cancer stem cell properties in head and neck squamous cell carcinoma. *PNAS* **104**, 973–978.
- Reya, T., Morrison, S.J., Clarke, M.F., and Weissman, I.L. (2001). Stem cells, cancer, and cancer stem cells. *Nature* **414**, 105–111.
- Richter, S., Gieldon, L., Pang, Y., Peitzsch, M., Huynh, T., Leton, R., Viana, B., Ercolino, T., Mangelis, A., Rapizzi, E., et al. (2019). Metabolome-guided genomics to identify pathogenic variants in isocitrate dehydrogenase, fumarate hydratase, and succinate dehydrogenase genes in pheochromocytoma and paraganglioma. *Genet. Med.* **21**, 705–717.
- Ritchie, M.E., Phipson, B., Wu, D., Hu, Y., Law, C.W., Shi, W., and Smyth, G.K. (2015). Limma powers differential expression analyses for RNA-sequencing and microarray studies. *Nucleic Acids Res.* **43**, e47.
- Schulz, A., Meyer, F., Dubrovskaya, A., and Borgmann, K. (2019). Cancer stem cells and radioresistance: DNA repair and beyond. *Cancers (Basel)* **11**, 862.
- Sertorio, M., Nowrouzi, A., Akbarpour, M., Chetal, K., Salomonis, N., Brons, S., Mascia, A., Ionascu, D., McCauley, S., Kupneski, T., et al. (2020). Differential transcriptome response to proton versus X-ray radiation reveals novel candidate targets for combinatorial PT therapy in lymphoma. *Radiother. Oncol.* **155**, 293–303.
- Shao, N., Mao, J., Xue, L., Wang, R., Zhi, F., and Lan, Q. (2019). Carnosic acid potentiates the anticancer effect of temozolomide by inducing apoptosis and autophagy in glioma. *J. Neurooncol.* **141**, 277–288.
- Shi, W., Oshlack, A., and Smyth, G.K. (2010). Optimizing the noise versus bias trade-off for Illumina whole genome expression BeadChips. *Nucleic Acids Res.* **38**, e204.
- Singh, S.K., Hawkins, C., Clarke, I.D., Squire, J.A., Bayani, J., Hide, T., Henkelman, R.M., Cusimano, M.D., and Dirks, P.B. (2004). Identification of human brain tumour initiating cells. *Nature* **432**, 396.
- Smyth, G.K. (2004). Linear models and empirical bayes methods for assessing differential expression in microarray experiments. *Stat. Appl. Genet. Mol. Biol.* **3**, Article3.
- Stone, K.R., Mickey, D.D., Wunderli, H., Mickey, G.H., and Paulson, D.F. (1978). Isolation of a human prostate carcinoma cell line (DU 145). *Int. J. Cancer* **21**, 274–281.
- Suckert, T., Rassamegevanon, T., Müller, J., Dietrich, A., Graja, A., Reiche, M., Löck, S., Krause, M., Beyreuther, E., and von Neubeck, C. (2020). Applying tissue slice culture in cancer research—insights from preclinical proton radiotherapy. *Cancers* **12**, 1589.

Cell Reports Article



- Tanner, R.L., Baily, N.A., and Hilbert, J.W. (1967). High-energy proton depth-dose patterns. *Radiat. Res.* **32**, 861–874.
- Tsao, T., Beretov, J., Ni, J., Bai, X., Bucci, J., Graham, P., and Li, Y. (2019). Cancer stem cells in prostate cancer radioresistance. *Cancer Lett.* **465**, 94–104.
- Tseng, Y.D., Cutter, D.J., Plastaras, J.P., Parikh, R.R., Cahlon, O., Chuong, M.D., Dedeckova, K., Khan, M.K., Lin, S.-Y., McGee, L.A., et al. (2017). Evidence-based review on the use of proton therapy in lymphoma from the particle therapy cooperative group (PTCOG) lymphoma subcommittee. *Int. J. Radiat. Oncol. Biol. Phys.* **99**, 825–842.
- Vitti, E.T., and Parsons, J.L. (2019). The radiobiological effects of proton beam therapy: impact on DNA damage and repair. *Cancers (Basel)* **11**, 946.
- Wang, Z., Guo, H.Y., and Huang, Y.L. (2015). Escopoletin treatment induces apoptosis and arrests cell cycle at G0/G1 phase in the oral squamous cancer cell lines. *Int. J. Clin. Exp. Med.* **8**, 11496–11501.
- Weber, D.C., Habrand, J.L., Hoppe, B.S., Hill Kayser, C., Laack, N.N., Langendijk, J.A., MacDonald, S.M., McGovern, S.L., Pater, L., Perentesis, J.P., et al. (2018). Proton therapy for pediatric malignancies: fact, figures and costs. A joint consensus statement from the pediatric subcommittee of PTCOG, PROS and EPTN. *Radiother. Oncol.* **128**, 44–55.
- Wilson, R.R. (1946). Radiological use of fast protons. *Radiology* **47**, 487–491.
- Wong, C.C., Qian, Y., and Yu, J. (2017). Interplay between epigenetics and metabolism in oncogenesis: mechanisms and therapeutic approaches. *Oncogene* **36**, 3359–3374.
- Yen, C.S., Chen, J.C., Chang, Y.F., Hsu, Y.F., Chiu, P.T., Shiu, C., Chuang, Y.F., Ou, G., and Hsu, M.J. (2016). Lovastatin causes FaDu hypopharyngeal carcinoma cell death via AMPK-p63-survivin signaling cascade. *Sci. Rep.* **6**, 25082.
- Zhang, D., Lin, K., Lu, Y., Rycaj, K., Zhong, Y., Chao, H., Calhoun-Davis, T., Shen, J., and Tang, D.G. (2017). Developing a novel two-dimensional culture system to enrich human prostate luminal progenitors that can function as a cell of origin for prostate cancer. *Stem Cells Transl. Med.* **6**, 748–760.
- Zhang, Q., Shi, S., Yen, Y., Brown, J., Ta, J.Q., and Le, A.D. (2010). A subpopulation of CD133+ cancer stem-like cells characterized in human oral squamous cell carcinoma confer resistance to chemotherapy. *Cancer Lett.* **289**, 151–160.
- Zhang, X., Lin, S.H., Fang, B., Gillin, M., Mohan, R., and Chang, J.Y. (2013). Therapy resistant cancer stem cells have differing sensitivity to photon versus proton beam radiation. *J. Thorac. Oncol.* **8**, 1484–1491.

STAR★METHODS

KEY RESOURCES TABLE

REAGENT or RESOURCE	SOURCE	IDENTIFIER
Antibodies		
ALDH1A1	Santa Cruz	sc-374076, RRID:AB_10916407
CXCR4	Abcam	ab124824, RRID:AB_10975635
Tri-Methyl-Histone H3 (Lys27)	Cell Signaling	#9733, RRID:AB_2616029
CD133/2	Miltenyi Biotec	clone 293C3, RRID:AB_244344
CXCR4	eBioscience	clone 12G5, RRID:AB_1659706
CD44	Miltenyi Biotec	clone DB105, RRID:AB_2726385
β -catenin	Cell Signaling Technology	#8480, RRID:AB_11127855
Histone H3	Cell Signaling Technology	#4499, RRID:AB_10544537
E-cadherin	Cell Signaling Technology	#3195, RRID:AB_2291471
Oct-4	Cell Signaling Technology	#2750, RRID:AB_823583
Tri-methyl-histone H3 (Lys36)	Cell Signaling Technology	#4909, RRID:AB_1950412
Phospho-AKT (Ser473)	Cell Signaling Technology	#4060, RRID:AB_2315049
Tri-methyl-histone H3 (Lys4)	Cell Signaling Technology	#9751, RRID:AB_2616028
GAPDH	Santa Cruz Biotechnology	sc-25778, RRID:AB_10167668
Phospho-H2AX	Merck Millipore	clone JBW301, RRID:AB_309864
53BP1	Cell Signaling Technology	#4937, RRID:AB_10694558
Biological samples		
Primary prostate cultures	Peitzsch et al. (2016); Mukha et al. (2021)	EK152052013
Chemicals, peptides, and recombinant proteins		
WIT medium	Stemgent	#00-0045-500
Dulbecco's Modified Eagle Medium	Sigma-Aldrich	D5648
Roswell Park Memorial Institute (RPMI) 1640 Medium	Sigma-Aldrich	R0883
Minimum Essential Medium with Earle's salts	Sigma-Aldrich	M4655
Fetal bovine serum	PAA Laboratories	N/A
Mammary epithelial cell basal medium	Lonza	#: CC-3151
Epidermal growth factor (EGF)	Peptotech	AF-100-15
Fibroblast growth factor (FGF)	Peptotech	100-18B
Critical commercial assays		
Epigenetics Screening Library	Cayman Chemical	#11076
p160ROCK inhibitor Y-27632 dihydrochloride	Selleckchem	S1049
Monochlorobimane	Life Technologies	M1381MP
5-(and-6)-carboxy-20,70-dichlorodihydro fluorescein diacetate acetyl ester (CM-H2DCFDA)	Invitrogen Molecular Probes	C6827
Deposited data		
Agilent-072363 SurePrint G3 Human GE v3 8x60K Microarray 039494 (Agilent product no: G4851C)	Microarray Unit at Genomics and Proteomics Core Facility (GPCF, DKFZ, Heidelberg, Germany)	GEO Submission (GSE192817) [NCBI tracking system #22614078]
EPIC array (v1_b4, Illumina)	Microarray Unit at Genomics and Proteomics Core Facility (GPCF, DKFZ, Heidelberg, Germany)	GEO Submission (GSE192899) [NCBI tracking system #22615751]
Experimental models: Cell lines		
DU145	ATCC	HTB-81
PC3	ATCC	CRL-1435

(Continued on next page)

Continued

REAGENT or RESOURCE	SOURCE	IDENTIFIER
LNCaP	ATCC	CRL-1740
FaDu	DSMZ	ACC 784
Cal33	DSMZ	ACC 447
SAS	JCRB	JCRB0260
UT-SCC-14	JCRB	CVCL_7810
LN229	ATCC	CRL-2611
U87MG	ATCC	HTB-14
HaCaT	CLS	300493
RWPE-1	ATCC	CRL-11609
Radioresistant sublines (RR)	Cojoc et al. (2015) ; Kurth et al. (2015) ; Peitzsch et al. (2016)	N/A

Experimental models: Organisms/strains

NMRI (nu/nu) mice	OncoRay breeding facility at Technical University Dresden, Germany	TVV 2016–78, TVV2018-50
-------------------	--	-------------------------

Software and algorithms

GraphPad Prism, version 8		N/A
SPSS (v23)		N/A
R (version 3.5.2)		N/A
Bioconductor package RnBeads 2.0	Müller et al. (2019)	N/A
wateRmelon package	Pidsley et al. (2013)	N/A
R package methylumi	version 2.36.0.	N/A
Mathematical modeling of cancer cell plasticity	Poleszczuk and Enderling (2016) ; Poleszczuk et al. (2015), 2018	N/A
nonlinear least-squares solver lsqnonlin	MATLAB ver. R2019a	N/A
ordinary differential equation solver ode23s	MATLAB ver. R2019a	N/A

RESOURCE AVAILABILITY**Lead contact**

Further information and requests for resources and reagents should be directed to and will be fulfilled by the lead contact, Claudia Peitzsch (claudia.peitzsch@uniklinikum-dresden.de).

Material availability

This study did not generate new unique reagents.

Data and code availability

Gene expression (Agilent array) and DNA methylation (EPIC array) were submitted to the GEO repository. The records have been assigned the GEO accession number GSE192817 [NCBI tracking system #22614078] and GSE192899 [NCBI tracking system #2261575122614078]. Any additional information required to reanalyze the data reported in this paper is available from the lead contact upon request. This paper does not report original code.

EXPERIMENTAL MODEL AND SUBJECT DETAILS**Cell lines and culture conditions**

Experiments were performed with established PCa cell lines DU145 (#HTB-81, RRID:CVCL_0105, ATCC), PC3 (#CRL-1435, RRID:CVCL_0035, ATCC) and LNCaP (#CRL-1740, RRID:CVCL_0395, ATCC), HNSCC cell lines FaDu(DD) (RRID:CVCL_VP44, DSMZ), Cal33 (ACC 447, RRID:CVCL_1108, DSMZ), SAS (RRID:CVCL_1675, JCRB), and UT-SCC-14 (RRID:CVCL_7858, JCRB), as well as the GBM cell line LN229 (RRID:CVCL_0393, ATCC). The putative GBM cell line U87MG (RRID:CVCL_0022, ATCC) may not represent the tumor of origin ([Allen et al., 2016](#)). All cells were cultured according to the manufacturer's recommendations in a humidified incubator supplemented with 5% CO₂ at 37°C. FaDu, Cal33, PC3 and DU145 cells were maintained in Dulbecco's Modified Eagle Medium (DMEM, #5671, Sigma-Aldrich) and LNCaP in Roswell Park Memorial Institute (RPMI) 1640 Medium (#R6504, Sigma-Aldrich) containing 10% fetal bovine serum (FBS; A15-751, PAA Laboratories), 1 mM L-glutamine (#G7513, Sigma-Aldrich), 1% HEPES (1 M; #15630106, PAA Laboratories), 1% sodium pyruvate (100 mM; #S8636, Sigma-Aldrich) and 1% MEM non-essential

amino acids (100x; #M7145, Sigma-Aldrich). LN229 and U87MG were maintained in Minimum Essential Medium (MEM) with Earle's salts (#M4655, Sigma-Aldrich) containing 10% FBS, 1% penicillin-streptomycin (#P4333, Sigma-Aldrich), and 1% sodium pyruvate (#S8636, Sigma-Aldrich). Normal cell line controls included immortalized prostate cell line RWPE-1 (RRID:CVCL_3791, ATCC) cultured in keratinocyte serum free medium (K-SFM, # 17005042, Invitrogen) containing bovine pituitary extract (BPE) and human recombinant epidermal growth factor (EGF) as well as the keratinocyte cell line HaCaT (RRID:CVCL_0038, CLS) propagated in DMEM media. All cell lines were genotyped using microsatellite polymorphism analysis to validate identity and were tested regularly for mycoplasma contamination. Cells were not further used above passage 20. The radioresistant sublines (RR) were established from parental PCa and HNSCC cell lines after irradiation with multiple fractions of 4 Gy irradiation to select cell clones with intrinsic and acquired radioresistance. The molecular and functional characterization of these RR-sublines has been previously published (Cojoc et al., 2015; Kurth et al., 2015; Peitzsch et al., 2016).

Subcutaneous xenograft tumor model and tumor irradiation

The animal facility and experimental procedure are in line with the institutional guidelines, German animal welfare regulations, the European directive (2010/63/EU) and were approved by authorities (approval TVV 2016–78, DD24-5131/35482 and TVV2018-50, DD24.1–5131/449/52, Dresden, Germany). The experiments were performed using sex-mixed 8- to 10-week-old mice from outbred strain NMRI (nu/nu) obtained from the OncoRay breeding facility at Technical University Dresden. For immunosuppression, one to three days before transplantation of source tumors on the right hind leg the nude mice underwent 4 Gy total body irradiation (200 kV X-rays, 0.5 mm Cu filter, 1 Gy/min, n = 6–15 per cohort). Mice were observed twice a week for body weight and tumor volume using blinded manual caliper measurements. The mice were randomly assigned to untreated control, photon (5.2 Gy per fraction), and proton irradiation (4.8 Gy per fraction) followed by local irradiation in five fractions as soon as the tumor volume reached a diameter of approximately 7 mm. Both doses were considered equal under the assumption of a generic RBE of 1.1.

After the last fraction, tumors were harvested, formalin-fixed and embedded in paraffin (FFPE). The FFPE biopsies were cut into 10 μ m thick slices using a microtome. Upon deparaffination, the sections were blocked with PBS buffer containing 5% murine serum and stained with following primary antibodies overnight: ALDH1A1 (Santa Cruz, H-4, sc-374076, mouse, 1:50), CXCR4 antibody (Abcam, clone: UMB2, ab124824, rabbit, 1:100), and Tri-Methyl-Histone H3 (Lys27) (Cell Signaling, C36B11, rabbit, #9733, 1:200) in PBS buffer containing 1% bovine serum albumin (BSA, #P06-1391025, pan-biotech) and 0.1% Triton X-100. Upon washing, the slides were stained for 1 h with secondary goat-anti-rabbit or anti-mouse antibody labelled with Alexa Fluor 488 (#A-11008) or Alexa Fluor 555 (#A-21428, Invitrogen, 1:500). The cell nuclei were visualized through counterstaining with 4',6-diamidino-2-phenylindole (DAPI, #62247, Thermo Fisher Scientific). Sections were mounted with Mowiol 4–88 medium (#0713.1, Roth). Hematoxylin and eosin staining was used for histological examination. Four xenograft tumors per cohort including three different biopsy locations were imaged using Imager M1 (Zeiss) with a defined exposure time. Mean pixel intensity as well as area positivity was automatically analyzed using ImageJ software.

Primary prostate cultures

Primary prostate material was collected from prostate cancer patients between 2015 and 2019 upon radical prostatectomy and pathologically evaluated. Enrolled patients were contacted by a clinical oncologist (S.F., C.G.) and agreed to participate in this study by signing the informed consent form. The study and experimental procedure were approved by the local ethics committee (Institutional Review Board, Faculty of Medicine, Technische Universität Dresden, EK152052013). Primary material was transported within advanced DMEM/F12 media (#31331093, Life Technologies) directly from surgery to pathological examination (U.S.). Four to 24 h after surgery, biopsy material including validated prostate cancer and adjacent normal tissues (benign hyperplasia, BPH) were digested over night with 1 mg/mL collagenase II (Invitrogen) shaking at 37°C (Drost et al., 2016; Frame et al., 2016). Primary cultures from PCa and corresponding normal prostate tissue were plated in optimized WIT medium (WIT-P, #00-0045-500; Stemgent) supplemented with 10 μ M p160ROCK inhibitor Y-27632 dihydrochloride (Selleckchem, #S1049) on collagen-coated plates (Zhang et al., 2017). Primary cultures were not further used past passage 5. The gene expression profiling and functional characterization of the primary cultures including clinical characteristics of enrolled patients was previously published (Mukha et al., 2021). The median age of included patients was determined as being 68 years [range: 62; 76], a median Gleason score of 7 [3 + 3; 5 + 5] and a median PSA level at diagnosis with 8.82 ng/mL [5.14; 38].

METHOD DETAILS

Cell irradiation

Photon irradiation was performed using 200 kV X-rays (Yxlon Y.TU 320; 0.5 mm copper filter) at a dose rate of 1.3 Gy/min at 20 mA. Proton irradiation was performed at the Research Facility of the University Proton Therapy Dresden (UPTD) (as described in (Beyreuther et al., 2018)) with 150 MeV protons at a horizontally fixed beam line with a dose rate of 3 Gy/min. A dedicated beam shaping system consisting of a double-scattering device and a ridge filter provided a laterally extended 10 \times 10 cm² field with a 2.6 cm spread-out Bragg peak (SOBP) (Helmbrecht et al., 2016). Cells were positioned with a polycarbonate range shifter in the middle of the SOBP, resulting in a dose-averaged LET value of 3.7 keV/ μ m. Monolayer culture plates or flasks were placed vertically to the horizontal beam axis at a 90° angle, whereas 3D cultures were positioned at a 42° angle using a dedicated setup as previously

Cell Reports Article



described (Suckert et al., 2020). Daily dosimetry with a Markus ionization chamber (model 34045, PTW) and Unidos dosimeter (PTW) readout ensured consistent irradiation conditions. The lateral dose homogeneity of the proton field was verified by daily 2D dose measurements with the Lynx scintillation detector (IBA Dosimetry). Applied physical doses of either radiation types ranged from 2 to 8 Gy. The proton beam at UPTD was available for radiobiological experiments every 3–4 months, causing an increased biological variability between independent repeats.

Colony formation assay

For the two-dimensional (2D) colony formation assay, cells were plated under single cell conditions in 6-well or 96-well plates with numbers ranging from 100 to 2000 cells per well depending on the cell line and format and irradiated 24 h after plating. After 10–14 days, colonies were fixed with 10% formaldehyde (VWR) and stained with 0.05% crystal violet (Sigma-Aldrich). Colonies containing at least 50 cells were counted using a stereomicroscope (Zeiss). Plating efficiency (PE) and surviving fraction (SF) were calculated as follows:

$$PE = (\text{Number of counted colonies}) / (\text{Number of seeded cells}) \times 100$$

$$SF = (\text{Number of counted colonies}) / (\text{Number of seeded cells} \times PE) \times 100$$

For the three-dimensional (3D) colony formation assay, 100 μL of a media-matrigel (# 354248, Corning) mixture (1:20) containing 1000 cells was added to each well of 96-well plates coated with 50 μL low-melting agarose (1%, # A9414, Sigma) to prevent adhesion. The formed polymerized cell-matrix was carefully overlaid with 50 μL of media per well with or without chemical inhibitors as pre-treatment 24 h before irradiation depending on the experiment. All samples were plated in technical triplicates. The plates were incubated at 37°C and 5% CO_2 in a humidified incubator for 10–14 days, scanned using an Imaging Cytometer (Celigo, Nexcelom), and colonies with a diameter >50 μm were counted using ImageJ software.

Treatment with epigenetic compounds and CSC-targeting agents

Cells were seeded in 96-well plates for 2D or 3D colony-formation assay, sphere formation, and γH2AX assay and the Epigenetics Screening Library (Cayman Chemical, cat. number #11076 (Gorodetska et al., 2019)) was added with a final concentration of 5 μM the next day. Another 24 h later, plates were irradiated and formed colonies counted at d10, spheres at d14 and γH2AX foci formation after 24 h. GBM cell lines LN229 and U87MG did not form distinguishable 2D-colonies under 96-well conditions. Therefore, the area covered by cells per well was determined in percent using ImageJ software and used as a surrogate for the calculation of an approximated survival fraction. The chemical library screen using photons in cell lines LN229 and U87MG was performed in biological duplicates for each cell line and readout. Each replicate consisted of one well per compound and 46 DMSO control wells. Compounds with a plating efficiency of lower than 5% in the sham control were regarded as toxic and removed from further analysis. For each cell line and readout, the mean of the DMSO control values served as threshold to determine a radiosensitizing effect. Compounds with a lower clonogenic or spherogenic survival fraction and a higher γH2AX foci count than the DMSO control were classified as potentially radiosensitizing in the respective readout. The chemical library screen for the GBM cell lines U87MG and LN229 were performed for all three read-outs in biological triplicates. The screen comparing proton and photon irradiation with DU145, Cal33, and U87MG cells was performed once for each cell line.

Sphere formation assay

To evaluate the self-renewal potential, cells were grown as non-adherent multicellular cell aggregates, so-called sphere cultures. Cells were plated under single cell conditions at a density of 1,000 cells per well in 24-well or 96-well ultra-low attachment plates (#10023683, Corning) in mammary epithelial cell basal medium (MEBM, #CC-3151, Lonza) supplemented with 4 mg/mL insulin (#I9278, Sigma-Aldrich), B-27 (50x, 17504044, Invitrogen), 20 ng/mL epidermal growth factor (EGF, # AF-100-15, Peprotech), and 20 ng/mL fibroblast growth factor (FGF, # 100–18B, Peprotech). Media and supplements were refreshed once a week. Plates were automatically scanned after 14 days using the Celigo S Imaging Cell Cytometer (Brooks) and spheres with a diameter >100 μm were counted either manually or using ImageJ software. The sphere-forming capacity was calculated as the ratio of formed spheres relative to the number of plated cells in percent.

Flow cytometry analysis and fluorescence-activated cell sorting (FACS)

Cells were dissociated using Accutase (PAA Laboratories) and resuspended in PBS-based (PAA) staining buffer containing 5% FBS (PAA), 1% HEPES (25 mM, Sigma-Aldrich), and 1 mM EDTA (Sigma-Aldrich). Cell suspensions were stained with direct labelled anti-CD133/2-PE (clone 293C3, Miltenyi Biotec, dilution 1:10), anti-CXCR4-PE-Cy7 (clone 12G5, eBioscience, dilution 1:25), and anti-CD44-APC (clone DB105, Miltenyi Biotec, dilution 1:100) antibodies for 1 h on ice and protected from light. Cells incubated with the respective fluorochrome-labelled isotype were used as control to discriminate positive staining from unspecific background. Aldehyde dehydrogenase activity was analyzed using the ALDEFLUOR™ assay (#01700, Stemcell Technologies) according to the manufacturer's protocol. Cells incubated with the specific ALDH inhibitor diethylaminobenzaldehyde (DEAB, #01705) served



as negative control. Counter-staining with propidium iodide (PI), 4',6-diamidino-2-phenylindole (DAPI), or 7-amino-actinomycin D (7-AAD) (1:1000, 1 $\mu\text{g}/\text{mL}$, #A1310, Thermo Fisher Scientific) depending on the staining setup was used to exclude dead cells from downstream analysis. Samples were analyzed with the BD Celesta flow cytometer (Becton Dickinson) after compensation and acquired with BD FACSDiva 6.0 software. A minimum of 50,000–100,000 viable cell events were collected per sample. For data analysis, FlowJo software (version 7.6.2) was used.

To isolate defined cell populations after staining, cells were sorted with the BD FACS Aria III (BD Bioscience) using the 100 μm nozzle directly into culture media after exclusion of dead cells and doublets within the DIVA software. Reanalysis of the sorted cell suspension was used to determine purity.

Mass spectrometry-based analysis of Krebs cycle metabolites

Cells were seeded in triplicates at 200,000 cells per well in 6-well plates 24 h before irradiation. Five days after irradiation, cells were washed three times with ice-cold PBS and harvested in 500 μL methanol through scratching. One well was used to determine the exact cell number. Liquid chromatography-tandem mass spectrometry (LC-MS/MS) was used to determine concentrations of Krebs cycle metabolites (succinate, fumarate, malate, citrate, isocitrate, cis-aconitate, α -ketoglutarate, 2-hydroxyglutarate) as well as pyruvate, lactate, and four amino acids (glutamate, glutamine, aspartate, asparagine), as described previously (Richter et al., 2019). Quantification of metabolites was performed based on comparison to ratios of analyte peak areas to peak areas obtained from stable isotope labeled internal standards in samples to those observed in respective calibrators. Results were normalized to determined cell numbers.

Differential gene expression analysis

Gene expression profiling was performed in triplicates in six tumor cells lines (DU145, PC3, FaDu, Cal33, LN229, U87MG) 12 h and 5 days after irradiation either with 4 Gy of photons or protons in comparison to sham control. Total RNA was isolated using the RNeasy Kit (Qiagen) and Qubit RNA assay (Thermo Fischer Scientific) for quantification. Samples containing 20 μL with an RNA concentration of 50 $\text{ng}/\mu\text{L}$ were shipped to the Microarray Unit at Genomics and Proteomics Core Facility (GPCF, DKFZ, Heidelberg, Germany) to perform global gene expression analysis with the Agilent-072363 SurePrint G3 Human GE v3 8 \times 60K Microarray 039494 (Agilent product no: G4851C) according to the manufacturer's recommendations. Raw data were transferred to the Omics IT and Data Management Core Facility (ODCF, DKFZ, Heidelberg) to ensure data management and depository. The raw data files were submitted to the GEO repository with accession number GSE192817 [NCBI tracking system #22614078]. Differential gene expression analysis was performed using R version 4.0.2 and Bioconductor package limma (Ritchie et al., 2015). Prior to analysis, the raw data were background-corrected using the normal-exponential (normexp) method (Shi et al., 2010) and normalized using quantile normalization (Oshlack et al., 2007). Statistical computation was moderated using the empirical Bayes statistics (Smyth, 2004) available in the limma package. Significantly differentially regulated genes between the treatment groups with p value < 0.05 and fold change >2 were combined and analyzed with the pathway analysis tools from Ingenuity Pathway Analysis (IPA, Qiagen) software, Gene Set Enrichment Analysis (GSEA), or g:Profiler to identify canonical pathways.

Genome-wide DNA methylation analysis

Genomic DNA was isolated from the cell cultures as described for differential gene expression analysis using the Qiamp DNA Mini Kit (Qiagen). 40 μL DNA solutions with a concentration of 25 $\text{ng}/\mu\text{L}$ were shipped to the Microarray Unit at Genomics and Proteomics Core Facility (GPCF, DKFZ, Heidelberg, Germany) to perform human DNA methylation bead array analysis with the EPIC array (v1_b4, Illumina). The raw data files were submitted to the GEO repository with accession number GSE192899 [NCBI tracking system #22615751]. Analysis was run with the R (version 3.5.2) and Bioconductor package RnBeads 2.0 (Müller et al., 2019) to determine beta (β) values that estimate the methylation level e.g., within gene bodies, promotor regions and CpG islands, and also perform differential methylation analysis in these regions.

Differential methylated regions (DMR) were visualized using volcano plots and included for downstream pathway analysis, gene enrichment and gene ontology (GO) analysis. Within the RnBeads settings configuration, background correction was performed using the R package methylumi (version 2.36.0.) and normalization using the dasen method from the wateRmelon package (Pidsley et al., 2013).

Western blot analysis

Cells were lysed in RIPA buffer (Santa Cruz Biotechnology) and the protein concentration of the lysates was measured using the bicinchoninic acid (BCA) Protein Assay Kit (Pierce) according to the manufacturer's recommendations. Protein lysates with an equalized protein concentration (10–20 μg) were separated by sodium dodecyl sulfate-polyacrylamide gel electrophoresis (SDS-PAGE, 4–20%) and transferred onto a nitrocellulose membrane (GE Healthcare). The membranes were blocked with PBS buffer containing 5% bovine serum albumin (BSA) and 0.1% Tween 20 and were incubated over night with following primary antibodies (dilution 1:1000): β -catenin rabbit monoclonal antibody (D10A8, #8480, Cell Signaling Technology (CST)), histone H3 rabbit monoclonal antibody (D1H2, #4499, CST), E-cadherin rabbit monoclonal antibody (24E10, #3195, CST), oct-4 rabbit polyclonal antibody (#2750, CST), tri-methyl-histone H3 (Lys36) rabbit monoclonal antibody (D5A7, #4909, CST), phospho-AKT (Ser473) rabbit monoclonal antibody (D9E, #4060, CST), sox2 rabbit monoclonal antibody (D6D9, #3579, CST), and tri-methyl-histone H3 (Lys4) rabbit monoclonal

Cell Reports Article



antibody (C42D8, #9751, CST). The glyceraldehyde 3-phosphate dehydrogenase (GAPDH) (FL335) rabbit polyclonal antibody (sc-25778, Santa Cruz Biotechnology) was used as loading control. Membranes were washed and incubated with species-appropriate horseradish peroxidase (HRP)-conjugated secondary antibody (CST, 1:20,000 dilution). The signal was visualized using the Enhanced Chemiluminescence (ECL) Western Blotting Detection Reagent (GE Healthcare) on films in a darkroom with appropriate developer and fixation solution. After scanning the films, semiquantitative analysis of protein expression relative to the loading control was performed using ImageJ software.

Determination of glutathione, reactive oxygen species, and mitochondrial membrane potential

To measure the level of reactive oxygen species (ROS) 24 h after irradiation, cells were incubated upon harvesting with 5 mmol 5-(and-6)-carboxy-20,70-dichlorodihydrofluorescein diacetate acetyl ester (CM-H2DCFDA, Invitrogen Molecular Probes, 1:2,000) in PBS buffer containing 5% FBS, 1 mM EDTA, and 1% HEPES for 20 min at 37°C. The same staining conditions were used to determine glutathione (GSH) levels with 40 mmol/L monochlorobimane (mBCl; #M1381MP, Life Technologies, 1:2000) and the mitochondrial membrane potential with the cell-permeant tetramethylrhodamine ethyl ester (TMRE, 100 nM, #T669, Thermo Fisher Scientific). After washing, samples were analyzed with the BD Celesta flow cytometer (Beckton Dickinson). Dead cells were excluded using DNA intercalating agents PI, DAPI, or 7-AAD. Solvent control with ethanol or DMSO at indicated concentrations was used as gating control. A minimum of 100,000 viable cells events were collected per sample and data were analyzed using FlowJo software (version 7.6.2).

Cell proliferation

Cells were seeded at a density of 1,000 cells per well in 96-well plates. Cell viability was analyzed every day over five days using the CellTiterGlo® Luminescent Assay (#G7570, Promega) according to the manufacturer's instructions. The luminescence signal was measured using a microplate reader (Tecan GENios Pro).

Immunofluorescence staining

Cells were plated at a density of 5,000 cells per well in 96-well black polystyrene microplates with a flat, clear bottom (#3603, Corning). Cells were irradiated with 4 Gy of photons or protons 24 h after seeding. At respective time points after irradiation (30 min and 24 h), cells were first fixed for 15 min in PBS supplemented with 4% formaldehyde. After washing, the cells were then blocked with 5% BSA in PBS overnight to prevent unspecific antibody binding, permeabilized with 1% BSA and 0.1% Triton X-100 in PBS, and incubated with the primary antibodies anti-phospho-H2AX (Ser139, clone JBW301, Merck Millipore, 1:250 dilution) and anti-53BP1 (Cell Signaling Technology, 1:500 dilution) at 4°C overnight. After washing, secondary goat anti-mouse IgG (H + L)-AlexaFluor488 (1:400, Thermo Fisher Scientific), anti-rabbit IgG (H + L)-AlexaFluor555 (1:400, Thermo Fisher Scientific) and DAPI (1 µg/mL, Sigma, 1:1000) were added for 1 h. After repeated washing, the slides were embedded in Mowiol 4-88 mounting medium (Carl Roth) and the clear bottom 96-well plates were covered with PBS buffer. Imaging was performed with the Observer microscope (Zeiss) using the same exposure time setup in the Zen software. 53BP1 and γH2AX foci were quantified using ImageJ's "find maxima" feature within the DAPI mask from >100 cells per population.

Cell death analysis

For cell death and apoptosis evaluation, cells were harvested 48 h after irradiation and stained with Annexin V Apoptosis detection kit (#V13242, Thermo Fisher Scientific) according to the manufacturer's instructions and analyzed using flow cytometer BD Celesta (BD Biosciences).

To determine Caspase 3/7 activity, cells were plated in triplicates in 96-well plates at a density of 2,000 cells per well and analyzed 72 h after irradiation using the Caspase-Glo® 3/7 assay (#G8090, Promega) according to the manufacturer's recommendations.

To determine the induction of autophagic foci, cells were plated in a 96-well black clear bottom plates (Corning) at a density of 3,000 cells per well and 24 h after irradiation analyzed using Cell Meter™ Autophagy Kit (#ABD-23000, Biomol) according to manufacturer's instructions. The plates were imaged with the fluorescence microscope Observer (Zeiss) using the Zen software. The number of autophagosomes per cell was quantified using ImageJ Software.

Senescence was evaluated 5 days after irradiation using the Senescence β-Galactosidase staining kit (#9860, Cell Signaling). Bright field images of fixed and stained cultures were taken with Axiovert200 (Zeiss) microscope. Number of blue stained cells per total cell number within field of view were counted manually.

Mathematical modeling of cancer cell plasticity upon irradiation

An ordinary differential equation version of existing models of cancer cell plasticity (Poleszczuk and Enderling, 2016; Poleszczuk et al., 2015, 2018) was created. Let x_i denote non-stem cancer cells (CC) that have proliferated i times and have not been exposed to radiation (undamaged CC) and let y_i denote non-stem cancer cells that have proliferated i times and have been irradiated (damaged CC). Similarly, let w and z denote cancer stem cells that have been either irradiated (damaged CSC) or not (undamaged CSC). The following model was considered:

$$x'_0(t) = -(\rho + d)x_0(t) + \rho(1 - s)(z(t) + w(t)) + \frac{m}{\lambda + 1}y_0(t),$$



$$x'_i(t) = -(\rho + d)x_i(t) + \rho(2x_{i-1}(t) + y_{i-1}(t)) + \frac{m}{\lambda + 1}y_i(t), \text{ for } 1 \leq i \leq p_{\text{cap}}$$

$$y'_0(t) = -(\rho + d)y_0(t) - cy_0(t) + vw(t) - \frac{m}{\lambda + 1}y_0(t),$$

$$y'_i(t) = -(\rho + d)y_i(t) - cy_i(t) + \rho y_{i-1}(t) - \frac{m}{\lambda + 1}y_i(t), \text{ for } 1 \leq i \leq p_{\text{cap}}$$

$$z'(t) = \rho s(z(t) + w(t)),$$

$$w'(t) = -vw(t) + c \sum_{i=0}^{p_{\text{cap}}} y_i(t),$$

where all parameters are assumed to be positive and the probability $s \leq 1$. The relationships between the compartments described by this system of equations are illustrated in Figure 2A. In this model we assume that CSCs can proliferate indefinitely, whereas CC can proliferate only p_{cap} times before they die (Figure S2A). Moreover, we assume that only irradiated cells can undergo plasticity events (Figure S2B). The first term in each of the equations for x_i and y_i accounts for the fact that CC undergo apoptosis with rate d and are then removed from the system, and proliferate with rate ρ , after which they are described by variable x_{i+1} or y_{i+1} . The last term of each of these equations accounts for mutations that decrease radiation induced damage. Here, $\lambda + 1$ is the average amount of damage caused by irradiation and m is the rate at which damage is reduced by one. The second term in the equation for x'_0 describes the asymmetric proliferation of CSC, which occurs at rate $\rho(1 - s)$, where s is the probability of symmetric division i.e., we assume that offspring of CSC are undamaged CC with full proliferation capacity (Figure S2A). The second term of the equation for x'_i accounts for the proliferation of non-stem cancer cells. We assume that the offspring of non-stem cells are undamaged non-stem cells. Proliferation decreases the remaining proliferation capacity of both, the parent cell and the daughter cell by 1. The terms $-cy_i$ in the equations for y'_i account for plasticity events that is non-stem cells turning into stem cells (Figure S2B). The term vw accounts for reverse plasticity events that is stem cells changing into a non-stem cell. Finally, the equation for z' describes symmetric proliferation of stem cells, both damaged and undamaged. The first term of the equation for w' accounts for reverse plasticity events and the second term for regular plasticity events.

This model was calibrated with experimental data with the assumption that ALDH is a perfect stemness marker i.e., all ALDH⁺ cells are CSCs and all ALDH⁻ cells are CCs. We used data obtained from the 3D colony formation assay of ALDH⁺ and ALDH⁻ population after irradiation with 4 Gy photons or protons (Figure 1D) to set the parameters SF_{CC} and SF_{CSC} , denoting the survival fraction of CC and CSC after irradiation, respectively. Moreover, this parameter value was used to define the average damage induced by irradiation $\lambda + 1 = 1 - \ln(SF_{\text{CC}})$. Some other parameter values were obtained from literature, see Table S1. The remaining parameter values were obtained by minimizing the least squares of the residuals between the ALDH⁺ ratio predicted by the model and the ALDH⁺ ratio obtained from the flow cytometry analysis of ALDH activity, as shown in Figure S1A. We have fitted one set of parameters per cell line and treatment type, and performed the fitting procedure for each experimental repeat, differing only in the initial ALDH⁺ ratio at day 0. For this purpose, the nonlinear least-squares solver lsqnonlin and the ordinary differential equation solver ode23 s from MATLAB ver. R2019a were used. Significant differences between the parameters for both treatments were analyzed using the sign test.

We couldn't replicate the behavior of the data when fitting a model without reverse plasticity events that is $v = 0$. In order to check whether this model could simulate a CSC ratio that decreases at first and increases at a later time point, as seen in the data, we summed the equations to obtain equations for cancer non-stem cells denoted a ($a = x + y$, where x and y are undamaged and damaged CC, respectively) and cancer stem cells denoted b ($b = w + z$, where z and w are undamaged and damaged CSC, respectively) and obtained the following system of equations:

$$a' = (\rho - d)a - 2\rho(x_{p_{\text{cap}}} + y_{p_{\text{cap}}}) - cy + \rho(1 - s)b,$$

$$b' = \rho sb + cy.$$

We are interested in the sign of the derivative $\left(\frac{b}{a+b}\right)'$. We have:



$$\left(\frac{b}{a+b}\right)' = \frac{b'(a+b) - b(a'+b')}{(a+b)^2} > 0$$

$$\Leftrightarrow b'a - a'b > 0$$

$$\Leftrightarrow psba + cya > (p-d)ab - 2p(x_{p_{cap}} + y_{p_{cap}})b - cyb + p(1-s)b^2$$

$$\Leftrightarrow 0 > p(1-s)b^2 + [(p-d-ps)a - 2p(x_{p_{cap}} + y_{p_{cap}}) - cy]b - cya$$

Let us denote the right-hand side of the above inequality by $f(b(t))$. We want to check whether the derivative $\left(\frac{b}{a+b}\right)'$ may be negative for $t < t^*$ and positive for $t > t^*$ for a certain $t > 0^*$ i.e. whether $f(b(t)) > 0$ for $t < t^*$ and $f(b(t)) < 0$ for $t > t^*$. Note, that $b(t)$ is an increasing function, since its derivative is positive, hence, this is equivalent to checking whether $f(b) > 0$ for $b < b^*$ and $f(b) < 0$ for $b > b^*$ for a certain $b^* > 0^*$. The quadratic function $f(b)$ can only be negative if it has two zeros, so let us assume it does and denote the zeros by b_1 and b_2 . According to Vieta's formula: $b_1 b_2 = \frac{-cya}{p(1-s)} \leq 0$, since $s < 1$, because it is a probability. Hence, the zeros have opposite signs or one of them is equal to zero. Therefore, either $f(b) > 0$ for $b > 0$ or $f(b) < 0$ for $b \in (0, b^*)$ and $f(b) > 0$ for $b > b^*$.

QUANTIFICATION AND STATISTICAL ANALYSIS

Experiments were performed in biological and technical triplicates for each cell line unless otherwise noted (with "n" denoting the total number of biological replicates). Group differences were analyzed by paired Student's t-test. A p value < 0.05 (*), < 0.01 (**), and < 0.001 (***) was regarded as statistically significant. The differences between cell survival curves were analyzed using GraphPad Prism or SPSS (v23) software by fitting the data into the linear-quadratic formula, where the fraction of surviving cells (SF) at a defined dose (D) is described by following formula using stratified linear regression: $SF = \exp(-1 * (\alpha * D + \beta * D^2))$. To statistically assess the difference of linear-quadratic models between photon and proton irradiation, data of the two groups were combined and two multivariable linear models were fitted to the natural logarithm of the surviving fraction; the first including dose and dose squared only, and the second including the interactions between treatment and dose and between treatment and dose squared additionally. The constant fit parameter was set to zero. The improvement in R^2 when including the treatment-related terms was evaluated by an F-test. To illustrate the differences of both irradiation types on clonogenic cell survival, the relative biological effectiveness (RBE) was calculated as the ratio of the physical doses with biological iso-effect: $RBE = D(Proton)/D(Photon)$.

Cell Reports, Volume 38

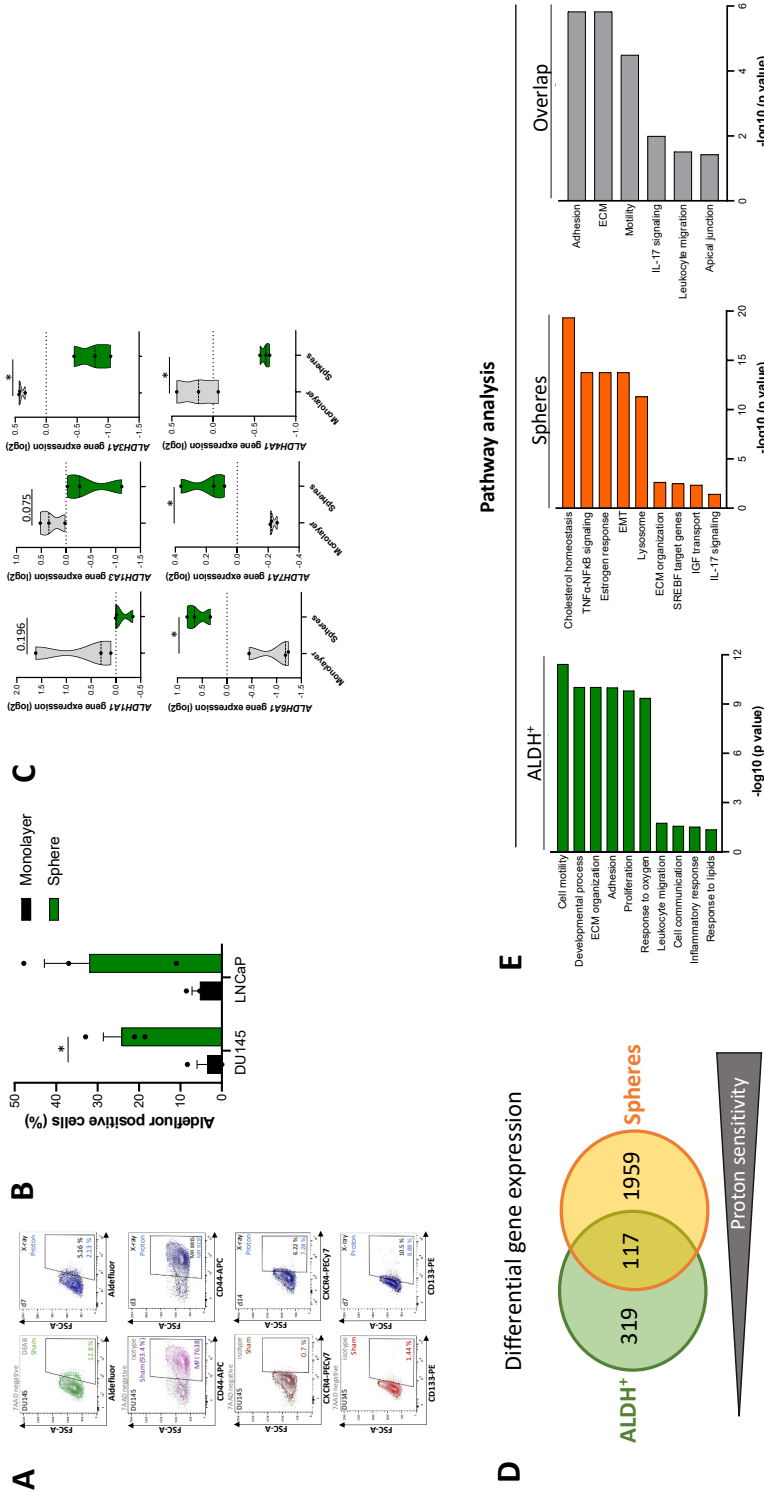
Supplemental information

Cellular plasticity upon proton irradiation determines tumor cell radiosensitivity

Iñaki Schniewind, Wahyu Wijaya Hadiwikarta, Julia Grajek, Jan Poleszczuk, Susan Richter, Mirko Peitzsch, Johannes Müller, Daria Klusa, Elke Beyreuther, Steffen Lök, Armin Lühr, Susanne Frosch, Christer Groeben, Ulrich Sommer, Mechthild Krause, Anna Dubrovska, Cläre von Neubeck, Ina Kurth, and Claudia Peitzsch

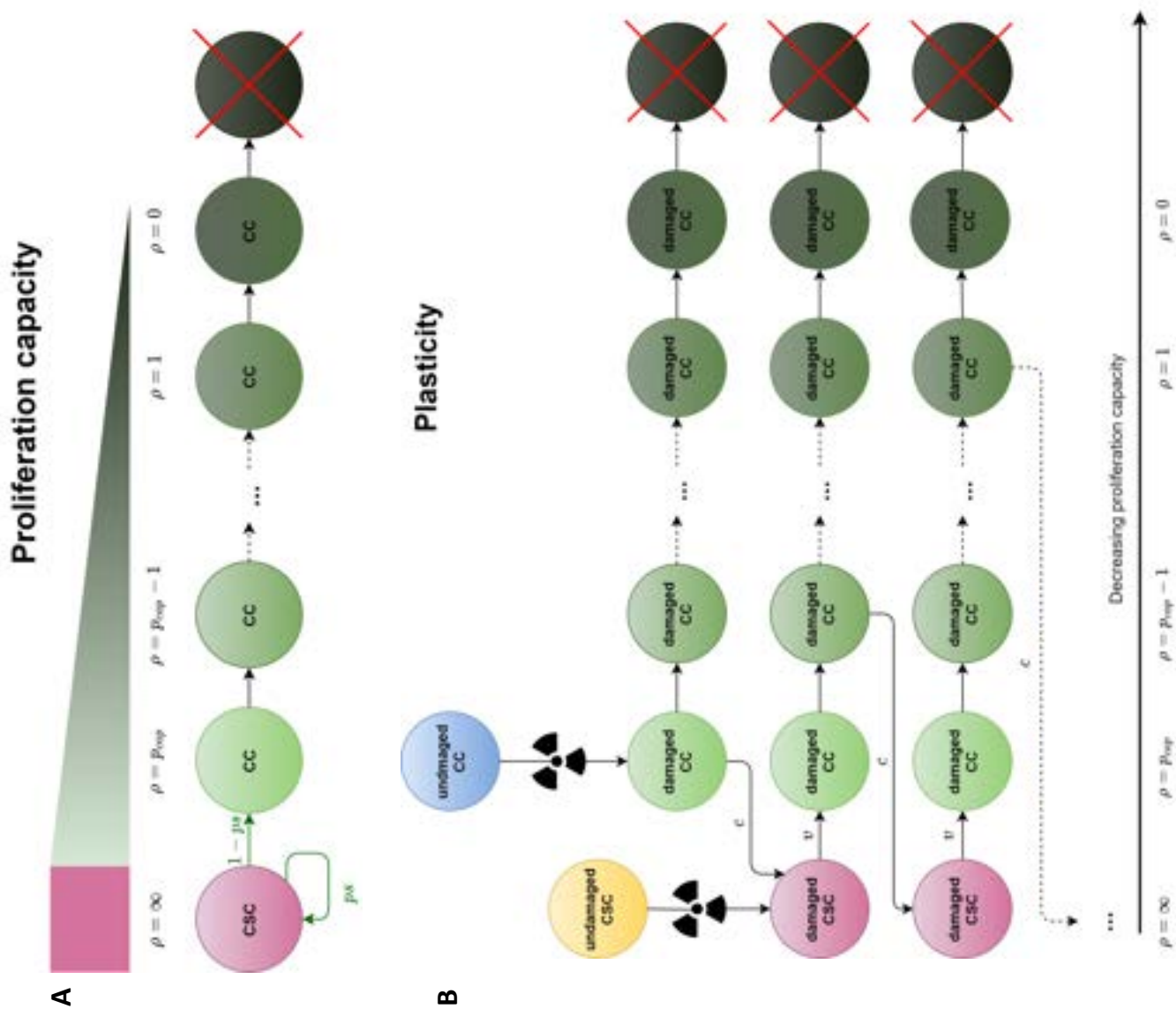
Supplementary Figure and Table

Supplementary Figure S1.



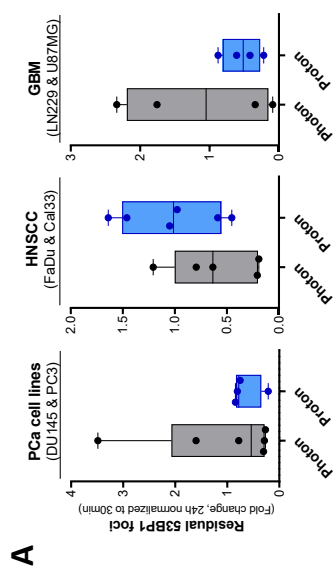
Supplementary Figure S1. Dynamic of putative cancer stem cell (CSC) marker expression upon proton irradiation (related to Figure 1). (A) Representative flow cytometry blots of aldehyde dehydrogenase (ALDH) activity, CD44, CD133 and CXCR4 cell surface expression in DU145 cells after proton irradiation. (B) ALDH activity in DU145 and LNCaP cells cultured as monolayer versus spheres (n=3, error bars=SEM, *p<0.05). (C) Gene expression of different the ALDH isoforms *ALDH1A1*, *ALDH1A3*, *ALDH3A1*, *ALDH6A1*, *ALDH7A1*, and *ALDH4A1* in DU145 cells under monolayer conditions compared to spheres culture (n=3, Agilent array, *p<0.05). (D) Comparative transcriptome analysis indicates 117 differentially regulated genes in the ALDH⁺ population and spheres compared to DU145 monolayer cultures. (E) Pathway analysis identified ALDH- and sphere-specific pathways as well as overlapping signatures.

Supplementary Figure S2



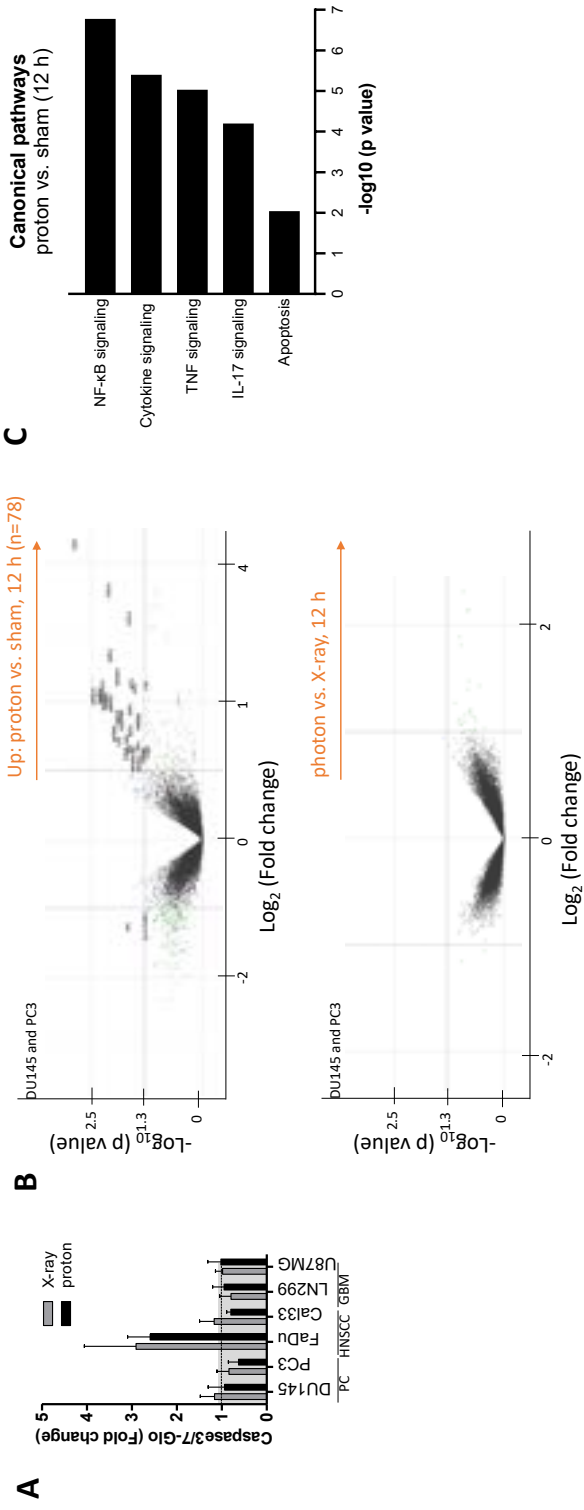
Supplementary Figure S2. Mathematical modeling framework to investigate selection upon irradiation (related to Figure 2 and Table S1). (A) CSCs can proliferate indefinitely, whereas cancer non-stem cells (CC) can only proliferate p_{cap} times before they die and are removed from the model. The parameter ρ denotes the remaining number of divisions for the given CC. We assume that CC that are created via symmetrical proliferation of CSC have $\rho = p_{cap}$. (B) We assume that only irradiated cells can undergo plasticity events. Irradiated non-stem cancer cells acquire a stem cell phenotype with rate c (plasticity events), whereas irradiated CSCs lose their stemness with rate v (reverse plasticity events). We assume that cells created in plasticity events or reverse plasticity events retain the damage and that CC that were created in reverse plasticity events have full proliferation capacity.

Supplementary Figure S3.



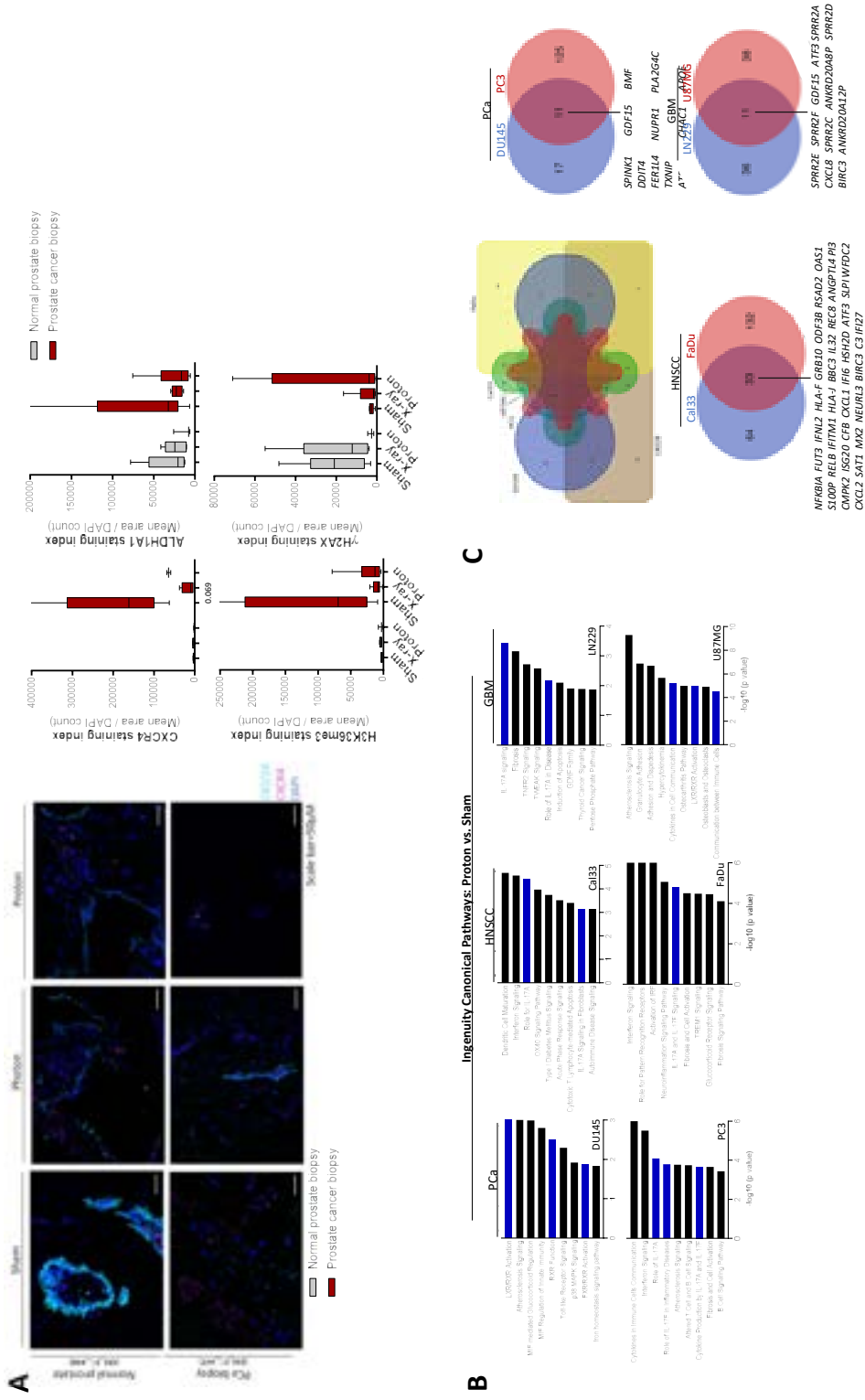
Supplementary Figure S3. Identification and characterization of proton-specific determinants of intracellular sensitivity with classical radiobiological assays (related to Figure 3). (A) Normalized residual 53BP1 foci count in PCa (DU145, PC3), HNSCC (FaDu, Cal33), and GBM cell lines (LN229, U87MG) 24 h after 4 Gy photon versus proton irradiation. (n=6, SEM).

Supplementary Figure S4.

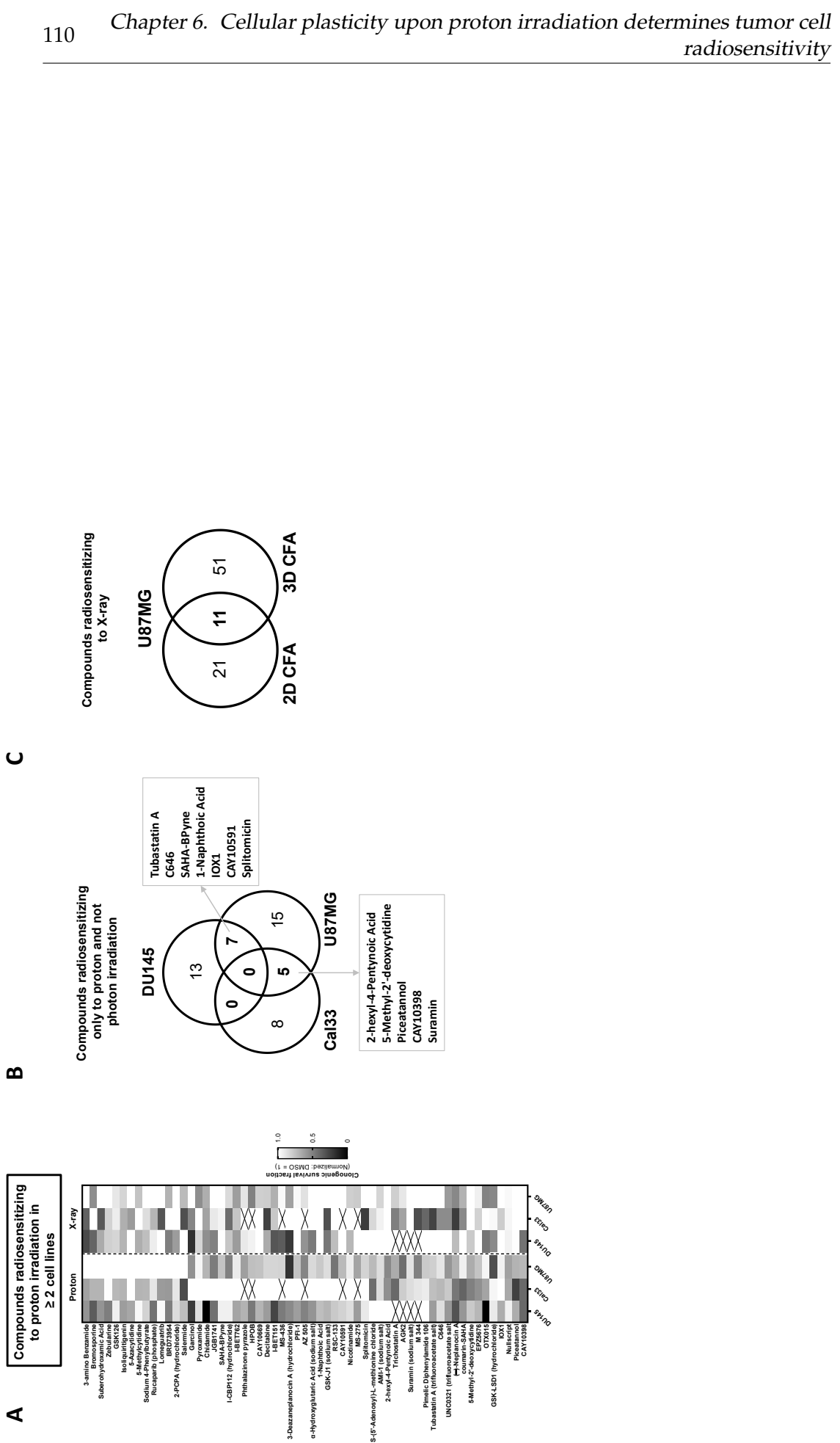


Supplementary Figure S4. Characterization of putative cell death mechanisms induced by proton irradiation (related to Figure 4). (A) Caspase-3/7 activation in DU145, PC3, FaDu, Cal33, LN229 and U87MG cell lines were determined 72 h after irradiation with 4 Gy (n=3, error bars=SEM). (B) Volcano blots illustrating comparative transcriptome analysis in PCa cell lines DU145 and PC3 12 h after single dose irradiation with 4 Gy of protons and photons in comparison to sham (n=4, two each). Highlighted genes are differentially regulated with a fold change $>|2$ and a p value <0.05 . (C) Ingenuity pathway analysis combining all significantly differentially regulated genes identified up-regulated NF- κ B pathway, IL-17 and TNF signaling within 12 h after proton irradiation while no altered gene expression was found 12 h upon photon irradiation.

Supplementary Figure S5



Supplementary Figure S5. Cellular plasticity and epigenetic modulation upon proton irradiation (related to Figure 5). (A) Immunofluorescence staining for ALDH1A1, CXCR4, H3K36me3, γ H2AX, cytokeratin 4/15 (CK4/15) and cleaved caspase-9 in sections of primary adjacent normal and PC biopsies fixed 24 h after 4 Gy irradiation (one patient, three locations). (B) Individual ingenuity pathway analyses for differentially regulated genes in DU145, PC3, FaDu, Cal33, LN229, and U87MG cells 5 days after 4 Gy irradiation comparing a proton-specific signature to sham control (n=3). (C) Venn diagram illustrates overlap of differentially regulated genes between cell lines and tumor entities.



Supplementary Figure S6. Epigenetic targeting to sensitize tumor cells to proton irradiation (related to Figure 6). (A) Heatmap including compounds with a radiosensitizing effect to proton irradiation in ≥ 2 cell lines. Values are normalized to the DMSO control. (B) Venn diagram showing compounds with a radiosensitizing effect only to proton but not to photon irradiation. (C) Venn Diagram showing the overlap of compounds with a radiosensitizing effect to photon irradiation in U87MG cells in the 2D and the 3D colony formation assay.

Table S1. Parameter values of the calibrated models for each cell line and treatment. Related to Figure 2.

Treatment	DU145	PC3	FaDu	Cal33	LN229	U87MG
Proliferation rate (ρ) [1/h]						
Both	$\frac{1}{34}$ (Stone et al., 1978)	$\frac{1}{27}$ (Kim et al., 2008)	$\frac{1}{30}$ (Abbaspour et al., 2017)	$\frac{1}{40}$ (www.dsmz.de)	$\frac{1}{31}$ (www.atcc.com)	$\frac{1}{34}$ (www.dsmz.de)
Apoptosis rate (d) [1/h]						
Both	$\frac{0.02}{24}$ Portz et al., 2012)	$\frac{0.09}{24}$ (Abbaspour et al., 2017)	$\frac{0.16}{24}$ (Yen et al., 2016)	$\frac{0.01}{24}$ (Wang et al., 2015)	$\frac{0.18}{24}$ (Shao et al., 2019)	$\frac{0.02}{24}$ (Jiang et al., 2018; Liu et al., 2018) ¹)
Symmetric division probability of CSC (s) (dimensionless)						
Photon	0.03 (Hu et al., 2017)	0.8 (Abbaspour et al., 2017)	0.0355	0.789	1	0.73 (Lubanska et al., 2014)
Proton	0.03 (Hu et al., 2017)	0.8 (Abbaspour et al., 2017)	1	0.822	1	0.73 (Lubanska et al., 2014)
Rate of plasticity event: CC turning into CSC (c) [1/h]						
Photon	1.2×10^{-11}	4.22×10^{-5}	1.54×10^{-9}	0.0018	0.0402	0.054
Proton	4.9×10^{-15}	6.72×10^{-7}	3.7×10^{-14}	0.001	5.05×10^{-7}	5.95×10^{-5}
Rate of reverse plasticity events: CSC turning into CC (v) [1/h]						
Photon	5.33×10^{-4}	0.105	0.046	4.3×10^{-12}	0.031	0.01
Proton	0.003	4.9×10^{-11}	0.0263	7.07×10^{-5}	0.0256	4.87×10^{-6}
Mutation rate (m) [1/h]						
Photon	1.82	6.85	0.0008	0.0318	27.58	32.65
Proton	0.011	0.28	0.0425	0.004	0.077	0.152
Proliferation capacity (p_{cap}) (dimensionless)						
Photon	3	1	4	14	3	4
Proton	4	7	33	12	4	14

Table S2. Radiobiological parameter describing cell-intrinsic radiosensitivity based on cell survival curves fitted to the linear-quadratic model. Related to Figure 1 and Figure 3.

Tumor entity	Cell line	Population	IR	α (Gy ⁻¹)	β (Gy ⁻²)	α/β (Gy)	SF _{photon} (4 Gy)	D(SF _{4Gy}) (Gy)	RBE(4Gy)
Prostate Ca	DU145	Parental	Photon	0.076	0.017	4.471	0.562	4.000	
		Proton		-0.049	0.065	-0.754		3.378	1.18
		RR subline	Photon	0.090	0.002	60.133	0.681	4.000	
		Proton		0.135	0.006	23.316		2.568	1.56
		ALDH ⁺ population	Photon	0.250	-0.011	-22.727	0.439	4.000	
		Proton		0.304	-0.024	-12.667		3.930	1.02
PC3	Parental	Photon	0.034	0.022	1.545	0.614	4.000		
		Proton		-0.051	0.056	-0.911		3.442	1.16
	RR subline	Photon	0.268	-0.010	-27.686	0.400	4.000		
		Proton		0.010	0.052	0.183		4.109	0.97
	ALDH ⁺ population	Photon	0.041	0.014	2.929	0.678	4.000		
		Proton		0.124	0.002	62.000		2.985	1.34
HNSCC	FaDu	Parental	Photon	0.152	0.017	8.941	0.415	4.000	
		Proton		0.088	0.024	3.667		4.493	0.89
	IR subline	Photon	0.150	0.011	13.627	0.460	4.000		
		Proton		0.254	0.005	50.800		2.889	1.38
	ALDH ⁺ population	Photon	0.181	-0.005	-36.200	0.525	4.000		
		Proton		0.160	-0.004	-40.000		4.540	0.88
Cal33	Parental	Photon	-0.006	0.023	-0.261	0.709	4.000		
		Proton		-0.099	0.050	-1.972		3.783	1.06
	IR subline	Photon	0.008	0.017	0.479	0.741	4.000		
		Proton		-0.088	0.459	-0.192		0.909	4.40
	ALDH ⁺ population	Photon	0.187	-0.013	-14.385	0.583	4.000		
		Proton		0.118	-0.003	-39.333		5.287	0.76
GBM	LN229	Parental	Photon	0.026	0.007	3.714	0.806	4.000	
		Proton		0.056	0.019	2.947		2.206	1.81
	ALDH ⁺ population	Photon	0.139	-0.008	-17.375	0.652	4.000		
		Proton		0.093	-0.004	-23.250		6.320	0.63
	U87MG	Parental	Photon	0.107	0.002	53.500	0.631	4.000	
		Proton		0.122	0.009	13.556		3.074	1.30
ALDH ⁺ population	Photon	0.239	-0.020	-11.980	0.529	4.000			
	Proton		0.148	-0.004	-37.000		4.970	0.80	

Chapter 7

Discussion

7.1 Achievement of research aims

The aim of this thesis was to explore the TME as a driver of treatment resistance and a source of combination therapy targets. I focused on two parts of the TME: the acidic niche and the tumor itself with its heterogeneous cancer cell phenotypes. I identified and analyzed two contributors to treatment resistance. First, I studied the enzyme CAIX, which acidifies the neighborhood of the tumor, impairs the immune response, and thereby reduces immune checkpoint inhibitor therapy effectiveness. Then, I investigated irradiation-induced cellular plasticity and the resulting stem cell dynamics in the tumor, which impact the tumor's radioresistance. As stated in my research aim, these potential resistance drivers and treatment targets were evaluated using mathematical and computational models.

First, I proposed a hybrid model of the tumor, immune cells, and the TME, which combined a partial differential equation model of substances present in the TME and an agent-based model of the cells in the TME [39]. To my knowledge, this was the first agent-based model including tumor-immune interactions, tumor cell metabolism, and the resulting acidosis of the TME, allowing for the study of combining immunotherapy with acidosis-targeting treatments such as CAIX suppression. I used this model to study tumoral CAIX expression as an immunotherapy biomarker and a promoter of immunotherapy resistance. However, the model contains other possible barriers to immunotherapy effectiveness that could be explored, such as hypoxia, fibrotic stroma accumulation, and cancer stem cell dynamics. Furthermore, the model can be easily extended to consider other putable factors impacting treatment resistance such as regulatory immune cells that attenuate immune response. This model realizes my first research aim by providing a computational tool for immunotherapy biomarker and combination therapy target determination and evaluation, which is available at <https://github.com/JuliaGrajek/acidicTumorABM3D>. Moreover, it corroborates my first research hypothesis that including tumor-immune-TME interactions in a model provides a promising framework for ICI biomarker identification.

To achieve my second research aim, i.e. study the impact of CAIX expression on the TME and immunotherapy effectiveness and evaluate it as a combination therapy target, I worked with the above-mentioned model, supplemented with an ordinary differential equation model presented in [40]. By using two different model types, I was able to tackle the research problem from different perspectives. The hybrid model was much more complex than the ODE model, allowing for a holistic exploration of the TME's impact on immunotherapy effectiveness. Therefore, it helped me determine new interesting research hypotheses. In line with my research aim, I investigated the impact of CAIX expression on the TME, including the pH in the TME, as well as the tumor burden, the quantity of the tumor infiltrate, and the

compositions of the tumor and the immune infiltrate. The simulations support my second research hypothesis that CAIX expression induces an immuno-suppressive TME. The model successfully replicated the qualitative behavior of the tumor and TME observed in a pre-clinical experiment. Moreover, it helped uncover interactions between CAIX expression and the TME which had not been studied experimentally, such as the composition of the immune infiltrate or PD-L1 expression. Also in line with my second research aim, I evaluated how CAIX inhibition increased ICI efficacy in heterogeneous tumor groups. Most importantly, I observed that CAIX expression determines ICI treatment outcomes regardless of tumoral PD-L1 expression a treatment begin. This is an important observation, as PD-L1 is a controversial biomarker for ICI therapy, which is nowadays used in clinical practice, even though research shows that it does not always discriminate responders from non-responders. My simulations imply that CAIX expression might serve as a potential confounder of PD-L1 measurements. By impairing immune infiltration and activity, it reduces IFN- γ -induced PD-L1 expression. When inhibiting CAIX, however, the increased immune activity might upregulate PD-L1 expression, increasing the need for ICIs. Therefore, I believe that patients with CAIX-positive tumors should not be excluded from anti-PD-1 therapy based on their pre-treatment PD-L1 expression alone. These shortly summarized findings support my second research hypothesis that CAIX induces an immunosuppressive TME, impairing immune response and ICI therapy and serving as a putative confounder for other ICI biomarkers. These conclusions postulated CAIX as a promising combination therapy treatment and motivated me to further investigate this marker.

The computational model described above established the impact of CAIX expression on the TME and immune response quite well and offered some initial promising insights into its impact on ICI effectiveness. However, incorporating a more refined model of treatment with anti-CAIX and anti-PD-1 (see the pharmacokinetic model described in section 2.2. in [39]) proved difficult. Firstly, it added additional parameters to the already quite complex model, impeding its calibration. Secondly, the discrete timestep of 12h was too long for the investigation of the pharmacokinetics model, as the drug molecules decayed much faster, making the observation of interesting dynamics futile. The second problem could be alleviated by recalibrating the model to reduce the timestep, which might be an interesting approach for future research, although it would significantly increase computation time. However, I decided that a continuous model would be better suited to complement my previous research, i.e. to investigate combination therapies with ICIs and CAIX inhibition. In the planned research, I was mainly interested in non-spatial outcomes, such as tumor burden after treatment, a target for which a differential equation model would be sufficient. Additionally, I was hoping to supplement the previous qualitative numerical simulations with quantitative research and mathematical analysis of the model, for which continuous models are usually more appropriate. Hence, in [40], I developed an ordinary differential equation model based on the insights from my previous modeling approach. I calibrated the model with *in vitro* data from [37], showing, that the model can quantitatively reproduce experimental findings and setting some realistic parameter values for further simulations. Mathematical analysis of a simplified yet realistic version of the proposed model, together with numerical simulations of the full model, led to the conclusion that a combination of CAIX suppression and a sufficiently strong ICI dose (anti-PD-1 alone, anti-CTLA-4 alone or in combination) was synergistic in the way that it led to a complete and durable response. Monotherapies or combinations of just ICIs, on the other hand, resulted in tumor recurrence after treatment interruption, even after

initial reductions in tumor burden. This model and its analysis substantiate thus my third research hypothesis, concerning the efficacy of transient combinations of anti-CAIX and ICIs.

Finally, I also investigated factors impacting radioresistance, in particular, cellular plasticity and the resulting CSC dynamics in irradiated tumors, in line with my fourth and final research aim. This work was motivated by experimental data collected by an interdisciplinary research group for a study led by Dr. Claudia Peitzsch from the National Centre for Tumor Diseases in Dresden, Germany. This research group compared the impact of photon and proton irradiation on CSC dynamics. Some of the data, in particular flow cytometry analysis data concerning the dynamics of populations with putative stem cell markers (ALDH, CD44, CXCR4 and CD133), was in the form of time series, offering a possibility for mathematical modeling. In particular, the data on the ALDH+ and ALDH- population was of interest, as we also had data concerning the survival fraction of ALDH+ and ALDH- cells per irradiation dose available, facilitating model calibration. My aim with this modeling was to dive deeper than the *in vitro* experiments and try to infer whether the observed dynamics could be explained by cellular phenotype plasticity, as stated by the fourth and final research hypothesis of this thesis. Therefore, I proposed an ordinary differential equation model of CC and CSC and calibrated it with the collected *in vitro* data, with the assumption that ALDH was a perfect stemness marker. This is of course a simplification, but the data concerning ALDH+ and ALDH- dynamics was the only data collected that was suitable for the calibration of our model and provided a reasonable estimate of CSC dynamics. Our modeling revealed that both, plasticity events and reverse plasticity events vitally impacted ALDH+ and ALDH- dynamics, and implied that proton irradiation induced a lower rate of plasticity events than photon irradiation, complementing the conclusions from the experimental part of our study [56].

In conclusion, I believe that the work presented in this thesis and the described publications are in line with the research aims stated in this thesis and the obtained results and conclusions support my research hypotheses.

7.2 Limitations and future perspectives

The limitations of the immunotherapy models are precisely stated in the discussion sections of [39] and [40]. In this section, I will just mention the most important limitations and present some perspectives for further research. Most critically, it should be noted that while the models suggest some interesting interactions between CAIX inhibition and immunotherapy effectiveness, and propose promising research targets, they are not fully validated and thus, the conclusions derived from them require further verification. The validation of the model predictions on a distinct data set was not possible due to the lack of data availability concerning CAIX expression and ICI treatment. However, I believe that my research substantiates the investigation of CAIX as a combination therapy target and might motivate the collection of appropriate data. This illustrates one of the applications of *in silico* modeling, where research hypotheses might be tested in a relatively quick, inexpensive and ethical way, to identify those, which should be pursued further.

An interesting observation based on the simulations with the hybrid model presented in [39] was the abundant stroma accumulation in CAIX KO tumors, which confounded decreased tumor volumes. Interestingly, stroma has been postulated

to have either pro- or anti-tumorigenic properties, depending on the immune infiltration [83]. Studying the impact of stroma on ICI was not inside the scope of the study presented in [39], but it seems to be another promising factor, whose impact on the combination of anti-CAIX and ICI therapy could be evaluated. In particular, our model could be used for such an investigation, if calibrated to represent a tumor type linked to chronic inflammation-induced fibrosis, such as lung cancer [104].

In [40], we observed a lower CSC fraction in the CAIX KO tumors in some preliminary simulations. Again, investigating CSC dynamics after CAIX inhibition was out of scope in this study, but since CSC are believed to be the main drivers of tumor progression and treatment resistance, this constitutes another research idea worth pursuing. This is further substantiated by some clinical studies, which propose that CAIX inhibition sensitizes tumors to chemotherapy, where CSC are usually believed to be the main resistance and recurrence factors. For a short explanation of these studies, see the discussion section of [40].

Finally, the model of cellular plasticity was developed for the purpose of deepening our understanding of the experimental data gathered in [56]. Therefore, it focused on the interactions between radiotherapy and cellular plasticity, ignoring the impact of other factors of the TME. As mentioned in the introduction, the TME also induces plasticity events, and in turn, the distribution of CSC in the tumor heavily impacts other parts of the TME. Hence, I believe that further exploration of the TME and cellular plasticity could deepen our understanding of radioresistance and increase radioresponse rates.

In conclusion, while my research has contributed to the clarification of the impact of the TME on treatment resistance, it has also unveiled new interesting research questions. Therefore, I believe that the interplay between the TME and treatment resistance remains a promising topic for further exploration.

References

- [1] H. Sung, J. Ferlay, R. L. Siegel, *et al.*, “Global cancer statistics 2020: Globocan estimates of incidence and mortality worldwide for 36 cancers in 185 countries”, *CA: A Cancer Journal for Clinicians*, vol. 71, no. 3, pp. 209–249, 2021. DOI: 10.3322/caac.21660.
- [2] J. Ferlay, M. Colombet, I. Soerjomataram, *et al.*, “Cancer statistics for the year 2020: An overview”, *International Journal of Cancer*, vol. 149, no. 4, pp. 778–789, Aug. 2021, ISSN: 1097-0215. DOI: 10.1002/IJC.33588.
- [3] F. Bray, M. Laversanne, E. Weiderpass, and I. Soerjomataram, “The ever-increasing importance of cancer as a leading cause of premature death worldwide”, *Cancer*, vol. 127, no. 16, pp. 3029–3030, Aug. 2021, ISSN: 1097-0142. DOI: 10.1002/CNCR.33587.
- [4] M. Nikolaou, A. Pavlopoulou, A. G. Georgakilas, and E. Kyrodimos, “The challenge of drug resistance in cancer treatment: A current overview”, *Clinical & Experimental Metastasis* 2018 35:4, vol. 35, no. 4, pp. 309–318, May 2018, ISSN: 1573-7276. DOI: 10.1007/S10585-018-9903-0.
- [5] M. M. Gottesman, O. Lavi, M. D. Hall, and J. P. Gillet, “Toward a better understanding of the complexity of cancer drug resistance”, *Annual Review of Pharmacology and Toxicology*, vol. 56, pp. 85–102, Jan. 2016, ISSN: 15454304. DOI: 10.1146/ANNUREV-PHARMTOX-010715-103111.
- [6] N. Chatterjee and T. G. Bivona, “Polytherapy and targeted cancer drug resistance”, *Trends in Cancer*, vol. 5, no. 3, pp. 170–182, Mar. 2019, ISSN: 2405-8033. DOI: 10.1016/J.TRECAN.2019.02.003.
- [7] N. M. Anderson and M. C. Simon, “The tumor microenvironment”, *Current Biology*, vol. 30, no. 16, R921–R925, Aug. 2020, ISSN: 0960-9822. DOI: 10.1016/J.CUB.2020.06.081.
- [8] M. E. Hardee, M. W. Dewhirst, N. Agarwal, and B. S. Sorg, “Novel imaging provides new insights into mechanisms of oxygen transport in tumors”, *Current molecular medicine*, vol. 9, no. 4, pp. 435–441, Apr. 2009, ISSN: 15665240. DOI: 10.2174/156652409788167122.
- [9] B. I. Ratnikov, D. A. Scott, A. L. Osterman, J. W. Smith, and Z. A. Ronai, “Metabolic rewiring in melanoma”, *Oncogene* 2017 36:2, vol. 36, no. 2, pp. 147–157, Jun. 2016, ISSN: 1476-5594. DOI: 10.1038/onc.2016.198.
- [10] M. Abbott and Y. Ustoyev, “Cancer and the immune system: The history and background of immunotherapy”, *Seminars in Oncology Nursing*, vol. 35, no. 5, Oct. 2019, 150923, ISSN: 0749-2081. DOI: 10.1016/J.SONCN.2019.08.002.
- [11] R. D. Schreiber, L. J. Old, and M. J. Smyth, “Cancer immunoediting: Integrating immunity’s roles in cancer suppression and promotion”, *Science*, vol. 331, no. 6024, pp. 1565–1570, Mar. 2011, ISSN: 00368075. DOI: 10.1126/science.1203486.

- [12] M. P. Rausch and K. T. Hastings, "Immune checkpoint inhibitors in the treatment of melanoma: From basic science to clinical application", *Cutaneous Melanoma: Etiology and Therapy*, pp. 121–142, Dec. 2017. DOI: 10.15586/CODON.CUTANEOUSMELANOMA.2017.CH9.
- [13] S. C. Wei, C. R. Duffy, and J. P. Allison, "Fundamental mechanisms of immune checkpoint blockade therapy", *Cancer Discovery*, vol. 8, no. 9, pp. 1069–1086, Sep. 2018, ISSN: 21598290. DOI: 10.1158/2159-8290.CD-18-0367.
- [14] J. A. Seidel, A. Otsuka, and K. Kabashima, "Anti-pd-1 and anti-ctla-4 therapies in cancer: Mechanisms of action, efficacy, and limitations", *Frontiers in Oncology*, vol. 8, Mar. 2018. DOI: 10.3389/FONC.2018.00086.
- [15] N. Patsoukis, Q. Wang, L. Strauss, and V. A. Boussiotis, "Revisiting the pd-1 pathway", *Science Advances*, vol. 6, no. 38, Sep. 2020, ISSN: 23752548. DOI: 10.1126/sciadv.abd2712.
- [16] D. B. Johnson, C. A. Nebhan, J. J. Moslehi, and J. M. Balko, "Immune-checkpoint inhibitors: Long-term implications of toxicity", *Nature Reviews Clinical Oncology* 2022 19:4, vol. 19, no. 4, pp. 254–267, Jan. 2022, ISSN: 1759-4782. DOI: 10.1038/s41571-022-00600-w.
- [17] T. R. Cottrell and J. M. Taube, "Pd-1 and emerging biomarkers in pd-1/pd-11 blockade therapy", *Cancer journal (Sudbury, Mass.)*, vol. 24, no. 1, pp. 41–46, Jan. 2018, ISSN: 1540336X. DOI: 10.1097/PP0.0000000000000301.
- [18] A. Ribas and J. D. Wolchok, "Cancer immunotherapy using checkpoint blockade", *Science*, vol. 359, no. 6382, pp. 1350–1355, Mar. 2018, ISSN: 10959203. DOI: 10.1126/science.aar4060.
- [19] R. J. Walsh, R. Sundar, and J. S. J. Lim, "Immune checkpoint inhibitor combinations—current and emerging strategies", *British Journal of Cancer* 2023, pp. 1–3, Feb. 2023, ISSN: 1532-1827. DOI: 10.1038/s41416-023-02181-6.
- [20] *Fda approves opdualag for unresectable or metastatic melanoma*, <https://www.fda.gov/drugs/resources-information-approved-drugs/fda-approves-opdualag-unresectable-or-metastatic-melanoma>, Accessed: 20.05.2023.
- [21] F. S. Hodi, S. J. O'Day, D. F. McDermott, *et al.*, "Improved survival with ipilimumab in patients with metastatic melanoma", *New England Journal of Medicine*, vol. 363, no. 8, pp. 711–723, Aug. 2010, ISSN: 0028-4793. DOI: 10.1056/NEJMoa1003466.
- [22] W. Jia, Q. Gao, A. Han, H. Zhu, and J. Yu, "The potential mechanism, recognition and clinical significance of tumor pseudoprogression after immunotherapy", *Cancer Biology & Medicine*, vol. 16, no. 4, pp. 655–670, Nov. 2019, ISSN: 20953941. DOI: 10.20892/J.ISSN.2095-3941.2019.0144.
- [23] S. Litière, S. Collette, E. G. D. Vries, L. Seymour, and J. Bogaerts, "Recist — learning from the past to build the future", *Nature Reviews Clinical Oncology* 2016 14:3, vol. 14, no. 3, pp. 187–192, Dec. 2016, ISSN: 1759-4782. DOI: 10.1038/nrclinonc.2016.195.
- [24] L. Seymour, J. Bogaerts, A. Perrone, *et al.*, "Irecist: Guidelines for response criteria for use in trials testing immunotherapeutics", *The Lancet Oncology*, vol. 18, no. 3, pp. e143–e152, Mar. 2017, ISSN: 1473-0488. DOI: 10.1016/S1473-0488(17)30074-8.

- [25] R. J. Walsh and R. A. Soo, "Resistance to immune checkpoint inhibitors in non-small cell lung cancer: Biomarkers and therapeutic strategies.", *Therapeutic advances in medical oncology*, vol. 12, Jan. 2020, ISSN: 1758-8340. DOI: 10.1177/1758835920937902.
- [26] N. Gaynor, J. Crown, and D. M. Collins, "Immune checkpoint inhibitors: Key trials and an emerging role in breast cancer", *Seminars in Cancer Biology*, vol. 79, pp. 44–57, Feb. 2022, ISSN: 1044-579X. DOI: 10.1016/J.SEMCANCER.2020.06.016.
- [27] J. J. Havel, D. Chowell, and T. A. Chan, "The evolving landscape of biomarkers for checkpoint inhibitor immunotherapy", *Nature Reviews Cancer*, vol. 19, no. 3, pp. 133–150, Mar. 2019, ISSN: 14741768. DOI: 10.1038/s41568-019-0116-x.
- [28] J. Sunshine and J. M. Taube, "Pd-1/pd-l1 inhibitors", *Current Opinion in Pharmacology*, vol. 23, pp. 32–38, Aug. 2015, ISSN: 1471-4892. DOI: 10.1016/J.COPH.2015.05.011.
- [29] A. Osipov, S. J. Lim, A. Popovic, *et al.*, "Tumor mutational burden, toxicity, and response of immune checkpoint inhibitors targeting pd(l)1, ctla-4, and combination: A meta-regression analysis", *Clinical Cancer Research*, vol. 26, no. 18, pp. 4842–4851, Sep. 2020, ISSN: 15573265. DOI: 10.1158/1078-0432.CCR-20-0458.
- [30] M. Yarchoan, A. Hopkins, and E. M. Jaffee, "Tumor mutational burden and response rate to pd-1 inhibition", *New England Journal of Medicine*, vol. 377, no. 25, pp. 2500–2501, Dec. 2017, ISSN: 0028-4793. DOI: 10.1056/NEJMc1713444.
- [31] D. Sha, Z. Jin, J. Budczies, K. Kluck, A. Stenzinger, and F. A. Sinicrope, "Tumor mutational burden as a predictive biomarker in solid tumors", *Cancer Discovery*, vol. 10, no. 12, pp. 1808–1825, Dec. 2020, ISSN: 21598290. DOI: 10.1158/2159-8290.CD-20-0522.
- [32] D. J. McGrail, P. G. Pilié, N. U. Rashid, *et al.*, "High tumor mutation burden fails to predict immune checkpoint blockade response across all cancer types", *Annals of Oncology*, vol. 32, no. 5, pp. 661–672, May 2021, ISSN: 0923-7534. DOI: 10.1016/J.ANNONC.2021.02.006.
- [33] S. R. Pillai, M. Damaghi, Y. Marunaka, E. P. Spugnini, S. Fais, and R. J. Gillies, "Causes, consequences, and therapy of tumors acidosis", *Cancer and Metastasis Reviews*, vol. 38, no. 1-2, pp. 205–222, Jun. 2019, ISSN: 15737233. DOI: 10.1007/s10555-019-09792-7.
- [34] P. C. McDonald and S. Dedhar, "Carbonic anhydrase ix (caix) as a mediator of hypoxia-induced stress response in cancer cells", *Sub-Cellular Biochemistry*, vol. 75, pp. 255–269, 2014, ISSN: 03060225. DOI: 10.1007/978-94-007-7359-2_13.
- [35] M. Lie, N. M. Mazure, V. Hofman, *et al.*, "High levels of carbonic anhydrase ix in tumour tissue and plasma are biomarkers of poor prognostic in patients with non-small cell lung cancer", *British Journal of Cancer*, vol. 102, no. 11, pp. 1627–1635, May 2010, ISSN: 1532-1827. DOI: 10.1038/sj.bjc.6605690.
- [36] M. Z. Jin and W. L. Jin, "The updated landscape of tumor microenvironment and drug repurposing", *Signal Transduction and Targeted Therapy*, vol. 5, no. 1, pp. 1–16, Dec. 2020, ISSN: 20593635. DOI: 10.1038/s41392-020-00280-x.

- [37] S. C. Chafe, P. C. McDonald, S. Saberi, *et al.*, "Targeting hypoxia-induced carbonic anhydrase ix enhances immune-checkpoint blockade locally and systemically", *Cancer Immunology Research*, vol. 7, no. 7, pp. 1064–1078, Jul. 2019, ISSN: 2326-6066. DOI: 10.1158/2326-6066.CIR-18-0657.
- [38] I. W. Mak, N. Evaniew, and M. Ghert, "Lost in translation: Animal models and clinical trials in cancer treatment", *American Journal of Translational Research*, vol. 6, no. 2, p. 114, 2014, ISSN: 19438141.
- [39] J. Grajek, J. N. Kather, and J. Poleszczuk, "An in silico model to study the impact of carbonic anhydrase ix expression on tumour growth and anti-pd-1 therapy", *Journal of the Royal Society Interface*, vol. 20, no. 198, Jan. 2023, ISSN: 1742-5662. DOI: 10.1098/RSIF.2022.0654.
- [40] J. Grajek and J. Poleszczuk, "Carbonic anhydrase ix suppression shifts partial response to checkpoint inhibitors into complete tumor eradication: Model-based investigation", *International Journal of Molecular Sciences*, vol. 24, no. 12, Jun. 2023, 10068, ISSN: 1422-0067. DOI: 10.3390/IJMS241210068.
- [41] D. Schaue and W. H. McBride, "Opportunities and challenges of radiotherapy for treating cancer", *Nature reviews. Clinical oncology*, vol. 12, no. 9, 527–540, Sep. 2015, ISSN: 17594782. DOI: 10.1038/NRCLINONC.2015.120.
- [42] D. Citrin, "Recent developments in radiotherapy", *The New England journal of medicine*, vol. 377, no. 11, pp. 341–350, 2017, ISSN: 1533-4406. DOI: 10.1056/NEJMRA1608986.
- [43] S. Adjemian, T. Oltean, S. Martens, *et al.*, "Ionizing radiation results in a mixture of cellular outcomes including mitotic catastrophe, senescence, methuosis, and iron-dependent cell death", *Cell Death & Disease*, vol. 11, no. 11, pp. 1–15, Nov. 2020, ISSN: 2041-4889. DOI: 10.1038/s41419-020-03209-y.
- [44] H. H. Chen and M. T. Kuo, "Improving radiotherapy in cancer treatment: Promises and challenges", *Oncotarget*, vol. 8, no. 37, pp. 62742–62758, Sep. 2017, ISSN: 19492553. DOI: 10.18632/ONCOTARGET.18409.
- [45] H. E. Barker, J. T. Paget, A. A. Khan, and K. J. Harrington, "The tumour microenvironment after radiotherapy: Mechanisms of resistance and recurrence", *Nature Reviews Cancer*, vol. 15, no. 7, pp. 409–425, Jun. 2015, ISSN: 1474-1768. DOI: 10.1038/nrc3958.
- [46] B. M. Kim, Y. Hong, S. Lee, *et al.*, "Therapeutic implications for overcoming radiation resistance in cancer therapy", *International Journal of Molecular Sciences*, vol. 16, no. 11, pp. 26880–26913, Nov. 2015, ISSN: 1422-0067. DOI: 10.3390/IJMS161125991.
- [47] I. Larionova, M. Rakina, E. Ivanyuk, Y. Trushchuk, A. Chernyshova, and E. Denisov, "Radiotherapy resistance: Identifying universal biomarkers for various human cancers", *Journal of Cancer Research and Clinical Oncology*, vol. 148, no. 5, pp. 1015–1031, Feb. 2022, ISSN: 1432-1335. DOI: 10.1007/S00432-022-03923-4.
- [48] Y. Liu, M. Yang, J. Luo, and H. Zhou, "Radiotherapy targeting cancer stem cells "awakens" them to induce tumour relapse and metastasis in oral cancer", *International Journal of Oral Science*, vol. 12, no. 1, pp. 1–12, Jun. 2020, ISSN: 2049-3169. DOI: 10.1038/s41368-020-00087-0.

- [49] H. Bartelink, J.-C. Horiot, P. Poortmans, *et al.*, "Recurrence rates after treatment of breast cancer with standard radiotherapy with or without additional radiation", *New England Journal of Medicine*, vol. 345, no. 19, pp. 1378–1387, 2001, PMID: 11794170. DOI: 10.1056/NEJMoa010874.
- [50] B. M. Beadle, A. Jhingran, S. S. Yom, P. T. Ramirez, and P. J. Eifel, "Patterns of regional recurrence after definitive radiotherapy for cervical cancer", *International Journal of Radiation Oncology*Biophysics*, vol. 76, no. 5, pp. 1396–1403, Apr. 2010, ISSN: 0360-3016. DOI: 10.1016/J.IJROBP.2009.04.009.
- [51] S. Senthil, F. J. Lagerwaard, C. J. Haasbeek, B. J. Slotman, and S. Senan, "Patterns of disease recurrence after stereotactic ablative radiotherapy for early stage non-small-cell lung cancer: A retrospective analysis", *The Lancet Oncology*, vol. 13, no. 8, pp. 802–809, Aug. 2012, ISSN: 1470-2045. DOI: 10.1016/S1470-2045(12)70242-5.
- [52] E. Vlashi, W. H. McBride, and F. Pajonk, "Radiation responses of cancer stem cells", *Journal of Cellular Biochemistry*, vol. 108, no. 2, pp. 339–342, Oct. 2009, ISSN: 1097-4644. DOI: 10.1002/JCB.22275.
- [53] A. M. McCord, M. Jamal, E. S. Williams, K. Camphausen, and P. J. Tofilon, "Cd133+ glioblastoma stem-like cells are radiosensitive with a defective dna damage response compared with established cell lines", *Clinical Cancer Research*, vol. 15, no. 16, pp. 5145–5153, Aug. 2009, ISSN: 10780432. DOI: 10.1158/1078-0432.CCR-09-0263.
- [54] C. R. Arnold, J. Mangesius, I. I. Skvortsova, and U. Ganswindt, "The role of cancer stem cells in radiation resistance", *Frontiers in Oncology*, vol. 10, Feb. 2020, ISSN: 2234943X. DOI: 10.3389/fonc.2020.00164.
- [55] J. E. Visvader and G. J. Lindeman, "Cancer stem cells in solid tumours: Accumulating evidence and unresolved questions", *Nature Reviews Cancer*, vol. 8, no. 10, pp. 755–768, Sep. 2008, ISSN: 1474-1768. DOI: 10.1038/nrc2499.
- [56] I. Schniewind, W. W. Hadiwikarta, J. Grajek, *et al.*, "Cellular plasticity upon proton irradiation determines tumor cell radiosensitivity", *Cell Reports*, vol. 38, no. 8, Feb. 2022, 110422, ISSN: 2211-1247. DOI: 10.1016/J.CELREP.2022.110422.
- [57] M. A. Olivares-Urbano, C. Griñán-Lisón, J. A. Marchal, and M. I. Núñez, "Csc radioresistance: A therapeutic challenge to improve radiotherapy effectiveness in cancer", *Cells*, vol. 9, no. 7, Jul. 2020, 1651, ISSN: 2073-4409. DOI: 10.3390/CELLS9071651.
- [58] M. Krause, A. Dubrovskaja, A. Linge, and M. Baumann, "Cancer stem cells: Radioresistance, prediction of radiotherapy outcome and specific targets for combined treatments", *Advanced Drug Delivery Reviews*, vol. 109, pp. 63–73, Jan. 2017, ISSN: 0169-409X. DOI: 10.1016/J.ADDR.2016.02.002.
- [59] A. Schulz, F. Meyer, A. Dubrovskaja, and K. Borgmann, "Cancer stem cells and radioresistance: Dna repair and beyond", *Cancers*, vol. 11, no. 6, Jun. 2019, 862, ISSN: 2072-6694. DOI: 10.3390/CANCERS11060862.
- [60] M. C. Cabrera, R. E. Hollingsworth, and E. M. Hurt, "Cancer stem cell plasticity and tumor hierarchy", *World Journal of Stem Cells*, vol. 7, no. 1, pp. 27–36, Jan. 2015, ISSN: 1948-0210. DOI: 10.4252/WJSC.V7.I1.27.
- [61] E. Vlashi and F. Pajonk, "Cancer stem cells, cancer cell plasticity and radiation therapy", *Seminars in Cancer Biology*, vol. 31, pp. 28–35, Apr. 2015, ISSN: 1044-579X. DOI: 10.1016/J.SEMCANCER.2014.07.001.

- [62] X. Zheng, C. Yu, and M. Xu, "Linking tumor microenvironment to plasticity of cancer stem cells: Mechanisms and application in cancer therapy", *Frontiers in Oncology*, vol. 11, Jun. 2021, 678333, ISSN: 2234943X. DOI: 10.3389/fonc.2021.678333.
- [63] P. K. Das, S. Pillai, M. A. Rakib, *et al.*, "Plasticity of cancer stem cell: Origin and role in disease progression and therapy resistance", *Stem Cell Reviews and Reports*, vol. 16, no. 2, pp. 397–412, Jan. 2020, ISSN: 2629-3277. DOI: 10.1007/S12015-019-09942-Y.
- [64] W. P. Levin, H. Kooy, J. S. Loeffler, and T. F. DeLaney, "Proton beam therapy", *British Journal of Cancer*, vol. 93, no. 8, pp. 849–854, Sep. 2005, ISSN: 1532-1827. DOI: 10.1038/sj.bjc.6602754.
- [65] Z. Chen, M. M. Dominello, M. C. Joiner, and J. W. Burmeister, "Proton versus photon radiation therapy: A clinical review", *Frontiers in Oncology*, vol. 13, Mar. 2023, 1230, ISSN: 2234943X. DOI: 10.3389/fonc.2023.1133909.
- [66] H. Willers, A. Allen, D. Grosshans, *et al.*, "Toward a variable rbe for proton beam therapy", *Radiotherapy and Oncology*, vol. 128, no. 1, pp. 68–75, Jul. 2018, ISSN: 0167-8140. DOI: 10.1016/J.RADONC.2018.05.019.
- [67] R. A. Mitteer, Y. Wang, J. Shah, *et al.*, "Proton beam radiation induces dna damage and cell apoptosis in glioma stem cells through reactive oxygen species", *Scientific Reports*, vol. 5, no. 1, pp. 1–12, Sep. 2015, ISSN: 2045-2322. DOI: 10.1038/srep13961.
- [68] Q. Fu, Y. Quan, W. Wang, *et al.*, "Response of cancer stem-like cells and non-stem cancer cells to proton and gamma-ray irradiation", *Nuclear Instruments and Methods in Physics Research Section B: Beam Interactions with Materials and Atoms*, vol. 286, pp. 346–350, Sep. 2012, ISSN: 0168-583X. DOI: 10.1016/J.NIMB.2012.01.032.
- [69] C. Peitzsch, M. Cojoc, L. Hein, *et al.*, "An epigenetic reprogramming strategy to resensitize radioresistant prostate cancer cells", *Cancer Research*, vol. 76, no. 9, pp. 2637–2651, May 2016, ISSN: 15387445. DOI: 10.1158/0008-5472.CAN-15-2116.
- [70] S. Bekisz and L. Geris, "Cancer modeling: From mechanistic to data-driven approaches, and from fundamental insights to clinical applications", *Journal of Computational Science*, vol. 46, Oct. 2020, 101198, ISSN: 1877-7503. DOI: 10.1016/J.JOCS.2020.101198.
- [71] N. S. Mak and M. L. Stephens, "History of the rs in toxicity testing: From russel and burch to 21st century toxicology", in *Reducing, Refining and Replacing the Use of Animals in Toxicity Testing*. D. G. Allen and M. D. Waters, Eds., vol. 19, 2014, pp. 1–39, ISBN: 978-1-84973-652-7.
- [72] F. Barré-Sinoussi and X. Montagutelli, "Animal models are essential to biological research: Issues and perspectives", *Future Science OA*, vol. 1, no. 4, Nov. 2015, ISSN: 20565623. DOI: 10.4155/FSO.15.63.
- [73] C. G. Begley and L. M. Ellis, "Raise standards for preclinical cancer research", *Nature* 2012 483:7391, vol. 483, no. 7391, pp. 531–533, Mar. 2012, ISSN: 1476-4687. DOI: 10.1038/483531a.
- [74] G. E. P. Box and N. R. Draper, *Empirical Model-Building and Response Surface*. 1987, pp. 424–424, ISBN: 978-0471810339.

- [75] L. G. de Pillis and A. E. Radunskaya, "Modeling tumor-immune dynamics", in *Mathematical Models of Tumor-Immune System Dynamics*, A. Eladdadi, P. Kim, and D. Mallet, Eds., vol. 107, Springer, 2014, ISBN: 978-1-4939-1792-1.
- [76] V. A. Kuznetsov, I. A. Makalkin, M. A. Taylor, and A. S. Perelson, "Nonlinear dynamics of immunogenic tumors: Parameter estimation and global bifurcation analysis", *Bulletin of Mathematical Biology*, vol. 56, no. 2, pp. 295–321, 1994, ISSN: 15229602. DOI: 10.1007/BF02460644.
- [77] R. Eftimie, J. L. Bramson, and D. J. Earn, "Interactions between the immune system and cancer: A brief review of non-spatial mathematical models", *Bulletin of Mathematical Biology*, vol. 73, no. 1, pp. 2–32, Jan. 2011, ISSN: 15229602. DOI: 10.1007/s11538-010-9526-3.
- [78] J. D. Butner, Z. Wang, D. Elganainy, *et al.*, "A mathematical model for the quantification of a patient's sensitivity to checkpoint inhibitors and long-term tumour burden", *Nature Biomedical Engineering*, vol. 5, no. 4, pp. 297–308, Jan. 2021, ISSN: 2157-846X. DOI: 10.1038/s41551-020-00662-0.
- [79] X. Lai and A. Friedman, "Combination therapy of cancer with cancer vaccine and immune checkpoint inhibitors: A mathematical model", *PLOS ONE*, vol. 12, no. 5, e0178479, May 2017, ISSN: 1932-6203. DOI: 10.1371/JOURNAL.PONE.0178479.
- [80] A. Radunskaya, R. Kim, and T. W. II, "Mathematical modeling of tumor immune interactions: A closer look at the role of a pd-1 inhibitor in cancer immunotherapy", *Spora: A Journal of Biomathematics*, vol. 4, no. 1, pp. 25–41, Apr. 2018, ISSN: 2473-5493. DOI: 10.30707/SPORA4.1Radunskaya.
- [81] O. Milberg, C. Gong, M. Jafarnejad, *et al.*, "A qsp model for predicting clinical responses to monotherapy, combination and sequential therapy following ctla-4, pd-1, and pd-11 checkpoint blockade", *Scientific Reports*, vol. 9, no. 1, pp. 1–17, Aug. 2019, ISSN: 2045-2322. DOI: 10.1038/s41598-019-47802-4.
- [82] J. Gong, A. Chehrazi-Raffle, S. Reddi, and R. Salgia, "Development of pd-1 and pd-11 inhibitors as a form of cancer immunotherapy: A comprehensive review of registration trials and future considerations", *Journal for immunotherapy of cancer*, vol. 6, no. 1, Jan. 2018, ISSN: 2051-1426. DOI: 10.1186/s40425-018-0316-z.
- [83] J. N. Kather, J. Poleszczuk, M. Suarez-Carmona, *et al.*, "In silico modeling of immunotherapy and stroma-targeting therapies in human colorectal cancer", *Cancer Research*, vol. 77, no. 22, pp. 6442–6452, Nov. 2017, ISSN: 15387445. DOI: 10.1158/0008-5472.CAN-17-2006.
- [84] J. N. Kather, P. Charoentong, M. Suarez-Carmona, *et al.*, "High-throughput screening of combinatorial immunotherapies with patient-specific in silico models of metastatic colorectal cancer", *Cancer Research*, vol. 78, no. 17, pp. 5155–5163, Sep. 2018, ISSN: 15387445. DOI: 10.1158/0008-5472.CAN-18-1126.
- [85] H. N. Weerasinghe, P. M. Burrage, K. Burrage, and D. V. Nicolau, "Mathematical models of cancer cell plasticity", *Journal of Oncology*, vol. 2019, 2019, ISSN: 16878469. DOI: 10.1155/2019/2403483.
- [86] C. M. van Leeuwen, A. L. Oei, J. Crezee, *et al.*, "The alfa and beta of tumours: A review of parameters of the linear-quadratic model, derived from clinical radiotherapy studies", *Radiation Oncology*, vol. 13, no. 1, pp. 1–11, May 2018, ISSN: 1748717X. DOI: 10.1186/s13014-018-1040-z.

- [87] S. J. McMahon, "The linear quadratic model: Usage, interpretation and challenges", *Physics in Medicine & Biology*, vol. 64, no. 1, 01TR01, Dec. 2018, ISSN: 0031-9155. DOI: 10.1088/1361-6560/AAF26A.
- [88] V. Y. Yu, D. Nguyen, F. Pajonk, *et al.*, "Incorporating cancer stem cells in radiation therapy treatment response modeling and the implication in glioblastoma multiforme treatment resistance", *International Journal of Radiation Oncology*Biophysics*, vol. 91, no. 4, pp. 866–875, Mar. 2015, ISSN: 0360-3016. DOI: 10.1016/J.IJROBP.2014.12.004.
- [89] V. Y. Yu, D. Nguyen, D. OConnor, *et al.*, "Treating glioblastoma multiforme (gbm) with super hyperfractionated radiation therapy: Implication of temporal dose fractionation optimization including cancer stem cell dynamics", *PLOS ONE*, vol. 16, no. 2, e0245676, Feb. 2021, ISSN: 1932-6203. DOI: 10.1371/JOURNAL.PONE.0245676.
- [90] X. S. Qi, F. Pajonk, S. McCloskey, *et al.*, "Radioresistance of the breast tumor is highly correlated to its level of cancer stem cell and its clinical implication for breast irradiation", *Radiotherapy and Oncology*, vol. 124, no. 3, pp. 455–461, Sep. 2017, ISSN: 0167-8140. DOI: 10.1016/J.RADONC.2017.08.019.
- [91] A. Dhawan, M. Kohandel, R. Hill, and S. Sivaloganathan, "Tumour control probability in cancer stem cells hypothesis", *PLOS ONE*, vol. 9, no. 5, e96093, May 2014, ISSN: 1932-6203. DOI: 10.1371/JOURNAL.PONE.0096093.
- [92] F. Forouzannia, S. Sivaloganathan, and M. Kohandel, "A mathematical study of the impact of cell plasticity on tumour control probability", *Mathematical Biosciences and Engineering*, vol. 17, 2020. DOI: 10.3934/mbe.2020284.
- [93] K. Leder, K. Pitter, Q. Laplant, *et al.*, "Mathematical modeling of pdgf-driven glioblastoma reveals optimized radiation dosing schedules", *Cell*, vol. 156, no. 3, pp. 603–616, Jan. 2014, ISSN: 0092-8674. DOI: 10.1016/J.CELL.2013.12.029.
- [94] J. A. Dean, S. K. Tanguturi, D. Cagney, *et al.*, "Neuro-oncology phase i study of a novel glioblastoma radiation therapy schedule exploiting cell-state plasticity", vol. 25, no. 6, 2022. DOI: 10.1093/neuonc/noac253.
- [95] J. Poleszczuk and H. Enderling, "Cancer stem cell plasticity as tumor growth promoter and catalyst of population collapse", *Stem Cells International*, vol. 2016, 2016, ISSN: 16879678. DOI: 10.1155/2016/3923527.
- [96] E. Bonabeau, "Agent-based modeling: Methods and techniques for simulating human systems", *Proceedings of the National Academy of Sciences of the United States of America*, vol. 99, no. suppl. 3, pp. 7280–7287, May 2002, ISSN: 00278424. DOI: 10.1073/pnas.082080899.
- [97] S. Railsback and V. Grimm, *Agent-Based and Individual-Based Modeling: A practical introduction*, second edition. Princeton University Press, 2019, ISBN: 978-0-691-1982-2.
- [98] J. Poleszczuk, P. Hahnfeldt, and H. Enderling, "Evolution and phenotypic selection of cancer stem cells", *PLOS Computational Biology*, vol. 11, no. 3, A. Rzhetsky, Ed., e1004025, Mar. 2015, ISSN: 1553-7358. DOI: 10.1371/journal.pcbi.1004025.
- [99] J. Poleszczuk and H. Enderling, "Cancer stem cell plasticity as tumor growth promoter and catalyst of population collapse", *Stem Cells International*, vol. 2016, 2016, ISSN: 16879678. DOI: 10.1155/2016/3923527.

- [100] C. B. Harley, "Telomere loss: Mitotic clock or genetic time bomb?", *Mutation Research DNAging*, vol. 256, no. 2-6, pp. 271–282, Mar. 1991, ISSN: 09218734. DOI: 10.1016/0921-8734(91)90018-7.
- [101] A. Eramo, F. Lotti, G. Sette, *et al.*, "Identification and expansion of the tumorigenic lung cancer stem cell population", *Cell Death and Differentiation*, vol. 15, no. 3, pp. 504–514, Mar. 2008, ISSN: 13509047. DOI: 10.1038/sj.cdd.4402283.
- [102] L. Yang, P. Shi, G. Zhao, *et al.*, "Targeting cancer stem cell pathways for cancer therapy", *Signal Transduction and Targeted Therapy*, vol. 5, no. 1, pp. 1–35, Feb. 2020, ISSN: 2059-3635. DOI: 10.1038/s41392-020-0110-5.
- [103] J. Thoms and R. G. Bristow, "Dna repair targeting and radiotherapy: A focus on the therapeutic ratio", *Seminars in Radiation Oncology*, vol. 20, no. 4, pp. 217–222, 2010, ISSN: 1053-4296. DOI: 10.1016/j.semradonc.2010.06.003.
- [104] S. Noguchi, A. Saito, and T. Nagase, "Yap/taz signaling as a molecular link between fibrosis and cancer", *International Journal of Molecular Sciences*, vol. 19, no. 11, Nov. 2018, 3674, ISSN: 1422-0067. DOI: 10.3390/IJMS19113674.